Synthesis and Reactivity of Non-Heme Iron-Nitrosyl Complexes that Model the Active Sites of NO Reductases

by

Hai T. Dong

A dissertation submitted in partial fulfillment
of the requirements for the degree of
Doctor of Philosophy
(Chemistry)
in The University of Michigan
2021

Doctoral Committee

Professor Nicolai Lehnert, Chair
Professor Vincent L. Pecoraro
Professor Stephen W. Ragsdale
Professor Nathaniel Szymczak

Hai T. Dong

haitdong@umich.edu

ORCID iD: 0000-0002-8914-3045

Dedication

To my mom, Nguyễn Thị Thu Hà, to my late father Đồng Như Thành, to my brothers Sơn and Dũng, and to my late stepfather Vũ Xuân Lân.

Acknowledgements

I couldn't imagine finishing my PhD without the constant support from the people closest to me. I owe my development as a scientist, a chemist, a mentor, and, especially, a person to my family, mentors, labmates, and friends, without whom, I would not be the person I am today.

My journey to complete the PhD would not have been possible without the constant encouragement, support, and mentorship of my advisor, Professor Nicolai Lehnert. The day I first met you was not when I came to your office to talk to you about my rotation, it was during my visitation weekend when I sat at the same table as you. I had no idea at that time that I was about to share an incredible journey in science with you. You have shown me, from the first day I joined the lab, how much fun science could be. You have shown me your dedication to teaching and inspired me to become the best scientist I could be. I remember in my laboratory rotation, you have dedicated a great amount of time in your busy schedule to teach me how to do DFT one-on-one that entire semester. You have given me all the learning opportunities I asked for and more. You have been my biggest ally when things were tough both inside and outside of the laboratory. You have never let me settle for even a moment in my PhD and you have pushed me harder than anyone has, and for that, I am grateful. You consistently set the bar higher every time I thought I had met the expectation and in doing so you made me believe in myself through every new challenge in grad school and achieved more than I thought I could. I am grateful for your lessons, your criticism,

your rigor, your attention to detail through every project I started in the laboratory. You taught me to be the scientist I am today.

I have been extremely fortunate to have learned from many professors in the department. To my committee, Profs. Vincent Pecoraro, Nathaniel Szymczak, and Stephen Ragsdale, thank you for your feedback and support. I want to thank my undergrad advisor, Prof. Hairong Guan, who inspired me to pursuit a PhD in chemistry and instill in me the desire to become a great educator like you. I want to thank the late Prof. William Connick who have given me my first opportunity to do research as an unexperienced first-year undergraduate student and Prof. Bruce Ault who have shown me kindness and have guided me through college as a chemistry major.

To my labmates, past and present, I am grateful to have shared this journey with you all. I have never encountered such a diverse group of extremely smart and hardworking people. Thank you, Dr. Corey J. White, for your mentorship and the time we spent being on the non-heme team with all the ups and downs. Thank you, Brad, for being an awesome friend in the lab, whose friendship is important to me. Thank you, Jill, for being there during the toughest time of my PhD and for always being kind to other people, I learned a lot from you. Allie, thank you for being an awesome friend and a greater bubble tea partner. Molly, Victor, Lizzie, Virginia, Garrett, Matt, Subhra, thank you for your comradery. I will miss the coffee breaks and the fun time we share in lab together. You guys made my PhD a fun and relaxed experience.

To my students, thank you Stephanie for being my first undergraduate student and for being patient with me when I was an inexperience mentor in my second year of PhD. You have shown resiliency in science and you have always showed up with the highest level of work ethic, for that, I am grateful to have had the chance to be your mentor. Thank you, Yu, for an awesome summer of fun with ligand synthesis. Abby, thank you for your hard work during the last two semesters of

my PhD. You have made my last semesters of PhD fun and together we have grown so many cool crystal structures. Michael, thank you for your dedication to the science and willingness to always learn and improve. Thank you, Jessica and Wei, for giving me the chance to mentor you in my early inexperienced days. I wish you all the best on your future endeavors.

I want to thank the staffs in the chemistry department who have made my time in the PhD program much easier. In particular, I want to thank Liz Oxford, Katie Foster, Roy Wentz, Tracy Stevenson, and many others for always being positive and welcoming, for excelling at what they do daily to make our lives easier.

I especially want to thank Dr. Jeff Kampf, who has helped me obtaining so many beautiful crystal structures, for always being patient to look through my crystals to find the best set of data. I will always enjoy our conversations about science and, occasionally, life outside of the laboratory.

I want to thank all my friends, both in Ann Arbor and around the world who have in some ways supported me throughout my PhD. I am grateful to have known a lot of kind and good friends who are there for both the ups and the downs of my time here. Suyeon, thank you for being an awesome thesis writing partner, I am excited to see the things that you will accomplish in your PhD at Cornell.

To Michael Wade Wolfe, I really do not know where to start. We have been best friends since day one in the program when we first met in the Szymczak lab. We have been through the lowest and the highest points of our lives in the past 5 years together. A lot of things have changed in my PhD, but the only constant has always been our friendship. Thank you for being the best friend a guy could have asked for. I will miss the daily lunch/coffee breaks. I have always enjoyed our random walks around the campus to talk about science, life, and pretty much anything in the

world. I am looking forward to seeing you succeed at whatever you choose to do in life next. Just like you said, and I agreed, life is an anime and we are at the best arc so we should enjoy it.

I want to thank my family and my extended family at home who have always been there not only for me but also for my mom and my brother. There are too many people to thank so I would like to just say that I hope to see you all soon in Vietnam to celebrate this milestone in life.

And lastly, to my mom and my two brothers, this PhD is a team effort. I would not have been able to be here without my mom constant sacrifices and love. She is a woman of science and is my first and my biggest role model in life. She has loved, cared, and supported me and my brothers unconditionally every day since the day I was born. I do not know how you could have done all of this for us and more as a single mom. Thank you for giving me the life that I am living and for always reminding me of the important values in life. You are my compass in life, my best friend, and my best teammate in science. Thank you for always holding me accountable for my actions and for teaching me how to be a good person. You are incredible and I love you so much.

Table of Contents

List of Schemes

List of Tables

List of Figures

Abstract

As we are inching closer to the end of the COVID-19 pandemic, it is important for us to be better prepared for other potential pandemic scenarios such as a potential new strain of super bacteria that can resist known antibiotics. Nitric oxide (NO) is utilized by our immune system to fight invading pathogens. Through natural selection, some pathogens have adapted flavodiiron proteins (FDPs) to reduce NO to nitrous oxide (N_2O) (so-called flavodiiron NO reductases, FNORs). These enzymes protect the microbes from nitrosative stress and mitigate the toxicity of NO generated in the human immune response. Mechanistic studies on the *Thermatoga maritima* (*Tm*) FDP have shown that a high-spin (hs) diiron dinitrosyl intermediate, or [hs-{Fe(NO)}^{7}]$_2$ in Enemark-Feltham notation, is the critical intermediate that forms prior to NO reduction. However, the succeeding steps of the reaction and the other intermediates prior to N_2O release have remained elusive.

In this thesis, several new mono- and dinuclear Fe(II) model complexes are reported. The reactivity of these complexes towards NO and hyponitrite ($N_2O_2^{2-}$) was then investigated to (a) explore different mechanistic possibilities for FNORs, (b) determine under which conditions different mechanistic pathways are activated, and (c) characterize potential intermediates of the reaction. Whereas mechanistic studies on *Tm* FDP favor the so-called *direct NO reduction* pathway, no diiron dinitrosyl model complex is able to mediate this reaction. All known model

systems prior to my work require one-electron reduction to generate N_2O (the *semireduced* pathway) via a proposed hs-{Fe(NO)}^{7}/hs-{Fe(NO)}^{8} intermediate.

Here, I report the new model complex $[Fe^{II}_2((Py_2PhO_2)MP)(OAc)_2]^-$ (**1**), which is the first model system that can catalyze the direct reduction of NO to N_2O. My results show that reduction potential is a key trigger to activate the direct NO reduction pathway in diiron complexes. The reaction of **1** with NO is so efficient (even at -80°C) that the isolation of reaction intermediates was not possible. By using a mononuclear model of **1** I was able to isolate a highly activated mononuclear hs-{FeNO}^{7} complex with a record low N–O stretching frequency of 1689 cm^{-1}. These studies demonstrate that hs-{FeNO}^{7} species with N–O stretching frequencies ≤ 1700 cm^{-1} are activated for direct NO reduction, but that a diiron core is critically important to enable this reaction. Additionally, the role of second coordination sphere hydrogen bond donors and the chemistry of non-heme iron complexes with hyponitrite relevant for the NO reduction in FNORs were also evaluated through the synthesis and characterization of new complexes reported in this thesis.

Using mononuclear systems, I explored unique reactions that hs-{FeNO}^{8} complexes can mediate. The hs-{FeNO}^{7} complex with the weak-field ligand BMPA-tBu_2PhOH forms a dinitrosyl iron complex (DNIC) upon reduction, in line with previous observations in the literature. When TPA is used as the ligand scaffold, stabilization of an unprecedented complex with a $Fe_2(NO)_2$ diamond core structure is observed instead. This complex is stabilized by a change to the low-spin state of the iron centers. I propose that a similar $Fe_2(NO)_2$ motif is the key intermediate for DNIC formation when the irons remain high-spin.

Finally, to investigate iron-nitrosyl complexes beyond the {FeNO}^{8} state, a novel ls-{FeNO}$^{8\text{-}10}$ series (prepared by Peters and coworkers) was spectroscopically and theoretically

characterized. The results show that a reverse-dative Fe→B interaction is the key to stabilize the unique oxidation states that go beyond the $\{FeNO\}^8$ state.

Chapter 1

Introduction

Adapted from (1) Lehnert, N.; Fujisawa, K.; Camarena, S.; Dong, H. T.; White, C. J. Activation of Non-Heme Iron-Nitrosyl Complexes: Turning up the Heat. *ACS Catal.* 2019, *9*, 10499-10518 and the submitted article (2) Lehnert, N.; Kim, E.; Dong, H. T.; Harland, J. B.; Hunt, A. P.; Manickas, E. C.; Oakley, K. M.; Pham, J.; Reed, G.; Alfaro, V. S. The Biologically Relevant Coordination Chemistry of Nitric Oxide: Electronic Structure and Reactivity. *Chem. Rev.,* 2021, *manuscript accepted after revision*

1.1 Historical View of NO as A Molecule

Nitric oxide has been viewed for a long time as an environmental pollutant due to its highly toxic and corrosive properties. It is generated from the burning of fossil fuels in power plants, furnaces and engines. It is one of the main contributors to chemical smog happen around industrial areas. NO is poisonous to humans at very low concentrations of only 100 ppm in air, by formation of highly toxic NO_2, shutting down respiration, disabling iron-sulfur proteins like aconitase and reacting with oxy-hemoglobin (oxy-Hb, Hb(II)-O_2) to form met-Hb (Hb(III), with iron in the +III state). This view of NO was quickly changed in the 1980s when it was first realized that NO plays an important role in immune defense and signaling in humans. NO sparked the curiosity of the scientific community, which lead to a new era of research on its role in the human body. This eventually lad to it being named the "Molecule of the Year" by the Science magazine, and subsequently in 1998 the Nobel Prize in Medicine was awarded to Furchgott, Ignarro and Murad for the discovery that NO is an endogenously produced vasodilator in mammals, and an important

signaling molecule in general.[1-3] Iron plays a dominant role in much of the biologically relevant chemistry of NO, including NO generation, sensing, and break-down, which explains the surge in studies on the iron-based coordination chemistry of NO and its oxidized and reduced derivatives (especially nitrite and HNO) in the last four decades.

In mammals, nitric oxide is produced by the Nitric Oxide Synthase (NOS) family of enzymes, which use a {heme-thiolate} active site, similar to Cyt. P450s, to oxidatively convert L-arginine to citrulline and NO.[4-7] Mammals make use of the fact that NO is actually highly toxic, and use it for immune defense.[8,9] For example, our macrophages use inducible NOS (iNOS) to produce up to micromolar concentrations of NO (and other toxic chemicals, especially superoxide) to kill invading pathogens.[10,11] In particular, NO is able to inhibit a number of important enzymes (including Cyt. P450s, heme-copper oxidases (respiration), etc.) and break down iron-sulfur cluster, which are all believed to be ways in which NO can kill infectious microbes. In addition, NO and superoxide combine in a very fast reaction (second order rate constant, $k = 5\times10^9\ M^{-1}s^{-1}$) to generate peroxynitrite,

$$NO + O_2^- \rightarrow ONOO^- \qquad \textbf{(1)}$$

which is a highly toxic molecule that oxidatively damages cells, including pathogens, and which is therefore another key component of immune defense. However, NO's important function in immune defense has a dark side as well:[12] here, the constant flux of micromolar concentrations of NO produced in areas of chronic infection (inflammation) causes tissue and cartilage degradation, organ failure, etc.[13,14] Similarly, overproduction of NO causes neurodegeneration and neuropathic pain,[15,16] and NO is also being considered now a key contributor to neurodegenerative diseases.[17] Finally, NO is a key player in septic shock.[18-21]

Interestingly, a number of pathogens have evolved defense strategies against NO toxicity, using flavodiiron NO reductases (FNORs) to catalyze the breakdown of NO by reduction to less toxic N_2O,[22-28] following the 'classic' NO reduction reaction in denitrification:

$$2\ NO + 2\ e^- + 2\ H^+ \rightarrow N_2O + H_2O \quad \textbf{(2)}$$

Here, transcription factors are used to sense NO, and when NO is detected, transcription of genes expressing these defense proteins is induced.[24]

1.2 Flavodiiron Nitric Oxide Reductases (FNORs)

NO eliminating enzymes are found in pathogens and they function to combat nitrosative stress. Besides nitric oxide dioxygenases, pathogens can also express FNORs, which are active in low oxygen environments.[23] FNORs are scavenging flavodiiron proteins (FDPs) whose gene sequences are found in numerous pathogenic bacteria, including *Escherichia coli*, *Klebsiella pneumoniae*, and *Salmonella typhimurium*.[24] Considering the ability of these pathogens to counteract NO-based immune defense mechanisms and prolong disease, studying these enzymes is of particular interest. Unsolved questions surrounding these enzymes include (but are not limited to) what determines specificity of NO reduction activity in these enzymes, what is the mechanism of this reaction, how does the SCS contribute to catalysis and what is the nature of the key, N-N-coupled intermediates. These questions, along with structural and reactivity properties, are addressed in the following.

FDPs contain a conserved minimal structural core that consists of N-terminal metallo-β-lactamase-like and C-terminal flavodoxin-like domains.[29] The metallo-β-lactamase-like domain houses the diiron catalytic site, whereas the flavodoxin-like domain contains a flavin mononucleotide (FMN) cofactor capable of transferring electrons to the diiron site.[29] Within a single monomer of the minimal structural core, the diiron site and the FMN cofactor are ~35 Å

away, which renders electron transfer between them essentially impossible without additional cofactors.[29,30] However, in the "head-to-tail homodimer" quaternary structure of FDPs (see Figure 1.1), the two monomers are arranged such that the diiron site of one monomer is only ~5 Å away from the FMN cofactor of the other monomer, enabling fast and efficient electron transfer between them (Figure 1.2).[30]

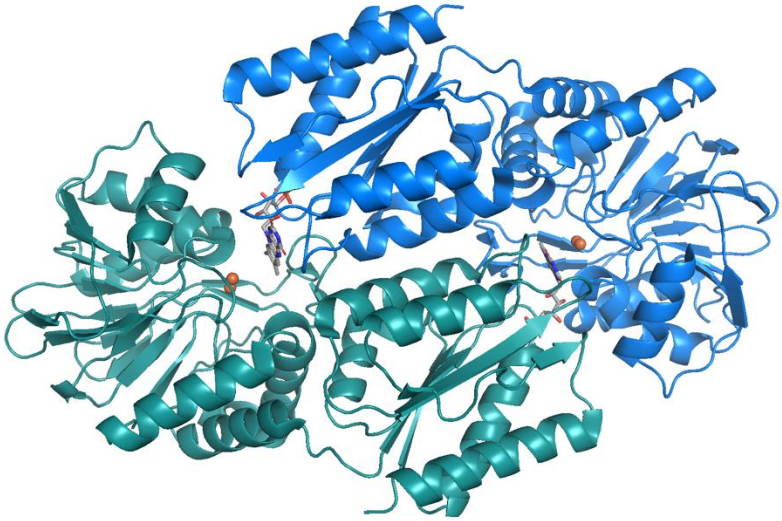

Figure 1.1 PYMOL generated image of the crystal structure of *M. thermoacetica* FDP (*Mt* FDP; PDB: 1YCH), showing the homodimer with the two monomers in blue and cyan in a "head-to-tail" arrangement. Iron atoms and FMN are shown as orange spheres and gray ball-and-stick models, respectively.

FDPs can be grouped together based on how well these enzymes mediate dioxygen reductase (O_2R) or nitric oxide reductase (NOR) activity. FDPs were first recognized as O_2Rs for their ability to protect microanaerobic bacteria from residual O_2, by reducing it in a non-metabolic (scavenging) function to water.[29] In addition, because of how FDPs act as scavenging enzymes in the presence of O_2 and NO to counteract oxidative and nitrosative stress, respectively, it is hypothesized that NOR function evolved from O_2R function in these enzymes.[23] However, it is worth noting that not all FDPs have NOR and/or O_2R functionality. While *Desulfovibrio gigas* Rubredoxin Oxygen:Oxidoreductase (*Dg* ROO) and *Moorella thermoacetica* FDP (*Mt* FDP)

exhibit NOR and O_2R reactivity at similar rates, *Thermotoga maritima* FDP (*Tm* FDP) and FDP from *E. histolytica* exhibit better O_2R than NOR reactivity.[28,31-33] On the other hand, *Escherichia coli* flavorubredoxin (*Ec* FlRd) exhibits better NOR than O_2R activity, making this enzyme a bona fide FNOR.[34] However, there are no obvious differences in the iron coordination spheres and active site structures between O_2Rs and NORs, so the structural and/or electronic differences responsible for this dichotomy have yet to be definitively determined (see discussion below).

Considering the primary coordination sphere, the diiron core binding motif is generally conserved across all FDPs. In the diiron core, each iron is 5C with a sixth site left open for substrate binding, as shown in Figure 1.2.[30] Here, each iron coordinates to two histidine residues and one carboxylate residue (either aspartate or glutamate). Bridging hydroxo and carboxylate (usually aspartate) ligands position the iron centers between 3.3 - 3.6 Å apart. A notable exception includes *Dg* ROO, which has one of the histidine ligands unbound from one of the irons and replaced with water.[29] Kurtz and coworkers expressed deflavinated *Tm* FDP with mutated plasmids that replace His90 (one of the Fe-coordinating histidine ligands) to assess whether altering the primary coordination sphere of one of the iron centers would modulate NOR or O_2R activity.[31] Among the variants, there exists little change to the substrate binding pocket, other Fe-coordinating residues, and Fe-ligand distances. For the H90N and H90A variants, the respective Fe-O_{Asn} and Fe-OH_2 bond distances are 2.3 and 2.4 Å, respectively, versus 2.4 Å for the Fe-N_{His} bond in wt enzyme.[31] Not surprising, this variation in the primary coordination sphere does not drastically alter steady-state NOR activity (0.05 and 0.09 s^{-1} for H90A and H90N, respectively, versus 0.03 s^{-1} for wt enzyme), as is the case for steady-state O_2R activity.[31] In addition, total conservation of the primary coordination sphere is observed for both *Mt* FDP and *Tm* FDP, although lower NOR reactivity (relative to O_2R reactivity) was found in the latter compared to the former enzyme.[31,33]

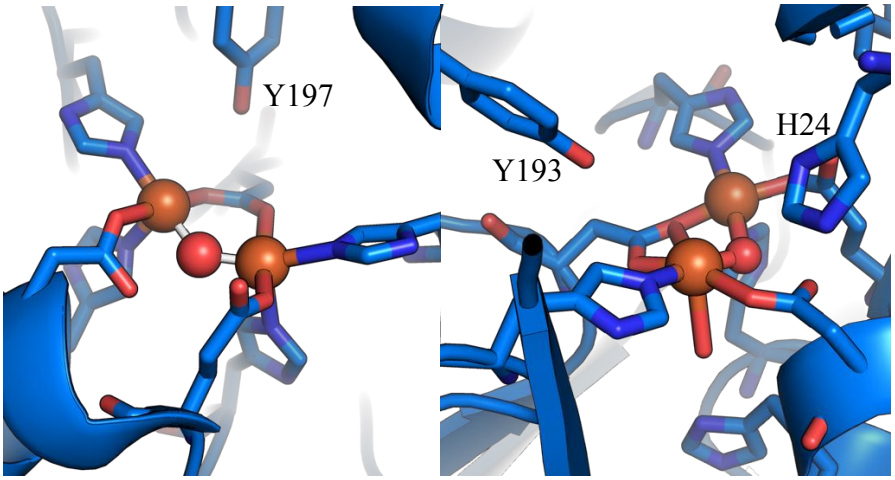

Figure 1.2 Left: PYMOL generated image of the crystal structure of the active site of deflavinated *T. maritima* FDP, including the proposed SCS hydrogen-bond donor Y197 (PDB: 1VME). Right: PYMOL generated image of the crystal structure of the active site of *D. gigas* ROO, including the proposed SCS hydrogen-bond donors H24 and Y193 (PDB: 1E5D).

Differences between primary NORs and similarly NOR and O_2R active enzymes start to come to light when considering the SCS and beyond. Comparison of *Dg* ROO and *Mt* FDP shows that both enzymes contain histidine and tyrosine residues within hydrogen-bonding distances of iron-bound substrates, and both enzymes act as decent NORs.[28,33] Moreover, mutation studies using *Mt* FDP revealed a ~7-fold and ~34-fold reduction in NOR reactivity when the tyrosine and histidine residues (Y195 and H25, represented for the analgous *Dg* ROO as Y193 and H24 in Figure 1.2), respectively, were substituted for non-hydrogen bonding residues.[30] While it is clear that the SCS residues Tyr and His are important for NOR activity, whether these residues truly distinguish NORs from O_2Rs is not clear, since it was not reported how their removal by mutagenesis affected the O_2R activity of the enzyme. In *M. marburgensis* FDP, the SCS Tyr is oriented away from the active site, towards one of the carboxylate residues, but this enzyme still shows O_2R activity, which indirectly supports these ideas (assuming that the Tyr stays in this position during catalysis).[35] In addition, *Tm* FDP, which is primarily a O_2R, lacks the histidine that is available for hydrogen-bonding in the SCS of the *Mt* FDP active site.[31] The *Tm* FDP active site does contain the SCS

tyrosine (Figure 1.2), and site-directed mutagenesis studies show that this residue is crucial for NOR activity of this enzyme.[36] Beyond the catalytic site, clusters of aromatic residues have been found in conserved positions near the active site and the FMN cofactor of most FDPs, which include tryptophan and tyrosine residues.[37] These amino acids are hypothesized to protect the enzymes from oxidative damage when dioxygen reduction occurs, by reducing radical species or highly reactive intermediates.[38]

1.3 Electronic Structure of Non-Heme Hs-{FeNO}^{7} Complexes and Mechanism of NO Reduction by FNORs

Since NO is a redox non-innocent ligand, it is often difficult to determine the exact electronic structure of transition-metal nitrosyl complexes. To overcome this complication in terms of communication, the Enemark-Feltham notation is often utilized.[39] The general form of the Enemark-Feltham notation is $\{M(NO)_x)^n$ where x is the number of nitric oxide bound to the metal center M and n is the total number of e^- in the d orbitals of the metal center M and the NO π^* MOs. The properties of hs-{FeNO}^{7} complexes have been studied in much detail using a variety of spectroscopic techniques including UV-Vis absorption, IR, rRaman, MCD, EPR, XAS and NRVS, besides other methods. Since NO is a non-innocent ligand, the electronic structure of hs-{FeNO}^{7} complexes is not a priori clear. Solomon and coworkers used XAS, rRaman, UV-Vis absorption, MCD and EPR spectroscopy in combination with scattered-wave (SW) SCF-Xα calculations to investigate the electronic structures of the hs-{FeNO}^{7} complexes [Fe(Me$_3$TACN)(N$_3$)$_2$(NO)] and $[Fe(EDTA)(NO)]^{2-}$ as well as that of the ferrous NO adduct of the enzyme soybean lipoxygenase.[40,41] These studies showed that hs-{FeNO}^{7} complexes are best described as hs-Fe(III)-$^3NO^-$ systems, where the spins of hs-Fe^{III} (S = 5/2) and the triplet $^3NO^-$

ligand (S = 1) are antiferromagnetically (AF) coupled, resulting in the experimentally observed S_t = 3/2 spin state of these complexes.[41] This electronic structure is illustrated in the MO diagram in Figure 1.3. Further studies by Lehnert and coworkers have shown that the $^3NO^-$ ligand acts predominantly as a strong π-donor ligand in these complexes, leading to a very covalent Fe-NO bond.[42,43] This is reflected by the strong admixture of d-orbital character into the singly-occupied (β-spin, in a spin-unrestricted scheme) $^3NO^-(\pi^*)$ orbitals. The corresponding bonding combinations, $\pi^*_x\_d_{xz}$ and $\pi^*_y\_d_{yz}$ (with the Fe–N(O) vector corresponding to the z axis), usually have around 20-35% d_{xz}/d_{yz} contributions. Unlike the original SW SCF-Xα calculations by Solomon and coworkers, DFT calculations with typical functionals (BP86, B3LYP, etc.) do not show significant σ donation from the $2\sigma^*$ orbital of $^3NO^-$ to the hs-Fe^{III} center.[42,44] Instead, a weak π-backbonding interaction between the occupied (mixed) $\alpha\text{-}d_z^2/d_{xz}$ orbital of Fe and the empty in-plane $\alpha\text{-}\pi^*$ orbital of $^3NO^-$ is sometimes observed, which is related to the bending of the FeNO unit. Overall, $^3NO^-$ is a weak π-acceptor (α-spin manifold) and a strong π-donor (β-spin manifold) ligand in hs-$\{FeNO\}^7$ complexes.

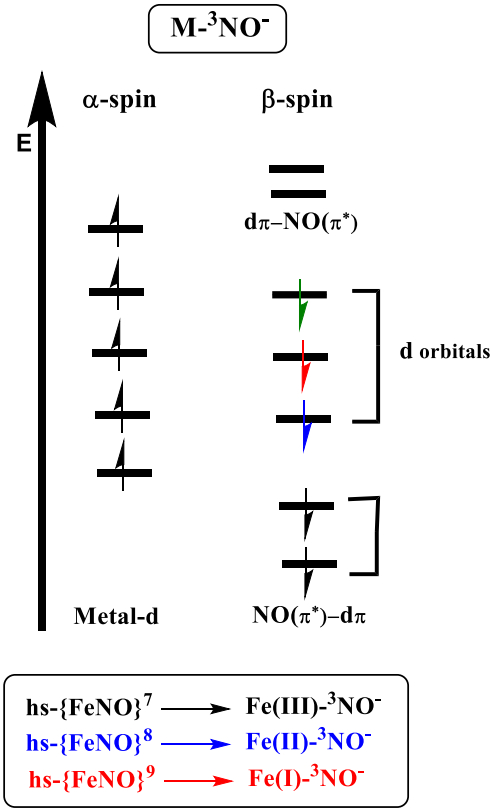

Figure 1.3 MO diagram showing the typical electronic structure of different hs-{MNO}$^{7-9}$ complexes, as indicated.

Stopped-flow experiments on wt *Tm* FDP by Caranto et al. show that coordination of the first NO ligand to the reduced diiron core of the enzyme is exceedingly fast and proceeds within the mixing time of the solutions (about 1.3 ms).[45] This is followed by a slower phase, which proceeds in 130 ms and which corresponds to the binding of the second NO and the formation of a diiron dinitrosyl intermediate, [hs-{FeNO}^{7}]$_2$. These assignments are based on the characteristic UV-Vis absorption features of non-heme hs-{FeNO}^{7} complexes, and were further confirmed by Mössbauer spectroscopy (see below). The [hs-{FeNO}^{7}]$_2$ intermediate then decays over the course of 120 seconds, along with the appearance of oxidized FMN cofactor. Importantly, only after forming the [hs-{FeNO}^{7}]$_2$ intermediate does cofactor oxidation occur. Using RFQ-EPR, sub-stoichiometric amounts of NO (~0.5 equivalent NO per diiron site) were added to *Tm* FDP to yield an intense S_t = 1/2 signal after 200 ms.[45] With a g-value of 2.10, the rapidly forming species was

identified as the diferrous mononitrosyl intermediate (see above), where the hs-Fe^{II} (S = 2) is AF coupled to the hs-$\{FeNO\}^7$ (S = 3/2) center, in agreement with the stopped-flow results. Using RFQ-Mössbauer spectroscopy, reactions with excess NO (~3 equivalents NO per diiron site) were conducted and then quenched at multiple time points. After 20 ms, the spectrum reveals a mixture of species that, based on simulated Mössbauer spectra, match up to the hs-Fe^{II}/hs-$\{FeNO\}^7$ species (76%) and the starting diferrous complex (16%), among others. Samples quenched at 200 ms and 2 s after NO addition also reveal a mixture of species, including the hs-Fe^{II}/hs-$\{FeNO\}^7$ intermediate (54%) and a new species, identified as the [hs-$\{FeNO\}^7$]$_2$ complex (41%; isomer shift δ = 0.71 mm/s and ΔE_Q = 1.85 mm/s). The data further show that the latter species is diamagnetic (S_t = 0), indicative of AF coupling between two S = 3/2 hs-$\{FeNO\}^7$ centers. After 120 s, the [hs-$\{FeNO\}^7$]$_2$ intermediate has completely disappeared and a new Fe^{III}_2 complex appears (13%; isomer shift δ = 0.47 mm/s and ΔE_Q = 0.99 mm/s), which is the product after N_2O release. Hence, even under RFQ conditions, no intermediate can be observed between the initial dinitrosyl intermediate and the diferric product. Accompanying UV-Vis measurements further show that a single turnover completes with the formation of the diferric product, before any Flavin oxidation occurs. In summary, these stopped-flow and RFQ experiments on *Tm* FDP have two important mechanistic implications: first, the diiron dinitrosyl intermediate, [hs-$\{FeNO\}^7$]$_2$, is the catalytically competent intermediate that is formed prior to any N_2O generation, ruling out other pathways where N-N coupling starts from the diiron mononitrosyl complex,[46] and second, the reaction follows the direct coupling pathway, where the flavin is not directly involved in catalysis (see below).

The latter result is further solidified in a follow up study by Kurtz and coworkers on deflavo-*Tm* FDP, which still undergoes NO reduction, albeit at a slower rate and lower yield than

the wt enzyme.[45,47] Using RFQ-EPR, sub-stoichiometric amounts of NO (0.6 equivalent NO per diiron site) were added to deflavo-*Tm* FDP and quenched after 200 ms to yield an intense $S_t = 1/2$ signal with a g value of ~2, which corresponds to the hs-Fe^{II}/hs-{FeNO}^{7} intermediate.[47] Using RFQ-Mössbauer, excess NO (~3 equivalents NO per diiron site) was added and first quenched after 100 ms to yield a prominent [hs-{FeNO}^{7}]$_2$ species, comprising 55% of total iron in the sample. This species shows isomer shift and quadrupole splitting parameters of 0.74 and 1.85 mm/s, respectively. Additionally, a Fe^{III}_2 species appears in the Mössbauer spectra with isomer shift and quadrupole splitting parameters of 0.44 and 0.92 mm/s, respectively, which are distinct from the as-isolated, oxidized state of deflavo-*Tm* FDP. After 60 s, the Fe^{III}_2 product is the predominant species in the Mössbauer spectra, and no signal of the starting Fe^{II}_2 species remains. With the absence of the FMN cofactor, these RFQ experiments demonstrate the ability of *Tm* FDP to reduce NO to N_2O via an [hs-{FeNO}^{7}]$_2$ intermediate, without the assistance of the Flavin cofactor.

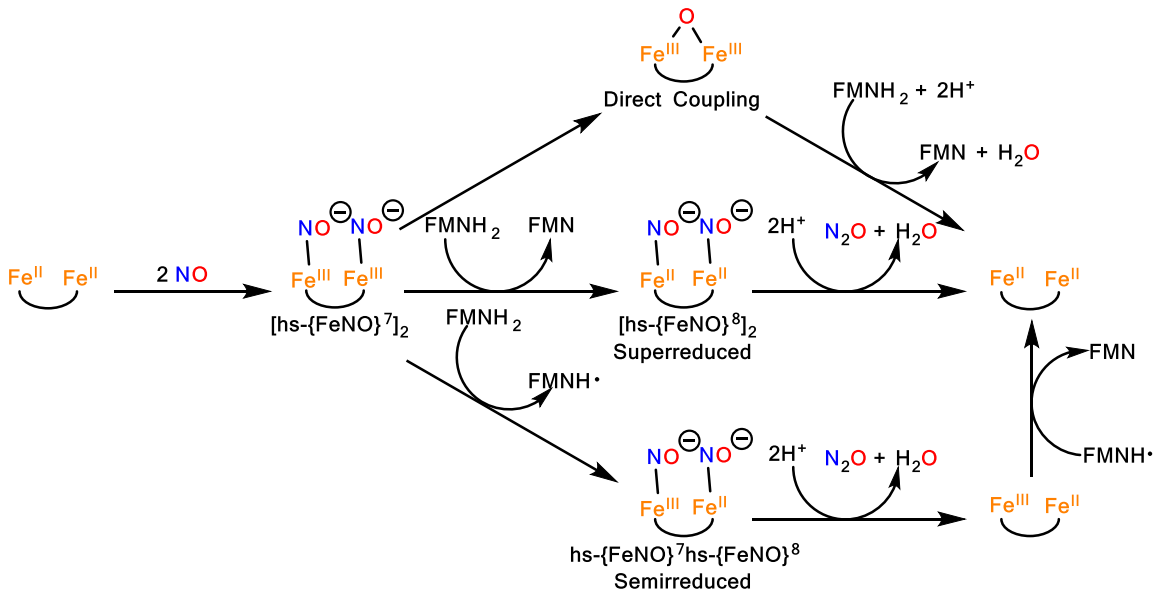

Scheme 1.1 Mechanistic possibilities for N-N coupling from the [hs-{FeNO}^{7}]$_2$ intermediate in FNORs.

Alternatively, the FMN cofactor could reduce the [hs-{FeNO}^{7}]$_2$ intermediate by either one or two electrons (and potentially transfer protons) under turnover, creating highly reactive hs-{FeNO}^{7}/hs-{FeNO}^{8} or [hs-{FeNO}^{8}]$_2$ intermediates prior to N-N bond formation. These pathways are shown in Scheme 1.1, middle and bottom, and are referred to as the *semireduced* and *superreduced* mechanisms. In particular, the semireduced mechanism has been demonstrated in model complexes as a highly efficient pathway for NO reduction (see below).[48-50] In this case, N-N bond formation from the hs-{FeNO}^{7}/hs-{FeNO}^{8} intermediate yields N_2O and a mixed-valent Fe^{II}/Fe^{III} μ-oxo (or μ-hydroxo) product. This step would be followed by another electron and proton transfer to the diiron center to release water and regenerate the diferrous active site. A variation of the semireduced pathway is the superreduced mechanism, where the FMN cofactor transfers two electrons (and possibly protons) to the diferrous dinitrosyl complex, generating a [hs-{FeNO}^{8}]$_2$ intermediate, which subsequently releases N_2O and water and regenerates the diferrous form of the active site. Intramolecular superreduction has not been observed yet in model complexes, possibly because the semireduced mechanism is so efficient that the complex proceeds to generate N_2O after the first reductive equivalent has been transferred to the [hs-{FeNO}^{7}]$_2$ complex.[51] Just like in the case of the RFQ studies on *Tm* FDP, intermediates of NO reduction have not been observed in model complexes either, leaving us with a large knowledge gap about the nature of the N-N coupled intermediates in these systems (and which are therefore omitted in Scheme 1.1). Further studies are necessary to elucidate the mechanistic details of NO reduction by non-heme diiron complexes.

Alternative explanations for the lack of NOR reactivity of sMMO and RNR have recently been proposed, based on spectroscopic and theoretical studies on *Tm* FDP.[52] One possible explanation involves the differences in bridging ligands between the iron centers in the active sites

of NOR-active FDPs and the NOR-unreactive enzymes sMMO and RNR. For the diferrous forms of sMMO and RNR, the exchange coupling constants between the iron centers are only J = 0.5 cm^{-1} and J = -0.5 cm^{-1}, respectively.[53,54] Compared to diferrous *Tm* FDP, this weaker exchange coupling can be attributed to the lack of hydroxo bridges between the iron centers.[55,56] However, the presence of bridging carboxylates only may not be enough to (a) force the open binding sites on each iron center to be in the proper syn conformation, and (b) keep the iron centers at a close distance. Accordingly, the lack of NOR activity in sMMO and RNR could be linked to less rigid diiron centers in these enzymes that impede N-N coupling. Another possible explanation is based on the fact that both sMMO and RNR lack proper SCS residues near the diiron site, unlike many FDPs (Figure 1.2).[55,56] Here, the lack of a tyrosine and/or histidine SCS residue could preclude NOR activity in these enzymes, as demonstrated in mutagenesis experiments with FDPs that highlight the crucial roles of these amino acid side chains for catalysis (see above).[30,36]

1.4 Enzymes and Model Complexes

Enzymes are often challenging subjects of study due to their complicated structure and the lack of spectroscopic handles. Direct investigations of reactions in enzymes are often obscured by the massive amount of amino acids that construct its structure. Dynamics of these amino acids often produce noisy signals in NMR spectroscopy as well as reducing the resolution of protein X-ray crystal structures, thus, lowering the clarity of direct enzymatic investigation. At the same time, the desired reactions that these metalloenzymes catalyze are often carried out at the active site at which the metal center is coordinated. Therefore, model complexes that mimic the active site of complicated massive enzymes are key tools utilized in bioinorganic chemistry to investigate important mechanisms of metalloenzymes, identify putative intermediates, and elucidate the roles

that the metals' first and second coordination sphere (SCS) play in catalysis (including H-bonding and electrostatic interactions). Generally, studies on model complexes and enzymes are seen as complimentary methods to each other in order to investigate a desired reaction in details. On the one hand, models are not the same as the "real" enzymes, but on the other hand, they allow us to explore a given enzymatic reaction in a broader perspective, investigate the reactivity spectrum of key intermediates and identify site reactions that may be suppressed in the enzyme, trap intermediates at cryogenic temperatures (typical at -80 ^{o}C), define the spectroscopic signatures of such intermediates for future identification in enzymes, and develop small-molecule catalysts that can catalyze similar reactions as the enzymes. Reactions can be conducted in strictly controlled environments, for example water-free conditions, in the hopes of trapping intermediates that may not be accessible in aqueous environments. Finally, the influence of steric and electronic effects on a given reaction are often more straightforward to investigate in model systems, where modifications to the ligand scaffold with predictable outcomes can easily be made, compared to creating corresponding variants in enzymes where we are restricted by the naturally occurring amino acids.

1.5 Model Complexes of FNORs

Due to the debate about the mechanism of NO activation in FNORs (Scheme 1.1) and the challenges in identifying intermediates in the protein, model complexes have been employed to study the mechanism of FNORs.[22] For example, Lippard's synthetic model complex [Fe_2(N-Et-HPTB)(O_2CPh)$(NO)_2$]$(BF_4)_2$ (N-Et-HPTB = N,N,N′,N′-tetrakis-(2-(1-ethylbenzimidazolyl))-2-hydroxy-1,3-diaminopropane; see Figure 1.5a) is capable of stabilizing a [hs-{FeNO}^{7}]$_2$ species that produces substoichiometric N_2O upon photocleavage of one of the Fe–NO bonds.[57] This

generates a bridging mononitrosyl that is proposed to be attacked by the photocleaved NO, generating N_2O and a bridging μ-oxo product. While this mechanism is chemically feasible, detailed enzyme studies on the *T. maritima* FDP by Kurtz and coworkers[45,47,58] have shown that although a diiron mononitrosyl is generated in this enzyme upon sequential addition of NO equivalents, the diiron dinitrosyl complex, [hs-{FeNO}^{7}]$_2$, is the catalytically relevant intermediate that accumulates before any N_2O is formed (see above).[45,47]

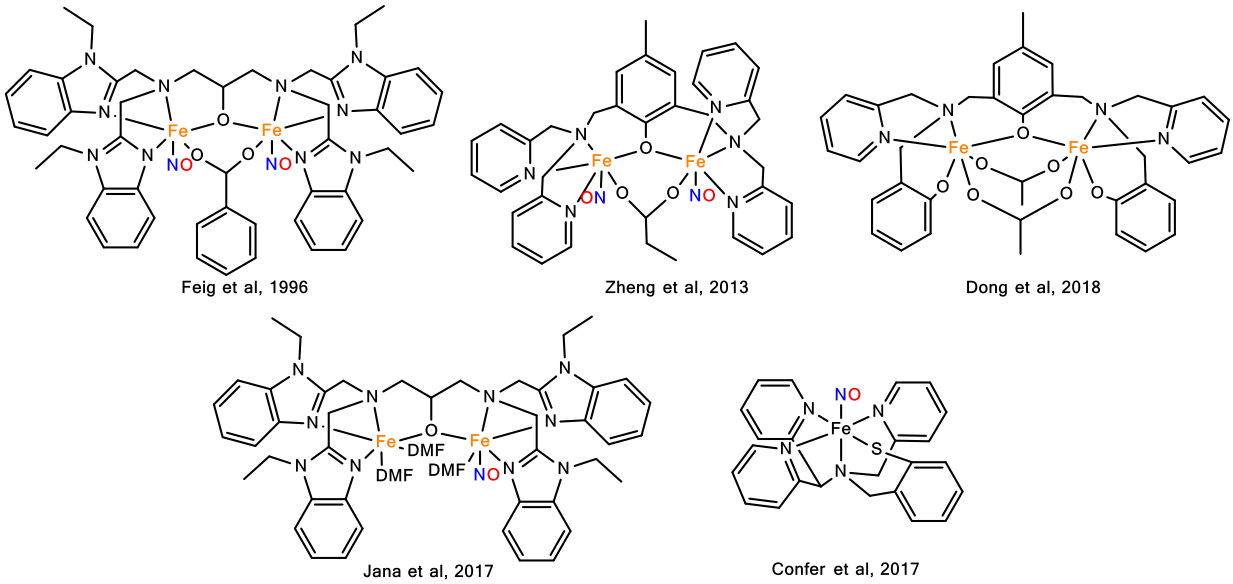

Figure 1.4 Functional model complexes for FNORs that show N_2O generation via photochemistry, direct reduction, semireduction, and superreduction.

Since the FMN cofactor distinguishes FNORs from other non-heme diiron enzymes like methane monooxygenase (MMO)[59] and ribonucleotide reductase (RNR),[60] which lack such efficient NO reductase activity, it might be expected that the FMN cofactor participates in catalysis by activating the initially formed [hs-{FeNO}^{7}]$_2$ dimer via reduction (following the "semireduction" or "superreduction" pathways). In support of these ideas, synthetic mono- and dinuclear non-heme hs-{FeNO}^{7} complexes are typically stable in solution,[50,61-65] due to the covalent nature of the Fe–NO bond,[41] and these complexes show no propensity to generate N_2O

without the assistance of a chemical reductant. Interestingly, however, mechanistic studies on the deflavinated *T. maritima* FDP (discussed in more detail below) suggest that N–N coupling can occur *without* the participation of the FMN cofactor in a "direct-reduction" pathway,[47] indicating at a minimum that this reaction is possible.

Our efforts to model the active site of FNORs were inspired (in terms of ligand choice and modifications) by the efforts to model the active site of purple acid phosphatases.[66-73] We have previously reported the stable [hs-{FeNO}^{7}]$_2$ model complex, [Fe$_2$(BPMP)(OPr)(NO)$_2$](X)$_2$ (X = BPh_4^-, OTf^-, BF_4^-) ($BPMP^-$ = 2,6-bis[(bis(2-pyridylmethyl)amino)methyl]-4-methylphenolate; see Figure 1.4), which contains two coplanar hs-{FeNO}^{7} units (in a *cis* orientation) with an N-N distance of 2.803 Å.[50] The coplanar orientation of the NO units is believed to aid in N-N coupling. While the $BPMP^-$ ligand is symmetric, the crystal structure of the [hs-{FeNO}^{7}]$_2$ complex reveals that it coordinates each iron center asymmetrically, with one NO bound trans to a tertiary amine while the other NO is bound trans to a pyridine. This is reflected in slightly different Fe–NO bond lengths at 1.774 Å and 1.796 Å and Fe-N-O angles at 155.5º and 144.7º, respectively, typical for non-heme hs-{FeNO}^{7} complexes. The two hs-{FeNO}^{7} units with S_t = 3/2 are then AF coupled in the dimer, to afford a total spin of S_t = 0 in the ground state. Typical exchange coupling constants J for such [hs-{FeNO}^{7}]$_2$ complexes are in the 5 – 20 cm^{-1} range ($\underline{H} = -2J(\underline{S}_1 \bullet \underline{S}_2)$).[60,61,74,75]. A more detailed description of the hs-{FeNO}^{7} electronic structure is presented in the next section. The complex [Fe$_2$(BPMP)(OPr)(NO)$_2$](X)$_2$ is capable of undergoing a one-electron reduction via external reductants, leading to very rapid *intramolecular* N-N coupling and quantitative N_2O release.[49] This complex can turn over in the 156 ms dead time of a stopped-flow IR instrument, with $k_{obs} > 10^2$ s^{-1} at room temperature, following the semireduced mechanism. Indeed, the mixed-valent byproduct of this reaction, where one electron is delivered via the chemical reductant and

the other one is provided by the diferrous core, is captured at -80 °C by EPR spectroscopy. In contrast, Meyer's $[L\{Fe(NO)\}_2(\mu\text{-}OOCR)](X)_2$ [hs-$\{FeNO\}^7]_2$ model complex (where L is a dinucleating pyrazole/triazacyclononane ligand 4,4'-((1H-pyrazole-3,5-diyl)bis(methylene))bis(1-methyl-1,4,7-triazonane), R is Me or Ph, and X^- is ClO_4^- or BPh_4^-) contains two hs-$\{FeNO\}^7$ units in *trans* orientation (Figure 1.4).[75] This complex does not generate N_2O upon reduction, but instead, the one-electron reduced complex undergoes a redox and ligand disproportionation to form a $[\{Fe(NO)_2\}^9]_2$ DNIC dimer and the diferrous complex (both characterized by X-ray crystallography). Based on these findings, the relative orientation of the Fe-N-O units is expected to be a key structural pre-requisite for efficient N_2O formation in diiron complexes.

So far, no synthetic [hs-$\{FeNO\}^7]_2$ model complex is known that formally undergoes *intramolecular* superreduction. We believe that this is due to the fact that semireduction is such an efficient process that once the [hs-$\{FeNO\}^7]_2$ unit is reduced by one electron, fast intramolecular N_2O generation is observed before a second electron can be transferred. In agreement with this, DFT calculations on the complex $[Fe_2(BPMP)(OPr)(NO)_2](X)_2$ show that semireduction and superreduction have essentially identical barriers for N-N bond formation (see below).[62] However, there are some examples of NO activation via *inter*molecular N–N coupling by the superreduced mechanism in non-heme mononitrosyl species. The first example is Goldberg's $[Fe(NO)(N_3PyS)]BF_4$ complex, where N_3PyS is (N-(2-(l1-sulfaneyl)benzyl)-1,1-di(pyridin-2-yl)-N-(pyridin-2-ylmethyl)methanamine) (Figure 1.4), which can be chemically reduced to the hs-$\{FeNO\}^8$ state. This species is metastable at room temperature ($t_{1/2}$ = 0.5 hr) and slowly releases substiochiometric amounts of N_2O (54%) over 20 hrs.[65] Majumdar's diiron mononitrosyl complex, $[Fe_2(N\text{-}Et\text{-}HPTB)(NO)(DMF)_3](BF_4)_3$ (Figure 1.4), on the other hand, undergoes rapid and quantitative *intermolecular* N–N coupling upon reduction of the Fe^{II}/hs-$\{FeNO\}^7$ to the Fe^{II}/hs-

{FeNO}^{8} complex, affording N_2O in 89 % yield within 5 minutes.[64] Although these complexes do not directly model the FNOR mechanism, they further demonstrate that reduction is a potent means of activating otherwise stable non-heme hs-{FeNO}^{7} complexes for N–N coupling (and other reactivity), and that superreduction is in principle possible.

Our laboratory has recently evaluated the energetic differences of the super-, semi-, and direct-reduction mechanisms, and elucidated the nature of all hyponitrite intermediates that form after N–N coupling but precede N–O cleavage, with an *in silico* study of the complex $[Fe_2(BPMP)(OPr)(NO)_2]^{2+/+/0}$ in the [hs-{FeNO}^{8}]$_2$, hs-{FeNO}^{7}/hs-{FeNO}^{8}, and [hs-{FeNO}^{7}]$_2$ redox states.[62] While N–N coupling from the [hs-{FeNO}^{7}]$_2$ complex has a dissociative potential energy surface, consistent with the stability of the [hs-{FeNO}^{7}]$_2$ complex in the absence of any external reductant, the [hs-{FeNO}^{8}]$_2$ and hs-{FeNO}^{7}/hs-{FeNO}^{8} species are both activated for N–N coupling. Reduction of a hs-{FeNO}^{7} unit leads to a decrease in covalency of the corresponding Fe–NO π-bonds and an increase in radical character of the bound $^3NO^-$ ligand, which causes the increase in reactivity.[63] Interestingly, the activation barrier for N–N bond formation from the hs-{FeNO}^{7}/hs-{FeNO}^{8} dimer (semireduction) is only 1-2 kcal/mol larger than what is predicted for superreduction, which starts from the [hs-{FeNO}^{8}]$_2$ state, in agreement with our report on the semireduced mechanism for N–N coupling in this model complex.[49] Upon radical N–N coupling to generate N-bound $N_2O_2^{2-}$, the hyponitrite must rearrange in order to facilitate N–O bond cleavage and formation of a μ-oxo product. This is achieved in two sequential steps, first from the N–N coordinated structure to a "side-on" N–O coordinated species, a binding mode that was recently observed experimentally in a dinickel complex.[76] This is followed by rearrangement to a κ^2-$O_2N_2^{2-}$ bound species with a bridging μ-oxo group. Finally, N–O bond cleavage and N_2O release occurs, with a very low free energy barrier of

only 5.6 kcal/mol. The key κ^2-$O_2N_2^{2-}$ binding mode of hyponitrite that is primed for N_2O release is only possible due to the flexibility in coordination mode of the bridging carboxylate (propionate/acetate) ligand, which undergoes a carboxylate shift to a monodentate coordination mode to allow for $N_2O_2^{2-}$ binding in the κ^2 geometry. Importantly, N_2O release provides a substantial thermodynamic driving force for the reaction of -17.4 kcal/mol.

Overall, these results identify the structural and electronic prerequisites of NO activation in FNORs and related diiron complexes. A coplanar orientation of the two Fe-N-O units is essential for facile N–N coupling. The mechanism by which NO is reduced is then highly dependent on the redox-tuning of the diiron core, and correspondingly, the strength of the Fe–NO bonds. These properties can be tuned in chemical systems quite dramatically depending on the nature of the coligands, while FNORs likely use both primary and secondary coordination sphere interactions to tune the reactivity of the NO ligands to facilitate N–N coupling.

1.6 Scope of Thesis

As discussed above, there is currently a debate concerning the mechanistic pathway of NO reduction in FNORs. At the same time, characterization of species prior to N_2O formation is important to prove that the proposed mechanistic pathway suggested by DFT is valid. Therefore, my thesis is focussed on tackling these questions from multiple angles to find a way to access key intermediates of NO reduction by diiron cores and study them.

In **Chapter 2**, I focus on testing the feasibility of the direct reduction pathway using model complexes of the non-heme diiron active site of FNORs. In this chapter, I hypothesize that by replacing two pyridine groups of the $[BPMP]^-$ ligand with two phenolate groups, I can obtain a more donating trianionic ligand, $[(Py_2PhO_2)MP]^{3-}$ = (2,6-Bis[((2-hydroxybenzyl)(2-

pyridylmethyl)amino)methyl]-4-methylphenol), which gives rise to more reducing iron centers, thus, capable of donating two equivalents of electrons to perform the direct reduction of NO to N_2O. The results show that my new model complex $[Fe_2((Py_2PhO_2)MP)(OAc)_2](CoCp_2)$ can indeed stabilize much more reducing iron centers with redox potentials shifted about 1V more negative, compared to $[Fe_2(BPMP)(OPr)(NO)_2](X)_2$. This new complex can directly reduce NO to N_2O quantitatively, proving that the direct reduction pathway is indeed a valid mechanistic possibility for FNORs.

In **Chapter 3**, I attempt to find a way to trap the NO species that is formed at -80ºC by $[Fe_2((Py_2PhO_2)MP)(OAc)_2](CoCp_2)$ in chapter 1. I hypothesize that if I can separate the iron centers of $[Fe_2((Py_2PhO_2)MP)(OAc)_2](CoCp_2)$ and react them with NO, I can potentially trap a mononitrosyl iron complex that have similar electronic property to the one I observed at -80 ºC, thus, giving further insight into the key features of direct reduction of FNORs.

Hyponitrite intermediate is an important intermediate of the mechanism of NO reduction in FNORs and it is formed right before N_2O release. One can approach designing a system to stabilize hyponitrite in different ways. First approach is to design a model complex with moderate NO reduction capability to slow down the reaction enough in order to trap and observe species at low temperature or potentially thermodynamically trap the hyponitrite intermediate. The other is to introduce hyponitrite ligand directly into the system to see how hyponitrite as a ligand interact with model complexes that has been shown to be efficient at NO reduction.

In **Chapter 4**, I explore the role of the different secondary coordination sphere hydrogen bonds group towards stabilization of intermediates in the NO reduction reaction of FNORs. Here I rationalize that the use of a scaffold that can retain the primary coordination sphere similar to the BPMP ligands is an important starting point since this complex has been proven to be able to

stabilize the diiron dinitrosyl intermediate while the bis-phenolate version can directly reduce NO to N_2O. With that in mind I targeted three different ligands, BPMP-$NHCOC(CH_3)_3$, BPMP-$NH_2CH_2C(CH_3)_3$ and BPMP-NH_2. There three ligands represent different level of acidity at the proton of amine and serves as a great starting point for our exploration into the secondary coordination sphere space.

In **Chapter 5**, I explore the fundamental coordination chemistry of trans-hyponitrite with iron complexes. In this study, I chose trans-hyponitrite as a target for investigation because of the availability of this compound and its stability and ease of handling. Cis-hyponitrite has been proposed to be the crucial intermediate in the NO reduction of FNORs, however, cis-hyponitrite precursors are often instable at room temperature and have the tendency to be explosive. Therefore, I opted to try and understand the chemistry of trans-hyponitrite first as it has also been proposed to be important in the mechanisms of heme complexes and NorBC. Using a series of mononuclear iron complexes, I tested their reactivity with sodium hyponitrite in different solvents. The result show that sodium trans-hyponitrite decomposes very quickly in protic solvent therefore I opted for an aprotic solvent. In this case, I chose acetonitrile acetonitrile. I was able to observe a range of reactivity between these hyponitrite ligands and non-heme iron complexes providing structural insight into how these unique ligands interact with different iron centers.

In **Chapter 6**, I want to revisit the semireduction mechanism of model complex of FNORs and explore the property of these hs-$\{FeNO\}^7$ moiety after undergo reduction to form hs-$\{FeNO\}^8$ complex. For this purpose, I once again turn to the isolation of these iron centers using mononuclear iron nitrosyl complexes with analogous primary coordination sphere to $[Fe_2(BPMP)(OPr)(NO)_2](X)_2$ and explore their reductive chemistry. The hs-$\{FeNO\}^7$ complex, [Fe(TPA)(OTf)(NO)](OTf), is chosen due to its well defined coordination environment and its

similarity to the primary coordination environment of $[Fe_2(BPMP)(OPr)(NO)_2](X)_2$. Interestingly, further exploration of the property of this hs-$\{FeNO\}^7$ reveals that it is has a very unique electronic structure that is on the border of spin-crossover that can be induced by coordination of solvent. Further investigation into this chemistry reveals unexpected insight into the decomposition pathways of hs-$\{FeNO\}^8$ complexes.

In **Chapter 7**, I want to explore the electronic structure of iron nitrosyl complexes that is beyond the $\{FeNO\}^8$ oxidation state. These complexes are rarely observed because adding additional electrons into an $\{FeNO\}^8$ complex would be very difficult due to formation of either a low valent Fe(I)/Fe(0) center or an NO^{2-}/NO^{3-} species which are extremely unstable. In recent study, Chalkley et al reported a series of stable $\{FeNO\}^{8-10}$ complexes using their unique ligand scaffold trisphosphineborane ligand (TPB = Tris[2-(di-iso-propylphosphino)phenyl]borane).[77] These complexes are suggested to be low spin complexes and the reduction is suggested to be iron centered reduction. However, their Mossbauer data show little to no change in isomer shift which are usually sensitive towards changes in iron oxidation state. Therefore, I set out to solve this mystery using NRVS and DFT as the key techniques to access the electronic structure of this seires.

1.7 References

1. Furchgott, R. F. Endothelium-Derived Relaxing Factor: Discovery, Early Studies, and Identification as Nitric Oxide (Noble Lecture). *Angew. Chem. Int. Ed.* **1999**, *38*, 1870-1880.
2. Ignarro, L. Nitric Oxide: A Unique Endogenous Signaling Molecule in Vascular Biology (Nobel Lecture). *Angew. Chem. Int. Ed.* **1999**, *38*, 1882-1892.
3. Murad, F. Discovery of Some of the Biological Effects of Nitric Oxide and Its Role in Cell Signaling (Nobel Lecture). *Angew. Chem. Int. Ed.* **1999**, *38*, 1856-1868.
4. Stuehr, D. J. Structure-Function Aspects in the Nitric Oxide Synthases. *Annu. Rev. Pharmacol. Toxicol.* **1997**, *37*, 339-359.
5. Gorren, A. C. F.; Mayer, B. Nitric-Oxide Synthase: A Cytochrome P450 Family Foster Child. *Biochem. Biophys. Acta* **2007**, *1770*, 432-445.
6. Santolini, J. The Molecular Mechanism of Mammalian NO-Synthase: A Story of Electrons and Protons. *J. Inorg. Biochem.* **2011**, *105*, 127-141.

7. Childers, K. C.; Garcin, E. D. In *Nitric Oxide: Synthesis and Action*; John Wiley & Sons, Ltd.: Chichester, 2017, p 1-10.
8. Fang, F. C. Mechanisms of Nitric Oxide-Related Antimicrobial Activity. *J. Clin. Invest.* **1997**, *99*, 2818-2825.
9. Bogdan, C. Nitric oxide and the immune response. *Nat. Immunol.* **2001**, *2*, 907-916.
10. Stuehr, D. J.; Gross, S. S.; Sakuma, I.; Levi, R.; Nathan, C. F. Activated Murine Macrophages Secrete a Metabolite of Arginine with the Bioactivity of Endothelium-Derived Relaxing Factor and the Chemical Reactivity of Nitric Oxide. *J. Exp. Med.* **1989**, *169*, 1011-1020.
11. MacMicking, J.; Xie, Q.-W.; Nathan, C. Nitric Oxide and Macrophage Function. *Annu. Rev. Immunol.* **1997**, *15*, 323-350.
12. Nathan, C. Is iNOS Beginning to Smoke? *Cell* **2011**, *147*, 257-258.
13. Russell, J. A.; Singer, J.; Bernard, G. R.; Wheeler, A.; Fulkerson, W.; Hudson, L.; Schein, R.; Summer, W.; Wright, P.; Walley, K. R. Changing pattern of organ dysfunction in early human sepsis is related to mortality. *Crit. Care Med.* **2000**, *28*, 3405-3411.
14. Smith, K. J.; Lassmann, H. The Role of Nitric Oxide in Multiple Sclerosis. *Lancet. Neurol.* **2002**, *1*, 232-241.
15. Cameron, N. E.; Cotter, M. A. In *Nitric Oxide, Peripheral Neuropathy, and Diabetes*; Kalsner, S., Ed.; Birkhäuser: Boston, Massachusetts, 2000; Vol. 2,, p 307-326.
16. Brown, G. C.; Bal-Price, A. Inflammatory Neurodegeneration Mediated by Nitric Oxide, Glutamate, and Mitochondria. *Mol. Neurobiol.* **2003**, *27*, 325-355.
17. Nakamura, T.; Oh, C. K.; Liao, L.; Zhang, X.; Lopez, K. M.; Gibbs, D.; Deal, A. K.; Scott, H. R.; Spencer, B.; Masliah, E.; Rissman, R. A.; Yates, J. R., 3rd; Lipton, S. A. Noncanonical transnitrosylation network contributes to synapse loss in Alzheimer's disease. *Science* **2021**, *371*.
18. Kuhl, S. J.; Rosen, H. Nitric Oxide and Septic Shock. From Bench to Bedside. *West. J. Med.* **1998**, *163*, 176-181.
19. Murray, P. T.; Wylam, M. E.; Umans, J. G. Nitric Oxide and Septic Vascular Dysfunction. *Anesth. Analg.* **2000**, *90*, 89-101.
20. Vincent, J.-L.; Zhang, H.; Szabo, C.; Preiser, J.-C. Effects of Nitric Oxide in Septic Shock. *Am. J. Respir. Crit. Care Med.* **2000**, *161*, 1781-1785.
21. Titheradge, M. A. Nitric Oxide in Septic Shock. *Biochim. Biophys. Acta* **1999**, *1411*, 437-455.
22. Khatua, S.; Majumdar, A. Flavodiiron Nitric Oxide Reductases: Recent Developments in the Mechanistic Study and Model Chemistry for the Catalytic Reduction of NO. *J. Inorg. Biochem.* **2015**, *142*, 145-153.
23. Gardner, A. M.; Helmick, R. A.; Gardner, P. R. Flavorubredoxin, an Inducible Catalyst for Nitric Oxide Reduction and Detoxification in *Escherichia coli*. *J. Biol. Chem.* **2002**, *277*, 8172-8177.
24. Gardner, A. M.; Gessner, C. R.; Gardner, P. R. Regulation of the Nitric Oxide Reduction Operon (*norRVW*) in *Escherichia coli*. Role of NorR and s^{54} in the Nitric Oxide Stress Response. *J. Biol. Chem.* **2003**, *278*, 10081-10086.
25. Hutchings, M. I.; Mandhana, N.; Spiro, S. The NorR Protein of *Escherichia coli* Activates Expression of the Flavorubredoxin Gene norV in Response to Reactive Nitrogen Species. *J. Bacteriol.* **2002**, *184*, 4640-4643.
26. Gomes, C. M.; Giuffrè, A.; Forte, E.; Vicente, J. B.; Saraiva, L. M.; Brunori, M.; Teixeira, M. A Novel Type of Nitric-oxide Reductase. *Escherichia Coli* Flavorubredoxin. *J. Biol. Chem.* **2002**, *277*, 25273-25276.

27. Tucker, N. P.; D'Autréaux, B.; Studholme, D. J.; Spiro, S.; Dixon, R. DNA Binding Activity of the *Escherichia coli* Nitric Oxide Sensor NorR Suggests a Conserved Target Sequence in Diverse Proteobacteria. *J. Bacteriol.* **2004**, *186*, 6656-6660.
28. Rodrigues, R.; Vicente, J. B.; Félix, R.; Oliveira, S.; Teixeira, M.; Rodrigues-Pousada, C. *Desulfovibrio gigas* Flavodiiron Protein Affords Protection against Nitrosative Stress In Vivo. *J. Bacteriol.* **2006**, *188*, 2745-2751.
29. Frazão, C.; Silva, G.; Gomes, C. M.; Matias, P.; Coelho, R.; Sieker, L.; Macedo, S.; Liu, M. Y.; Oliveira, S.; Teixeira, M.; Xavier, A. V.; Rodrigues-Pousada, C.; Carrondo, M. A.; Le Gall, J. Structure of a dioxygen reduction enzyme from *Desulfovibrio gigas*. *Nat. Struct. Biol.* **2000**, *7*, 1041-1045.
30. Silaghi-Dumitrescu, R.; Kurtz, D. M., Jr.; Ljungdahl, L. G.; Lanzilotta, W. N. X-ray Crystal Structures of *Moorella thermoacetica* FprA. Novel Diiron Site Structure and Mechanistic Insights into a Scavenging Nitric Oxide Reductase. *Biochemistry* **2005**, *44*, 6492-6501.
31. Fang, H.; Caranto, J. D.; Mendoza, R.; Taylor, A. B.; Hart, P. J.; Kurtz, D. M. Histidine Ligand Variants of a Flavo-Diiron Protein: Effects on Structure and Activities. *J. Biol. Inorg. Chem.* **2012**, *17*, 1231-1239.
32. Vicente, J.; Tran, V.; Pinto, L.; Teixeira, M.; Singh, U. A Detoxifying Oxygen Reductase in the Anaerobic Protozoan *Entamoeba histolytica*. *Eukaryot. Cell* **2012**, *11*, 1112-1118.
33. Silaghi-Dumitrescu, R.; Coulter, E. D.; Das, A.; Ljungdahl, L. G.; Jameson, G. N. L.; Huynh, B. H.; Kurtz, D. M., Jr. A flavodiiron protein and high molecular weight rubredoxin from *Moorella thermoacetica* with nitric oxide reductase activity. *Biochemistry* **2003**, *42*, 2806-2815.
34. Vicente, J. B.; Teixeira, M. Redox and Spectroscopic Properties of the *Escherichia coli* Nitric Oxide-detoxifying System Involving Flavorubredoxin and Its NADH-oxidizing Redox Partner. *J. Biol. Chem.* **2005**, *280*, 34599-34608.
35. Seedorf, H.; Hagemeier, C.; Shima, S.; Thauer, R.; Warkentin, E.; Ermler, U. Structure of coenzyme $F_{420}H_2$ oxidase (FprA), a di-iron flavoprotein from methanogenic Archaea catalyzing the reduction of O_2 to H_2O. *FEBS J.* **2007**, *274*, 1588-1599.
36. Biswas, S.; Kurtz, D. M.; Montoya, S. R.; Hendrich, M. P.; Bominaar, E. L. The Catalytic Role of a Conserved Tyrosine in Nitric Oxide-Reducing Non-heme Diiron Enzymes. *ACS Catal.* **2020**, *10*, 8177-8186.
37. Martins, M. C.; Romão, C. V.; Folgosa, F.; Borges, P. T.; Frazão, C.; Teixeira, M. How superoxide reductases and flavodiiron proteins combat oxidative stress in anaerobes. *Free Rad. Biol. Med.* **2019**, *140*, 36-60.
38. Romão, C. V.; Vicente, J. B.; Borges, P. T.; Victor, B. L.; Lamosa, P.; Silva, E.; Pereira, L.; Bandeiras, T. M.; Soares, C. M.; Carrondo, M. A.; Turner, D.; Teixeira, M.; Frazão, C. Structure of *Escherichia coli* Flavodiiron Nitric Oxide Reductase. *J. Mol. Biol.* **2016**, *428*, 4686-4707.
39. Enemark, J. H.; Feltham, R. D. Principles of Structure, Bonding, and Reactivity for Metal Nitrosyl Complexes. *Coord. Chem. Rev.* **1974**, *13*, 339-406.
40. Zhang, Y.; Pavlosky, M. A.; Brown, C. A.; Westre, T. E.; Hedman, B.; Hodgson, K. O.; Solomon, E. I. Spectroscopic and Theoretical Description of the Electronic Structure of the S = 3/2 Nitrosyl Complex of Non-heme Iron Enzymes. *J. Am. Chem. Soc.* **1992**, *114*, 9189-9191.
41. Brown, C. A.; Pavlosky, M. A.; Westre, T. E.; Zhang, Y.; Hedman, B.; Hodgson, K. O.; Solomon, E. I. Spectroscopic and Theoretical Description of the Electronic Structure of S = 3/2 Iron-Nitrosyl Complexes and Their Relation to O_2 Activation by Non-Heme Iron Enzyme Active Sites *J. Am. Chem. Soc.* **1995**, *117*, 715-732.

42. Berto, T. C.; Hoffman, M. B.; Murata, Y.; Landenberger, K. B.; Alp, E. E.; Zhao, J.; Lehnert, N. Structural and Electronic Characterization of Non-Heme Fe(II)-Nitrosyls as Biomimetic Models of the Fe_B Center of Bacterial Nitric Oxide Reductase (NorBC). *J. Am. Chem. Soc.* **2011**, *133*, 16714–16717.
43. Speelman, A.; Zhang, B.; Krebs, C.; Lehnert, N. Structural and Spectroscopic Characterization of a High-Spin $\{FeNO\}^6$ Complex with an Iron(IV)-NO^- Electronic Structure. *Angew. Chem. Int. Ed.* **2016**, *55*, 6685-6688.
44. Berto, T. C.; Speelman, A.; Zheng, S.; Lehnert, N. Mono- and Dinuclear Non-Heme Iron-Nitrosyl Complexes: Models for Key Intermediates in Bacterial Nitric Oxide Reductases. *Coord. Chem. Rev.* **2013**, *257*, 244-259.
45. Caranto, J. D.; Weitz, A.; Hendrich, M. P.; Kurtz, D. M., Jr. The Nitric Oxide Reductase Mechanism of a Flavo-Diiron Protein: Identification of Active-Site Intermediates and Products. *J. Am. Chem. Soc.* **2014**, *136*, 7981–7992.
46. Kurtz, D. M., Jr. Flavo-Diiron Enzymes: Nitric Oxide or Dioxygen Reductases? *Dalton Trans.* **2007**, 4115-4121.
47. Caranto, J. D.; Weitz, A.; Giri, N.; Hendrich, M. P.; Kurtz, D. M., Jr. . A Diferrous-Dinitrosyl Intermediate in the N_2O-Generating Pathway of a Deflavinated Flavo-Diiron Protein. *Biochemistry* **2014**, *53*, 5631–5637.
48. Jana, M.; White, C. J.; Pal, N.; Demeshko, S.; Meyer, F.; Lehnert, N.; Majumdar, A. Functional Models for the Mono- and Dinitrosyl Intermediates of FNORs: Semireduction versus Superreduction of NO. *J. Am. Chem. Soc.* **2020**, *142*, 6600-6616.
49. White, C. J.; Speelman, A. L.; Kupper, C.; Demeshko, S.; Meyer, F.; Shanahan, J. P.; Alp, E. E.; Hu, M.; Zhao, J.; Lehnert, N. The Semireduced Mechanism for Nitric Oxide Reduction by Non-Heme Diiron Complexes: Modeling Flavodiiron Nitric Oxide Reductases. *J. Am. Chem. Soc.* **2018**, *140*, 2562-2574.
50. Zheng, S.; Berto, T. C.; Dahl, E. W.; Hoffman, M. B.; Speelman, A. L.; Lehnert, N. The Functional Model Complex $[Fe_2(BPMP)(OPr)(NO)_2](BPh_4)_2$ Provides Insight into the Mechanism of Flavodiiron NO Reductases. *J. Am. Chem. Soc.* **2013**, *135*, 4902−4905.
51. Lehnert, N.; Fujisawa, K.; Camarena, S.; Dong, H. T.; White, C. J. Activation of Non-Heme Iron-Nitrosyl Complexes: Turning up the Heat. *ACS Catal.* **2019**, *9*, 10499-10518.
52. Weitz, A. C.; Giri, N.; Frederick, R. E.; Kurtz, D. M.; Bominaar, E. L.; Hendrich, M. P. Spectroscopy and DFT Calculations of Flavo–Diiron Nitric Oxide Reductase Identify Bridging Structures of NO-Coordinated Diiron Intermediates. *ACS Catal.* **2018**, *8*, 11704-11715.
53. Hendrich, M. P.; Munck, E.; Fox, B. G.; Lipscomb, J. D. Integer-spin EPR studies of the fully reduced methane monooxygenase hydroxylase component. *J. Am. Chem. Soc.* **1990**, *112*, 5861-5865.
54. Pulver, S. C.; Tong, W. H.; Bollinger, J. M.; Stubbe, J.; Solomon, E. I. Circular Dichroism and Magnetic Circular Dichroism Studies of the Fully Reduced Binuclear Non-Heme Iron Active Site in the *Escherichia coli* R2 Subunit of Ribonucleoside Diphosphate Reductase. *J. Am. Chem. Soc.* **1995**, *117*, 12664-12678.
55. Rosenzweig, A. C.; Nordlund, P.; Takahara, P. M.; Frederick, C. A.; Lippard, S. J. Geometry of the soluble methane monooxygenase catalytic diiron center in two oxidation states. *Chem. Biol.* **1995**, *2*, 409-418.
56. Logan, D. T.; Su, X.-D.; Åberg, A.; Regnström, K.; Hajdu, J.; Eklund, H.; Nordlund, P. Crystal structure of reduced protein R2 of ribonucleotide reductase: the structural basis for oxygen activation at a dinuclear iron site. *Structure* **1996**, *4*, 1053-1064.

57. Jiang, Y.; Hayashi, T.; Matsumura, H.; Do, L. H.; Majumdar, A.; Lippard, S. J.; Moënne-Loccoz, P. Light-Induced N_2O Production from a Non-heme Iron–Nitrosyl Dimer. *J. Am. Chem. Soc.* **2014**, *136*, 12524-12527.
58. Hayashi, T.; Caranto, J. D.; Wampler, D. A.; Kurtz, D. M., Jr.; Moënne-Loccoz, P. Insights into the Nitric Oxide Reductase Mechanism of Flavodiiron Proteins from a Flavin-Free Enzyme. *Biochemistry* **2010**, *49*, 7040−7049.
59. Coufal, D. E.; Tavares, P.; Pereira, A. S.; Hyunh, B. H.; Lippard, S. J. Reactions of Nitric Oxide with the Reduced Non-Heme Diiron Center of the Soluble Methane Monooxygenase Hydroxylase. *Biochemistry* **1999**, *38*, 4504-4513.
60. Haskin, C. J.; Ravi, N.; Lynch, J. B.; Muenck, E.; Que, L., Jr. Reaction of NO with the Reduced R2 Protein of Ribonucleotide Reductase from *Escherichia coli*. *Biochemistry* **1995**, *34*, 11090-11098.
61. Feig, A. L.; Bautista, M. T.; Lippard, S. J. A Carboxylate-Bridged Non-heme Diiron Dinitrosyl Complex. *Inorg. Chem.* **1996**, *35*, 6892-6898.
62. Van Stappen, C.; Lehnert, N. Mechanism of N-N Bond Formation by Transition Metal-Nitrosyl Complexes: Modeling Flavodiiron Nitric Oxide Reductases. *Inorg. Chem.* **2018**, *57*, 4252-4269.
63. Speelman, A. L.; White, C. J.; Zhang, B.; Alp, E. E.; Zhao, J.; Hu, M.; Krebs, C.; Penner-Hahn, J.; Lehnert, N. Non-heme High-Spin $\{FeNO\}^{6-8}$ Complexes: One Ligand Platform Can Do It All. *J. Am. Chem. Soc.* **2018**, *140*, 11341-11359.
64. Jana, M.; Pal, N.; White, C. J.; Kupper, C.; Meyer, F.; Lehnert, N.; Majumdar, A. Functional Mononitrosyl Diiron(II) Complex Mediates the Reduction of NO to N_2O with Relevance for Flavodiiron NO Reductases. *J. Am. Chem. Soc.* **2017**, *140*, 14380-14383.
65. Confer, A. M.; McQuilken, A. C.; Matsumura, H.; Moënne-Loccoz, P.; Goldberg, D. P. A Nonheme, High-Spin $\{FeNO\}^8$ Complex that Spontaneously Generates N_2O. *J. Am. Chem. Soc.* **2017**, *139*, 10621-10624.
66. Neves, A.; de Brito, M. A.; Vencato, I.; Drago, V.; Griesar, K.; Haase, W. $Fe^{III}Fe^{III}$ and $Fe^{II}Fe^{III}$ Complexes as Synthetic Analogues for the Oxidized and Reduced Forms of Purple Acid Phosphatases. *Inorg. Chem.* **1996**, *35*, 2360-2368.
67. Belle, C.; Gautier-Luneau, I.; Karmazin, L.; Pierre, J.-L.; Albedyhl, S.; Krebs, B.; Bonin, M. Regio-Directed Synthesis of a ZnIIFeIII Complex from an Unsymmetrical Ligand and Its Relevance to Purple Acid Phosphatases. *Eur. J. Inorg. Chem.* **2002**, *2002*, 3087-3090.
68. Lanznaster, M.; Neves, A.; Bortoluzzi, A. J.; Aires, V. V. E.; Szpoganicz, B.; Terenzi, H.; Severino, P. C.; Fuller, J. M.; Drew, S. C.; Gahan, L. R.; Hanson, G. R.; Riley, M. J.; Schenk, G. A New Heterobinuclear $Fe^{III}Cu^{II}$ Complex with a Single Terminal Fe^{III}–O(phenolate) Bond. Relevance to Purple Acid Phosphatases and Nucleases. *J. Biol. Inorg. Chem.* **2005**, *10*, 319-332.
69. Neves, A.; Lanznaster, M.; Bortoluzzi, A. J.; Peralta, R. A.; Casellato, A.; Castellano, E. E.; Herrald, P.; Riley, M. J.; Schenk, G. An Unprecedented Fe^{III}(m-OH)Zn^{II} Complex that Mimics the Structural and Functional Properties of Purple Acid Phosphatases. *J. Am. Chem. Soc.* **2007**, *129*, 7486-7487.
70. Peralta, R. A.; Bortoluzzi, A. J.; de Souza, B.; Jovito, R.; Xavier, F. R.; Couto, R. A. A.; Casellato, A.; Nome, F.; Dick, A.; Gahan, L. R.; Schenk, G.; Hanson, G. R.; de Paula, F. C. S.; Pereira-Maia, E. C.; de P. Machado, S.; Severino, P. C.; Pich, C.; Bortolotto, T.; Terenzi, H.; Castellano, E. E.; Neves, A.; Riley, M. J. Electronic Structure and Spectro-Structural Correlations of $Fe^{III}Zn^{II}$ Biomimetics for Purple Acid Phosphatases: Relevance to DNA Cleavage and Cytotoxic Activity. *Inorg. Chem.* **2010**, *49*, 11421-11438.

71. Bosch, S.; Comba, P.; Gahan, L. R.; Schenk, G. Dinuclear Zinc(II) Complexs with Hydrogen Bond Donors as Structural and Functional Phosphatase Models. *Inorg. Chem.* **2014**, *53*, 9036-9051.
72. Daumann, L. J.; Schenk, G.; Ollis, D. L.; Gahan, L. R. Spectroscopic and Mechanistic Studies of Dinuclear Metallohydrolases and Their Biomimetic Complexes. *Dalton Trans.* **2014**, *43*, 910-928.
73. Camargo, T. P.; Maia, F. F.; Chaves, C.; de Souza, B.; Bortoluzzi, A. J.; Castilho, N.; Bortolotto, T.; Terenzi, H.; Castellano, E. E.; Haase, W.; Tomkowicz, Z.; Peralta, R. A.; Neves, A. Synthesis, Characterization, Hydrolase and Catecholase Activity of a Dinuclear Iron(III) Complex: Catalytic Promiscuity. *J. Inorg. Biochem.* **2015**, *146*, 77-88.
74. Herold, S.; Lippard, S. J. Carboxylate-Bridged Diiron(II) Complexes: Synthesis, Characterization, and O2-Reactivity of Models for the Reduced Diiron Centers in Methane Monooxygenase and Ribonucleotide Reductase. *J. Am. Chem. Soc.* **1997**, *119*, 145-156.
75. Kindermann, N.; Schober, A.; Demeshko, S.; Lehnert, N.; Meyer, F. Reductive Transformations of a Pyrazolate-Based Bioinspired Diiron−Dinitrosyl Complex. *Inorg. Chem.* **2016**, *55*, 11538-11550.
76. Ferretti, E.; Dechert, S.; Demeshko, S.; Holthausen, M. C.; Meyer, F. Reductive Nitric Oxide Coupling at a Dinickel Core: Isolation of a Key *cis*-Hyponitrite Intermediate en route to N_2O Formation. *Angew. Chem. Int. Ed.* **2019**, *58*, 1705-1709.
77. Chalkley, M. J.; Peters, J. C. A Triad of Highly Reduced, Linear Iron Nitrosyl Complexes: $\{FeNO\}^{8-10}$. *Angew. Chem. Int. Ed.* **2016**, *55*, 11995-11998.

Chapter 2

Non-Heme Diiron Model Complexes Can Mediate Direct NO Reduction: Mechanistic Insight into Flavodiiron NO Reductases

Adapted from published article: Dong, H. T.; White, C. J.; Zhang, B.; Krebs, C.; Lehnert, N. Non-Heme Diiron Model Complexes Can Mediate Direct NO Reduction: Mechanistic Insight into Flavodiiron NO Reductases. *J. Am. Chem. Soc.* **2018**, *140*, 13429-13440.

Acknowledgement: I would like to thank Dr. Corey J. White for his mentorship during my rotation in the early stage of this project. I would like to thank Dr. Bo Zhang and Prof. Carsten Krebs at the Pennsylvania State University who performed all the Mössbauer experiments and the corresponding data analysis in this chapter.

As discussed in **Chapter 1**, a new mechanism of N-N coupling has been observed by our group for the model complex $[Fe_2(BPMP)(OPr)(NO)_2](X)_2$ (H[BPMP] = 2,6-bis[[bis(2-pyridylmethyl)amino]methyl]-4-methylphenol, see Figure 2c; OPr^- = propionate bridging ligand, $X^- = BPh_4^-$, OTf^-), which is the first functional model system for FNORs. This [hs-$\{FeNO\}^7]_2$ complex is stable and has been structurally and spectroscopically characterized.[1] Upon one electron reduction, however, the complex shows very fast ($k_{obs} > 100\ s^{-1}$) and quantitative N_2O formation, using the semireduced mechanism shown in Scheme 1.1.[2] The semireduced mechanism is therefore a very efficient pathway for N_2O formation from a diiron core. Based on our results for $[Fe_2(BPMP)(OPr)(NO)_2](X)_2$ and the ability of this complex to mediate N_2O formation via the

semireduced pathway, I hypothesized that a complex with more reducing iron centers might allow for the direct reduction of NO to N_2O from the $[\{FeNO\}^7]_2$ intermediate.

To test the feasibility of this hypothesis, I prepared the model complex $[Fe^{III}_2((Py_2PhO_2)MP)(OPr)_2](OTf)$ (**1**) $[(Py_2PhO_2)MP]^{3-}$ = 2,6-Bis[((2-hydroxybenzyl)(2-pyridylmethyl)amino)methyl]-4-methylphenol where two of the pyridine groups in the H-BPMP ligand used previously are replaced by more electron-donating phenolate groups (Figure 2.1).[3] Complex **1** was characterized through spectroscopic methods and electrochemical studies. This complex can be reduced (using $CoCp_2$) to the diferrous complex (**2**), which was structurally characterized using X-ray crystallography. Excitingly, the reduced complex produces N_2O in quantitative yield when reacted with NO, making (**2**) the first model complex that is capable of mimicking the direct reduction of NO to N_2O as proposed for FNORs.[4] Additionally, the products after reduction of NO to N_2O at both room temperature and -80°C were spectroscopically characterized, providing further insight into the mechanism of N_2O generation by **2**.

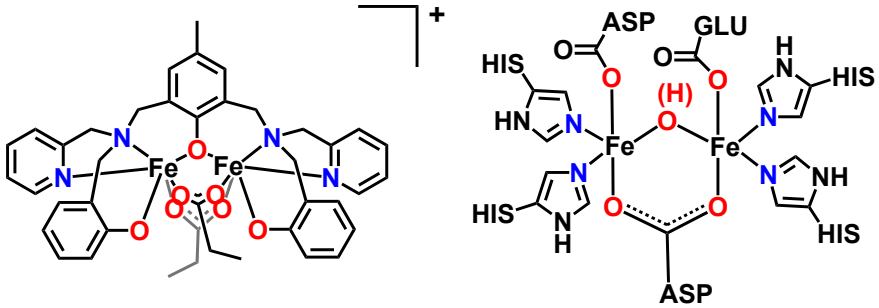

Figure 2.1 Left: Complex **1**. Right: Simplified drawing of the active site of FNORs.[5]

2.1 Synthesis and Spectroscopic Characterization of Complexes 1 and 2

Synthesis of the diferric complex $[Fe^{III}_2((Py_2PhO_2)MP)(OPr)_2](OTf)$ (**1**) was accomplished by reaction of $Fe(OTf)_2$ with the ligand in the presence of excess NaOPr (OPr^- = propionate) under ambient condition. The analogous complexes with acetate (OAc^-) bridges, $[Fe^{III}_2((Py_2PhO_2)MP)(OAc)_2](OTf)$ (**1-OAc**), and the corresponding perchlorate salts were also

prepared (the latter for X-ray crystallography) for comparison. The deep-blue complex **1** is characterized by a broad absorption band at 630 nm (ε = 6840 $M^{-1}cm^{-1}$, in CH_2Cl_2) as shown in Figure 2.2. ^{1}H-NMR spectroscopy in CD_2Cl_2 shows signals ranging from -10 to 50 ppm. The wide range of chemical shifts as well as the broad nature of the features are an indication of paramagnetic iron centers. The Mössbauer spectrum of complex **1** shows a quadrupole doublet with an isomer shift δ = 0.54 mm/s and a quadrupole splitting parameter ΔE_Q = 1.10 mm/s (Figure 2.3). These parameters are consistent with an antiferromagnetically (AF) coupled high-spin diferric complex, and they are also in agreement with the Mössbauer parameters of the **1-OAc** complex, which have previously been reported (δ = 0.54 mm/s, ΔE_Q = 1.06 mm/s).[6] Indeed, magnetic susceptibility measurement of **1-OAc** show weak AF coupling between the Fe centers, with a reported coupling constant J = -6.0 ($\pm$1) cm^{-1}. X-band electron paramagnetic resonance (EPR) spectroscopy of **1** at 4 K in frozen CH_2Cl_2 solution further reveals that **1** is EPR silent, in agreement with these results.

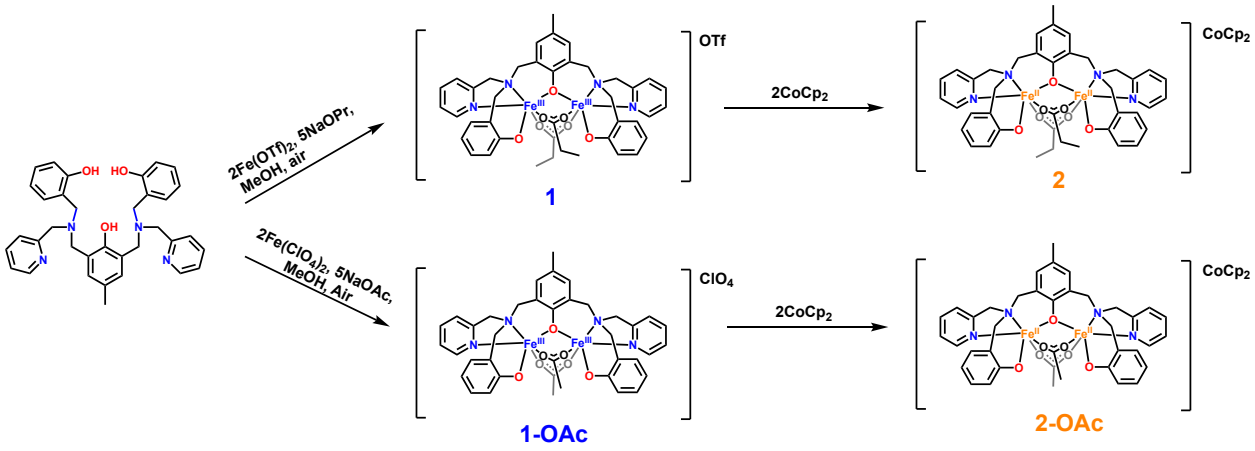

Scheme 2.1 Synthesis of **1**, **1-OAc**, **2**, and **2-OAc**.

Interestingly, previous studies have shown that by replacing a pyridine on the H-BPMP ligand by one phenolate group, the redox potential of the diiron complex is shifted by approximately 500 mV.[7] To assess the redox properties of our complex, the cyclic voltammogram

(CV) of complex **1** in dichloromethane (CH_2Cl_2) was recorded by scanning negatively from the open circuit potential at various scan rates. The resulting CVs of **1** are shown in Figure 2.4. Two reversible redox couples are observed with $E_{1/2}$ of -0.28 V and -1.0 V versus Fc^+/Fc. These correspond to the Fe^{III}/Fe^{III} to Fe^{III}/Fe^{II} and Fe^{III}/Fe^{II} to Fe^{II}/Fe^{II} couples, respectively. *Importantly, compared to complex [Fe2(BPMP)(OPr)2](OTf) studied previously, these redox potentials are negatively shifted by about 1 V, demonstrating that our goal to prepare a more electron-rich analog of the BPMP⁻ complex has been accomplished.* Compared to FNORs, complex **1** shows a more negative redox potential of about 300 mV.[8,9]

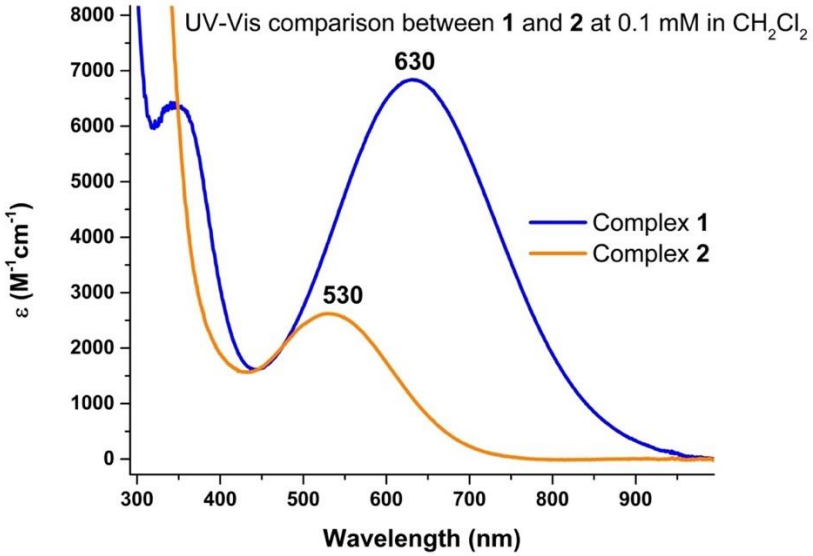

Figure 2.2 Absorption spectra of complexes **1** and **2** in dichloromethane at 0.1 mM concentration at room temperature.

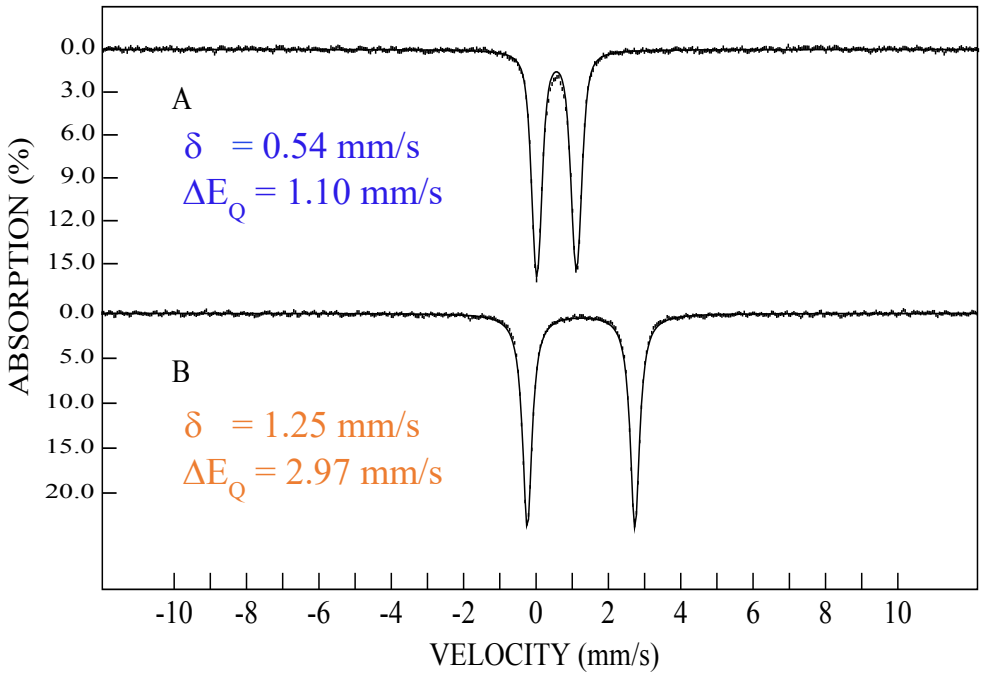

Figure 2.3 4.2 K/53 mT Mössbauer characterization of complexes **1** (A, top) and **2** (B, bottom). The solid lines overlaying the experimental data are simulations using the parameters quoted in the main text.

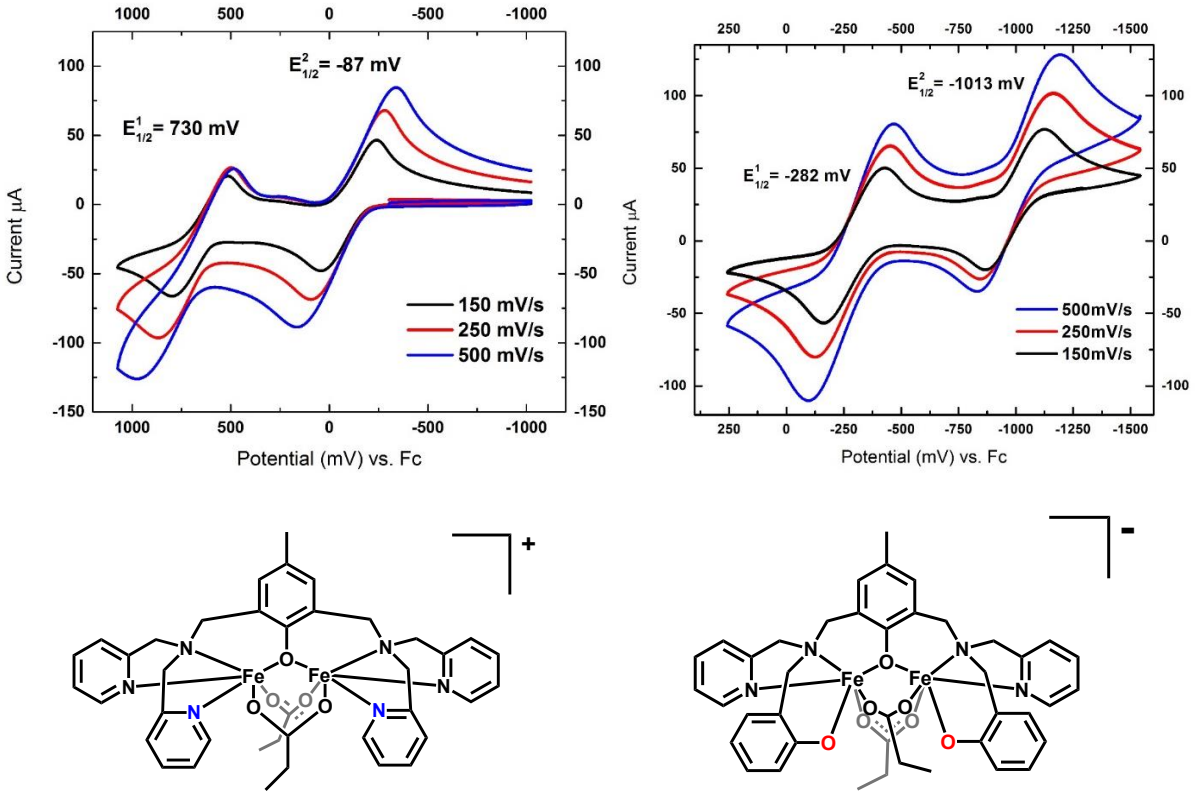

Figure 2.4 Left: $[Fe_2(BPMP)(OPr)_2](X)$ and its redox potentials measured by cyclic voltammetry. Right: $[CoCp_2][Fe_2((Py_2PhO_2)MP)(OAc)_2]$ with the redox potentials shifted by about -1 V, due to the use of a more electron-donating coligand. Adapted from ref. [10].

The diferrous state of **1-OAc**, denote here as **2-OAc**, has been reported to be unstable and thus prevented further spectroscopic and structural characterization in a previous report.[6] In this work, however, I show that complex **1** can conveniently be reduced to the diferrous complex **2** *in situ* by addition of exactly 2 equivalents of cobaltocene ($CoCp_2$), as illustrated by a corresponding redox titration. The reduction leads to the disappearance of the 630 nm band of **1**, and a smaller band appears at 530 nm (ε = 2620 $M^{-1}cm^{-1}$, in CH_2Cl_2) indicating the formation of **2** (Figure 2.2). This goes along with a characteristic color change of the solution from dark blue to dark orange. The Mössbauer spectrum of **2** (Figure 2.3) shows a quadrupole doublet with δ = 1.25 mm/s and ΔE_Q = 2.97 mm/s, consistent with a high-spin diferrous complex. X-band EPR spectroscopy of **2** at 4 K in frozen CH_2Cl_2 solution reveals that **2** is EPR silent, as expected. Note that complex **2** can also be accessed by direct reaction of $H_3[(Py_2PhO_2)MP]$ with $Fe(OTf)_2$ in the presence of base and the bridging propionate (NaOPr), but, as mentioned above, it is advantageous to enter this chemistry via the diferric complex **1**, which is much more stable. Interestingly, complex **2** shows an unexpected temperature-dependent property where it changes color from deep orange to very faint yellow (almost no color) when a solution of this compound is cooled down from room temperature to -80 ºC in dichloromethane. The absorption band at 530 nm disappears as the temperature decreases, and the resulting absorption spectrum shows just a weak feature at ~500 nm (Figure 2.5, top). I hypothesize that in solution, the bridging propionate ligands of complex **2** are fluxional, such that at room temperature, these ligands can dissociate (partly or completely) to form five-coordinate iron centers. As the temperature is decreased, the propionates (either dissociated or still bound as monodentate ligands) rebind to the iron centers (driven by entropy), forming six-coordinate Fe(II) centers with two bridging propionates at -80 ºC. This hypothesis is

supported by the crystal structure of **2-OAc** and the Mössbauer spectra of the reaction product of **2** with NO at -80 °C.

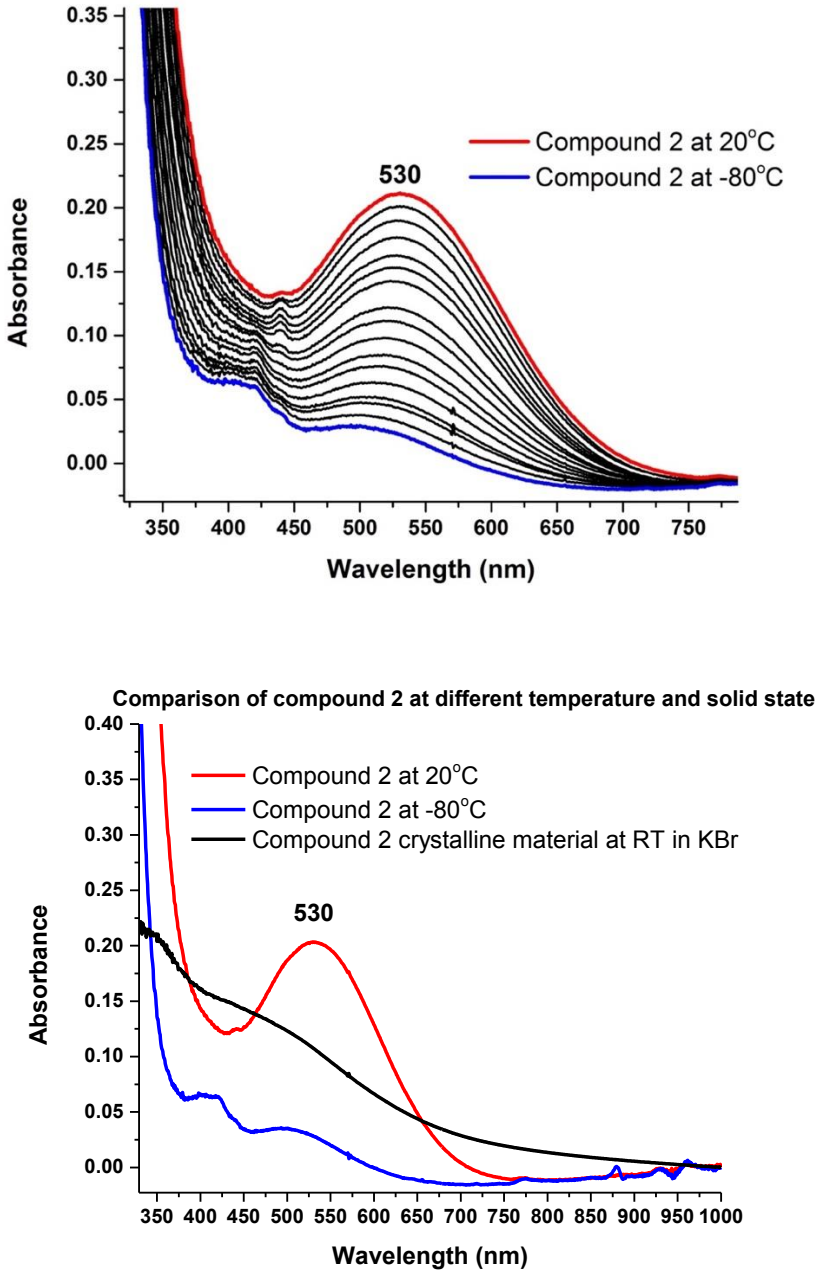

Figure 2.5 Top: spectral changes in the absorption spectrum of **2** upon cooling from room temperature to -80 °C. Note that these changes are fully reversible. In the process, the color of the solution changes from deep orange to light yellow. The spectra were collected at 0.1 mM concentration of **2** in dichloromethane. Bottom: Comparison of the UV-Vis spectrum obtained from crystalline material in KBr (black line) with the absorption spectra of complex **2** in solution at RT (red line) and -80 °C (blue line).

2.2 Structural Comparison of Complexes 1-OAc and 2-OAc

Structural characterization of complex **1** has proven to be challenging due to the high degree of disorder caused by the $–CH_2CH_3$ groups of the bridging propionate ligands, and further disorder introduced by the counter anion.[11] Initially, I attempted to determine the crystal structure of complex **1**. For this purpose, I diffused toluene into an acetonitrile solution of the complex to grow single crystals of **1**. In our best attempt, I obtained a structure for **1** in which the position of the diiron core, the ligand scaffold, and the triflate counter anion are well defined. However, the propionate groups are highly disordered, making it impossible to locate the electron density associated with the propionate side chains. The obtained structure of the $\{Fe^{III}_2((Py_2PhO_2)MP)\}$ core itself is very similar to that of **1-OAc**, in the case of which a fully solved crystal structure has been reported in the literature.[6] However, the structure of the diferrous complex **2-OAc** could not be obtained so far. Conveniently, I can generate **2-OAc** by reduction of **1-OAc** with two equivalents of $CoCp_2$, thus allowing us to isolate, crystallize, and structurally characterize **2-OAc** for the first time. By diffusion of hexane into a solution of **2-OAc** in CH_2Cl_2, orange rod crystals of this complex could be obtained, suitable for diffraction. The crystal structure of **2-OAc** is shown in Figure 7.

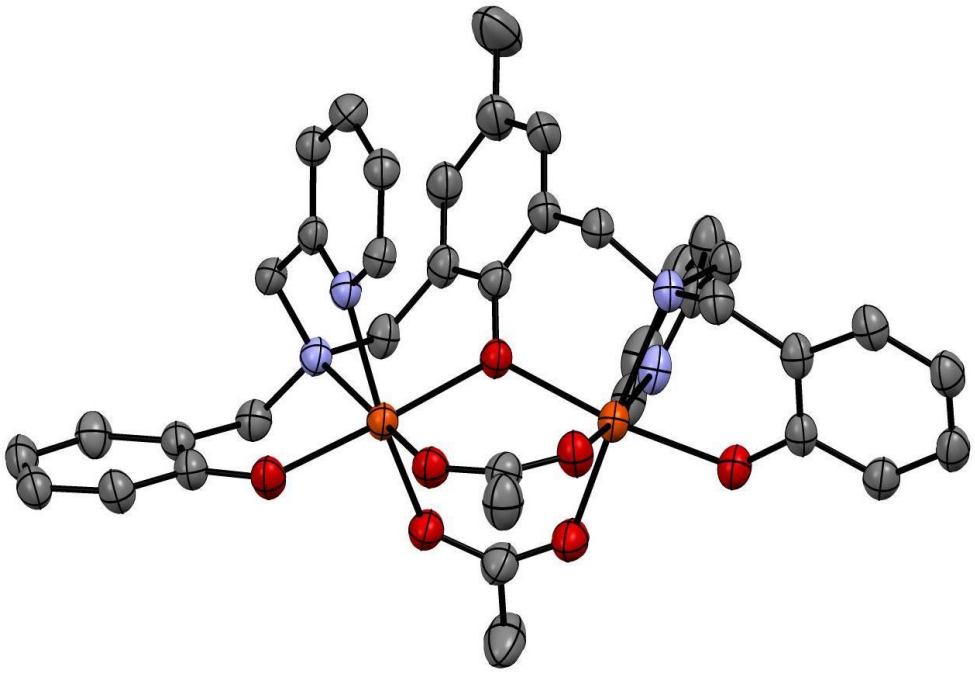

Figure 2.6 Crystal structure of 2-OAc, obtained from diffusion of hexane into a saturated solution of 2-OAc in dichloromethane. The numbering scheme is similar to that reported for the crystal structure of 1-OAc for better comparison. Solvent molecules, the CoCp2+ counter cation, and hydrogen atoms have been omitted for clarity.

Table 1 compares the structural parameters for **1-OAc** and **2-OAc**. Both complexes have very similar structures that feature two six-coordinate iron centers that are connected by the central phenolate unit and the two bridging carboxylate (acetate) ligands. In **2-OAc**, the metal-ligand bonds are all elongated as expected, due to the reduction of the iron centers from +III to +II (see Table 2.1). In **1-OAc**, the two iron centers are essentially equivalent. Upon reduction to **2-OAc**, the diiron core become much more asymmetric, as evident from the Fe-O(carboxylate) bond distances: whereas these bond lengths are essentially all equivalent in **1-OAc**, they differ by up to 0.1 Å in **2-OAc**. In the reduced complex, each iron has one short and one long Fe-O(carboxylate) bond, which suggests that these bridging ligands can be fluxional in solution. This supports the idea that the iron centers in **2-OAc** could become five-coordinate at room temperature in solution, which would explain the temperature-dependent changes in the absorption spectrum of this compound. In this regard, it should be noted that the absorption spectrum of **2-OAc** in the

crystalline form is equivalent to that of the low-temperature form in solution (Figure S4, bottom). This strongly indicates that the low-temperature form of **2-OAc** in solution has a similar structure as the crystal structure of this complex (Figure 2.6) with six-coordinate Fe(II) centers and two bridging carboxylate ligands. At room temperature, the Fe(II) centers could then become five-coordinate, as discussed above. This would also explain why the process is fully reversible.

Table 2.1 Structural comparison between **1-OAc** and **2-OAc**. Values are listed in Å and deg.

Structure	**1-OAc (ref. 27)**	**2-OAc** [a]
Fe1-O1	2.054	2.1
Fe2-O1	2.055	2.077
Fe1-Fe2	3.528	3.572
Fe1-O1-Fe2	118.34	117.57
Fe1-N1	2.179	2.247
Fe2-N3	2.169	2.253
Fe1-N2	2.134	2.22
Fe2-N4	2.127	2.253
Fe1-O4	1.965	2.143
Fe2-O5	1.993	2.093
Fe1-O6	1.98	2.107
Fe2-O7	1.956	2.188

[a] This work.

The bonds between the iron centers and the amine ligands are also significantly elongated in **2-OAc** compared to **1-OAc**. Despite the significant elongation of the bonds around the iron centers, the core structure of **2-OAc** remains intact and strongly resembles that of **1-OAc** in our crystal structure as shown in Figure 2.6.

2.3 Reaction of 2 with NO Gas at Room Temperature

Upon addition of NO gas into the headspace of a dark orange solution of **2**, the solution changes color immediately to red. Notably, the IR spectrum of the resulting reaction product does not show any band associated with an N-O stretch (for high-spin $\{FeNO\}^7$ complexes, the N-O stretch is usually observed in the 1700 – 1800 cm^{-1} range[12]). I therefore conducted an IR gas headspace analysis of the reaction flask and detected N_2O in high yield (Figure 2.7). Further experiments determined *that N_2O is generated in quantitative yield in the reaction of **2** with NO gas as shown in Figure 2.8.* The same result is obtained when complex **2**, generated directly by metalation of $H_3[(Py_2PhO_2)MP]$ with $Fe(OTf)_2$, is used. Similarly, **2-OAc** generates quantitative amounts of N_2O when reacted with NO gas. *This result shows, for the first time, that non-heme diiron sites can in fact directly reduce NO to N_2O from the $\{FeNO\}^7$ redox state.* This provides support for the proposal that FNORs are able to mediate direct NO reduction to N_2O from the diferrous state, without involvement of the flavin cofactor in the reaction. Interestingly, N_2O production by **2** does not require any external source of acid, which confirms our previous result that water formation is not required as a driving force for N_2O generation from NO.[7] This suggests the formation of a bridging μ-oxo unit, Fe^{III}-O-Fe^{III}, as the direct reaction product besides N_2O. Indeed, the Mössbauer spectrum of the product after the reaction of **2** with NO gas at room temperature shows two quadrupole doublets which are responsible for ~95% of iron, with parameters that are consistent with two antiferromagnetically (AF) coupled high-spin diferric complexes (Figure 2.13D). The isomer shifts and quadrupole splittings of the two diferric components, 0.53 and 0.80 mm/s (71%) and 0.52 and 1.70 mm/s (22%), respectively, are different from the diferric complex **1** (see Figure 2.3, top), in agreement with the formation of unique

diferric products after the reduction of NO. The two diferric reaction products likely differ in the exact ligation of the iron centers, leading to the observed difference in quadrupole splittings. The absorption spectrum of the product shows a shift in the main absorption band from 530 nm in complex **2** to 470 nm with a shoulder at 515 nm, in agreement with the color change from dark orange to red (Figure 2.9, black). Excitingly, when two equivalents of acetic acid are added to this red product solution, it immediately turns back to the deep blue color of complex **1**. Absorption spectra and mass spectrometry show that the product has indeed turned back into complex **1** after acetic acid addition, supporting the idea that the diferric reaction products contain Fe^{III}-O-Fe^{III} units. Subsequent addition of two equivalents of $CoCp_2$ regenerates complex **2/2-OAc**, which can be reacted again with NO gas to produce a second, quantitative amount of N_2O as shown by gas headspace IR (Figure 2.10). Through this experiment I have successfully demonstrated the capability of our complex to carry out the catalytic reduction of NO to N_2O, via the proposed catalytic cycle shown in Figure 2.16. Note that because $CoCp_2$ reacts directly with NO gas (see Experimental Section), it is not possible to run the reaction of **1** with NO under catalytic conditions (i.e., with excess $CoCp_2$, NO and acetic acid).

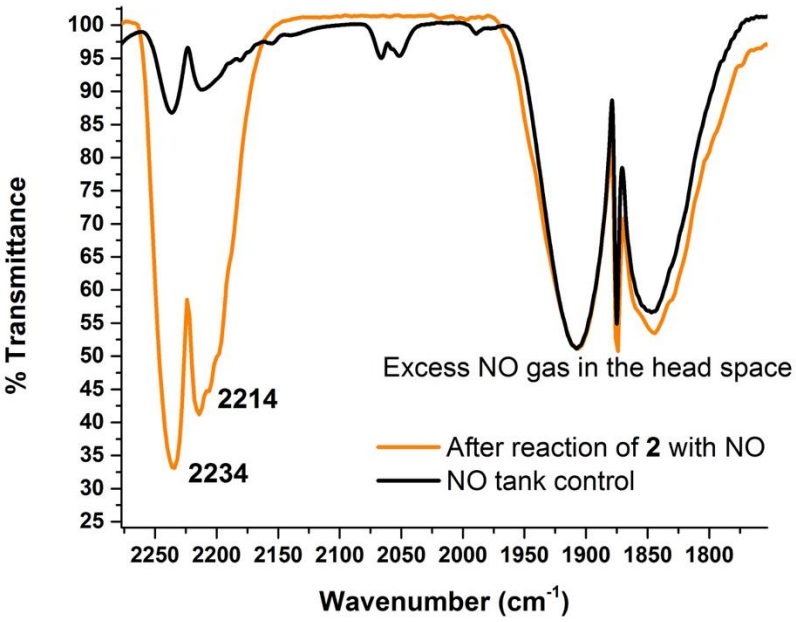

Figure 2.7 IR gas headspace detection of N_2O at room temperature (RT), showing the prominent N-N stretch of N_2O at 2234 and 2214 cm^{-1}, which is used to quantify N_2O production.

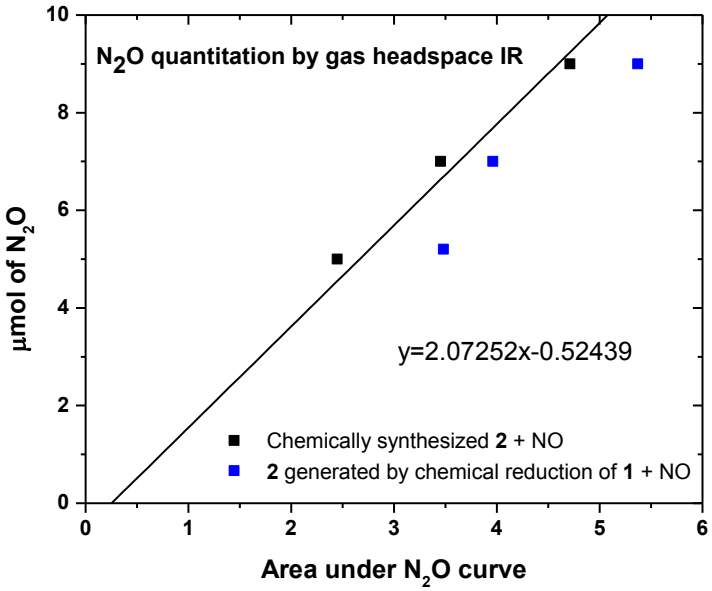

Figure 2.8 Calibration curve for the quantitative detection of N_2O by IR gas headspace analysis. Data for the reaction of **2** with NO gas at room temperature are indicated. See ref. 4 for the procedure to generate the calibration curve. The black line is the calibration curve generated from Piloty's acid, the black dots are the observed amounts of N_2O formed in our experiments using chemically synthesized **2**, and the blue dots are from complex **2** generated by chemical reduction of complex **1** by $CoCp_2$, quantified using the calibration curve.

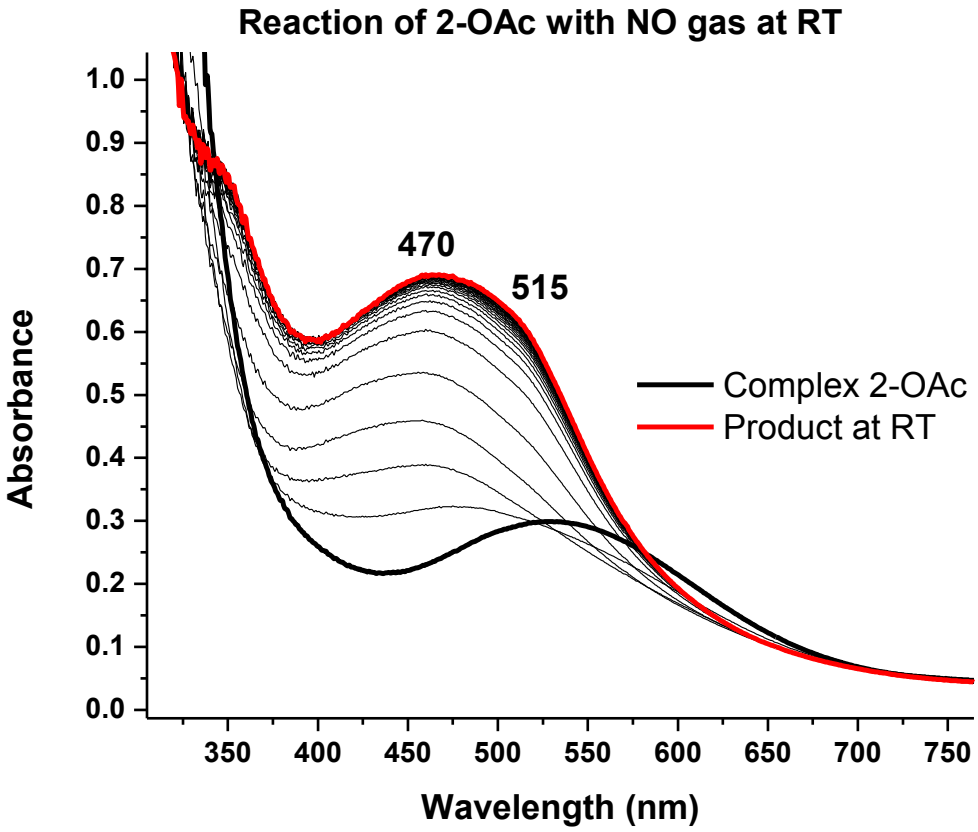

Figure 2.9. Changes in the absorption spectrum of **2-OAc** upon reaction with NO gas at room temperature. These spectral changes occur in less than a minute. Spectra were collected at a concentration of 0.1 mM **2-OAc** in dichloromethane.

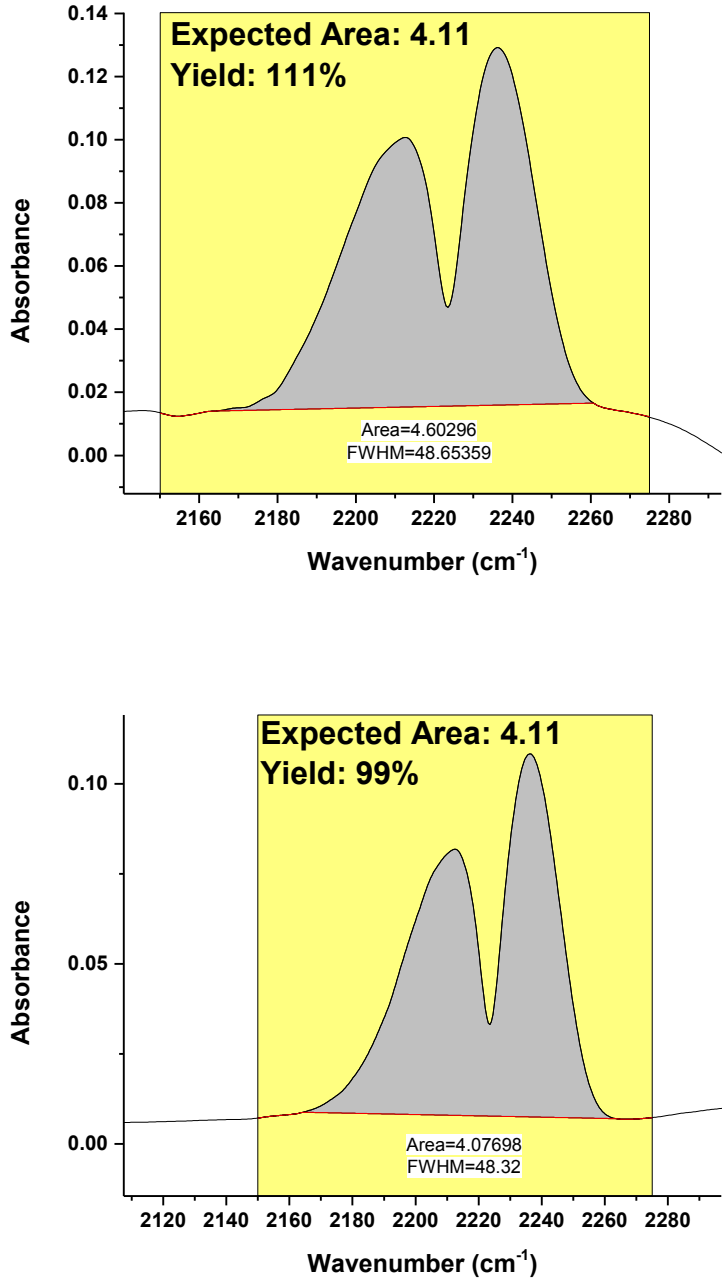

Figure 2.10. Comparison of the IR gas headspace analysis for N_2O formation for the reaction of 8 μmol of **2-OAc** with NO gas in dichloromethane at room temperature. Top: first cycle, bottom: second cycle. Since $CoCp_2$ also reacts with NO gas directly to produce N_2O, it is difficult to quantify the amount of N_2O that is solely generated by **2-OAc** when an excess amount of $CoCp_2$ is present in the reaction mixture. Therefore, I decided to run the reaction in cycles and only add quantitative amounts of $CoCp_2$ as needed to reduce **1-OAc**

The observed reactivity for **2** with NO is in stark contrast to our previously reported complex $[Fe_2(BPMP)(OPr)(NO)_2](X)_2$, which forms a diferrous dinitrosyl complex that is stable in both the solid and solution state at room temperature.[1,2] Our results prove that the strongly donating ligand scaffold in **2** is indeed necessary to create more reducing iron centers that are able to promote direct N-N coupling of NO for N_2O formation.

2.4 Reaction of 2 with NO Gas at -80°C

In order to study the mechanism of N_2O generation in more detail, I monitored the reaction of **2** with NO gas at low temperatures (-80 °C) by a combination of spectroscopic and analytical methods. Solution UV-Vis spectroscopy of the reaction mixture at -80 °C (Figure 2.11, red) shows the appearance of a new absorption band at 430 nm with a shoulder at 525 nm, indicating that the reaction still proceeds, even at this low temperature. Accordingly, solution and gas headspace IR spectroscopy confirm the formation of N_2O under these conditions. Further kinetic analysis of the UV-Vis data in Figure 2.11 delivers a $k_{obs} = 0.1\ s^{-1}$ for the reaction at -80 °C. Curiously, however, the maximum yield of N_2O at -80 °C is only about 10 – 30% (depending on the exact experimental conditions), even when the reaction mixture is kept for 90 minutes (note that there are no more changes in the UV-Vis spectrum past ~30 minutes reaction time). I then further analyzed the reaction mixture at -80 °C after the "steady state" was reached (no more spectral changes). At this point, low-temperature IR spectroscopy shows two bands at 1726 and 1707 cm^{-1} (see Figures 2.12), which indicates the presence of $\{FeNO\}^7$ complexes in solution as potential intermediates of the reaction. Electron paramagnetic resonance spectroscopy (EPR) reveals two signals at $g_{eff} = 3.94$ (major component) and $g = 2.01$ (minor species); however, double integration of the spectrum reveals that these signals correspond to only ~5% of total iron. Mössbauer spectroscopy indicates

the presence of at least three distinct Fe-species in the reaction mixture at -80 ºC. The 4.2K / 53mT spectrum (Figure 2.13A) shows a quadrupole doublet associated with the diferrous precursor (δ = 1.25 mm/s, ΔE_Q = 3.01. mm/s, 34% red line), a quadrupole doublet with parameters indicative of the EPR-silent [{FeNO}^{7}]$_2$ complex (δ = 0.70 mm/s, ΔE_Q = 1.26 mm/s, 21%, blue line), and a magnetically split component exhibiting broad absorption features extending from -10 to +10 mm/s (ca 45% intensity). In the 60 K/0 mT spectrum (Figure 2.13B), the magnetically split component collapses into two quadrupole doublets with parameters typical of high-spin ferric and ferrous iron, suggesting that the broad magnetic component emanates from a mixed-valent Fe^{II}/Fe^{III} complex (δ = 1.23 mm/s, ΔE_Q = 2.89 mm/s, 23%, turquois line, δ = 0.56 mm/s, ΔE_Q = 0.93 mm/s, 23%, orange line). Additional spectra indicate a ferromagnetically coupled Fe^{II}/Fe^{III} cluster with an S_{tot}=9/2 electronic ground state. The Mössbauer parameters determined for this species are strikingly similar to those reported previously for $(Et_4N)[Fe_2(salmp)_2]$, a similar species with ferromagnetically coupled Fe^{II}/Fe^{III} centers and the same S_{tot}=9/2.[13] This complex is a dimer with two bridging phenolate ligands that connect the two iron centers. This indicates that in our mixed-valent intermediate, additional bridging phenolates might be present, which might then favor the S_{tot}=9/2 ground state. Importantly, this mixed-valent species is distinctly different from the mixed-valent state that is accessible by simple one-electron reduction of **1** and **1-OAc**. The mixed-valent state of **1-OAc** has been reported to have an S_{tot}=1/2 electronic ground state with J = -5.3 cm^{-1}, suggesting a weak AF coupling between the two iron centers.[6] Mössbauer spectroscopy of this species shows no magnetically split components in the presence of a magnetic field (as observed for the mixed-valent reaction intermediate), but instead, two sets of quadrupole doublets can be fit that correspond to a high spin ferric (δ = 0.53 mm/s, ΔE_Q = 0.96 mm/s, 50%) and a high spin ferrous (δ = 1.13 mm/s, ΔE_Q = 2.86 mm/s, 50%) center. I expect the mixed-valent form of **1**,

when prepared by simple (electro)chemical reduction, to have similar properties (since **1** and **1-OAc** only differ slightly in the nature of the carboxylate bridges). Therefore, the mixed-valent reaction intermediate formed at -80 °C is clearly a distinct species that likely contains phenolate-bridged iron centers.

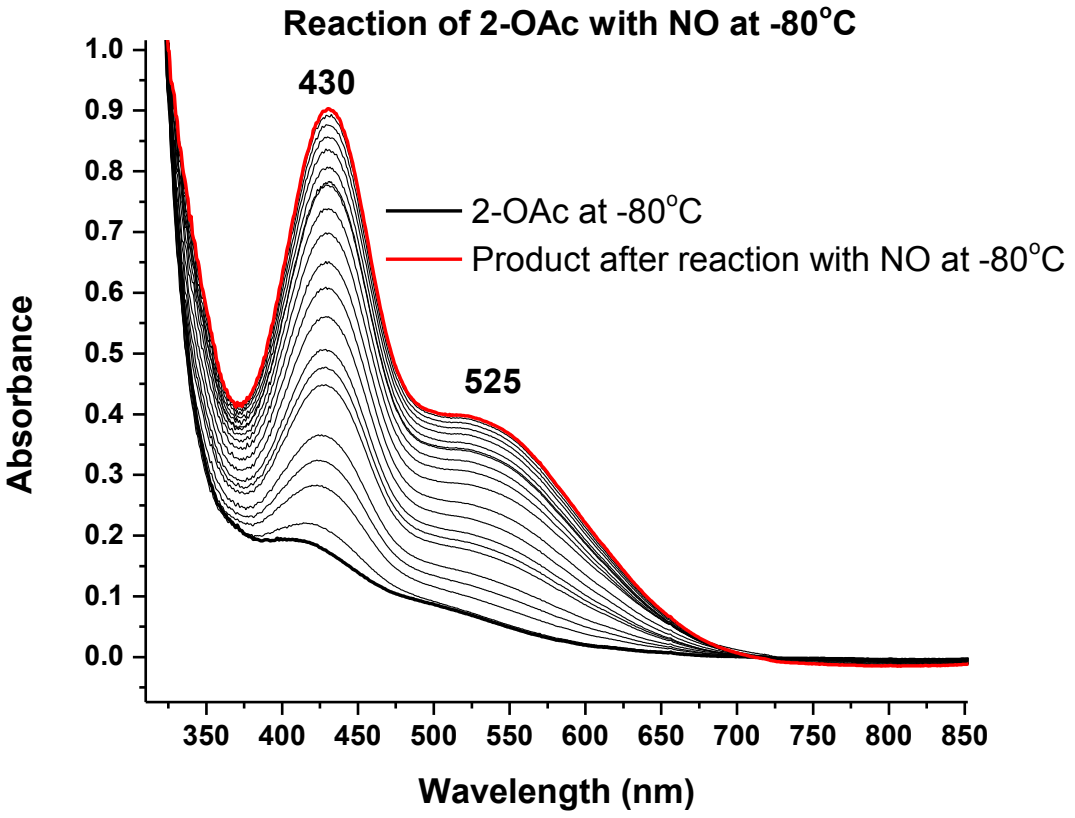

Figure 2.11. Changes in the absorption spectrum of **2-OAc** upon reaction with NO gas at -80 °C. Spectral changes stop after about 30 minutes of reaction time. Spectra were collected at a concentration of 0.1 mM **2-OAc** in dichloromethane.

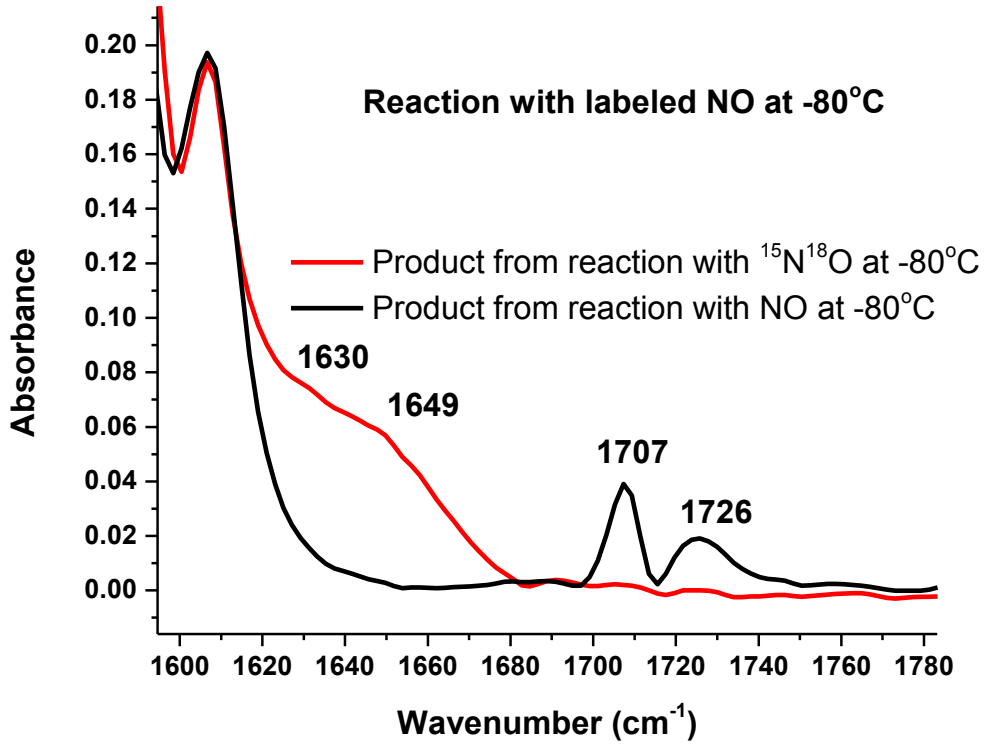

Figure 2.12. $^{15}N^{18}O$ labelling study using solution IR spectroscopy. The data show the product of the reaction of 5 mM **2** with NO/$^{15}N^{18}O$ gas (black/red spectra) in dichloromethane at -80 °C. The spectra demonstrate that the two signals at 1707 and 1726 cm^{-1} originate from N-O stretches in nitrosyl complexes that are formed in the low-temperature reaction.

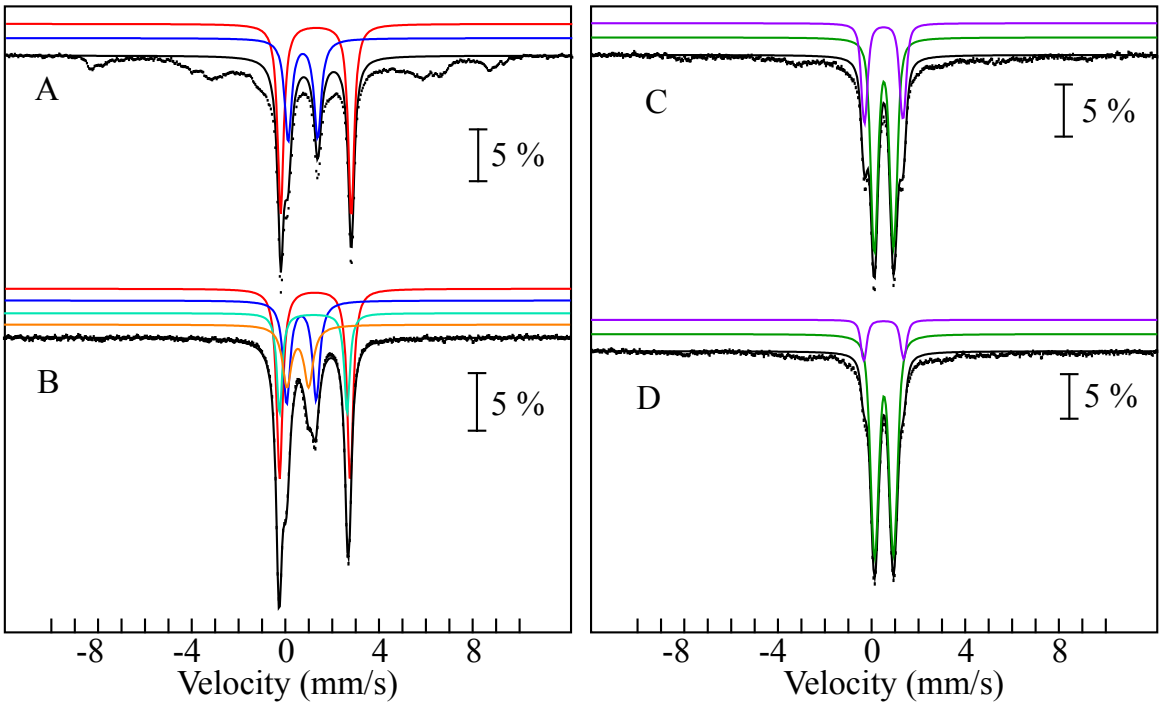

Figure 2.13. Mössbauer spectra of a sample of **2** reacted with NO gas at -80 °C for 60 min, recorded at 4.2 K/53 mT (A) and 60 K/0 mT (B). (C) 4.2 K/53 mT spectrum of a duplicate sample of (A), after warming to RT. Simulation parameters: δ = 0.53 mm/s, ΔE_Q = 0.82 mm/s, 53%, green line and δ = 0.51 mm/s, ΔE_Q = 1.64 mm/s, 22%, purple line. (D) 4.2 K/53 mT spectrum of a sample of **2** reacted with NO gas at RT for 15 min. Simulation parameters: δ = 0.53 mm/s, ΔE_Q = 0.80 mm/s, 71%, green line and δ = 0.52 mm/s, ΔE_Q = 1.70 mm/s, 22%, purple line. In all spectra, the black line overlaying the experimental data represents the sum of all individual contributions from the fit. Spectral features not captured by the simulation are attributable to the broad, magnetically split features of the S=9/2 species.

These results imply that when the reaction is conducted at -80 °C, complex **2** proceeds with NO binding and N_2O release, but that a significant fraction of the complex is kinetically trapped in off-pathway intermediates, and these species are unable to re-enter the reaction pathway as long as the reaction mixture is kept at -80 °C. This includes the experimentally observed $[\{FeNO\}^7]_2$ complex, responsible for the observed N-O stretching bands in the low-temperature IR spectra and further identified by Mössbauer spectroscopy (see above), which must be kinetically trapped in a conformation that does not allow N_2O formation to proceed. In this regard, it is interesting to note that the complex using the dinucleating pyrazolate/triazacyclononane hybrid ligand, denoted as

[L{Fe(NO)}$_2$(μ-OOCR)](X)$_2$, which contains two orthogonal Fe-N-O units, is unable to produce N_2O upon reduction (in contrast to [Fe$_2$(BPMP)(OPr)(NO)$_2$](X)$_2$, where the Fe-N-O units are in a *cis* position).[14] The presence of unreacted diferrous precursor is likely due to the fact that this complex contains six-coordinate Fe(II) centers at low temperature (see above), which lowers their affinity for NO. The formation of the Fe^{II}/Fe^{III} mixed-valent species at low-temperature could be due to redox comproportionation between the Fe^{III}/Fe^{III} reaction product and the precursor **2**, or this species could correspond to the product of oligomerization of the diferric reaction product and the diferrous complex. It is also possible that the reaction proceeds by a different mechanism at low temperature; this point requires further study. I have attempted to isolate the mixed-valent complex (by precipitation) as a solid at -80 ^oC for further characterization. However, under these conditions, all iron-containing species seem to precipitate, and I was not able to derive further information about the S_{tot}=9/2 intermediate from these mixtures (which also seem to decompose at room temperature, even in the solid state

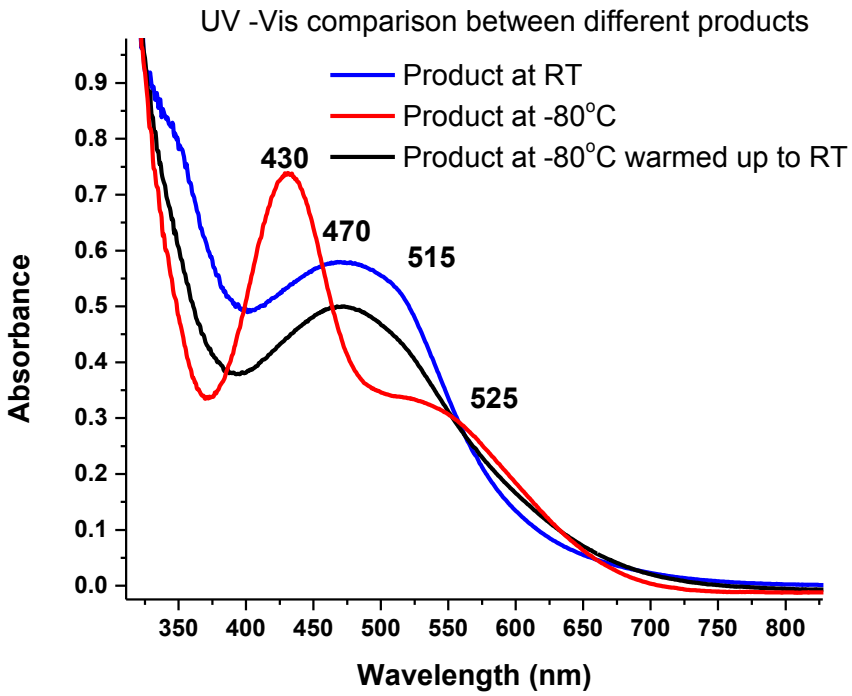

Figure 2.14. UV-visible absorption spectra of the reaction product of 0.1 M **2** with excess NO in CH_2Cl_2 at -80 °C (red), of this product warmed up to RT (blue), and of the product that is obtained when the reaction is conducted at RT (black).

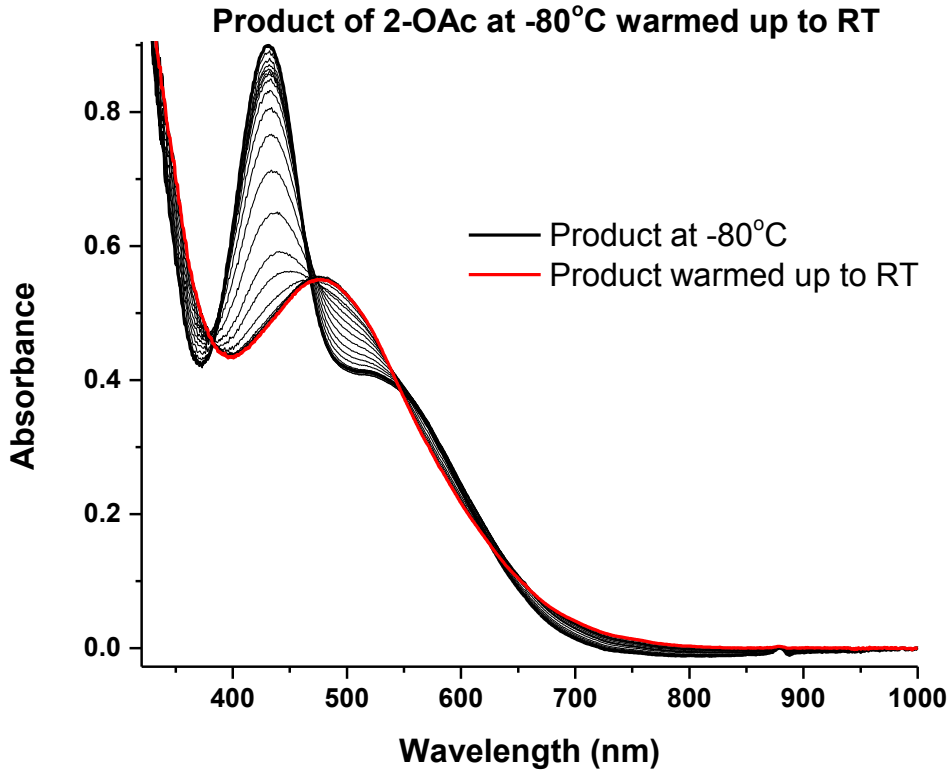

Figure 2.15 Changes in the absorption spectrum of the reaction product of **2-OAc** and NO gas (reaction run at -80 °C; see Figure S11) upon warming up of the solution to room temperature over the course of 45 minutes. Spectra were collected at a concentration of 0.1 mM **2-OAc** in dichloromethane.

Upon warming up of the solution to room temperature, the species observed at low temperature are "activated" and proceed to produce N_2O, leading to a close to quantitative yield of N_2O as determined by IR gas headspace analysis. Curiously, the diferric product obtained in this way differs slightly (by UV-Vis and Mössbauer spectroscopy; see Figures 2.13 and 2.14) from the one obtained when the reaction is run directly at room temperature (see above). As shown in Figure 10, when the reaction is run at room temperature, the product shows a broad absorption band at 470 nm with a shoulder at 515 nm, and no discernible intermediate it detected during the reaction. At low temperature, an absorption band at 430 nm appears first (see above), and upon warming to room temperature, this band disappears and new features, which resemble the

absorption features of the room temperature product, appear at 470 nm with a shoulder at 515 nm (see Figure 2.15). When the low-temperature reaction mixture is warmed up to room temperature, the Mössbauer spectrum reveals again two diferric products (~80% total iron, see Figure 2.13C) with parameters typical for AF coupled high-spin Fe^{III}/Fe^{III} complexes. Here, the two components show isomer shifts and quadrupole splittings of 0.53 mm/s and 0.82 mm/s (53%) and 0.51 mm/s and 1.64 mm/s (22%), respectively. Hence, the same products are formed as in the room temperature reaction, but in a different ratio (which explains the slight differences in the absorption spectra of the warmed up low-temperature and the room temperature products). As mentioned above, these results indicate that the diferric product exists in the form of different coordination isomers with slightly different properties.

2.5 The Nature of the $[\{FeNO\}^7]_2$ Intermediate Observed at Low Temperature

The observation of the two IR bands at 1726 and 1707 cm^{-1} (Figure S31), which belong to the $[\{FeNO\}_7]^2$ intermediate observed by Mössbauer spectroscopy and shown to be EPR silent (see above), indicates that the reaction of **2** with NO proceeds via the formation of a diferrous dinitrosyl intermediate, similar to the mechanism proposed for FNORs by Kurtz and coworkers.[15] However, isolation and further characterization of this species have proven to be challenging. I therefore used DFT calculations, which have proven to be effective at predicting structural parameters and vibrational properties of non-heme (hs) iron-nitrosyl complexes,[16-18] to gain further insight into the properties of this species. Based on our previously obtained crystal structure of $[Fe_2(BPMP)(OPr)(NO)_2](BPh_4)_2$, I constructed an analogous model, $[Fe_2((Py_2PhO_2)MP)(OPr)(NO)_2]$, and then optimized the structure of this species in the AF coupled state using BP86/TZVP.[19-22] The fully optimized structure of this complex is shown in Figure 2.17.

The calculations predict the N-O stretching frequencies for this structure to be ν_{sym}(N-O) = 1723 cm^{-1} and ν_{asym}(N-O) = 1678 cm^{-1}, respectively, which is in good agreement with our experimental observations. This result therefore supports our conclusion that the two IR bands at 1726 and 1707 cm^{-1} observed by IR spectroscopy correspond to the dinitrosyl species observed by Mössbauer spectroscopy, and that this is indeed a diferrous dinitrosyl intermediate. However, it should be noted that the intermediate observed by Mössbauer spectroscopy is unable to mediate N_2O formation (at low temperature), and hence, the two Fe-N-O units are probably not coplanar in this structure. Since the available information about this intermediate is limited, I did not attempt further calculations on structural isomers of [Fe_2((Py_2PhO_2)MP)(OPr)$(NO)_2$].

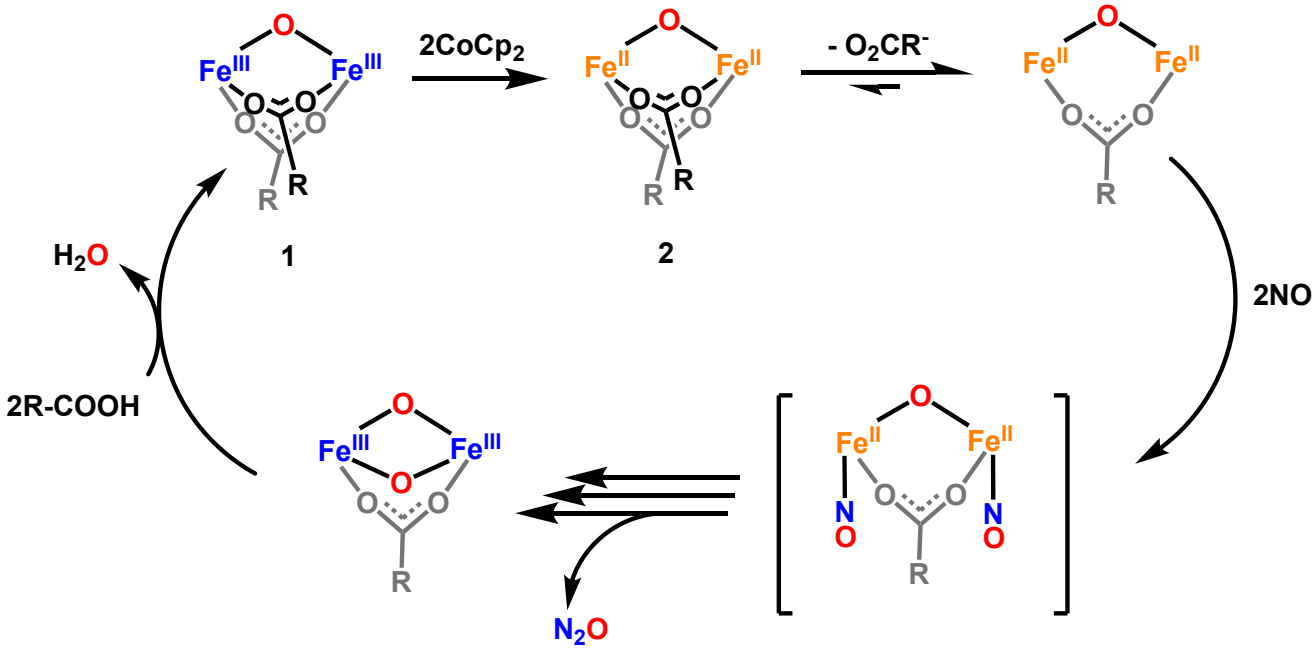

Figure 2.16. Proposed catalytic cycle of NO reduction at room temperature by complexes **2/2-OAc** in CH_2Cl_2. Here, the **R** group is a general alkyl chain (R = -CH_2CH_3 in complex **2** and -CH_3 in complex **2-OAc**.

Compared to our previous model complex [Fe_2(BPMP)(OPr)$(NO)_2$]$(X)_2$, which shows the N-O stretch at 1765 cm^{-1}, the low-temperature intermediate observed here has distinctively lower N-O stretching frequencies, which is in agreement with the idea that [(Py_2PhO_2)MP]$^{3-}$ is a stronger

donating ligand than [BPMP]$^-$. This trend can be explained with the triplet NO$^-$ ligand being predominantly a π-donor from its singly-occupied π* orbitals in these types of complexes (which are best described as Fe(III)-NO$^-$).[23,24] Here, more electron-rich iron centers show **reduced** charge donation from the NO$^-$ ligand, leading to an increase in the electron density in the π* orbitals of NO$^-$, and correspondingly, a decrease in the N-O stretch. This effect further reduces the covalency of the Fe-NO bond, and hence, weakens this bond (and lowers the Fe-NO stretch). The lower N-O stretching frequencies for the low-temperature [{FeNO}^{7}]$_2$ intermediate observed here (compared to the [BPMP]$^-$ complex), in combination with our DFT results, are therefore again consistent with the formation of a dinitrosyl complex of type "[Fe$_2$((Py$_2$PhO$_2$)MP)(OPr)(NO)$_2$]" in our experiments. As shown recently, N-N bond formation constitutes the key energy barrier for the reduction of NO to N$_2$O by non-heme diiron sites;[18] thus, weakening of the Fe-NO bonds in the presence of a strongly donating coligand is in fact advantageous for NO reduction. As the result, the highly donating ligand used here is suitable for allowing for the *direct reduction* of NO to N$_2$O, without the need to add any extra reducing equivalents to activate the hs-{FeNO}^{7} units.

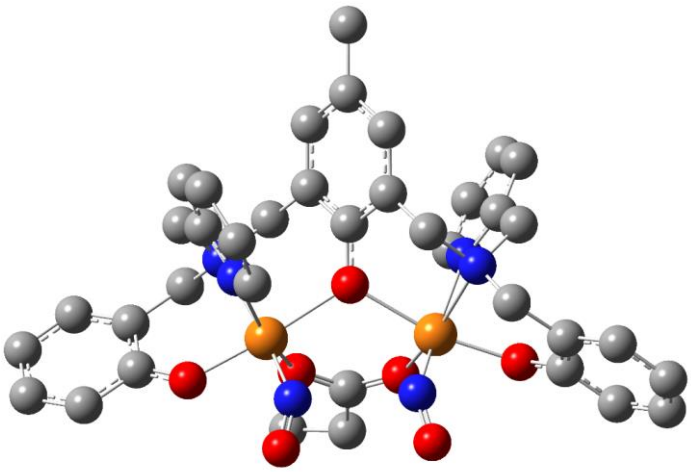

Figure 2.17. DFT-optimized structure (BP86/TZVP) of the proposed diferrous dinitrosyl intermediate formed at -80 °C. The spin densities are calculated to be about -3 and +3 for each iron center and about +0.5 and -0.5 for each NO ligand. The calculated stretching frequencies of the N-O units are ν_{sym}(N-O) = 1723 cm^{-1} and ν_{asym}(N-O) = 1678 cm^{-1}.

2.6 Conclusions

In conclusion, the direct reduction of NO to N_2O by a diferrous diiron complex was achieved here for the first time, using the new model complex $[Fe_2((Py_2PhO_2)MP)(OPr)_2](OTf)$. Although previous work on $[Fe_2(BPMP)(OPr)(NO)](X)_2$ ($X = BPh_4^-$, OTf^-) has shown that reduction of non-heme diiron dinitrosyl complexes induces fast and efficient N-N coupling and N_2O generation,[1,2] our new results demonstrate that this is **not** a requirement for N_2O production. In fact, *I show here that via tuning of the iron redox potential, the direct pathway for NO reduction can be activated*. In comparison to our previously reported model complex, $[Fe_2(BPMP)(OPr)_2](OTf)_2$, the redox potentials of $[Fe_2((Py_2PhO_2)MP)(OPr)_2](OTf)$ are shifted negatively by about 1 V, which was accomplished by the simple substitution of a pyridine ligand with a phenolate group at each iron center. This large negative shift in potential makes the Fe^{III}/Fe^{III} redox state of the dimer accessible, thus allowing the reaction to go forward by oxidizing the diiron core by two electrons. Importantly, I was able to demonstrate the ability of this model complex to perform multiple turnovers of (quantitative) NO reduction in the presence of acetic acid, which mimics the reactivity of the enzyme. Despite the lack of structural characterization, our results further indicate that the product of NO reduction is a bridging diferric oxo product.

In summary, our results provide direct support for the recent proposal that FNORs mediate NO detoxification via direct NO reduction by their diferrous active sites, without the involvement of the flavin cofactor in the reaction.[4] In the protein, a fine tuning of the redox potential of the diiron active site could be accomplished by the electrostatic environment of the diiron core, hydrogen bonding, etc., as demonstrated for blue copper proteins.[25] Finally, our results show that N-N bond formation by **2** proceeds with a very small activation barrier, allowing the reaction to

proceed, even at -80 °C. The direct reduction mechanism is therefore a surprisingly facile pathway for NO reduction to N_2O, if the diiron core has the "right" redox potentials. Further work will now focus on identifying the precise nature of the intermediates observed at low temperature, and on determining the exact redox potentials needed to activate the direct reduction pathway of NO.

2.7 Experimental Section

Reactions were generally performed using inert gas (Schlenk) techniques. All solvents were dried and freeze pump thawed to remove dioxygen and water. Preparation and handling of air sensitive materials was performed under a dinitrogen atmosphere in an MBraun glovebox, equipped with a circulating purifier (O_2, H_2O <0.1 ppm). Nitric oxide (99.95%) was first passed through an Ascarite II column and then a -80 °C cold trap to remove higher nitrogen oxide impurities prior to use.

Infrared spectra of solid samples were obtained using PerkinElmer BX and GX and Bruker Alpha-E FTIR spectrometers. The IR spectra of solution samples were obtained in thin-layer solution cells equipped with CaF_2 windows. Gas IR spectra were obtained using a Pike Technologies short-path HT gas cell with 100 mm path length, equipped with CaF_2 windows, on the same instruments.

UV-Vis/Immersion Probe: Spectra were obtained using an Analytic Jena Specord S600 UV-Vis spectrometer. Dip probe experiments used the same spectrometer, with a Helma low-temperature immersion probe.

^{1}H-NMR spectra were recorded on a Varian Inova 400 MHz instrument and referenced against residual solvent signals.

Electron paramagnetic resonance spectra were recorded on a Bruker-X-band EMX spectrometer equipped with Oxford Instruments liquid nitrogen and liquid helium flow cryostats. EPR spectra were typically obtained on frozen solutions using ~20 mW microwave power and 100 kHz field modulation with the amplitude set to 1 G. Sample concentrations were ~2 mM, and ~ 4 mM for reaction products.

Cyclic voltammograms (CVs) were obtained on a CH instruments CHI660C electrochemical workstation using a three component system, consisting of a glassy carbon working electrode, a platinum auxiliary electrode, and a Ag wire reference electrode. CVs were recorded in 0.1 M tetrabutylammonium triflate in CH_2Cl_2. Potentials were corrected to the Fc/Fc^+ standard by independently measuring the ferrocene/ferrocenium couple under the same conditions (Fc/Fc^+ = 624 mV vs. SHE).

Elemental analysis: Elemental analyses were conducted by Atlantic Microlabs (Norcross, GA)

Structure Determination. Orange rods of **$[Fe_2((Py_2PhO_2)MP)(OAc)_2](CoCp_2)$ (2-OAc)** were grown from a dichloromethane/hexane solution of the compound at 25 ºC. A crystal of dimensions 0.20 x 0.05 x 0.05 mm was mounted on a Rigaku AFC10K Saturn 944+ CCD-based X-ray diffractometer equipped with a low temperature device and a Micromax-007HF Cu-target micro-focus rotating anode (λ = 1.54187 Å), operated at 1.2 kW power (40 kV, 30 mA). The X-ray intensities were measured at 85(1) K with the detector placed at a distance of 42.00 mm from the crystal. A total of 2028 images were collected with an oscillation width of 1.0° in ω. The exposure times were 1 sec. for the low angle images, and 4 sec. for high angle. Rigaku d*trek images were exported to CrysAlisPro for processing and corrected for absorption. The integration of the data yielded a total of 83840 reflections to a maximum 2θ value of 139.83° of which 10012

were independent and 8304 were greater than 2σ(I).[26,27] The final cell constants (Table S1) were based on the xyz centroids of 17825 reflections above 10σ(I). Analysis of the data showed negligible decay during data collection. The structure was solved and refined with the Bruker SHELXTL (version 2016/6)[28] software package, using the space group C2/c with Z = 8 for the formula $C_{51}H_{53}N_4O_7Cl_4Fe_2Co + CH_2Cl_2$. All non-hydrogen atoms were refined anisotropically with the hydrogen atoms placed in idealized positions. Full matrix least-squares refinement based on F2 converged at R1 = 0.0553 and wR2 = 0.1500 [based on I > 2sigma(I)], R1 = 0.0668 and wR2 = 0.1616 for all data. Two dichloromethane solvate molecules were disordered in two orientations but were able to be refined with discrete atomic positions. The SQUEEZE subroutine of the PLATON program suite[29,30] was used to address additional disordered solvent present in four accessible voids of the lattice. Further details are presented in Table S1 and are given as Supporting Information in a CIF file.

Mössbauer spectroscopy. The Mössbauer sample of **1** was prepared by metallating the ligand, $H_3[(Py_2PhO_2)MP$, with $^{57}Fe(OTf)_3$ in the presence of NaOPr (see below). The subsequent preparation of samples of **2** and of the reaction products was carried out using **1** as precursor. Samples were dissolved in butyronitrile and then slowly frozen at liquid nitrogen temperature in a cold well under a dinitrogen atmosphere.

Mössbauer data were recorded on a spectrometer from WEB Research, equipped with a Janis SVT-400 variable-temperature cryostat. All isomer shifts are quoted relative to the centroid of the spectrum of α-Fe at room temperature. Simulation of the Mössbauer spectra was conducted with the WMOSS spectral analysis package, using the Spin Hamiltonian shown in the following equation:

$$\mathbf{H} = \beta \mathbf{S} \cdot \mathbf{g} \cdot \mathbf{B} + \mathrm{D}\left(\mathbf{S_z^2} - \frac{S(S+1)}{3}\right) + E\left(\mathbf{S_x^2} - \mathbf{S_y^2}\right) + \frac{eQV_{zz}}{4}\left[\mathbf{I_z^2} - \frac{I(I+1)}{3} + \frac{\eta}{3}\left(\mathbf{I_x^2} - \mathbf{I_y^2}\right)\right]$$

$$+\mathbf{S}\cdot\mathbf{A}\cdot\mathbf{I}-g_n\beta_n\mathbf{B}\cdot\mathbf{I}$$

The first term represents the electronic Zeeman effect, the second and third term represent the axial and rhombic zero field splitting (ZFS), the fourth term describes the interaction between the nuclear quadrupole moment and the electric field gradient, the fifth term represents the magnetic hyperfine interaction of the electronic spin with the ^{57}Fe nucleus, and the last term describes the ^{57}Fe nuclear Zeeman effect.

DFT calculations. Gaussian 09 was used to carry out all of the calculations performed here.[31] The optimization of the broken symmetry structure of the diferrous dinitrosyl intermediate, $[Fe_2((Py_2PhO_2)MP)(OPr)(NO)_2]$, was performed with the gradient corrected functional BP86, which has been shown to give good geometric structures for related $\{MNO\}^n$ species,[18] and the TZVP basis set. A guess calculation is performed first on the ferromagnetically coupled state of the dimer, and used as the initial guess to generate the broken-symmetry wavefunction. Subsequent single point calculations during the geometry optimization were carried out to ensure that the two iron centers remain antiferromagnetically coupled (and are not spin quenched). A frequency calculation was further performed on the optimized structure to determine the N-O stretching frequencies.

2,6-Bis[((2-hydroxybenzyl)(2-pyridylmethyl)amino)methyl]-4-methylphenol ($H_3[(Py_2PhO_2)MP]$, H_3L). H_3L was synthesized according to published procedures.[32] ^{1}H-NMR (400 MHz, Chloroform-*d*) δ 10.83 (s, 3H), 8.63 (d, 2H), 7.65 (td, 2H), 7.26 – 7.19 (m, 4H), 7.17 – 7.11 (m, 2H), 7.03 (d, 2H), 6.87 (s, 2H), 6.81 (d, 2H) 6.75 (td, 2H), 3.83 (s, 4H), 3.80 (s, 4H), 3.75 (s, 4H), 2.21 (s, 3H); see Figure S38.

$[Fe_2((Py_2PhO_2)MP)(OPr)_2](OTf)\cdot H_2O$ (1). To a solution of 0.1 g (0.178 mmol) of H_3L in 2 ml of Methanol, a solution of 100 mg (1.03 mmol) sodium propionate (denote as NaOPr) in 1 ml of MeOH was added. A solution of 155.7 mg (0.356 mmol) $Fe(OTf)_2\cdot 2CH_3CN$ in 1 mL of

methanol was then added to the stirring solution. The resulting solution was stirred for 30 minutes at 50 °C under ambient conditions and then filtered. The crude solid was washed with 2-propanol and diethyl ether until the filtrate is colorless to obtain the product as a dark blue solid; yield: 0.134g, 77%. Characterization: Elemental anal. calcd. for $C_{42}H_{43}Fe_2F_3N_4O_{10}S$: C, 51.34; H, 4.62; N, 5.70; found (1st attempt) (%):C, 51.07; H, 4.57; N, 5.50 (2nd attempt) (%):C, 51.56; H, 4.68; N, 5.82. Mass spectroscopy m/z: calcd. for the cationic fragment $C_{41}H_{43}Fe_2N_4O_7$: 815.18; Found: 815.19. Mass spectroscopy m/z: calcd. for the ^{57}Fe labeled cationic fragment $C_{41}H_{43}{}^{57}Fe_2N_4O_7$: 817.18; Found: 817.19 UV-Vis (CH_2Cl_2) (λ_{max}) 630 nm.

[Fe_2((Py_2PhO_2)MP)($OPr)_2$](ClO_4)•H_2O (1/ClO_4). A similar procedure was used as in the case of **1**, but the metalation was performed with $Fe(ClO_4)_2$ under ambient conditions. Characterization: Elemental anal. calcd. for $C_{42}H_{43}Fe_2N_4O_{11}Cl$: C, 52.78; H, 4.86; N, 6.01; found (%):C, 53.29; H, 4.85; N, 5.99.

[Fe_2((Py_2PhO_2)MP)($OAc)_2$](ClO_4)•H_2O (1-OAc). This complex was prepared and characterized according to a previously reported procedure.[6]

Complex **2** and **2-OAc** can be obtained through chemical reduction of **1** and **1-OAc**, respectively, using cobaltocene. Single crystals of **2-OAc** suitable for X-ray crystallography were grown by diffusion of hexane into a CH_2Cl_2 solution of the compound.

IR Gas Headspace Analysis for N_2O Detection. N_2O quantification was carried out by gas headspace analysis using infrared spectroscopy. The general protocol for gas headspace analysis is described in the following (taken from ref. [33]): to a sealed 25 ml round-bottom flask containing ~8.7 mg of [Fe_2((Py_2PhO_2)MP)($OPr)_2$](OTf) in 2.5 mL of CH_2Cl_2 were added ~2 equivalents of $CoCp_2$. After allowing the reduction to proceed, ~2 mL of NO gas were added into the headspace of the round-bottom flask. The reaction was allowed to stir for 15 minutes before

the headspace was transferred by vacuum to a sealed gas IR cell with CaF_2 windows. Quantification of N_2O was performed via integration of the prominent IR features at 2235 and 2212 cm^{-1} of this molecule (N-N stretching vibration) against separately determined N_2O standards, which were generated from the breakdown of Piloty's acid in basic solution under exactly the same conditions. Using this calibration method, a maximum N_2O yield of 105% ± 10% was obtained for **1**, as shown in Figure S25. The advantage of using Piloty's acid to construct the calibration curve is that this compound is a solid that can be weighted out at high accuracy. Hence, exact amounts of N_2O can be generated in this way. The disadvantage is that Piloty's acid has to be used in an aqueous environment, which is different from the organic solvents used for the reaction of **2** with NO gas. However, the error generated due to the somewhat different solubility of N_2O in water and organic media (at the concentrations used for the experiments) is well within the ± 10% error noted above.

Additional Control Experiments. As an additional control, NO-saturated CH_2Cl_2 was exposed to cobaltocene under identical conditions to those used for N_2O generation from the reaction of **2** with NO gas. While cobaltocene is able to reduce NO (NO is reduced around -1 V versus Fc/Fc^+ in organic solvents), the rate for N_2O generation and total percent yield differ greatly from those observed for **2**.[1] In addition, I am adding exactly two equivalents of $CoCp_2$ to the solution of **1** to generate **2** (prior to reaction with NO gas), so the amount of free $CoCp_2$ present in solution at the time when NO gas is added is minute, if there is any present at all. A direct reduction of NO by $CoCp_2$ can therefore be ruled out in our experiments.

2.8 References and Notes

1. Zheng, S.; Berto, T. C.; Dahl, E. W.; Hoffman, M. B.; Speelman, A. L.; Lehnert, N. The Functional Model Complex [Fe2(BPMP)(OPr)(NO)2](BPh4)2 Provides Insight into the Mechanism of Flavodiiron NO Reductases. *J. Am. Chem. Soc.* **2013**, *135*, 4902-4905.
2. White, C. J.; Speelman, A. L.; Kupper, C.; Demeshko, S.; Meyer, F.; Shanahan, J. P.; Alp, E. E.; Hu, M.; Zhao, J.; Lehnert, N. The Semireduced Mechanism for Nitric Oxide Reduction by Non-Heme Diiron Complexes: Modeling Flavodiiron Nitric Oxide Reductases. *J. Am. Chem. Soc.* **2018**, *140*, 2562-2574.
3. Dong, H. T.; White, C. J.; Zhang, B.; Krebs, C.; Lehnert, N. Non-Heme Diiron Model Complexes Can Mediate Direct NO Reduction: Mechanistic Insight into Flavodiiron NO Reductases. *J. Am. Chem. Soc.* **2018**, *140*, 13429-13440.
4. Caranto, J. D.; Weitz, A.; Hendrich, M. P.; Kurtz, D. M. The Nitric Oxide Reductase Mechanism of a Flavo-Diiron Protein: Identification of Active-Site Intermediates and Products. *J. Am. Chem. Soc.* **2014**, *136*, 7981-7992.
5. Silaghi-Dumitrescu, R.; Kurtz, D. M.; Ljungdahl, L. G.; Lanzilotta, W. N. X-ray Crystal Structures of Moorella thermoacetica FprA. Novel Diiron Site Structure and Mechanistic Insights into a Scavenging Nitric Oxide Reductase. *Biochemistry* **2005**, *44*, 6492-6501.
6. Neves, A.; de Brito, M. A.; Vencato, I.; Drago, V.; Griesar, K.; Haase, W. FeIIIFeIII and FeIIFeIII Complexes as Synthetic Analogues for the Oxidized and Reduced Forms of Purple Acid Phosphatases. *Inorg. Chem.* **1996**, *35*, 2360-2368.
7. Neves, A.; Aires de Brito, M.; Drago, V.; Griesar, K.; Haase, W. A new asymmetric N5O2-donor binucleating ligand and its first FeIIFeIII complex as a model for the redox properties of uteroferrin. *Inorganica Chimica Acta* **1995**, *237*, 131-135.
8. Gonçalves, V. L.; Vicente, J. B.; Pinto, L.; Romão, C. V.; Frazão, C.; Sarti, P.; Giuffrè, A.; Teixeira, M. Flavodiiron Oxygen Reductase from Entamoeba histolytica: MODULATION OF SUBSTRATE PREFERENCE BY TYROSINE 271 AND LYSINE 53. *J. Biol. Chem.* **2014**, *289*, 28260-28270.
9. Vicente, J. B.; Teixeira, M. Redox and Spectroscopic Properties of the Escherichia coli Nitric Oxide-detoxifying System Involving Flavorubredoxin and Its NADH-oxidizing Redox Partner. *J. Biol. Chem.* **2005**, *280*, 34599-34608.
10. Lehnert, N.; Fujisawa, K.; Camarena, S.; Dong, H. T.; White, C. J. Activation of Non-Heme Iron-Nitrosyl Complexes: Turning up the Heat. *ACS Catal.* **2019**, *9*, 10499-10518.
11. Campbell, V. D.; Parsons, E. J.; Pennington, W. T. Diiron and dicobalt complexes of a phenolate-bridged binucleating ligand with mixed phenolate and pyridine podands. *Inorg. Chem.* **1993**, *32*, 1773-1778.
12. Berto, T. C.; Speelman, A. L.; Zheng, S.; Lehnert, N. Mono- and dinuclear non-heme iron–nitrosyl complexes: Models for key intermediates in bacterial nitric oxide reductases. *Coord. Chem. Rev.* **2013**, *257*, 244-259.
13. Surerus, K. K.; Munck, E.; Snyder, B. S.; Holm, R. H. A binuclear mixed-valence ferromagnetic iron system with an S = 9/2 ground state and valence trapped and detrapped states. *J. Am. Chem. Soc.* **1989**, *111*, 5501-5502.
14. Kindermann, N.; Schober, A.; Demeshko, S.; Lehnert, N.; Meyer, F. Reductive Transformations of a Pyrazolate-Based Bioinspired Diiron–Dinitrosyl Complex. *Inorg. Chem.* **2016**, *55*, 11538-11550.
15. Caranto, J. D.; Weitz, A.; Giri, N.; Hendrich, M. P.; Kurtz, D. M. A Diferrous-Dinitrosyl Intermediate in the N2O-Generating Pathway of a Deflavinated Flavo-Diiron Protein. *Biochemistry* **2014**, *53*, 5631-5637.

16. Soma, S.; Van Stappen, C.; Kiss, M.; Szilagyi, R. K.; Lehnert, N.; Fujisawa, K. Distorted tetrahedral nickel-nitrosyl complexes: spectroscopic characterization and electronic structure. *JBIC Journal of Biological Inorganic Chemistry* **2016**, *21*, 757-775.
17. Fujisawa, K.; Soma, S.; Kurihara, H.; Dong, H. T.; Bilodeau, M.; Lehnert, N. A cobalt-nitrosyl complex with a hindered hydrotris(pyrazolyl)borate coligand: detailed electronic structure, and reactivity towards dioxygen. *Dalton Transactions* **2017**, *46*, 13273-13289.
18. Van Stappen, C.; Lehnert, N. Mechanism of N–N Bond Formation by Transition Metal–Nitrosyl Complexes: Modeling Flavodiiron Nitric Oxide Reductases. *Inorg. Chem.* **2018**, *57*, 4252-4269.
19. Perdew, J. P. Density-functional approximation for the correlation energy of the inhomogeneous electron gas. *Physical Review B* **1986**, *33*, 8822-8824.
20. Becke, A. D. Density-functional exchange-energy approximation with correct asymptotic behavior. *Physical Review A* **1988**, *38*, 3098-3100.
21. Schäfer, A.; Huber, C.; Ahlrichs, R. Fully optimized contracted Gaussian basis sets of triple zeta valence quality for atoms Li to Kr. *The Journal of Chemical Physics* **1994**, *100*, 5829-5835.
22. Schäfer, A.; Horn, H.; Ahlrichs, R. Fully optimized contracted Gaussian basis sets for atoms Li to Kr. *The Journal of Chemical Physics* **1992**, *97*, 2571-2577.
23. Berto, T. C.; Hoffman, M. B.; Murata, Y.; Landenberger, K. B.; Alp, E. E.; Zhao, J.; Lehnert, N. Structural and Electronic Characterization of Non-Heme Fe(II)–Nitrosyls as Biomimetic Models of the FeB Center of Bacterial Nitric Oxide Reductase. *J. Am. Chem. Soc.* **2011**, *133*, 16714-16717.
24. Brown, C. A.; Pavlosky, M. A.; Westre, T. E.; Zhang, Y.; Hedman, B.; Hodgson, K. O.; Solomon, E. I. Spectroscopic and Theoretical Description of the Electronic Structure of S = 3/2 Iron-Nitrosyl Complexes and Their Relation to O2 Activation by Non-Heme Iron Enzyme Active Sites. *J. Am. Chem. Soc.* **1995**, *117*, 715-732.
25. Hosseinzadeh, P.; Marshall, N. M.; Chacón, K. N.; Yu, Y.; Nilges, M. J.; New, S. Y.; Tashkov, S. A.; Blackburn, N. J.; Lu, Y. Design of a single protein that spans the entire 2-V range of physiological redox potentials. *Proceedings of the National Academy of Sciences* **2016**, *113*, 262.
26. r16, C. E. Rigaku Americas and Rigaku Corporation (2014), Rigaku Americas, 9009, TX, USA 77381-5209, Rigaku Tokyo, 196-8666, Japan.
27. 1.171.38.41., C. Rigaku Oxford Diffraction, 2015.
28. Sheldrick, G. Crystal structure refinement with SHELXL. *Acta Crystallographica Section C* **2015**, *71*, 3-8.
29. Spek, A. L. *J. Appl. Cryst.* **2003**, 7-13.
30. Spek, A. L. *Acta Cryst.* **2009**, *D65*, 148-155.
31. Frisch, M. J.; Trucks, G. W.; Schlegel, H. B.; Scuseria, G. E.; Robb, M. A.; Cheeseman, J. R.; Scalmani, G.; Barone, V.; Mennucci, B.; Petersson, G. A.; Nakatsuji, H.; Caricato, M.; Li, X.; Hratchian, H. P.; Izmaylov, A. F.; Bloino, J.; Zheng, G.; Sonnenberg, J. L.; Hada, M.; Ehara, M.; Toyota, K.; Fukuda, R.; Hasegawa, J.; Ishida, M.; Nakajima, T.; Honda, Y.; Kitao, O.; Nakai, H.; Vreven, T.; Montgomery, J. A.; Peralta, J. E.; Ogliaro, F.; Bearpark, M.; Heyd, J. J.; Brothers, E.; Kudin, K. N.; Staroverov, V. N.; Kobayashi, R.; Normand, J.; Raghavachari, K.; Rendell, A.; Burant, J. C.; Iyengar, S. S.; Tomasi, J.; Cossi, M.; Rega, N.; Millam, J. M.; Klene, M.; Knox, J. E.; Cross, J. B.; Bakken, V.; Adamo, C.; Jaramillo, J.; Gomperts, R.; Stratmann, R. E.; Yazyev, O.; Austin, A. J.; Cammi, R.; Pomelli, C.; Ochterski, J. W.; Martin, R. L.; Morokuma, K.; Zakrzewski, V. G.; Voth, G. A.; Salvador, P.; Dannenberg, J. J.; Dapprich, S.; Daniels, A. D.;

Farkas; Foresman, J. B.; Ortiz, J. V.; Cioslowski, J.; Fox, D. J. Gaussian 09, Revision B.01. *Wallingford CT* **2009**.
32. Krebs, B.; Schepers, K.; Bremer, B.; Henkel, G.; Althaus, E.; Mueller-Warmuth, W.; Griesar, K.; Haase, W. Model Compounds for the Oxidized Uteroferrin-Phosphate Complex with Novel Dinucleating Ligands Containing Phenolate and Pyridine Donors. *Inorg. Chem.* **1994**, *33*, 1907-1914.
33. White, C. J.; Speelman, A. L.; Kupper, C.; Demeshko, S.; Meyer, F.; Shanahan, J. P.; Alp, E. E.; Hu, M.; Zhao, J.; Lehnert, N. The Semireduced Mechanism for Nitric Oxide Reduction by Non-Heme Diiron Complexes: Modeling Flavodiiron NO Reductases. *J. Am. Chem. Soc.* **2018**.

Chapter 3

What is the Right Level of Activation of a High-Spin {FeNO}^{7} Complex to Enable Direct N-N Coupling? New Mechanistic Insight into Flavodiiron NO Reductases

Acknowledgement: I would like to acknowledge my undergraduate student Stephanie Camarena who have assisted me with carrying out important experiments that lead up to the findings described in this chapter. I would like to thank Dr. Debangsu Sil and Prof. Carsten Krebs at the Pennsylvania State University who performed all the Mössbauer experiments and the corresponding data analysis in this chapter. I would like to thank Dr. Jiyong Zhao, Dr. Esen E. Alp, Dr. Michael Y. Hu, and Dr. Barbara Lavina who have assisted me in the process of collecting NRVS data at the Argonne National Laboratory during the pandemic.

As mentioned in **Chapter 1**, recent computational studies by Van Stappen et al. using density functional theory (DFT) calculations on our model system $[Fe_2(BPMP)(OPr)(NO)_2]^{2+}$ have shown that this stable [hs-{FeNO}^{7}]$_2$ complex can be activated by one-electron reduction, leading to N-N coupling to form a cis-hyponitrite intermediate.[1] The calculated activation barrier for N-N bond formation in this complex is 13.7 kcal/mol. These results further indicate that it is essential to have the right conformation, with the two [FeNO] units in a coplanar (or syn/cis) arrangement, for N-N coupling to occur. In $[Fe_2(BPMP)(OPr)(NO)_2]^{2+}$, one-electron reduction of one of the hs-{FeNO}^{7} centers to the hs-{FeNO}^{8} state provides the necessary activation to allow for the N-N coupling reaction to proceed. The DFT calculations predict that the increased activation of the reduced hs-{FeNO}^{8} unit is reflected by a shift of the N-O stretch below 1700 cm^{-1}; however, this prediction could not be confirmed experimentally due to the very short lifetime of this

intermediate.[2] Nevertheless, based on these results, I speculated that a sufficiently activated [hs-{FeNO}^{7}]$_2$ complex might be able to mediate direct NO reduction, without the need for additional reducing equivalents, and that this level of activation would be indicated by a low N-O stretching frequency of ≤1700 cm^{-1}. This idea is supported by the high degree of stability of all of the reported [hs-{FeNO}^{7}]$_2$ model complexes in the literature, which all show ν(N-O) > 1750 cm^{-1}.[2-7] However, this hypothesis still awaits experimental verification.

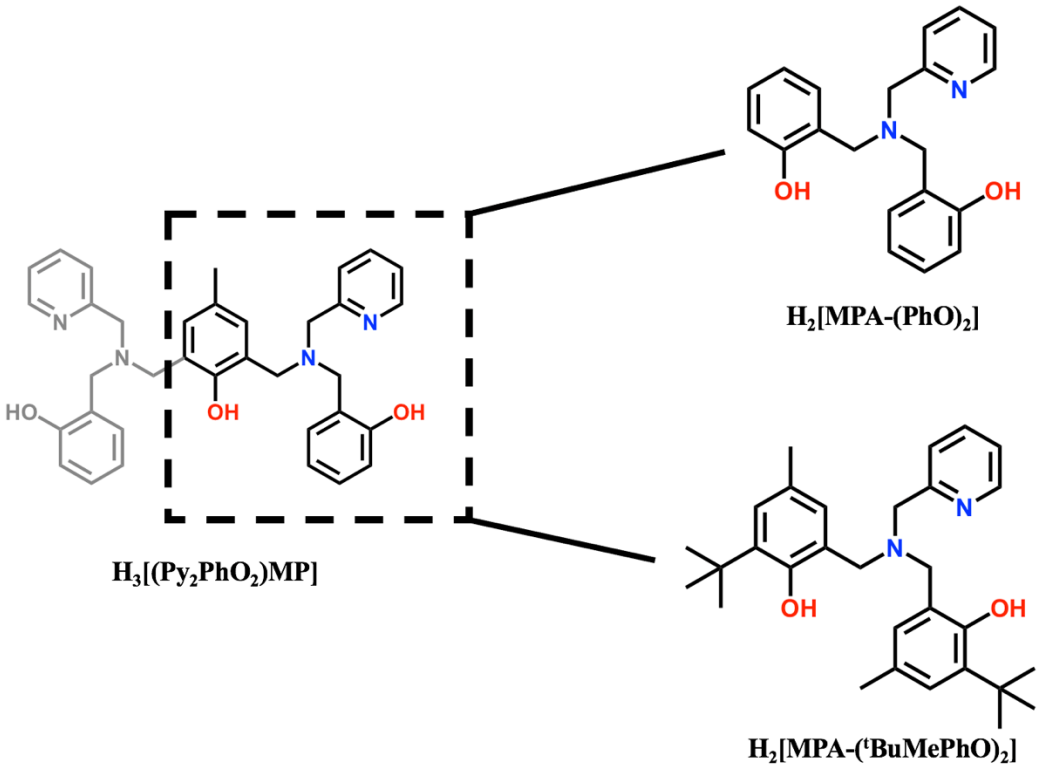

Scheme 3.1 Ligands used for this study that mimic half of the H$_3$[(Py$_2$PhO$_2$)MP] ligand used in **Chapter 2.**

In **Chapter 2**, I was able to show that the electron-rich complex [CoCp$_2$][Fe$^{II}_2$((Py$_2$PhO$_2$)MP)(OAc)$_2$] can in fact mediate direct NO reduction.[8] Here, (Py$_2$PhO$_2$)MP^{3-} is a derivative of the initially used ligand BPMP$^-$ where two Py (pyridine) donors (one per iron center) are replaced by strongly donating phenolate groups (Scheme 3.1, left). This diferrous complex is highly reactive with NO and can perform multiple cycles of quantitative direct NO reduction to

N_2O in the presence of excess protons and reductant. The product after reaction of this complex with NO is a ferric μ-oxo complex (as shown by Mössbauer spectroscopy), confirming that the complex does indeed perform NO reduction and **not** NO disproportionation. However, because of this high reactivity, no NO-bound intermediate could be isolated under ambient reaction conditions. Some evidence for NO-bound species was obtained in low-temperature IR studies, which indicate hs-$\{FeNO\}^7$ adducts with low N-O stretching frequencies of 1705-1730 cm^{-1}. Computational results further support the idea that hs-$\{FeNO\}^7$ complexes with N-O stretching frequencies ≤1700 cm^{-1} are activated for direct N-N coupling.[8] Going forward, this presented us with the unique challenge to construct a model system with a similar level of activation as the NO-bound intermediate of $[Fe^{II}_2((Py_2PhO_2)MP)(OAc)_2]^-$, but where NO reduction was somehow stalled, allowing us to isolate and study the electronic properties of the corresponding hs-$\{FeNO\}^7$ complex that has the proper level of activation for direct NO reduction.

In order to tackle this problem, I decided to take advantage of the fact that efficient NO reduction to N_2O seems to require a diiron complex.[9] In **chapter 3**, I therefore chose a new ligand system that corresponds to half of the $H_3[(Py_2PhO_2)MP]$ ligand, as indicated in Scheme 3.1, right, to promote the formation of corresponding, *mononuclear* complexes. Isolation of a highly activated mononuclear hs-$\{FeNO\}^7$ complex would in turn further support the hypothesis that diiron complexes are critical to allow for efficient NO reduction to occur. The resulting ligand system, $H_2[MPA\text{-}(PhO)_2]$ (bis(2-hydroxybenzyl)(2-pyridylmethyl)amine), was further decorated with sterically bulky groups to promote formation of mononuclear complexes, and to potentially provide steric protection for a reactive intermediate, which is a concept that is often employed in synthetic inorganic chemistry.[10-13] Iron complexes of the resulting ligand system, $H_2[MPA\text{-}(^tBuMePhO)_2]$, were then studied in direct comparison to those of the unfunctionalized version of

this ligand, H_2[MPA-$(PhO)_2$]. Excitingly, whereas the bulky ligand allowed for the isolation and characterization of a highly activated hs-{FeNO}^{7} complex, the ferrous complex of the unfunctionalized ligand undergoes N-N coupling and N_2O formation following the direct NO reduction mechanism, which is only the second demonstration of this reaction in a model complex. These results further demonstrate that I was able, for the first time, to capture the mononuclear version of a reactive [hs-{FeNO}^{7}]$_2$ complex that has sufficient activation for direct NO reduction. This complex was further studied using a number of spectroscopic methods, including UV-Vis, IR, Mössbauer and Nuclear Resonance Vibrational Spectroscopy (NRVS). These results are summarized in this chapter.

3.1 Synthesis and Characterization of the Ferrous Complexes with Ligands H_2[MPA-$(PhO)_2$] and H_2[MPA-(^{t}BuMePhO)$_2$]

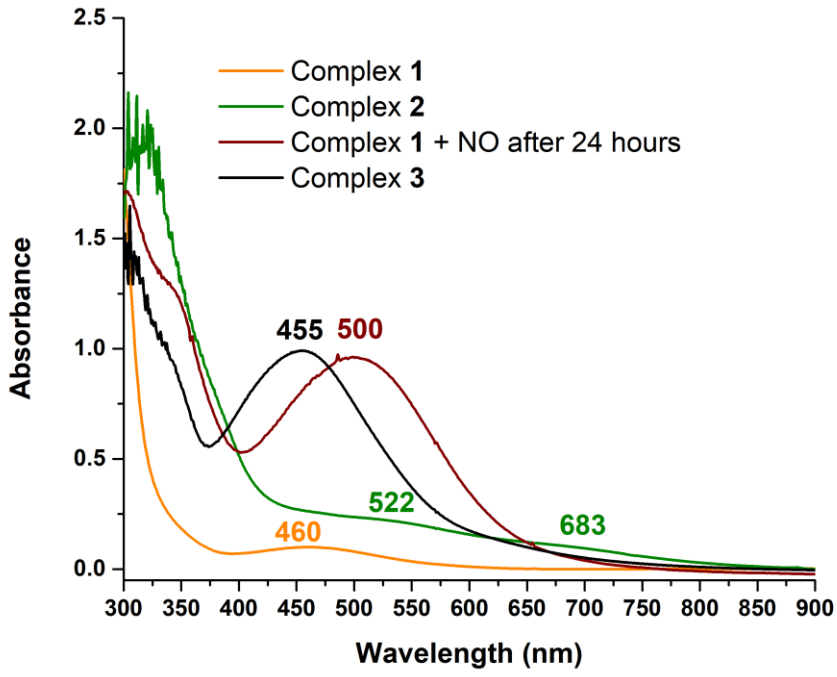

Figure 3.1 UV-Vis absorption spectra of complexes **1**, **2**, **3** and the product of the reaction of complex **1** with NO gas (after 24 hours), all collected in CH_2Cl_2 solution at room temperature.

The ligand H_2[MPA-(^{t}BuMePhO)$_2$] (2-pyridylamino-N,N-bis(2-methylene-4-methyl-6-tert-butylphenol)) is metalated by deprotonating the phenol groups of the ligand using KOMe in MeOH, followed by reaction with one equivalent of $Fe(OTf)_2$. MeOH is then removed under reduced pressure, and the crude product is re-dissolved in CH_2Cl_2, filtered, and recrystallized to obtain the pure, bright green crystalline product **2**. Complex **2** is characterized by a very broad absorption band at 522 nm with a small shoulder at 683 nm (see Figure 3.1). As mentioned in the Introduction, I had designed the ligand H_2[MPA-(^{t}BuMePhO)$_2$] to give mononuclear complexes, but, to our surprise, X-ray diffraction of a single-crystalline green prism of **2**, grown from slow diffusion of hexane into a saturated CH_2Cl_2 solution of **2** at -33 ^{o}C, revealed that **2** has a dimeric structure, [{Fe^{II}(MPA-(^{t}BuMePhO)$_2$)}$_2$]. As shown in Figure 3.2, in the crystal structure two monomers are bridged through the phenolate arms of the coligand, even in the presence of the bulky *tert*-butyl substituents in the secondary coordination sphere (SCS). The Fe-Fe distance in **2** is unusually short, 2.98 Å, and each iron is penta-coordinated with an adjacent, open coordination site. In the dimeric structure of **2** shown in Figure 3.2, the two open coordination sites are in trans position to each other. The Fe_2O_2 diamond core is slightly asymmetric, with Fe-O(Ph) bond distances of 2.12 and 2.04 Å, respectively. Complex **2** is EPR silent due to both iron centers being high-spin (hs) Fe(II). Mössbauer spectroscopy shows isomer shifts and quadrupole splittings of δ = 1.07 and ΔE_Q = 1.68 mm/s for **2**, in agreement with the hs-Fe(II) oxidation state.

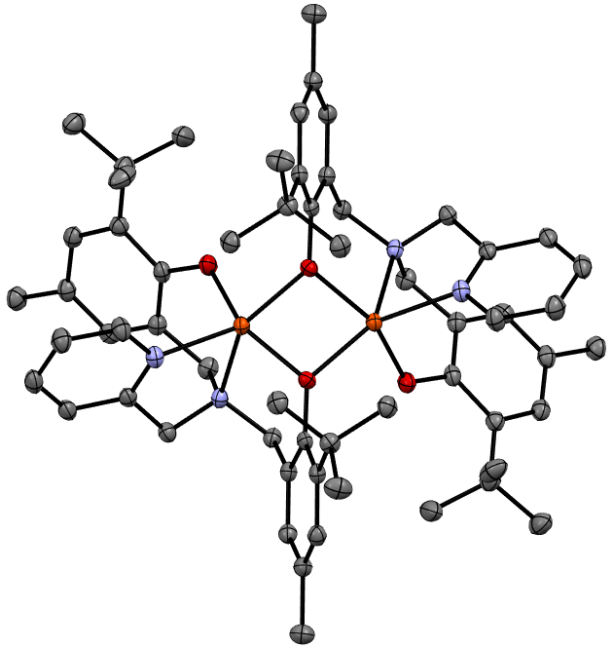

Figure 3.2 Crystal structure of complex **2** with ellipsoids drawn at 50% probability. Solvent molecules and hydrogen atoms are omitted for clarity.

The ferrous complex **1** was synthesized by metalation of H_2[MPA-$(PhO)_2$] with $Fe(OTf)_2$, using a similar protocol as described above for complex **2**, and obtained as a light orange crystalline product. Unlike complex **2**, complex **1** is unstable in the inert atmosphere of a glovebox and oxidizes even at very low concentrations of O_2. Based on the structure of **2** shown in Figure 3.2, I assumed that **1** also has a dimeric structure in solution, [{Fe(MPA-$(PhO)_2$)}$_2$], but further oligomerization is possible, as observed for similar types of ligands in previous studies.[14-17] Efforts to characterize complex **1** with X-ray diffraction proved to be difficult due to its high sensitivity towards residual O_2, and its predisposition to form very fine needles that do not sufficiently diffract. I was ultimately able to obtain a crystal structure that shows that the complex can form larger oligomeric structures, using again the phenolate groups as bridges. In the successful crystallization attempt, part of the material had decomposed over the course of the crystallization (several days), providing additional iron centers that bridge individual {Fe(MPA-$(PhO)_2$)} units. This leads to the formation of giant rings with the formula [Fe{Fe(MPA-$(PhO)_2$)}$(HCOO)_2$]$_8$, as

shown in Figure 3.3, that contain a total of sixteen Fe(II) centers. Here, the iron centers in the {Fe(MPA-$(PhO)_2$)} units are six-coordinate, with all of the coordination sites occupied by the ligand and additional formate ions that formed due to contamination during the workup process, and that bridge between the iron centers. These iron centers show an octahedral "N_2O_4" coordination environment. Additional iron centers, coordinated only by phenolate and formate groups with an octahedral "O_6" ligation, bridge between the {Fe(MPA-$(PhO)_2$)} units. The rings have a diameter of about 12 Å and, as evident from the side view in Figure 3.3, are bent. The iron centers are about 3.15 - 3.2 Å apart from each other in the structure. Interestingly, in the crystal lattice, the rings are stacked on top of each other, forming large channels that run through the crystal.

In contrast to this structure that contains two distinct types of iron(II) centers, characterization of freshly prepared complex **1** by Mössbauer spectroscopy, either in solution or as a precipitate, revealed the presence of only one type of iron species with an isomer shift and quadrupole splitting of δ = 1.15 mm/s and ΔE_Q = 2.89 mm/s, respectively. These parameters are indicative of hs-Fe(II) centers, and show that freshly prepared **1** does not contain the large ferrous wheels of [Fe{Fe(MPA-$(PhO)_2$)}$(HCOO)_2]_8$ type, which contain two different types of Fe(II) centers. Instead, I propose that freshly prepared **1** has a dimeric structure, [{Fe^{II}(MPA-$(PhO)_2$)}$_2$], similar to **2** (see Figure 3.2). Interestingly, whereas the Mössbauer isomer shifts are very similar for **1** and **2**, their quadrupole splittings are notably different, indicating that in **1**, the iron centers are likely six-coordinate in solution. The absorption spectrum of **1** in CH_2Cl_2 exhibits a weak band at 460 nm, as shown in Figure 3.1. Complex **1** is EPR silent due to the presence of hs-Fe(II) centers.

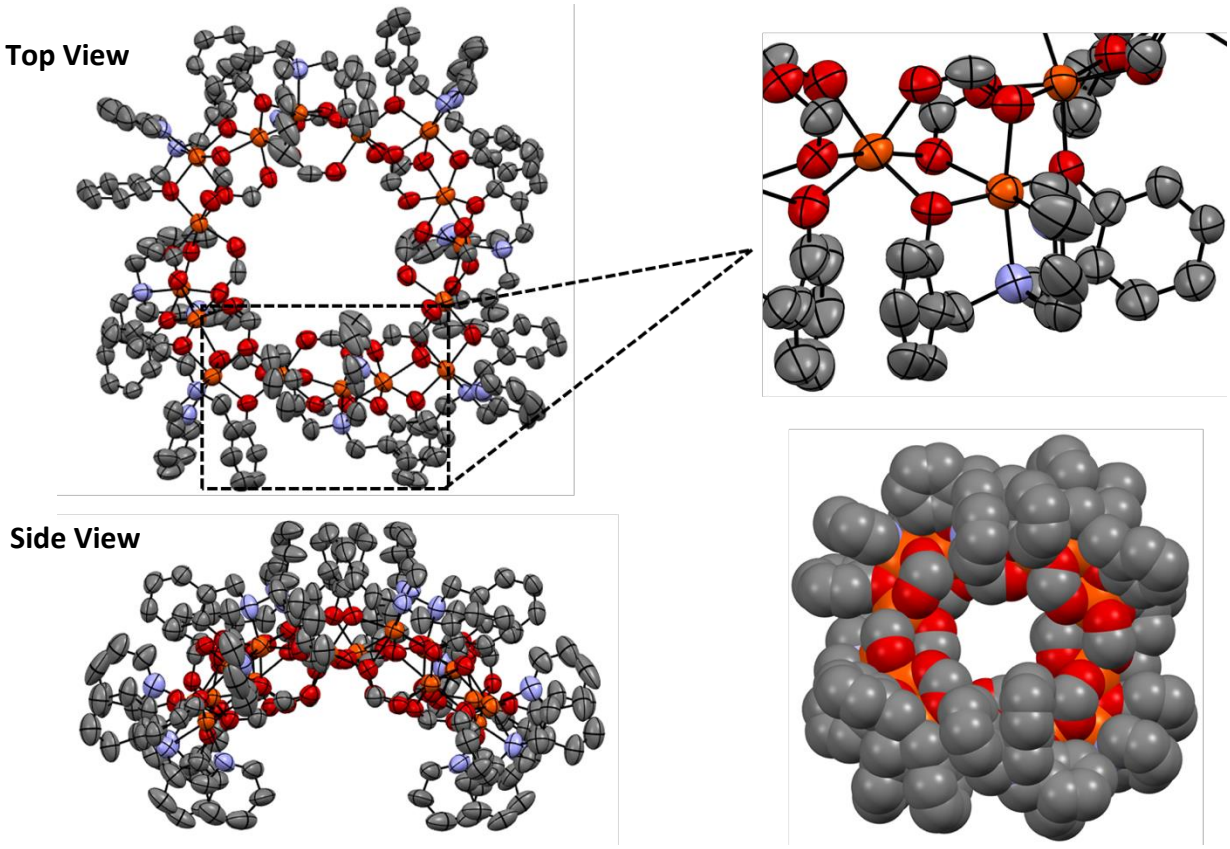

Figure 3.3 Crystal structure obtained for complex **1** from CH_3CN/ether solution over several days. Here, partial decomposition of the compound in solution provided extra iron centers which bridge {Fe(MPA-$(PhO)_2$)} units, giving rise to the large ring structure. Ellipsoids are drawn at 50% probability. Solvent molecules and hydrogen atoms are omitted for clarity.

3.2 Reactivity of Complex 2 with NO Gas

Exposure of the dimeric complex **2** to NO gas led to an immediate color change of the solution from green to very dark brown. The solution was then charged with hexane, and a clean, dark brown single-crystalline product was obtained after further recrystallization at -33 ^{o}C. X-ray diffraction of the brown block-shaped crystals revealed the formation of the unique, pseudo trigonal-bipyramidal mononitrosyl complex [Fe(MPA-(tBuMe-PhO)$_2$)(NO)] (**3**), as shown in Figure 3.4. Hence, although the ferrous precursor complex **2** is dimeric, the steric bulk provided by the tBuMe-PhO$^-$ arms forces the NO complex to become monomeric, which stabilizes the complex against further reactions (see Section III.3). Complex **3** is very sensitive and readily loses

NO under vacuum; however, this complex is stable in the solid state at room temperature under an inert atmosphere. Interestingly, **3** shows Fe-NO and N-O bond distances of 1.79 Å and 1.15 Å, respectively, which is in line with other hs-{FeNO}^{7} complexes previously characterized that contain phenolate ligands. For example, the complex [Fe(BMPA-^{t}Bu$_2$PhO)(OTf)(NO)] (**4**) shows Fe-NO and N-O bond distances of 1.78 Å and 1.10 Å, respectively. It is important to note that H$_2$[MPA-(^{t}BuMePhO)$_2$] is a more donating ligand than H[BMPA-^{t}Bu$_2$PhO], which should reduce the π-donation from the ^{3}NO$^-$ ligand to the Fe(III) center in **3** (note that hs-{FeNO}^{7} complexes have hs-Fe(III)-^{3}NO$^-$ type electronic structures where the ^{3}NO$^-$ ligand serves as a strong π-donor to the hs-Fe(III) center).[14,18] Accordingly, the Fe-NO and N-O bond distances in **3** are larger than those of **4**, indicative of a weaker Fe-NO bond in **3**. The Fe-N-O bond angle of **3** is 149^o, which is surprising, since the Fe-N-O bond of complexes with steric bulk in the SCS is usually closer to linear.[19] On the other hand, the small Fe-N-O angle is again in agreement with the large degree of NO reduction in **3**.[20] Interestingly, the NO moiety is bent towards the bulky tert-butyl group in the SCS, and not towards the pyridine ring, which I attribute to crystal packing effects in the solid state. The Fe-O(Ph) bond distances are 1.90 and 1.92 Å, respectively, and the Fe-N(Py) bond length is 2.14 Å.

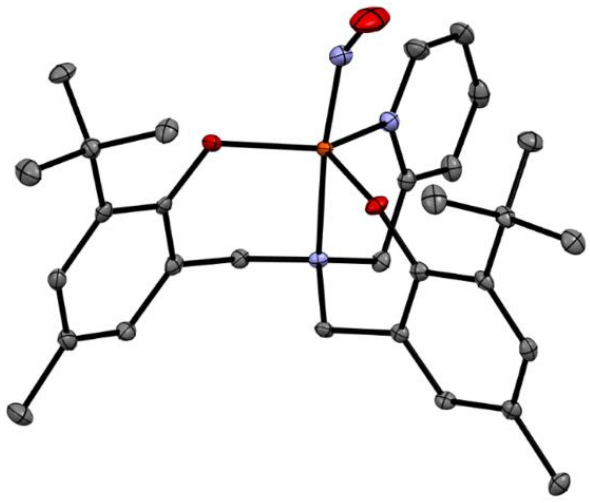

Figure 3.4. Crystal structure of complex **3** with ellipsoids drawn at 50% probability. The solvent molecules and hydrogen atoms are omitted for clarity.

Complex **3** is characterized by an absorption band at 452 nm in the UV-Vis spectrum (Figure 3.1) and shows an EPR spectrum with major signals at $g_{eff} = 4, 2$, typical for an axial hs-{FeNO}^{7} complex (see Figure 3.5, top). The EPR signals arise from antiferromagnetic coupling between the hs-Fe(III) center ($S = 5/2$) and the $^3NO^-$ ligand ($S = 1$), resulting in a complex with a total spin $S_t = 3/2$. What is unusual about the EPR spectrum of **3** is the large amount of hyperfine coupling that is visible on top of the $g_{eff} = 4$ signal. DFT calculations show that this is due to partial oxidation of the phenolate rings (π orbitals) in the complex, leading to the transfer of a distinct amount of radical character onto the phenolates. Figure 3.5, bottom shows a spin density plot of **3**, obtained with B3LYP/TZVP, which indicates calculated spin densities on the phenolate carbons. The observed hyperfine couplings in Figure 3.5, top therefore originate from the nuclear spins of the ^{13}C and ^1H atoms of the phenolate groups. In total, a spin density of about +0.19 is transferred to the phenolate rings (not counting the O atoms). In this sense, complex **3** could be considered a "non-classical" hs-{FeNO}^{7} complex with multiple, redox-active ligands, although only partial oxidation of the phenolates is observed here.

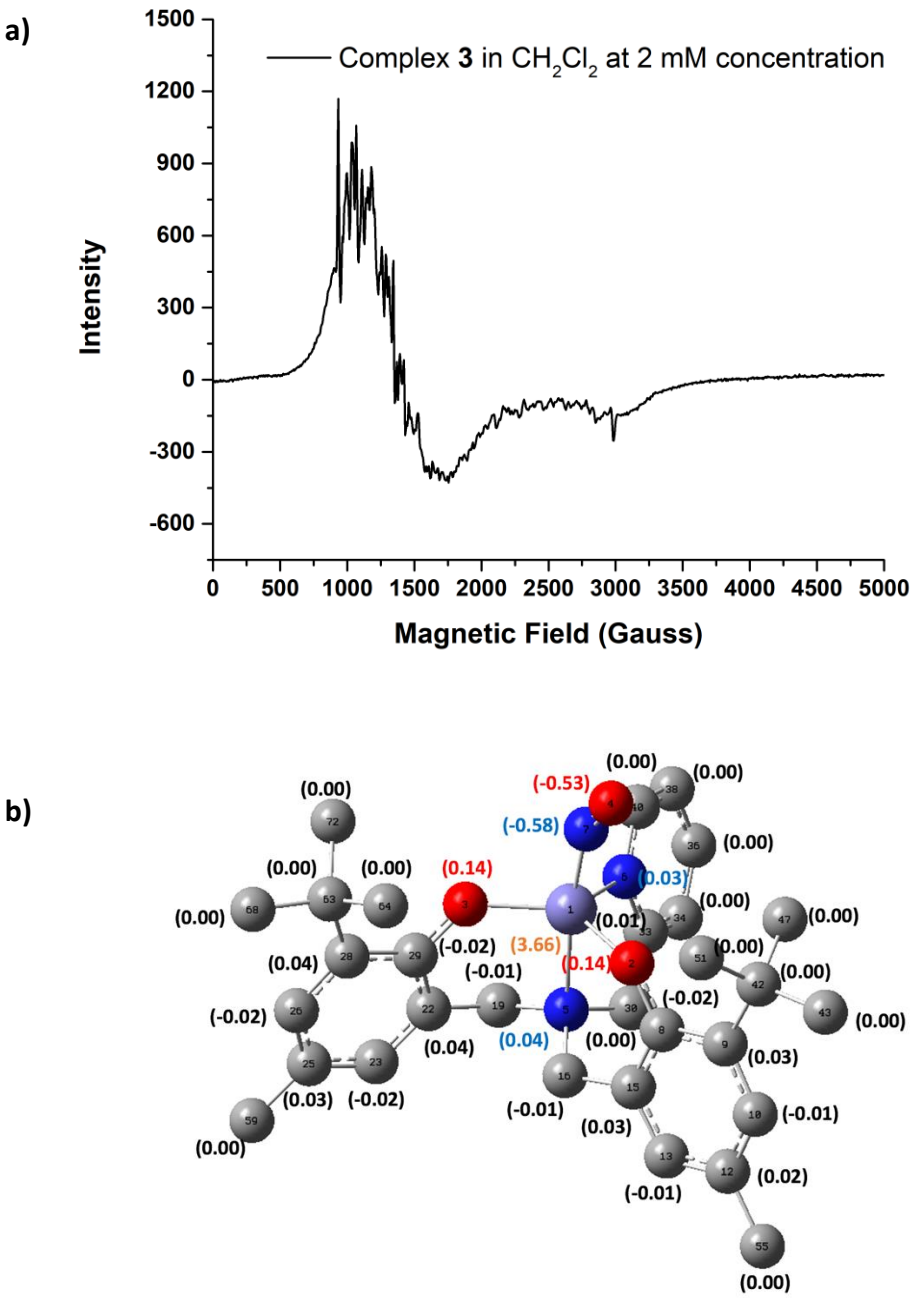

Figure 3.5 X-band EPR spectrum of complex **3** in CH_2Cl_2 at 2 mM concentration, showing signals at g_{eff} = 4, 2, typical for an S = 3/2 hs-{FeNO}^{7} complex, with additional hyperfine features. The EPR spectrum was collected at 4 K using ~20 mW microwave power and 100 kHz field modulation with the amplitude set to 1 G. b) Spin density plot (B3LYP/TZVP) with important spin density values indicated. Note that the total spin density of the phenolate rings is +0.19 (not counting the O atoms).

Mössbauer spectra exhibit an isomer shift of 0.56 mm/s and a quadrupole splitting of ΔE_Q = 0.92 mm/s for **3**. Importantly, solid state IR spectroscopy of **3** shows the N-O stretch of this

complex at 1689 cm^{-1}, which shifts to 1654 cm^{-1} in the ^{15}NO analog (Figure 3.6). *This is the lowest N-O stretching frequency reported so far for a mononuclear hs-{FeNO}^{7} complex*, which supports the idea that **3** contains a highly activated (reduced) NO ligand. In comparison, the N-O stretching frequency in **4** is located at 1742 cm^{-1}, in agreement with this conclusion. This result is also in agreement with the DFT-calculated N-O stretch for **3**, predicted at 1699 cm^{-1} with BP86/TZVP (this method has been shown to give particularly accurate N-O stretching frequencies in previous studies on hs-{FeNO}^{7} complexes[1]). The DFT calculations also reproduce the structural features of the [FeNO] unit well, with predicted Fe-NO and N-O bond distances of 1.74 and 1.18 Å (exp: 1.79 and 1.15 Å), respectively.

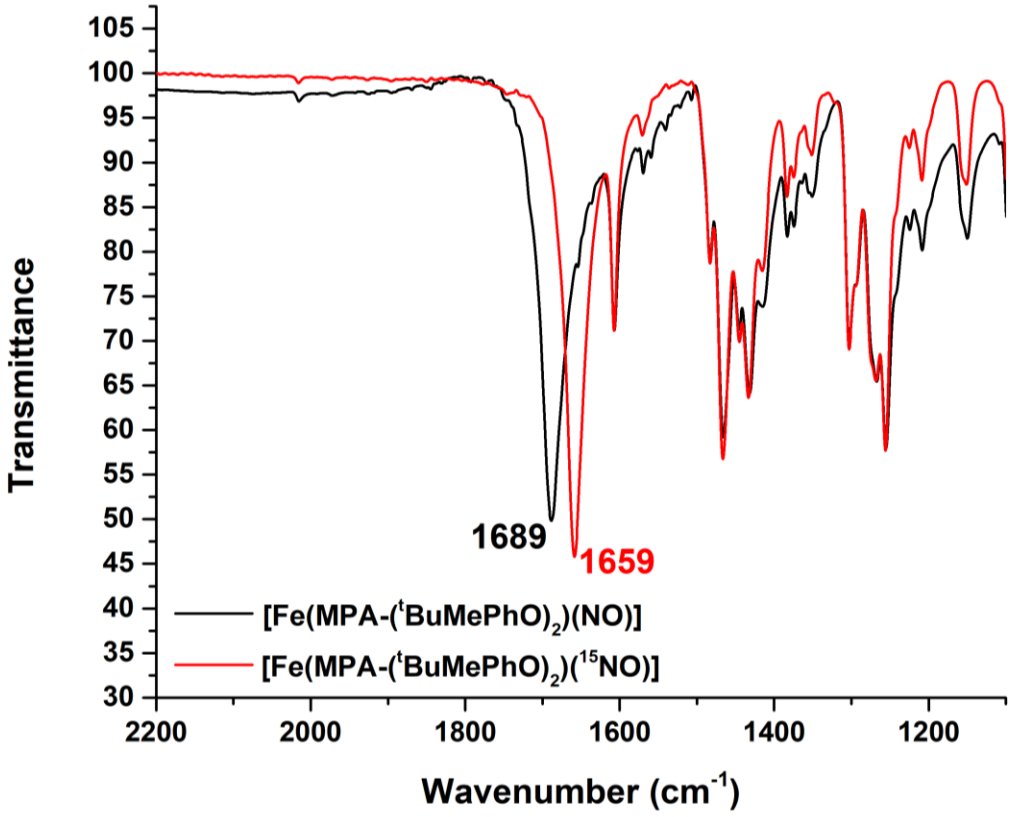

Figure 3.6 Solid state IR spectrum of complex **3**, taken in a KBr disk, which shows the N-O stretching frequency at 1689 cm^{-1}. This vibration shifts to 1659 cm^{-1} in the ^{15}NO-labeled form of complex **3**.

To further address the unique vibrational properties of **3**, NRVS was used to measure the Fe-NO stretch of this complex, which is observed at 467 cm^{-1} (Figure 3.7). This band shifts to 460 cm^{-1} upon ^{15}NO labeling, confirming the assignment of this feature to the Fe-NO stretch. As mentioned above, previous work has shown that the $^{3}NO^{-}$ ligand acts predominantly as a strong π-donor in hs-{FeNO}^{7} complexes, which is reflected by a direct correlation of the Fe-NO and N-O bond strengths, and hence, vibrational frequencies.[14] This is due to the fact that a reduction in π-donicity weakens the Fe-NO bond and lowers the Fe-NO stretch, and, at the same time, due to the increased electron density in the π* orbitals of the $^{3}NO^{-}$ ligand, weakens the N-O bond and lowers the N-O stretch as well. Hence, this direct correlation is a hallmark of complexes with a bound, $^{3}NO^{-}$ ligand. I have previously established this correlation with hs-{FeNO}^{7} complexes that feature N-O stretching frequencies in the 1720 - 1820 cm^{-1} range.[14] Complex **3** fits this analysis well and extends our correlation further into the <1700 cm^{-1} range for the N-O stretch. This is illustrated in Figure 3.8, where complex **3** is now added to the correlation line initially reported by Berto et al. in 2011.[14] Complex **3** lies on the lower end of the correlation line, due to being the most activated mononuclear hs-{FeNO}^{7} complex reported to this date. The weak Fe-NO and N-O bonds in **3** mean that this complex has an unprecedented, large amount of unpaired electron density in its π* orbitals, which is suitable for N-N coupling and N_2O formation. In addition, the weak Fe-NO bond in this complex lowers the activation barrier for N-N bond formation.[1] However, the complex lacks the ability to induce N-N bond formation and N_2O generation due to its strictly monomeric form. In contrast, the reaction of complex **1** with NO leads to almost quantitative N_2O formation (see next).

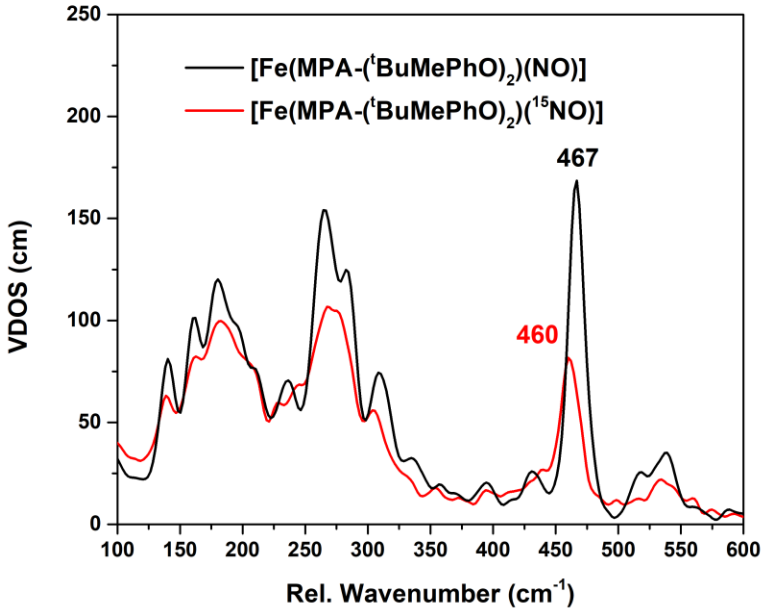

Figure 3.7 NRVS data of complex **3** (black) in comparison to the data of the ^{15}NO-labeled analog (red), showing the Fe-NO stretch at 467 cm^{-1}. Note that the difference in intensity of the Fe-NO stretch is due to only partial nitrosylation in the ^{15}NO-labeled complex, due to a lower concentration of the isotopically labeled gas.

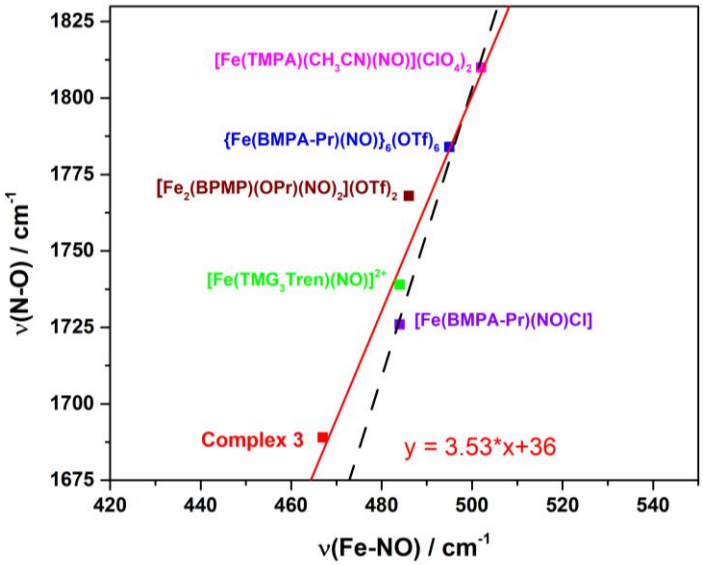

Figure 3.8 Fe-NO vs N-O stretching frequency correlation plot, generated from available data in the literature. Here, complex **3** extends the correlation to lower frequencies and in this way, helps refine the correlation line (previous fit: black dashed line; revised fit: red line), due to its lowest Fe-NO and N-O vibrational frequencies in the series so far.

3.3 Reactivity of Complex 1 with NO Gas: NO Reduction to N_2O

As discussed above, I propose that complex **3** represents a hs-$\{FeNO\}^7$ complex that has the right level of activation for direct NO reduction, but that is stabilized by the fact that it is forced to be monomeric, due to steric bulk. In order to obtain further support for this hypothesis, I then studied the reaction of complex **1** with NO, where such steric restrictions do not apply. Upon charging a round bottom flask containing a CH_2Cl_2 solution of freshly prepared complex **1** with excess NO gas, the solution immediately turned dark brown. The reaction was further monitored using UV-vis and IR spectroscopy. Analysis of the absorption spectra indicates that the reaction goes through two stages. Upon addition of NO, there is an immediate change in the signal at 460 nm, concomitant with the appearance of a new band at 451 nm (Figure 3.9a). IR spectra taken <5 min after NO addition show the formation of several different NO complexes with different degrees of activation with the major signal observed at 1734 cm^{-1}. The rapid formation of multiple NO complexes is then followed by a slower, second phase of the reaction. Here, the absorption signals slowly change over the course of 24 hours, showing a clean isobestic point at 484 nm, with the final product exhibiting a characteristic absorption band at 500 nm (Figure 3.9c). Solution IR data in Figure 3.10 show that this is concomitant with the disappearance of the N-O stretching signals in the IR spectrum, and the appearance of the N-N stretch of N_2O. After 24 hours, the total N_2O yield is 81%, indicating almost quantitative NO reduction by **1**. Solution IR data in Figure 3.10 show that after 24 h, there is still a noticeable amount of NO complex left in solution, with N-O stretching bands at 1750 and 1712 cm^{-1}, which likely accounts for the missing ~20% of iron-NO complexes that have not formed N_2O (yet). Considering the stability and slow decay observed for the NO complexes with N-O stretching frequencies >1710 cm^{-1} in the IR data, these are likely not the species responsible for N_2O formation.

These results further demonstrate the ability of the sterically unhindered complex **1** to mediate direct NO reduction, supporting the claim that both complexes **1** and **2** have suitable electronic properties to support this reaction, and that it is simply the inability of **3** to form dimeric (or oligomeric) structures that stabilizes this reactive species. In addition, complex **1** represents only the second example of direct NO reduction by a synthetic model complex.

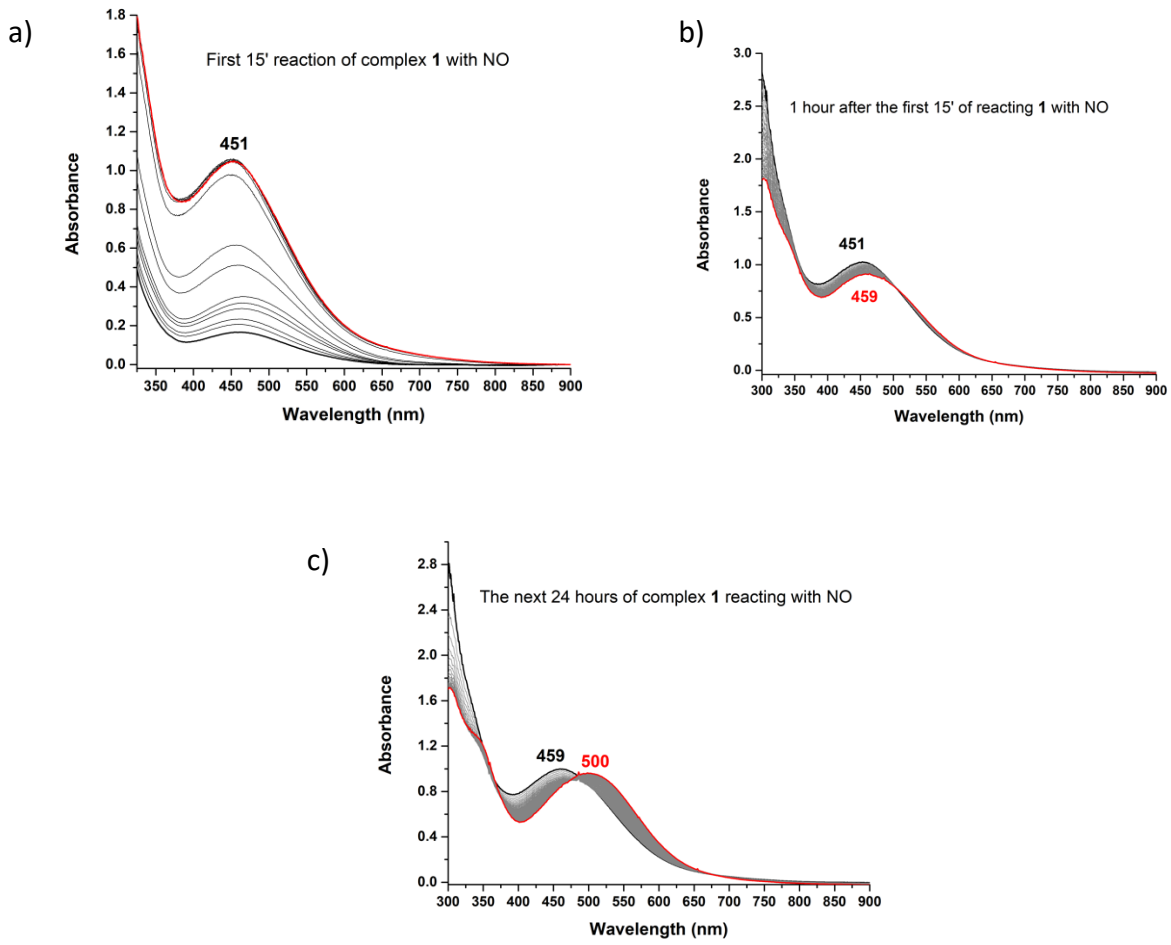

Figure 3.9 UV-Vis spectra monitoring the reaction of complex **1** with NO gas in DMF at 0.2 mM concentration at room temperature. The data were taken in the 24 hour time frame of the reaction a) was taken within the first 15 minutes of the reaction. b) was taken every five minutes after that for an hour. c) was taken every 15 minutes until the reaction is complete at around 25 hours mark (final spectrum in red).

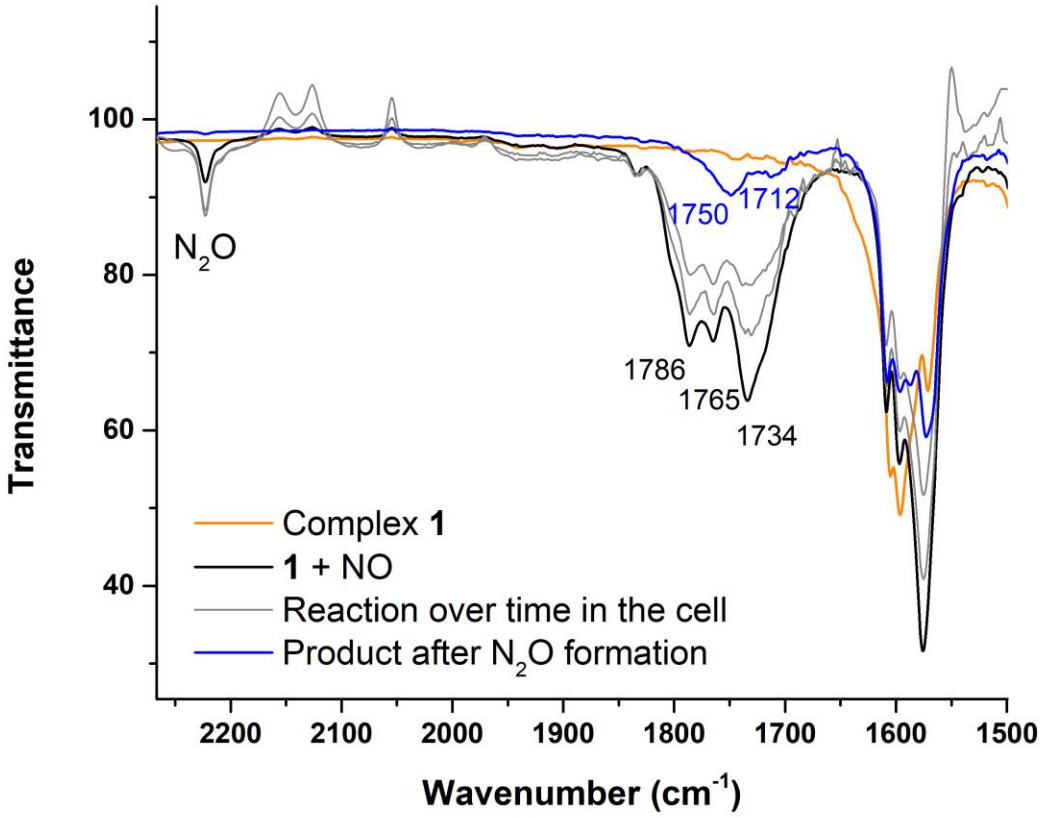

Figure 3.10 Solution IR spectra of the reaction of complex **1** with NO gas in CH_2Cl_2 at 10 mM concentration, showing the formation of multiple NO complexes right after the addition of NO gas (black line, taken immediately upon adding NO gas) and their disappearance over time (gray lines), concomitant with formation of N_2O as indicated. The final spectrum in blue was taken after 24 hours.

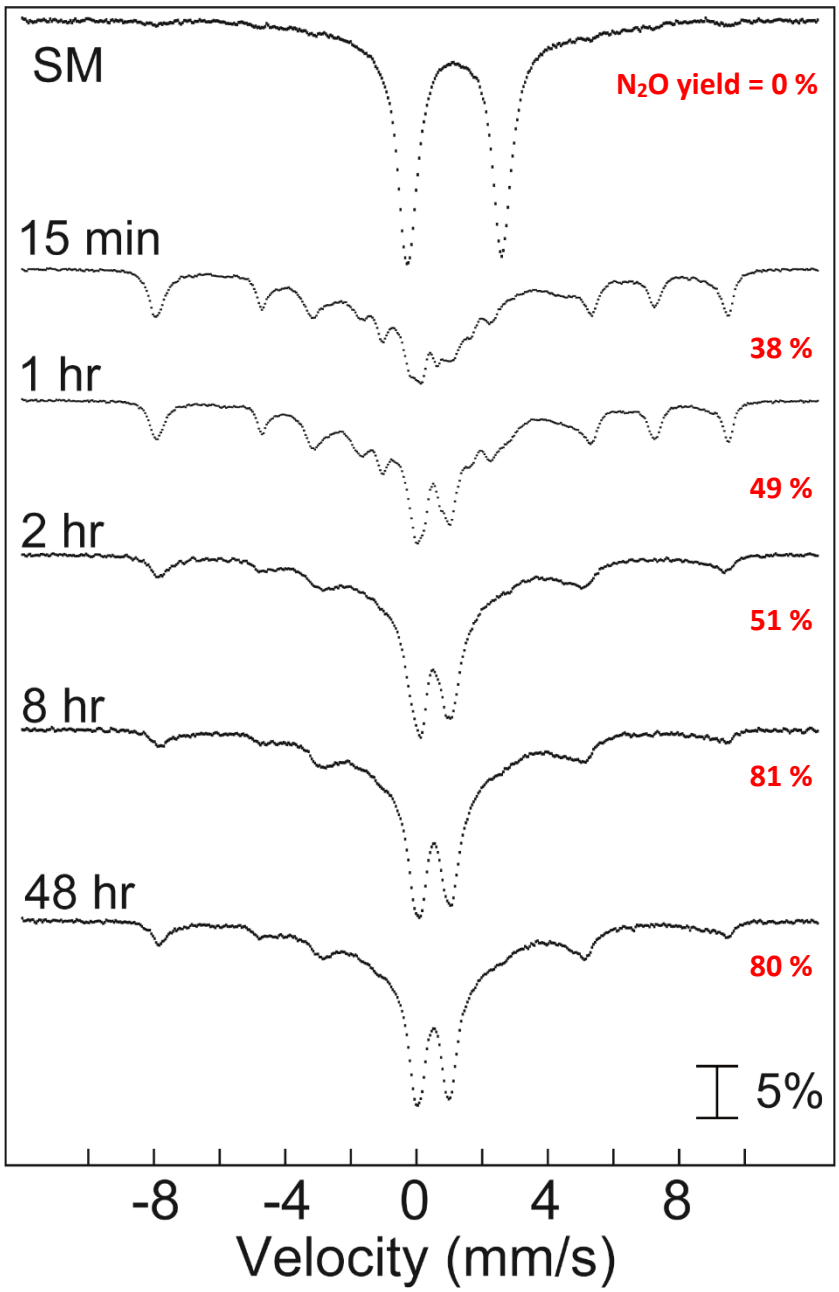

Figure 3.11 Mössbauer spectra following the reaction of **1** with NO gas at room temperature, at the indicated reaction times. SM = starting material (freshly prepared complex **1**). N2O yields at the given time points are indicated as red numbers on the right.

In order to obtain further insight into the mechanism of NO reduction by **1**, the reaction of this complex with NO gas at room temperature was then followed using EPR and Mössbauer spectroscopy. Figure 3.11 shows Mössbauer spectra that provide further insight into the evolution of iron species in solution during the reaction of **1** with NO, with N_2O yields at these time intervals

indicated as well (in red). As evident from the 15 minutes time point, reaction of NO with **1** is fast, leading to the consumption of the diferrous starting material and the generation of a mixture of iron-NO complexes in solution, as indicated by the solution IR data. Due to the ability of ligand H_2[MPA-$(PhO)_2$] to form oligomers, it is not clear what the different species are that form in solution. Gas head space analysis show that the N_2O yield at this time is 38%. EPR spectra taken at this time point show signals around $g_{eff} = 4$ and 2. Taken together, the spectroscopic data indicate the formation of mononitrosyl complexes ($S_t = 3/2$), diiron mononitrosyls (hs-Fe(II)/hs-$\{FeNO\}^7$, $S_t = 1/2$), diiron dinitrosyls ([hs-$\{FeNO\}^7$]$_2$, $S_t = 0$), and probably larger oligomers, as indicated in Scheme 3.2. Here, the $g_{eff} = 4$ signal would correspond to the mononitrosyl complex, whereas the $g = 2$ signal could be assigned to a hs-Fe(II)/hs-$\{FeNO\}^7$ dimer where the spins of the iron centers are antiferromagnetically coupled. Precedence of such species has been reported in the literature by Jana et al.[3,4] All of these species are likely in an equilibrium; however, only a [hs-$\{FeNO\}^7$]$_2$ complex with the NO ligands in cis position (or a corresponding unit in a larger oligomer) is able to go on and form N_2O. I propose that the cis-$[FeNO]_2$ dimer that is activated for N-N coupling only forms in low concentration, which would explain why N_2O formation only proceeds slowly in the reaction of **1** with NO gas.

After around 8 hours, no more changes are observed in the Mössbauer data, whereas the UV-Vis spectra still show subtle changes for up to 24 hours. During this time, additional N_2O is produced; however, the yield increases by only about ~1% (within error) between 8 and 24 hours. The yield at this time point is 80%, indicating that the reaction is not quantitative, and accordingly, the solution IR data show that there are remaining NO complexes in solution, which are trapped in unfavorable conformations preventing them from forming more N_2O (see above).

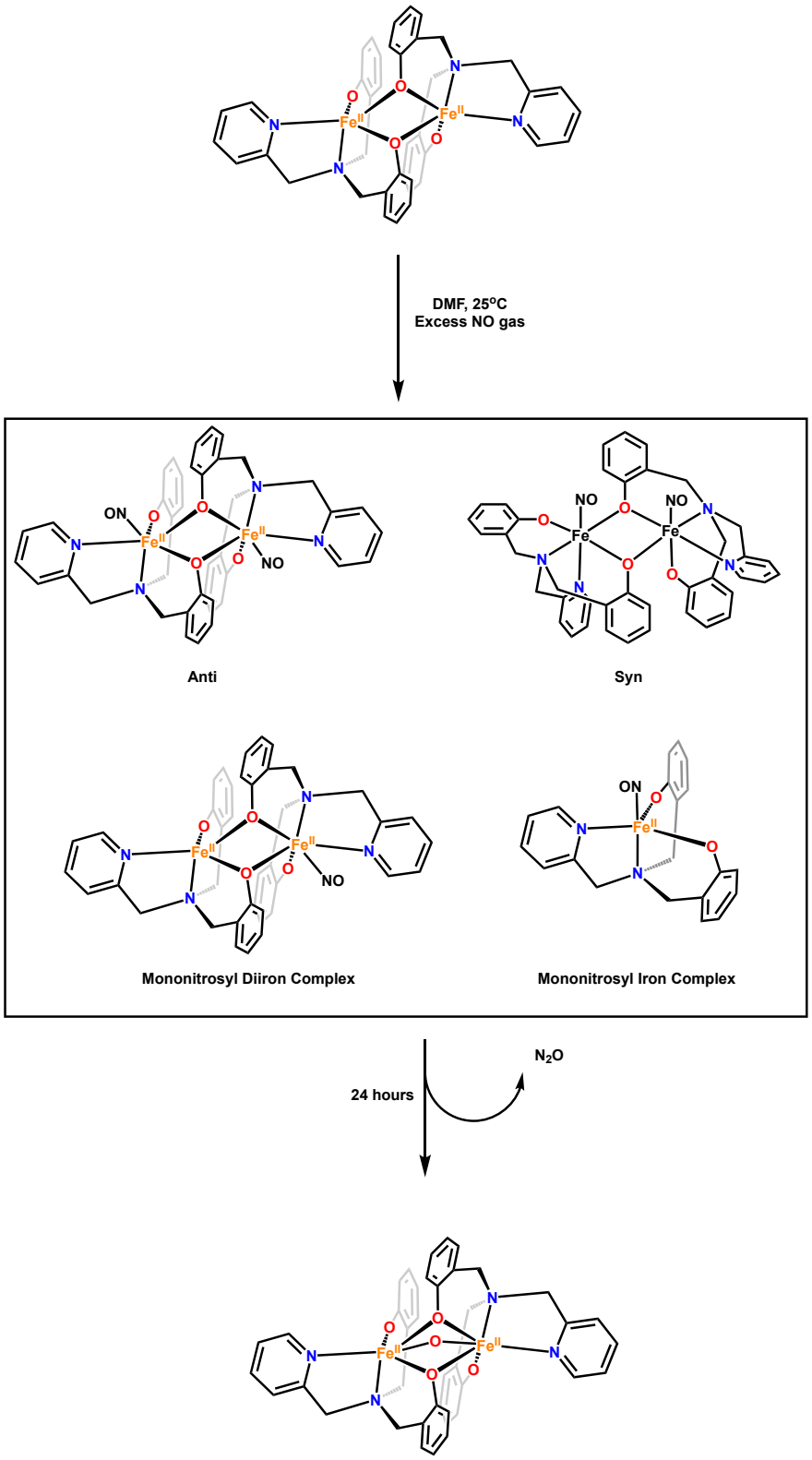

Scheme 3.2 Proposed reaction pathway and species presents in solution based on spectroscopic analysis.

3.4 Conclusions

In conclusion, I have demonstrated the stabilization of the most activated mononuclear hs-{FeNO}^{7} complexes using steric protection. I have shown that an analog of this complex without the steric protection is prone to N_2O formation via the direct reduction pathway. It is striking that whereas complex **1** directly reacts with NO to generate N_2O, the same is not true for complex **2**. I rationalize this difference with the need for a dimeric structure for a model system to mediate efficient NO reduction. I propose that in the case of **1**, due to the absence of steric bulk, the complex forms a diiron dinitrosyl intermediate, [{Fe^{II}(MPA-$(PhO)_2$)(NO)}$_2$], which rapidly proceeds to form N_2O, similar to our previous model complex, [Fe^{II}_2((Py_2PhO_2)MP)$(OAc)_2$]$^-$. In contrast, due to the sterically bulky phenolate groups, initial nitrosylation of **2** breaks up the dimeric structure, leading to the formation of the stable mononitrosyl complex **3**. *Complex **3** is the most activated hs-{FeNO}^{7} complex in the literature to this date*. The stabilization of this complex is achieved via classical inorganic design to incorporate steric protection in the secondary coordination sphere. Complex **1** can react with NO over the court of 24 hours to yield 81% of N_2O and a mixture of diferric products and potentially some unreacted mononitrosyl complexes. This result is very similar to what achieved in the enzymatic study carried out by Caranto et al where they observed ferric species and unreacted mononitrosyl complexes at the end of the reaction.[21] This result show that direct reduction can be achieved via a strongly activated hs-{FeNO}^{7} intermediate, however, these intermediate need to be able to dimerize for N-N bond formation to happen. This study confirms the theoretical suggestion that the direct reduction of NO to N_2O can happen with extremely activated hs-{FeNO}^{7} intermediate with the N-O stretching frequency < 1700 cm^{-1}. Even though the reaction of complex **1** is slow to reach completion, the initial formation of about 40% N_2O happens quite fast. I was unable to isolate any hyponitrite intermediate which is an

important intermediate on pathway towards formation of N_2O. Further ligand modification and redox tuning is currently underway to slow down the reaction enough to hopefully observe and trap this elusive intermediate.

3.5 Experimental Section

Reactions were generally performed using inert gas (Schlenk) techniques. All solvents were dried and freeze pump thawed to remove dioxygen and water. Preparation and handling of air sensitive materials was performed under a dinitrogen atmosphere in an MBraun glovebox, equipped with a circulating purifier (O_2, H_2O <0.1 ppm). Nitric oxide (99.95%) was first passed through an Ascarite II column and then a -80 ^oC cold trap to remove higher nitrogen oxide impurities prior to use.

Bis(2-hydroxybenzyl)(2-pyridylmethyl)amine (H_2[MPA-(PhO)$_2$]) was synthesized according to published procedures.[22] **2-pyridylamino-N,N-bis(2-methylene-4-methyl-6-tert-butylphenol) (H_2[MPA-(^{t}BuMePhO)$_2$])** was prepared according to published procedures.[23] The quality of these ligands was established by ^{1}H-NMR spectroscopy (400 MHz, Chloroform-*d*)

[{Fe(MPA-(PhO)$_2$)}$_2$] (1): Under an inert atmosphere, the ligand H_2[MPA-(PhO)$_2$] (100 mg, 0.31 mmol) and KOMe (43.8 mg, 0.62 mmol) are dissolved in a minimal amount of MeOH (about 5 ml) and stirred for 30 minutes. 136 mg (0.31 mmol) of Fe(OTf)$_2$.2CH_3CN is then added into the reaction and the solution immediately turns orange. The reaction is stirred for overnight at room temperature, and MeOH is then removed under reduce pressure. The crude product mixture is re-dissolved in CH_2Cl_2, and a solid impurity is removed via filtration. The CH_2Cl_2 is then removed under reduce pressure. The crude product is dissolved in CH_3CN, and diethyl ether is added for precipitation. The solution is allowed to recrystallize at -33 ^oC overnight. The solution

is then filtered under an inert atmosphere to yield light an orange product, complex **1**. Yield: 109 mg (92%).

[{Fe(MPA-(^{t}BuMePhO)$_2$)}$_2$] (2): Under an inert atmosphere, in a 20 ml vial, the ligand H_2[MPA-(^{t}BuMePhO)$_2$] (200 mg, 0.435 mmol) and KOMe (61 mg, 0.87 mmol) are dissolved in a minimal amount of MeOH (about 5 ml) and stirred for 30 minutes. 190 mg (0.435 mmol) of $Fe(OTf)_2.2CH_3CN$ is then added into the reaction and the solution immediately turns green. The reaction is stirred overnight at room temperature, and MeOH is then removed under reduce pressure. The crude product mixture is re-dissolved in CH_2Cl_2, and a solid impurity is removed via filtration. The filtrate is then layered with hexane, and recrystallization is carried out at -33 ºC overnight. Filtration yields a bright green crystalline product that is suitable for X-ray crystallography. Yield: 101 mg (45%). Elemental anal. calcd. for $C_{60}H_{76}Fe_2N_4O_4$ single crystals co-packed with CH_2Cl_2 (6:8 ratio): C, 63.03; H, 6.65; N, 4.90; found (%):C, 63.32; H, 6.90; N, 4.75.

[Fe(MPA-(tBuMePhO)$_2$)(NO)] (3): Under an inert atmosphere, in a 3-neck round bottom flask charged with a stir bar, 100 mg (0.097 mmol) of complex **2** is dissolve in a minimal amount of CH_2Cl_2 until the solution is homogeneous. Excess amount of dried and purified NO gas is then added into the gas headspace, and the solution immediately turns very dark brown. The reaction is stirred for 1 hour. The NO gas is then purged from the head space of the flask before hexane is added into the reaction mixture (from the top, with the septum removed to prevent build up of pressure), and the solution is allowed to recrystallize at -33 ºC overnight. The solution is then filtered under an inert atmosphere to yield very dark brown crystals of complex **3** that are suitable for X-ray crystallography. Yield: 30% Elemental anal. calcd. for $C_{30}H_{38}FeN_3O_3$: C, 66.18; H, 7.03; N, 7.72; found (%):C, 66.36; H, 7.27; N, 7.43. IR: ν(N–O) = 1689 cm^{-1}.

Structure Determination. Green prisms of **[{Fe(MPA-(tBuMePhO)$_2$)}$_2$]** were grown from a dichloromethane/hexanes solution of the compound at -33 ^{o}C. A crystal of dimensions 0.10 x 0.10 x 0.06 mm was mounted on a Rigaku AFC10K Saturn 944+ CCD-based X-ray diffractometer equipped with a low temperature device and a Micromax-007HF Cu-target micro-focus rotating anode (λ = 1.54187 Å) operated at 1.2 kW power (40 kV, 30 mA). The X-ray intensities were measured at 85(1) K with the detector placed at a distance of 42.00 mm from the crystal. A total of 2028 images were collected with an oscillation width of 1.0° in ω. The exposure times were 1 sec. for the low angle images, 5 sec. for high angle. Rigaku d*trek images were exported to CrysAlisPro for processing and corrected for absorption. The integration of the data yielded a total of 43,386 reflections to a maximum 2θ value of 138.64° of which 5421 were independent and 5012 were greater than 2σ(I). The final cell constants were based on the xyz centroids of 17,458 reflections above 10σ(I). Analysis of the data showed negligible decay during data collection. The structure was solved and refined with the Bruker SHELXTL (version 2018/3) software package, using the space group C2/c with Z = 4 for the formula $C_{62}H_{80}N_4O_4Cl_4Fe_2$. All non-hydrogen atoms were refined anisotropically with the hydrogen atoms placed in idealized positions. The complex lies on a two-fold rotation axis. Full matrix least-squares refinement based on F^2 converged at R1 = 0.0431 and wR2 = 0.1176 [based on I > 2sigma(I)], R1 = 0.0467 and wR2 = 0.1214 for all data.

Brown blocks of **[Fe(MPA-(^{t}BuMePhO)$_2$)(NO)]** were grown from a dichloromethane/hexanes solution of the compound at -33 ^{o}C. A crystal of dimensions 0.22 x 0.16 x 0.14 mm was mounted on a Rigaku AFC10K Saturn 944+ CCD-based X-ray diffractometer equipped with a low temperature device and a Micromax-007HF Cu-target micro-focus rotating anode (λ = 1.54187 Å) operated at 1.2 kW power (40 kV, 30 mA). The X-ray intensities were

measured at 85(1) K with the detector placed at a distance of 42.00 mm from the crystal. A total of 2028 images were collected with an oscillation width of 1.0° in ω. The exposure times were 1 sec. for the low angle images, 3 sec. for high angle. Rigaku d*trek images were exported to CrysAlisPro for processing and corrected for absorption. The integration of the data yielded a total of 19,767 reflections to a maximum 2θ value of 138.57° of which 4905 were independent and 4847 were greater than 2σ(I). The final cell constants were based on the xyz centroids of 17,758 reflections above 10σ(I). Analysis of the data showed negligible decay during data collection. The structure was solved and refined with the Bruker SHELXTL (version 2018/3) software package, using the space group P1bar with Z = 2 for the formula $C_{30}H_{38}N_3O_3Fe$. All non-hydrogen atoms were refined anisotropically with the hydrogen atoms placed in idealized positions. Full matrix least-squares refinement based on F^2 converged at R1 = 0.0408 and wR2 = 0.1139 [based on I > 2sigma(I)], R1 = 0.0412 and wR2 = 0.1143 for all data.

Pale yellow needles of **[Fe{Fe(MPA-(PhO)$_2$)}(HCOO)$_2$]$_8$** were grown by diffusion of diethyl ether into an acetonitrile solution of the compound at 20 ºC. A crystal of dimensions 0.05 x 0.02 x 0.02 mm was mounted on a Rigaku AFC10K Saturn 944+ CCD-based X-ray diffractometer equipped with a low temperature device and a Micromax-007HF Cu-target micro-focus rotating anode (λ = 1.54187 Å) operated at 1.2 kW power (40 kV, 30 mA). The X-ray intensities were measured at 85(1) K with the detector placed at a distance of 42.00 mm from the crystal. A total of 2028 images were collected with an oscillation width of 1.0° in ω. The exposure times were 10 sec. for the low angle images, 80 sec. for high angle. Rigaku d*trek images were exported to CrysAlisPro for processing and corrected for absorption. The integration of the data yielded a total of 79,913 reflections to a maximum 2θ value of 141.07° of which 19,891 were independent and 10,946 were greater than 2σ(I). The final cell constants were based on the xyz

centroids of 12,043 reflections above 10σ(I). Analysis of the data showed negligible decay during data collection. The structure was solved and refined with the Bruker SHELXTL (version 2018/3) software package, using the space group I-4 with Z = 4 for the formula $C_{176}H_{160}N_{16}O_{48}Fe_{16}$ [+ solvent]. All non-hydrogen atoms were refined anisotropically with the hydrogen atoms placed in idealized positions. The structure has two independent Fe_{16} clusters each on a -4 symmetry site of the lattice. Full matrix least-squares refinement based on F^2 converged at R1 = 0.0804 and wR2 = 0.2107 [based on I > 2sigma(I)], R1 = 0.1351 and wR2 = 0.2700 for all data. The SQUEEZE subroutine of the PLATON program suite was used to address the disordered solvent contained in solvent accessible voids present in the structure.

3.6 References

1. Van Stappen, C.; Lehnert, N. Mechanism of N-N Bond Formation by Transition Metal-Nitrosyl Complexes: Modeling Flavodiiron Nitric Oxide Reductases. *Inorg. Chem.* **2018**, *57*, 4252-4269.
2. White, C. J.; Speelman, A. L.; Kupper, C.; Demeshko, S.; Meyer, F.; Shanahan, J. P.; Alp, E. E.; Hu, M.; Zhao, J.; Lehnert, N. The Semireduced Mechanism for Nitric Oxide Reduction by Non-Heme Diiron Complexes: Modeling Flavodiiron Nitric Oxide Reductases. *J. Am. Chem. Soc.* **2018**, *140*, 2562-2574.
3. Jana, M.; Pal, N.; White, C. J.; Kupper, C.; Meyer, F.; Lehnert, N.; Majumdar, A. Functional Mononitrosyl Diiron(II) Complex Mediates the Reduction of NO to N_2O with Relevance for Flavodiiron NO Reductases. *J. Am. Chem. Soc.* **2017**, *140*, 14380-14383.
4. Jana, M.; White, C. J.; Pal, N.; Demeshko, S.; Meyer, F.; Lehnert, N.; Majumdar, A. Functional Models for the Mono- and Dinitrosyl Intermediates of FNORs: Semireduction versus Superreduction of NO. *J. Am. Chem. Soc.* **2020**, *142*, 6600-6616.
5. Zheng, S.; Berto, T. C.; Dahl, E. W.; Hoffman, M. B.; Speelman, A. L.; Lehnert, N. The Functional Model Complex $[Fe_2(BPMP)(OPr)(NO)_2](BPh_4)_2$ Provides Insight into the Mechanism of Flavodiiron NO Reductases. *J. Am. Chem. Soc.* **2013**, *135*, 4902−4905.
6. Jiang, Y.; Hayashi, T.; Matsumura, H.; Do, L. H.; Majumdar, A.; Lippard, S. J.; Moënne-Loccoz, P. Light-Induced N_2O Production from a Non-heme Iron–Nitrosyl Dimer. *J. Am. Chem. Soc.* **2014**, *136*, 12524-12527.
7. Kindermann, N.; Schober, A.; Demeshko, S.; Lehnert, N.; Meyer, F. Reductive Transformations of a Pyrazolate-Based Bioinspired Diiron−Dinitrosyl Complex. *Inorg. Chem.* **2016**, *55*, 11538-11550.

8. Dong, H. T.; White, C. J.; Zhang, B.; Krebs, C.; Lehnert, N. Non-Heme Diiron Model Complexes Can Mediate Direct NO Reduction: Mechanistic Insight into Flavodiiron NO Reductases. *J. Am. Chem. Soc.* **2018**, *140*, 13429-13440.
9. Lehnert, N.; Fujisawa, K.; Camarena, S.; Dong, H. T.; White, C. J. Activation of Non-Heme Iron-Nitrosyl Complexes: Turning up the Heat. *ACS Catal.* **2019**, *9*, 10499-10518.
10. Dahl, E. W.; Dong, H. T.; Szymczak, N. K. Phenylamino derivatives of tris(2-pyridylmethyl)amine: hydrogen-bonded peroxodicopper complexes. *Chem. Commun.* **2018**, *54*, 892-895.
11. Fujisawa, K.; Soma, S.; Kurihara, H.; Dong, H. T.; Bilodeau, M.; Lehnert, N. A Cobalt-Nitrosyl Complex with a Hindered Hydrotris(pyrazolyl)borate Coligand: Detailed Electronic Structure, and Reactivity towards Dioxygen. *Dalton Trans.* **2017**, *46*, 13273-13289.
12. Fujisawa, K.; Soma, S.; Kurihara, H.; Ohta, A.; Dong, H. T.; Minakawa, Y.; Zhao, J.; Alp, E. E.; Hu, M. Y.; Lehnert, N. Stable Ferrous Mononitroxyl $\{FeNO\}^8$ Complex with a Hindered Hydrotris(pyrazolyl)borate Coligand: Structure, Spectroscopic Characterization, and Reactivity Toward NO and O_2. *Inorg. Chem.* **2019**, *58*, 4059-4062.
13. MacBeth, C. E.; Golombek, A. P.; Young, V. G.; Yang, C.; Kuczera, K.; Hendrich, M. P.; Borovik, A. S. O_2 Activation by Nonheme Iron Complexes: A Monomeric Fe(III)-Oxo Complex Derived From O_2. *Science* **2000**, *289*, 938.
14. Berto, T. C.; Hoffman, M. B.; Murata, Y.; Landenberger, K. B.; Alp, E. E.; Zhao, J.; Lehnert, N. Structural and Electronic Characterization of Non-Heme Fe(II)-Nitrosyls as Biomimetic Models of the Fe_B Center of Bacterial Nitric Oxide Reductase (NorBC). *J. Am. Chem. Soc.* **2011**, *133*, 16714–16717.
15. Taft, K. L.; Delfs, C. D.; Papaefthymiou, G. C.; Foner, S.; Gatteschi, D.; Lippard, S. J. $[Fe(OMe)_2(O_2CCH_2Cl)]_{10}$, a Molecular Ferric Wheel. *J. Am. Chem. Soc.* **1994**, *116*, 823-832.
16. Taft, K. L.; Lippard, S. J. Synthesis and structure of $[Fe(OMe)_2(O_2CCH_2Cl)]_{10}$: a molecular ferric wheel. *J. Am. Chem. Soc.* **1990**, *112*, 9629-9630.
17. Sydora, O. L.; Wolczanski, P. T.; Lobkovsky, E. B. Ferrous Wheels, Ellipse $[(tBu_3SiS)FeX]_n$, and Cube $[(tBu_3SiS)Fe(CCSitBu_3)]_4$. *Angew. Chem. Int. Ed.* **2003**, *42*, 2685-2687.
18. Brown, C. A.; Pavlosky, M. A.; Westre, T. E.; Zhang, Y.; Hedman, B.; Hodgson, K. O.; Solomon, E. I. Spectroscopic and Theoretical Description of the Electronic Structure of S = 3/2 Iron-Nitrosyl Complexes and Their Relation to O_2 Activation by Non-Heme Iron Enzyme Active Sites *J. Am. Chem. Soc.* **1995**, *117*, 715-732.
19. Speelman, A. L.; White, C. J.; Zhang, B.; Alp, E. E.; Zhao, J.; Hu, M.; Krebs, C.; Penner-Hahn, J.; Lehnert, N. Non-heme High-Spin $\{FeNO\}^{6-8}$ Complexes: One Ligand Platform Can Do It All. *J. Am. Chem. Soc.* **2018**, *140*, 11341-11359.
20. Li, J.; Banerjee, A.; Pawlak, P. L.; Brennessel, W. W.; Chavez, F. A. Highest Recorded N–O Stretching Frequency for 6-Coordinate $\{Fe\text{-}NO\}^7$ Complexes: An Iron Nitrosyl Model for His_3 Active Sites. *Inorg. Chem.* **2014**, *53*, 5414-5416.
21. Caranto, J. D.; Weitz, A.; Hendrich, M. P.; Kurtz, D. M., Jr. The Nitric Oxide Reductase Mechanism of a Flavo-Diiron Protein: Identification of Active-Site Intermediates and Products. *J. Am. Chem. Soc.* **2014**, *136*, 7981–7992.
22. Zurita, D.; Scheer, C.; Pierre, J.-L.; Saint-Aman, E. Solution studies of copper(II) complexes as models for the active site in galactose oxidase. *Dalton Trans* **1996**, 4331-4336.

23. Tang, L.-Z.; Lin, C.-N.; Zhan, S.-Z. Effect of ligand modification on hydrogen production catalyzed by iron(III) complexes supported by amine-bis(phenolate) ligands. *Polyhedron* **2016**, *110*, 247-253.

Chapter 4

The Effects of Secondary Coordination Sphere Interactions on NO Reduction in FNORs Investigated Using Model Complexes

Acknowledgement: I would like to thank my undegraduate student Yu Zong for her assistance in the optimization of the ligand synthesis procedure and the crystal structure of the complex **3**. I would like to thank my undergraduate student Abigail Bracken for her assistance in obtaining the crystal structures of the precursor complexes **1** and **2**.

In **Chapter 4**, I explore the reactivity of model complexes of FNORs, featuring second coordination sphere (SCS) interactions, with NO gas. SCS hydrogen bonding effects have been shown computationally to play crucial roles in stabilizing the hyponitrite intermediate. Moreover, mutagenesis studies using *Mt* FDP revealed a ~7-fold and ~34-fold reduction in NOR reactivity when the tyrosine and histidine residues (Y195 and H25l, respectively) in the active site were substituted for non-hydrogen bonding residues.[1] Recent mutagenesis study with *T. maritima* FDP on the variant Y197F showed that this variant follows the same reaction path as the wild-type enzyme, up to and including the formation of the [hs-{FeNO}^{7}]$_2$ intermediate. However, no N_2O formation was observed. Instead, the [hs-{FeNO}^{7}]$_2$ intermediate forms an inactive mononitrosyl species.[2] The residue Y197 is proposed to assist in the rearrangement of the hyponitrite ligand by reducing the energetic barrier required for the Fe-N bonds scission. To study the effects of the SCS residues in FNORs, I designed a system that can mimic the interactions of the Y197 residue in the

active site. Here, I chose to modify the classic BPMP$^-$ ligand scaffold mentioned in **Chapter 2** since it can stabilize the [hs-{FeNO}^{7}]$_2$ intermediate.[3]

4.1 Synthesis and Characterization of [Fe$_2$(BPMP-NHCOC(CH$_3$)$_3$)(OAc)](OTf)$_2$ (2) and [Fe$_2$(MeOH)$_2$(BPMP-NHCOC(CH$_3$)$_3$)](OTf)$_3$ (3)

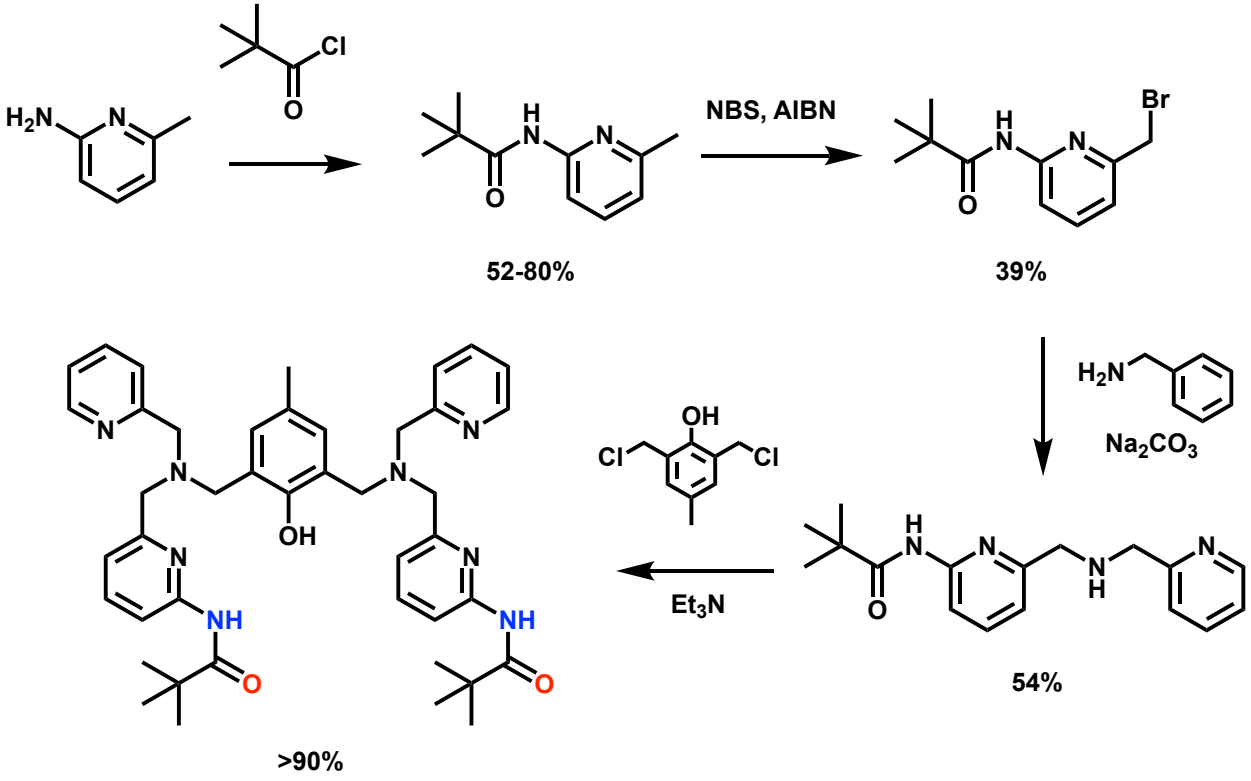

Scheme 4.1 Synthetic routes for the chosen ligand scaffolds.[4]

The ligand H[BPMP-NHCOC(CH$_3$)$_3$] was synthesized based on reported procedures with a modified work up detailed in the experimental section.[4] Complex **[Fe$_2$(BPMP-NHCOC(CH$_3$)$_3$)(OAc)$_2$](PF$_6$) (1)** were synthesized and reported in the literature.[5] This complex is structurally characterized by X-ray crystallography (Figure 4.1) and the reported result shows that the Fe···Fe distance is 3.45 Å. Importantly, complex **1** features hydrogen bonds between the SCS amides and the oxygen of the bridging acetate ligands. The hydrogen bond distances are 2.22

and 2.21 Å, respectively. Based on this crystal structure, I reasoned that nitrosylation to bind two NO molecules in place of one of the acetate bridging ligands would result in formation of a hydrogen bond to one of the newly bound NO, thus mimicing the active site of FNORs.

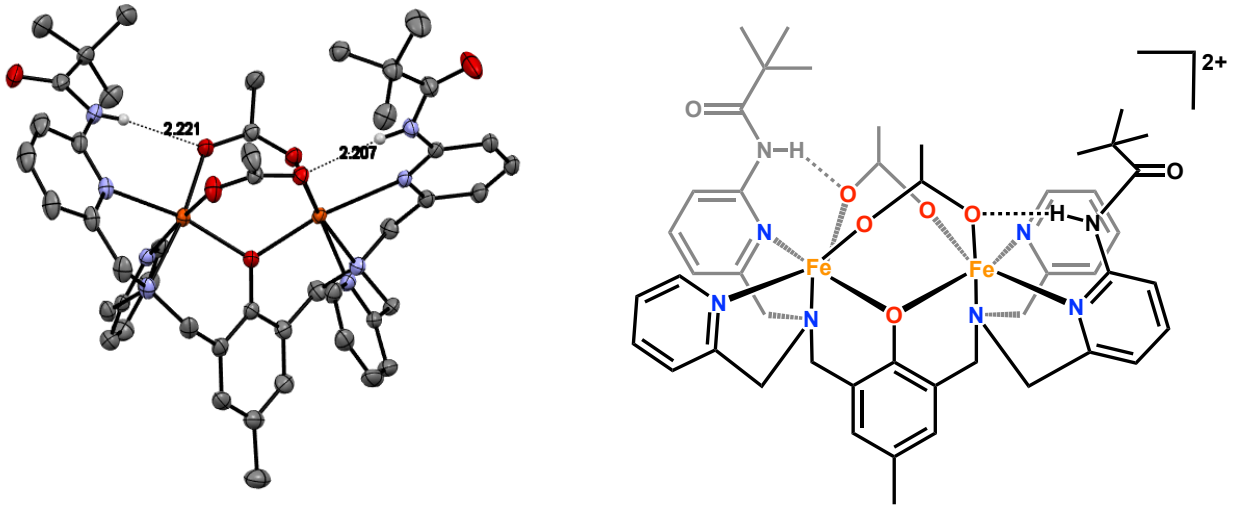

Figure 4.1 Left: Crystal structure of complex **1** with ellipsoids drawn at 50% probability. The triflate counter anion, solvent molecules, and hydrogen atoms are omitted for clarity. The crystal structure shows that hydrogen bonds are formed between the bridging acetate ligands and the protons of the amide functional groups. The crystal structure is taken from ref. [5]. Right: ChemDraw structure of complex **1**.

The ligand BPMP-NHCOC$(CH_3)_3$ was first deprotonated by one equivalent of KOMe and then metallated with two equivalents of $Fe(OTf)_2 \bullet 2CH_3CN$ (Scheme 4.2). One equivalent of NaOAc was subsequently added at the end of the reaction. The resulting mixture was worked up by first removing methanol under reduced pressure to yield a crude solid. The crude solid was redissolved in CH_2Cl_2 and filtered to remove salt byproducts. CH_2Cl_2 was then removed under reduced pressure. The solid was redissolved in THF and recrystallized via slow diffusion of diethylether at -33°C to yield a crystalline product. X-ray crystallography characterization of the crystals revealed the dimeric complex, **$[Fe_2$(BPMP-NHCOC$(CH_3)_3)$(OAc)$](OTf)_2$ (2)**, which features a single bridging acetate. Interestingly, the pseudo-octahedral geometry of the iron centers is completed with the coordination of the oxygen atoms of the amide groups. The Fe···Fe distance

is 3.64 Å which is elongated compare to complex **1** (3.45 Å). This observation highlights the role of the bridging acetate(s) in bringing the irons together and fix them at a closer distance. The Fe-O(Ac) bond lengths are 2.10 and 2.09 Å, respectively (Table 4.1). Interestingly, the acetate bridging ligand is extremely twisted to accommodate the coordination of the amides (Figure 4.2). The Fe-O(Amide) bond lengths are 2.15 and 2.09 Å, respectively, showing that they are strongly coordinated to the iron centers. This result shows that there is no open coordination site for NO ligation. This is a problem which can lead to destabilization of the $[hs\text{-}\{FeNO\}^7]_2$ intermediate. Further characterization of complex **2** with UV-Vis spectroscopy showed a broad band at 391 nm. IR spectroscopy revealed a signal at 1699 cm^{-1}, which is indicative of the bridging acetate ligand. This same signal is observed in the reported complex **1**.[5]

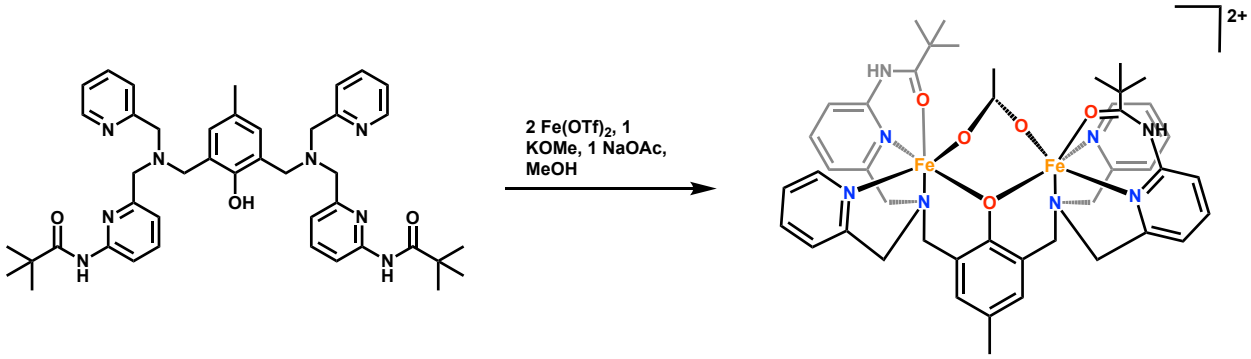

Scheme 4.2 Metallation scheme for ligands used in this chapter (the ChemDraw shows complex **2** as an example). The only difference is the equivalent of NaOAc used to form the bridging ligand.

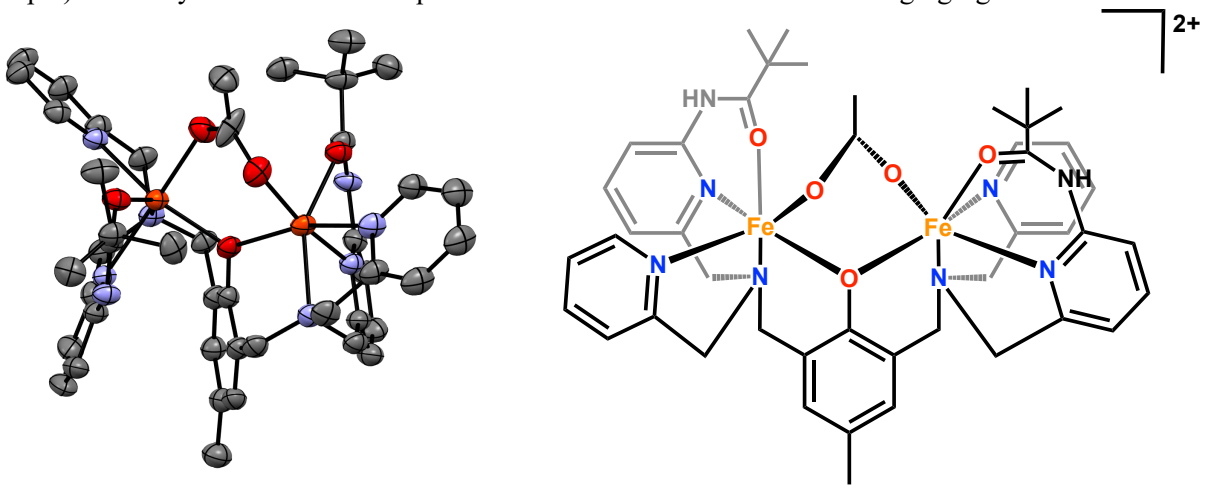

Figure 4.2 Left: Crystal structure of complex **2** with ellipsoids drawn at 50% probability. The triflate counter anion, solvent molecules, and hydrogen atoms are omitted for clarity. Right: Chemdraw of complex **2**.

To complete the series, I decided to remove the acetate bridging ligand completely to evaluate the Fe···Fe distances and their effects on reactivity of these complexes with NO gas. Complex **[Fe$_2$(BPMP-NHCOC(CH$_3$)$_3$)(MeOH)$_2$](OTf)$_3$** (**3**) (Figure 4.3) was synthesized according to the procedure described above for **2**, without the addition of NaOAc. X-ray crystallography of crystals, grown from slow diffusion of diethyl ether into a saturated solution of **3** in methanol, revealed a dimeric structure with an Fe···Fe distance of 3.80 Å (Figure 4.3, Table 4.1). The open coordination sites are occupied by MeOH solvent molecules, which complete the pseudo-octahedral geometry of the iron centers. Since solvent molecules often bind weakly to irons, it is likely this complex can be fully nitrosylated when react with NO gas. Complex **3** showed a UV-Vis signal at 386 nm. The solid-state IR spectrum of this complex in a KBr pellet revealed the lack of the C=O stretch of the acetate bridging ligand, observed at 1699 cm^{-1} in **2**.

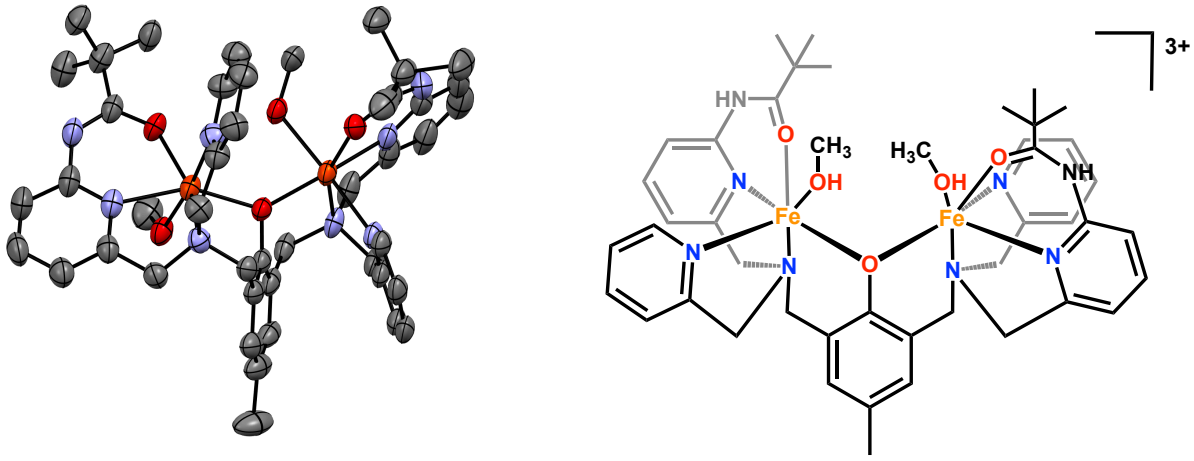

Figure 4.3 Left: Crystal structure of complex **3** with ellipsoids drawn at 50% probability. The triflate counter anion, solvent molecules, and hydrogen atoms are omitted for clarity. Right: ChemDraw of complex 3 showing the coordination environment of the complex.

Bonds	**[Fe$_2$(BPMP)(OPr)(NO$_3$)$_2$](BPh$_4$)$_2$ (ref[6])**	**1 (ref[5])**	**2**	**3**	**4**
Fe···Fe	3.47	3.45	3.64	3.76	3.59

Fe-O (Bridging)*	2.04	2.06	2.06	2.08	2.06
Fe-Oac*	2.03 (OPr)	2.10	2.10	N/A	2.07
Fe-O (Amide)*	N/A	N/A	2.12	2.08	2.06
Fe-N (tertiary)*	2.21	2.23	2.24	2.22	2.20
Fe-N (Pyr)*	2.16	2.25	2.18	2.20	2.19
Fe-NO	1.79	N/A	N/A	N/A	1.82
N-O	1.17	N/A	N/A	N/A	1.16
O···H (H-bond)	N/A	2.21	N/A	N/A	2.10

* = average value

Table 4.1 Comparison of structural parameters of different complexes mentioned in this chapter

4.2 Nitrosylation of Iron Complexes with NO Gas

First, I synthesized **[Fe_2(BPMP-NHCOC(CH_3)$_3$)(OAc)$_2$](OTf)** (**1-OTf**) using the procedure mentioned above and immediately reacted it with NO gas in CH_2Cl_2. The product was collected via gravity filtration after recrystallization with hexane overnight at -33 ^oC to prevent NO loss often observed with vacuum filtration. IR spectroscopy revealed a partially nitrosylated product due to the extremely low intensity of the N–O stretching band (Figure 4.4). This observation is expected because there is no open coordination sites for NO ligation. The weak NO band observed as a shoulder (Figure 4.4) corresponds to a small amount of NO complex formed due to the equilibrium with the dissociation of the acetate bridging ligand in solution (which favors binding of the acetate bridge at room temperature), as previously reported in **Chapter 2**.[7]

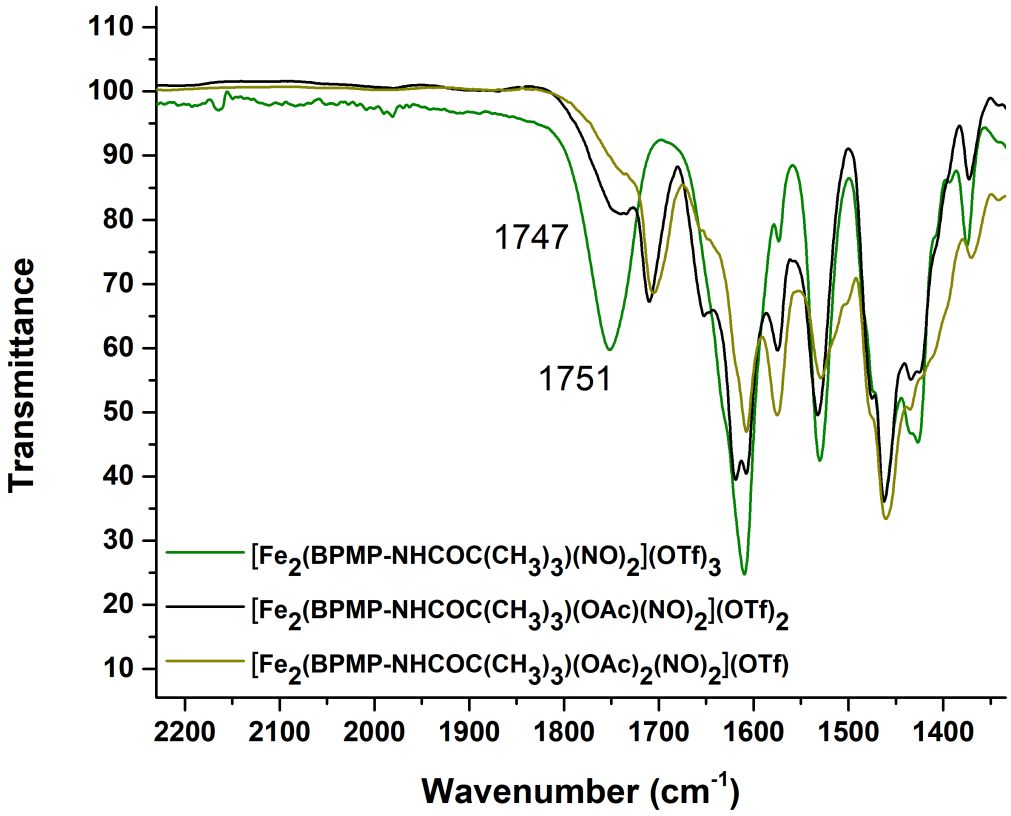

Figure 4.4 Solid state IR spectra of complexes with different amounts of bridging acetate ligands (from 0 to 2 bridging acetate ligands), showing that the complexes with acetate bridges reduce NO binding, resulting in weaker N-O bands in the IR spectrum.

Reaction of complex **2** with an excess amount of NO gas in CH_2Cl_2 at 25 ºC yielded a brown crystalline material. Recrystallization overnight via slow diffusion of hexane yielded a dark brown solid that was collected by gravity filtration through a filter frit. IR spectroscopy showed a new signal at 1746 cm^{-1} (Figure 4.6), which indicates the formation of a hs-$\{FeNO\}^7$ complex. The cyclic voltammogram of this complex showed a reduction at -1.30 V vs Fc^+/Fc. Interestingly, slow diffusion of NO saturated hexane into a saturated NO solution of this product in CH_2Cl_2 yielded single crystals suitable for X-ray diffraction. Surprisingly, the crystal structure revealed a mononitrosyl diiron complex, **[Fe_2(BPMP-NHCOC(CH_3)$_3$)(OAc)(NO)](OTf)** (**4**) (Figure 4.5),

where one of the amides is deprotonated. However, EPR spectroscopy in CH_2Cl_2 showed a weak signal for this complex, suggesting that there is only a small portion of this species formed in solution. Therefore, I propose that the majority of the complexes in solution is EPR silent. Complex **4** likely crystallized out due to having the lowest solubility, thus does not represent the bulk material. This observation indicates that complex **2** binds NO very weakly, likely due to the competitive ligation of the amides, which results in a low binding constant for NO. Indeed, Mössbauer spectroscopy showed that only 55% of the species in solution is complex **4**, the rest is unreacted starting material complex **2** formed via NO loss. Therefore, I propose that the dinitrosyl complex, if formed, was very short-lived and immediate lose NO to form complex **2** and **4**. Nevertheless, this crystal structure provides valuable insights into the structure of the potential dinitrosyl complex formed in solution.

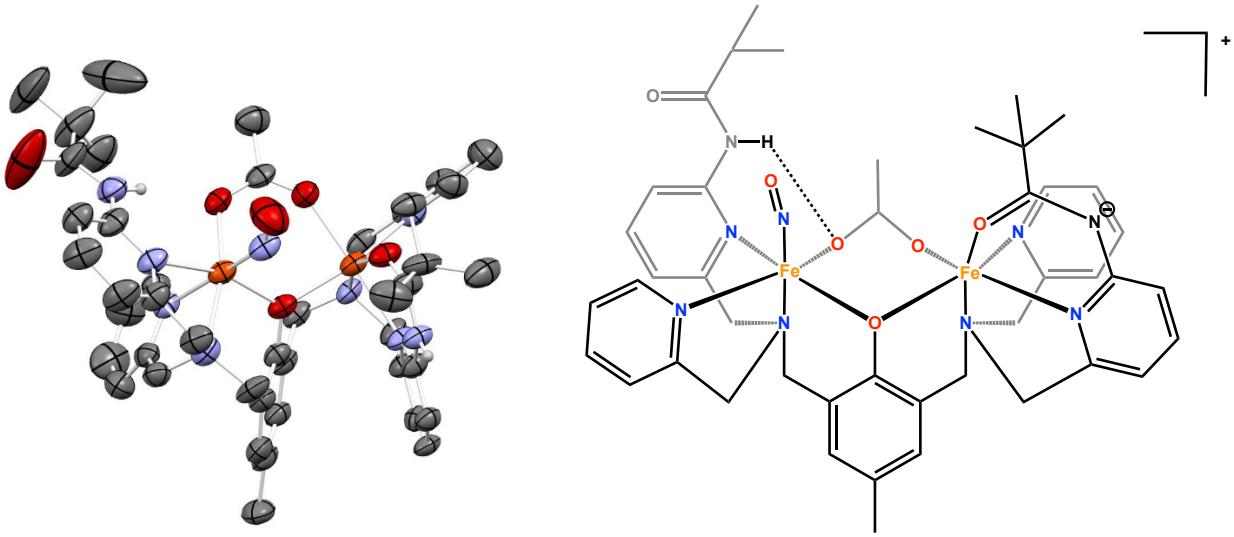

Figure 4.5 Left: Crystal structure of complex **4** with ellipsoids drawn at 50% probability. The triflate counter anion, solvent molecules, and hydrogen atoms are omitted for clarity. Right: ChemDraw structure of **4**.

I attempted to protonate this amide group by adding weak acid, $[Et_3NH_4]OTf$, into our reaction before adding NO gas. The intensity of the N-O band was monitored through several different control experiments shown in Figure 4.6. The result showed that protonation does not

play any role in increasing the intensity of the N–O stretching band. Instead, extra NO gas alone was enough to increase the intensity of this band. This observation confirmed that complex **2** binds NO very weakly and loses NO over time, even in solid state at -33 °C. Complex **4** was, indeed, a decomposition product in the bulk material that happened to crystallize out due to lower solubility.

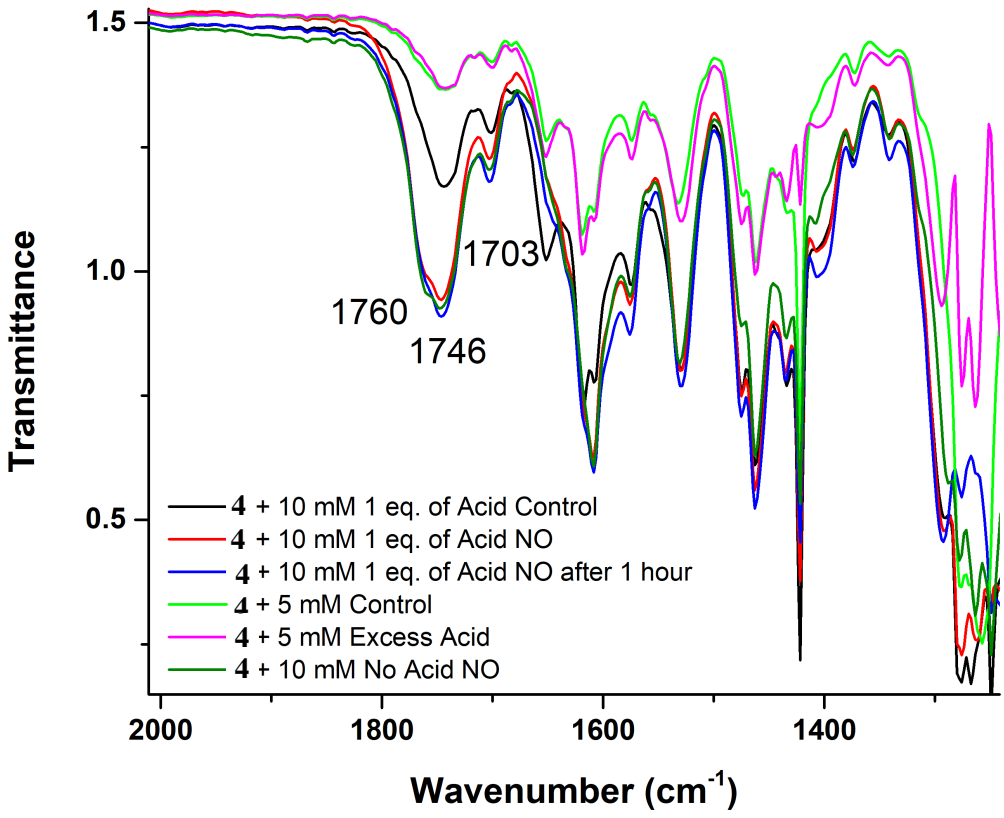

Figure 4.6 Control reactions with complex **4** showing that the amount of NO gas is the key to increase the intensity of the N-O stretching bands. The addition of the proton source $[Et_3NH_4]OTf$ does not affect the intensity of the N-O band.

Even though **4** was only a minor species, the crystal structure shown in Figure 4.5 still provides important structural information of the potential dinitrosyl complex. **4** has a bent FeNO moiety typical for hs-$\{FeNO\}^7$ complexes.[6,8-12] It is important to note that the formation of clean diiron mononitrosyl complexes is extremely hard to achieve in diiron systems. The reported

complex $[Fe_2(BPMP)(OPr)(NO)_2](BPh_4)_2$ can only form a dinitrosyl complex after nitrosylation. This is only the second example of such a complex in the literature, the other example is a complex reported by Majumdar and coworkers.[9,10] Here, the N–O and Fe–NO bond distances of complex **4** are 1.16 and 1.82 Å, respectively. These bond distances are very similar to that of $[Fe_2(BPMP)(OPr)(NO)_2](BPh_4)_2$ (1.17 and 1.79 Å). The Fe···Fe distance is shortened to 3.59 Å in the NO complex compared to the 3.64 Å observed in **2**. Fe–O bond distances of the bridging phenolate are 2.02 and 2.10 Å. The Fe–O bond distances of the acetate bridging ligand are 2.02 and 2.11 Å for the hs-$\{FeNO\}^7$ moiety and the hs-Fe(II) center, respectively. The Fe-O(amide) bond distance is 2.08 Å. In order to bind two NO molecules, I decided to remove the acetate bridging ligand completely to open up coordination sites for NO, using complex **3**.

Upon reacting the yellow complex **3** with NO gas in CH_2Cl_2, a green product was collected after recrystallization with hexane at -33 °C. IR spectroscopy of this product in a KBr pellet showed a much more intense N–O stretching band at 1751 cm^{-1} (Figure 4.4). Based on the structure of complex **3**, it is proposed that the NO molecules replaced the solvent molecules to bind both iron centers, thus forming the new complex **$[Fe_2(BPMP\text{-}NHCOC(CH_3)_3)(NO)_2](OTf)_3$ (5)**. This complex is EPR silent. Even though **5** formed a dinitrosyl product, because of the coordination of the amides to the irons, complex **5** does not feature hydrogen bonds with the bound NO ligands. To overcome the problem of amide coordination to the iron centers, it is necessary to go to SCS hydrogen bond donors that are non-coordinating, such as primary and secondary amines. Initial work on these new systems is presented in Chapter 8.

4.3 Experimental Section

N_2O yield determination.

Structure Determination.

Yellow needles of **2** were grown by layering a hexane/dichloromethane solution of the compound at 25 deg. C. A crystal of dimensions 0.15 x 0.07 x 0.02 mm was mounted on a Rigaku AFC10K Saturn 944+ CCD-based X-ray diffractometer equipped with a low temperature device and a Micromax-007HF Cu-target micro-focus rotating anode (l = 1.54187 Å) operated at 1.2 kW power (40 kV, 30 mA). The X-ray intensities were measured at 85(1) K with the detector placed at a distance of 42.00 mm from the crystal. A total of 2028 images were collected with an oscillation width of 1.0° in w. The exposure times were 1 sec. for the low angle images, 8 sec. for high angle. Rigaku d*trek images were exported to CrysAlisPro for processing and corrected for absorption. The integration of the data yielded a total of 44463 reflections to a maximum 2q value of 140.29° of which 10747 were independent and 9361 were greater than 2s(I). The final cell constants (Table 1) were based on the xyz centroids of 16480 reflections above 10s(I). Analysis of the data showed negligible decay during data collection. The structure was solved and refined with the Bruker SHELXTL (version 2018/3) software package, using the space group P1bar with Z = 2 for the formula $C_{49}H_{58}N_8O_{11}F_6S_2Cl_4Fe_2$. All non-hydrogen atoms were refined anisotropically with the hydrogen atoms placed in a combination of refined and idealized positions. Full matrix least-squares refinement based on F2 converged at R1 = 0.0734 and wR2 = 0.2015 [based on I > 2sigma(I)], R1 = 0.0808 and wR2 = 0.2131 for all data.

Yellow needles of **3** were grown by methanol/diethyl ether vapor diffusion of the compound at 25 deg. C. A crystal of dimensions 0.12 x 0.12 x 0.04 mm was mounted on a Rigaku AFC10K Saturn 944+ CCD-based X-ray diffractometer equipped with a low temperature device and a Micromax-007HF Cu-target micro-focus rotating anode (l = 1.54187 Å) operated at 1.2 kW power (40 kV, 30 mA). The X-ray intensities were measured at 85(1) K with the detector placed

at a distance of 42.00 mm from the crystal. A total of 2028 images were collected with an oscillation width of 1.0° in w. The exposure times were 1 sec. for the low angle images, 8 sec. for high angle. Rigaku d*trek images were exported to CrysAlisPro for processing and corrected for absorption. The integration of the data yielded a total of 181810 reflections to a maximum 2q value of 139.72° of which 22253 were independent and 18485 were greater than 2s(I). The final cell constants (Table 1) were based on the xyz centroids of 40190 reflections above 10s(I). Analysis of the data showed negligible decay during data collection. The structure was solved and refined with the Bruker SHELXTL (version 2018/3) software package, using the space group P2/n with Z = 4 for the formula 2($C_{45}H_{59}N_8O_5Fe_2$), 6(CF_3SO_3), 2.5(CH_4O). All non-hydrogen atoms were refined anisotropically with the hydrogen atoms placed in a combination of refined and idealized positions. Two trifilate anions and one bound methanol are disordered. Full matrix least-squares refinement based on F2 converged at R1 = 0.0859 and wR2 = 0.2388 [based on I > 2sigma(I)], R1 = 0.0973 and wR2 = 0.2589 for all data.

Brown needles of **4** were grown from a dichloromethane/hexane solution of the compound at -33 deg. C. A crystal of dimensions 0.14 x 0.04 x 0.04 mm was mounted on a Rigaku AFC10K Saturn 944+ CCD-based X-ray diffractometer equipped with a low temperature device and a Micromax-007HF Cu-target micro-focus rotating anode (λ = 1.54187 Å) operated at 1.2 kW power (40 kV, 30 mA). The X-ray intensities were measured at 85(1) K with the detector placed at a distance of 42.00 mm from the crystal. A total of 2028 images were collected with an oscillation width of 1.0° in ω. The exposure times were 5 sec. for the low angle images, 40 sec. for high angle. Rigaku d*trek images were exported to CrysAlisPro for processing and corrected for absorption. The integration of the data yielded a total of 15872 reflections to a maximum 2θ value of 139.93° of which 11248 were independent and 8437 were greater than 2σ(I). The final cell

constants (Table 1) were based on the xyz centroids of 15872 reflections above 10σ(I). Analysis of the data showed negligible decay during data collection. The structure was solved and refined with the Bruker SHELXTL (version 2018/3) software package, using the space group C2/c with Z = 8 for the formula $C_{46}H_{53}N_9O_9F_2SFe_2$ + [solvent]. All non-hydrogen atoms were refined anisotropically with the hydrogen atoms placed in idealized positions. Full matrix least-squares refinement based on F2 converged at R1 = 0.0693 and wR2 = 0.1879 [based on I > 2sigma(I)], R1 = 0.0891 and wR2 = 0.2073 for all data. The SQUEEZE subroutine of the PLATON program suite was used to address the disordered solvent in the two large cavities present in the structure.

Ligand Synthesis

Step 1: 2-amino-6-methylpyridine (20.86 g, 192 mmol) was stirred with 250 mL DCM. Et_3N (19.5 g, 192 mmol) was added to the flask. Pivaloyl chloride (23.5 g, 195 mmol) was added dropwise with stirring overnight at RT. The crude product was extracted three times with DI water, once with 500 mL 0.5 M HCl, and once with 500 mL 0.5 M $NaHCO_3$. The resulting organic product was dried with sodium sulfate and solvent was removing using rotary evaporation; yield: 19.42 g, 52%. ^{1}H-NMR (400 MHz, Chloroform-*d*) δ = 8.05 (d, *J* = 8.3 Hz, 1H), 7.58 (t, *J* = 7.9 Hz, 1H), 6.88 (d, *J* = 7.4 Hz, 1H), 2.45 (s, 3H), 1.32 (s, 9H), 1.26 (t, *J* = 1.8 Hz, 1H).

Step 2: *N*-(6-methylpyridin-2-yl)pivalamide (14.0 g, 72.9 mmol), *N*-bromosuccinimide (13.0 g, 73.0 mmol), and azobisisobutyronitrile (0.233 g, 1.42 mmol) were added to a 1-neck Schlenk flask with a glass stopcock and stir bar. The flask was flushed with N_2. CCl_4 (~250 mL) was added to the flask using cannula transfer under N_2 with stirring. A reflux condenser was attached to the flask under positive N_2 pressure. The flask was heated to 80ºC and stirred for 24 hours. The solids were filtered and solvent was removed using rotary evaporation. The product was isolated using a silica column. The mobile phase was 4:1 petroleum ether:ethyl acetate; yield:

7.72 g, 39%. ^{1}H-NMR (400 MHz, Chloroform-*d*) δ = 8.16 (d, *J* = 8.5 Hz, 1H), 8.01 (s, 1H), 7.67 (t, *J* = 7.9 Hz, 1H), 7.13 (dd, *J* = 7.5, 0.8 Hz, 1H), 4.40 (s, 2H), 1.31 (s, 9H).

Step 3: 2-picolylamine (4.86 g, 44.9 mmol) and sodium carbonate (4.60 g, 43.4 mmol) were stirred with ACN for 1 hour at 40ºC. *N*-(6-(bromomethyl)pyridin-2-yl)pivalamide (5.7 g, 21.0 mmol) was dissolved in ACN was added dropwise into the flask over 2 hours at 40ºC with stirring. The resulting product was filtered and separated using a basified silica column. Silica and silica plates were basified using hexanes with 10% Et_3N. The mobile phase was ethyl acetate with 10% methanol and 1% Et_3N; yield: 3.39 g, 54%. ^{1}H-NMR (400 MHz, Chloroform-*d*) δ 8.48 (dd, *J* = 4.9, 1.6 Hz, 1H), 8.08 – 8.01 (m, 2H), 7.56 (ddd, *J* = 7.8, 5.4, 3.3 Hz, 2H), 7.27 (d, *J* = 7.3 Hz, 1H), 7.09 (dd, *J* = 7.5, 4.9 Hz, 1H), 6.97 (d, *J* = 7.4 Hz, 1H), 4.04 (q, *J* = 7.1 Hz, 4H), 3.90 (s, 2H), 3.81 (s, 2H), 3.06 (s, 1H), 1.25 (s, 9H).

The rest of the steps for BPMP-NHCOC$(CH_3)_3$ are carried out as reported previously.[4]

Iron Complex synthesis:

$[Fe_2$(BPMP-NHCOC$(CH_3)_3)$(OAc)$](OTf)_2$ (2) In a glovebox, BPMP-NHCOC$(CH_3)_3$ ligand (100 mg, 0.137 mmol) and KOMe (9.62 mg, 0.137 mmol) were stirred with ~5 mL MeOH for 10 min. $Fe(OTf)_2 \cdot 2CH_3CN$ (120 mg, 0.275 mmol) was added and the contents were stirred for 10 min. NaOAc (11.25 mg, 0.137 mmol) was added and the contents were stirred overnight. A vacuum was used to remove the solvent and the dry product was dissolved in CH_2Cl_2. Solids were filtered out of the solution and a vacuum was used to remove the solvent to obtain crude product of complex **1**. Yield: Undetermined due to the impurities present in the bulk material. This is also reflected in the elemental analysis, which shows that the complex is not pure. More work is necessary to obtain a pure compound. Elemental analysis calculated for $C_{47}H_{55}F_6Fe_2N_8O_{11}S_2$: Expected: C, 47.13; H, 4.63; N, 9.36. Found: C, 43.05; H, 4.42; N, 8.31. This complex is then

redissolved into THF and recrystallize with ether to yield the desired yellow complex **1**. UV-Vis: 386 nm IR: ν(C=O) = 1699 cm^{-1}. Mössbauer spectroscopy: δ = 1.19 mm/s and ΔE_Q = 2.85 mm/s collected at 53 mT //, 4.2 K.

$[Fe_2(BPMP\text{-}NHCOC(CH_3)_3)(MeOH)_2](OTf)_3$ (3) In a glovebox, BPMP-$NHCOC(CH_3)_3$ ligand (100 mg, 0.137 mmol) and KOMe (9.62 mg, 0.137 mmol) were stirred with ~5 mL MeOH for 10 min. $Fe(OTf)_2 \cdot 2CH_3CN$ (120 mg, 0.275 mmol) was added and the contents were stirred overnight. A vacuum was used to remove the solvent and the dry product was dissolved in CH_2Cl_2. Solids were filtered out of the solution and a vacuum was used to remove the solvent to obtain crude product of complex **3**. This complex is then redissolved into THF and recrystallize with ether to yield the desired yellow complex **3**. Yield was not recorded. Elemental analysis calculated for $C_{50}Cl_2H_{61}F_9Fe_2N_8O_{14}S_3$: Expected: C, 40.99; H, 4.28; N, 7.80 Found: C, 40.91; H, 4.21; N, 8.17. UV-Vis: 391 nm

$[Fe_2(BPMP\text{-}NHCOC(CH_3)_3)(OAc)(NO)](OTf)$ (4) In a glovebox, 100 mg of complex **1** is dissolved in to a minimal amount of CH_2Cl_2 in a Schlenk flask charged with a stirrbar. The solution is then reacted with an excess amount of NO gas on a Schlenk line, causing the yellow solution to turn dark brown upon reacting with NO gas. The reaction is then allowed to stir overnight before hexane is then added to crash out the desired product. Yield determined based on Mössbauer spectroscopy: 55% with 45% unreacted/product formed due to the loss of NO overtime. The product is then gravity filtered through a frit and let air dry in the glovebox overnight. IR: ν(C=O) = 1746 cm^{-1}.

A similar nitrosylation protocol is used to nitrosylate complex **5**. Like complex **4**, complex **5** lose NO overtime and Mössbauer spectroscopy is required for determination of the amount of NO complex formed in this reaction. It is worth noting that even though both reactions used excess

amount of NO gas, complex **4** can only form mononitrosyl product. This is likely due to the immediate loss of NO upon nitrosylation at room temperature.

4.4 Appendix with Spectroscopic Data

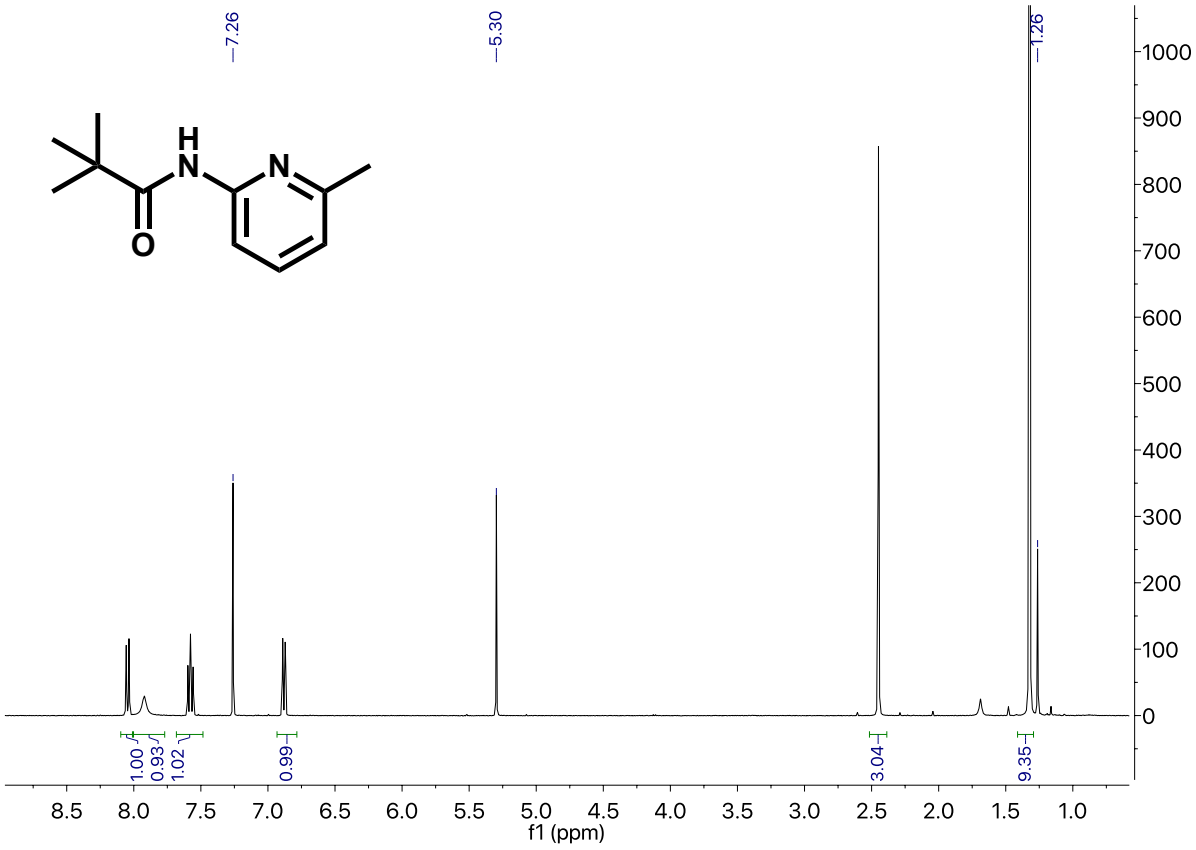

Figure 4.7 ^{1}H-NMR of *N*-(6-methylpyridin-2-yl)pivalamide in $CDCl_3$. The highlighted peak positions show ethyl acetate solvent residues (CH_2Cl_2 and hexane). The product overall is clean with correct integration of peaks.

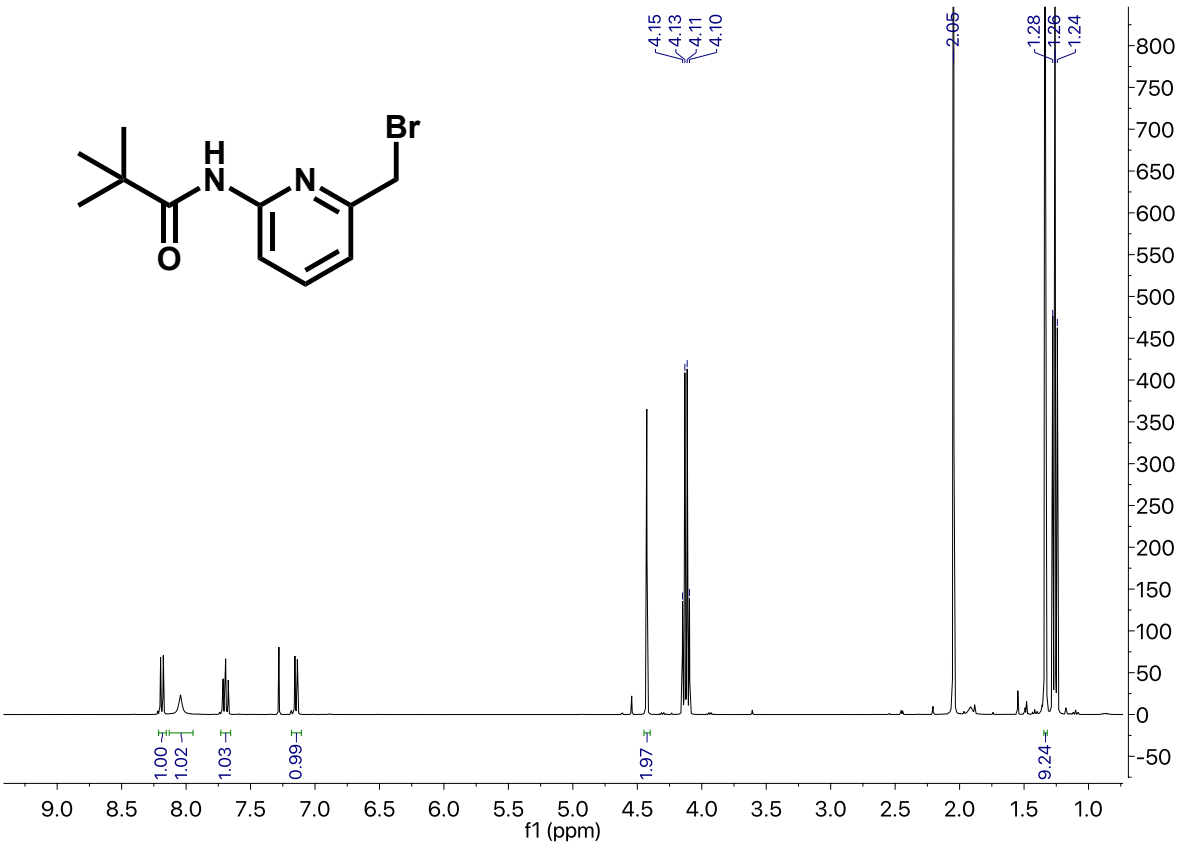

Figure 4.8 ^{1}H-NMR of mono-brominated product, *N*-(6-(bromomethyl)pyridin-2-yl)pivalamide, in $CDCl_3$. The highlighted peak positions show ethyl acetate solvent residues. The product overall is clean with correct integration of peaks.

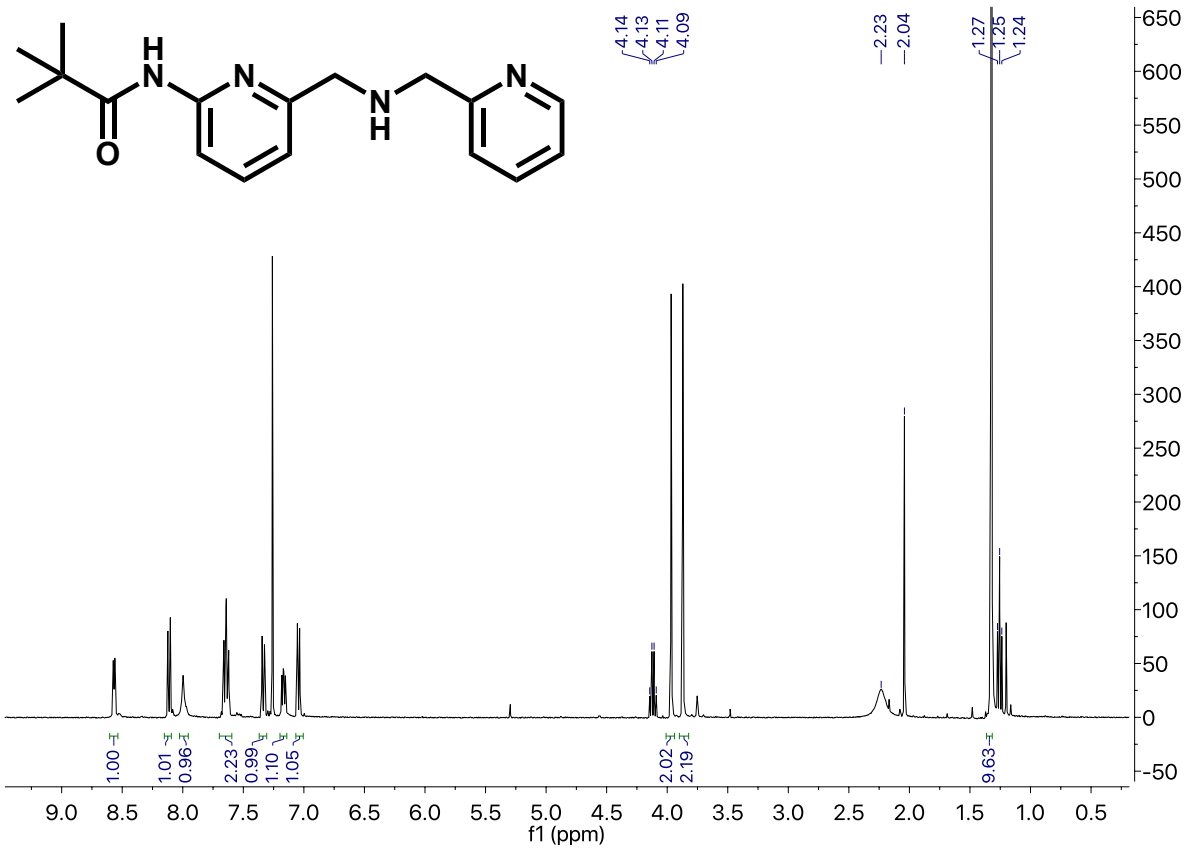

Figure 4.9 ^{1}H-NMR of N-(6-Pivaloylamido-2-pyridylmethyl)-N-(2-pyridylmethyl)amine in $CDCl_3$. The highlighted peak positions show ethyl acetate solvent residues. The product overall is clean with correct integration of peaks.

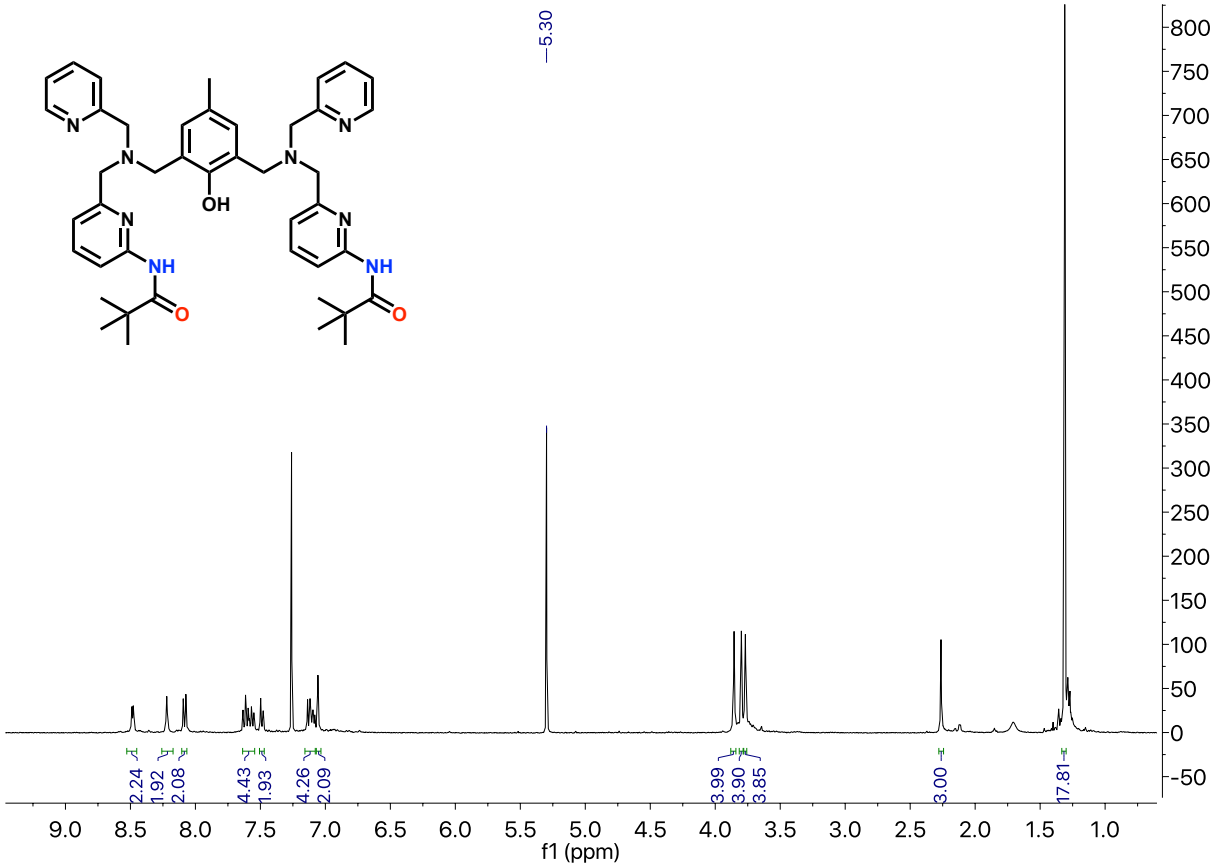

Figure 4.10 ^{1}H-NMR of N,N′-(6,6′-((((2-Hydroxy-5-methyl-1,3-phenylene)bis(methylene)bis((pyridin-2-ylmethyl)azanediyl))bis(methylene))bis(pyridine-6,2-diyl))bis(2,2-dimethylpropanamide) in $CDCl_3$. The highlighted peak positions show CH_2Cl_2 solvent residues. The product overall is clean with correct integration of peaks.

4.5 References

1. Silaghi-Dumitrescu, R.; Kurtz, D. M., Jr.; Ljungdahl, L. G.; Lanzilotta, W. N. X-ray Crystal Structures of *Moorella thermoacetica* FprA. Novel Diiron Site Structure and Mechanistic Insights into a Scavenging Nitric Oxide Reductase. *Biochemistry* **2005**, *44*, 6492-6501.
2. Biswas, S.; Kurtz, D. M.; Montoya, S. R.; Hendrich, M. P.; Bominaar, E. L. The Catalytic Role of a Conserved Tyrosine in Nitric Oxide-Reducing Non-heme Diiron Enzymes. *ACS Catal.* **2020**, *10*, 8177-8186.
3. White, C. J.; Speelman, A. L.; Kupper, C.; Demeshko, S.; Meyer, F.; Shanahan, J. P.; Alp, E. E.; Hu, M.; Zhao, J.; Lehnert, N. The Semireduced Mechanism for Nitric Oxide Reduction by Non-Heme Diiron Complexes: Modeling Flavodiiron Nitric Oxide Reductases. *J. Am. Chem. Soc.* **2018**, *140*, 2562-2574.
4. Comba, P.; Gahan, L. R.; Mereacre, V.; Hanson, G. R.; Powell, A. K.; Schenk, G.; Zajaczkowski-Fischer, M. Spectroscopic Characterization of the Active $Fe^{III}Fe^{III}$ and $Fe^{III}Fe^{II}$ Forms of a Purple Acid Phosphatase Model System. *Inorg. Chem.* **2012**, *51*, 12195-12209.

5. Bernhardt, P. V.; Bosch, S.; Comba, P.; Gahan, L. R.; Hanson, G. R.; Mereacre, V.; Noble, C. J.; Powell, A. K.; Schenk, G.; Wadepohl, H. An Approach to More Accurate Model Systems for Purple Acid Phosphatases (PAPs). *Inorg. Chem.* **2015**, *54*, 7249-7263.
6. Zheng, S.; Berto, T. C.; Dahl, E. W.; Hoffman, M. B.; Speelman, A. L.; Lehnert, N. The Functional Model Complex $[Fe_2(BPMP)(OPr)(NO)_2](BPh_4)_2$ Provides Insight into the Mechanism of Flavodiiron NO Reductases. *J. Am. Chem. Soc.* **2013**, *135*, 4902−4905.
7. Dong, H. T.; White, C. J.; Zhang, B.; Krebs, C.; Lehnert, N. Non-Heme Diiron Model Complexes Can Mediate Direct NO Reduction: Mechanistic Insight into Flavodiiron NO Reductases. *J. Am. Chem. Soc.* **2018**, *140*, 13429-13440.
8. Berto, T. C.; Hoffman, M. B.; Murata, Y.; Landenberger, K. B.; Alp, E. E.; Zhao, J.; Lehnert, N. Structural and Electronic Characterization of Non-Heme Fe(II)-Nitrosyls as Biomimetic Models of the Fe_B Center of Bacterial Nitric Oxide Reductase (NorBC). *J. Am. Chem. Soc.* **2011**, *133*, 16714–16717.
9. Jana, M.; White, C. J.; Pal, N.; Demeshko, S.; Meyer, F.; Lehnert, N.; Majumdar, A. Functional Models for the Mono- and Dinitrosyl Intermediates of FNORs: Semireduction versus Superreduction of NO. *J. Am. Chem. Soc.* **2020**, *142*, 6600-6616.
10. Jana, M.; Pal, N.; White, C. J.; Kupper, C.; Meyer, F.; Lehnert, N.; Majumdar, A. Functional Mononitrosyl Diiron(II) Complex Mediates the Reduction of NO to N_2O with Relevance for Flavodiiron NO Reductases. *J. Am. Chem. Soc.* **2017**, *140*, 14380-14383.
11. Dong, H. T.; Speelman, A. L.; Kozemchak, C. E.; Sil, D.; Krebs, C.; Lehnert, N. The $Fe_2(NO)_2$ Diamond Core: A Unique Structural Motif in Non-Heme Iron-NO Chemistry. *Angew. Chem. Int. Ed.* **2019**, *131*, 17859-17863.
12. Berto, T. C.; Speelman, A.; Zheng, S.; Lehnert, N. Mono- and Dinuclear Non-Heme Iron-Nitrosyl Complexes: Models for Key Intermediates in Bacterial Nitric Oxide Reductases. *Coord. Chem. Rev.* **2013**, *257*, 244-259.

Chapter 5

Non-heme Iron Trans-Hyponitrite Complexes

Acknowledgement: I would like to acknowledge Michael O. Lengel who assisted me with carrying out N_2O yield experiments, the IR spectroscopy labeling study, and the generation of the new N_2O calibration curve in this study. I would like to thank Dr. Debangsu Sil and Prof. Carsten Krebs for carrying out all the Mössbauer experiments and the corresponding data analysis. I would like to thank Prof. George B. Richter Addo for his detailed protocol for the synthesis of $Na_2{}^{15}N_2O_2$.

The goal of **Chapter 5** is to explore the biologically relevant coordination chemistry of hyponitrite with *non-heme* iron centers. In particular, I report the first structural characterization of a unique non-heme iron-hyponitrite complex, using the model $[Fe_2(BMPA\text{-}PhO)_2(OTf)_2]$ as the starting point. The results underline the plasticity and versatility of hyponitrite as a ligand, which can interact with metal centers both through its N- and O-atoms, with the potential to form a multitude of bridging structures. In addition, based on the Lewis-acidity of the iron center, different reactions are observed, as summarized in this chapter.

5.1 Reaction of $[Fe(TPA)(MeCN)_2](OTf)_2$ (1) with $Na_2N_2O_2$

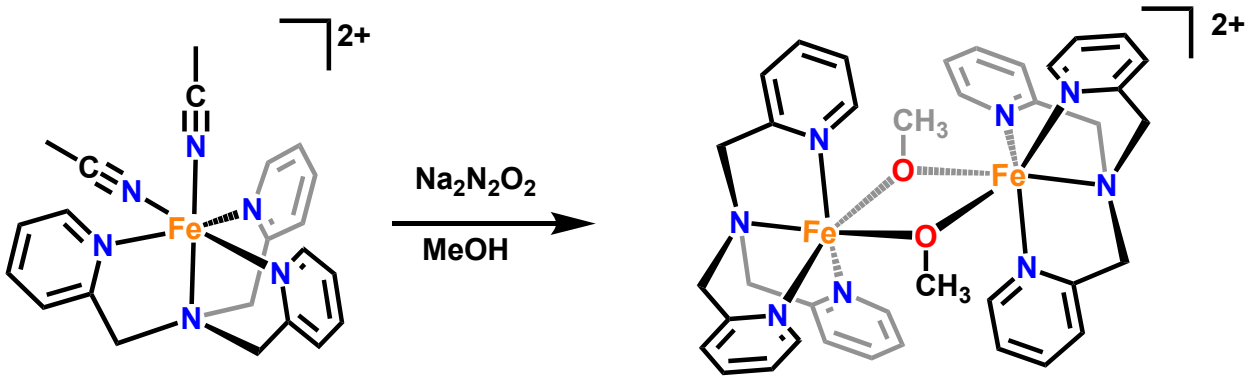

Scheme 5.1 Reaction Scheme of complex **1** with $Na_2N_2O_2$ in MeOH.

In order to explore the coordination chemistry of non-heme iron complexes and hyponitrite, I synthesized the ferrous complex $[Fe(TPA)(MeCN)_2](OTf)_2$ (**1**, TPA = tris(methylpyridyl)amine) using a reported procedure.[1] Complex **1** was then reacted with dried, commercially available sodium trans-hyponitrite ($Na_2N_2O_2$) in methanol (Scheme 5.1). The orange solution of complex **1** immediately changed color to red, accompanied by a distinct change in the UV-Vis spectrum. Here, the absorption band of **1** at 380 nm shifted to 413 nm upon the addition of $Na_2N_2O_2$ in methanol. The reaction was worked up according to a procedure described in the experimental section of this chapter. Single crystals suitable for X-ray diffraction were obtained by slow diffusion of ether into a saturated MeCN solution of the product at room temperature. X-ray crystallography revealed a dimeric complex, $[Fe_2(TPA)_2(OMe)_2](OTf)_2$ (**2**), with a Fe_2O_2 diamond core structure formed by the bridging methoxide ligands (Figure 5.1). I hypothesized that $Na_2N_2O_2$ reacted with methanol (either bound or unbound to complex **1**) to form N_2O, H_2O, and methoxide under this reaction condition. To determine whether complex **1** played a role in the formation of N_2O, I performed a control experiment to quantify the amount of N_2O formed in a methanol solution that only contains $Na_2N_2O_2$ and 15-crown-5. A yield of 60-75% of N_2O was obtained within 15 minutes. This result showed that a significant amount of $Na_2N_2O_2$ would have already

reacted with methanol to form N_2O even before this solution was added into a solution of complex **1** (Scheme 5.2).

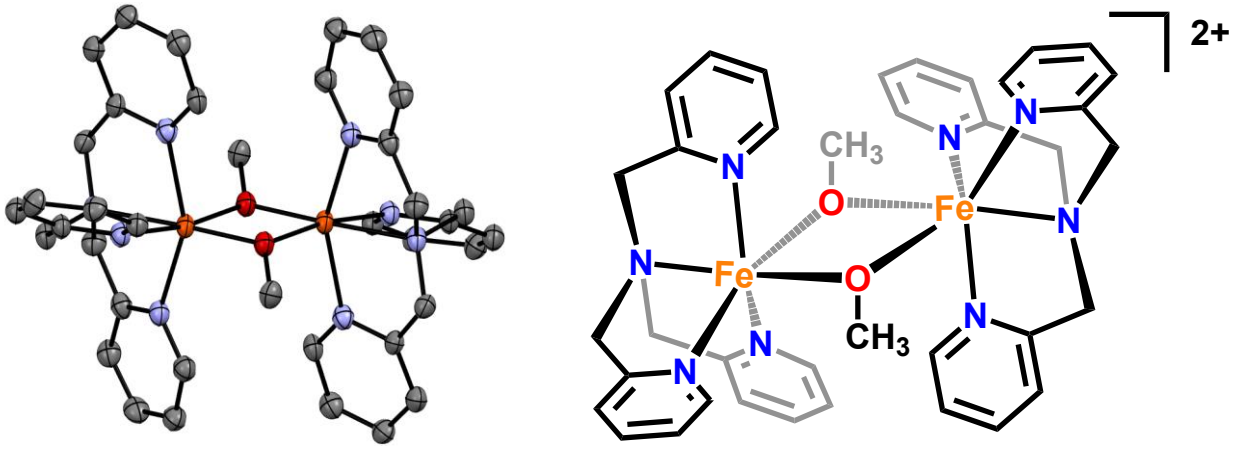

Figure 5.1 Left: Crystal structure of the complex **2** with ellipsoids drawn at 50% probability. The triflate counter anions, solvent molecules, and hydrogen atoms are omitted for clarity. Right: ChemDraw structure of complex **2**.

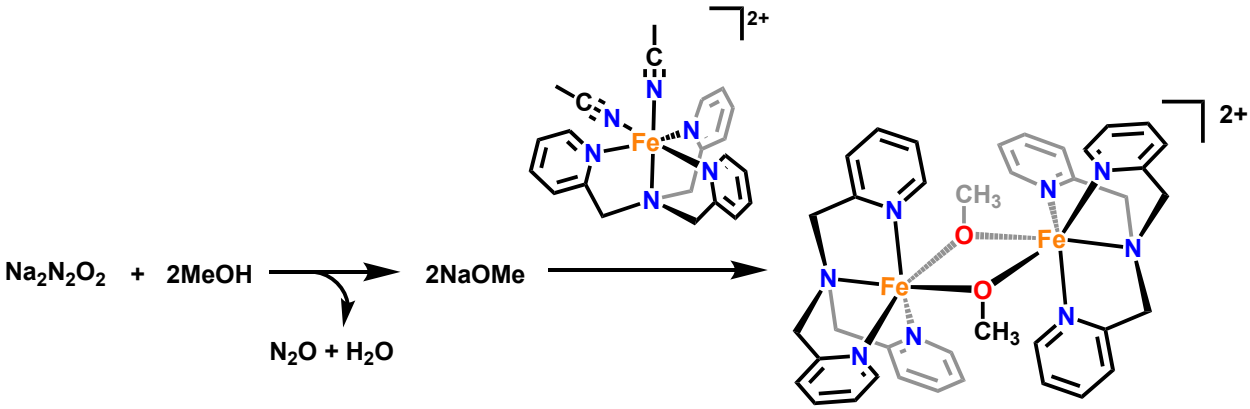

Scheme 5.2 Proposed formation of complex **2** due to decomposition of the $Na_2N_2O_2$ salt in methanol.

To overcome this problem, I changed the solvent of this reaction to acetonitrile (MeCN). Reaction of **1** with $Na_2N_2O_2$/15-crown-5 in MeCN gave a new product with a distinct UV-Vis absorption band at 445 nm. To my surprise, structural characterization and mass spectrometry revealed that this product corresponds to the previously reported complex $[Fe_2(TPA)_2(NO)_2](OTf)_2$ (**3**), which features the $Fe_2(NO)_2$ diamond core structure that is shown in **Chapter 6**. Here, two ls-Fe(II) centers are bridged by two singlet NO^- ligands.[2] I hypothesized

that in this case, hyponitrite indeed binds to two molecules of **1**. However, instead of forming a stable hyponitrite complex, the N=N bond is broken due to the strong Lewis acidity of the Fe(II) centers in **1**. This is surprising because by reducing the hs-{FeNO}^{7} complex, [Fe(TPA)(NO)(OTf)](OTf), to hs-{FeNO}^{8}, I can obtain the same complex **3** through dimerization the unstable hs-{FeNO}^{8} complex (Scheme 5.3).

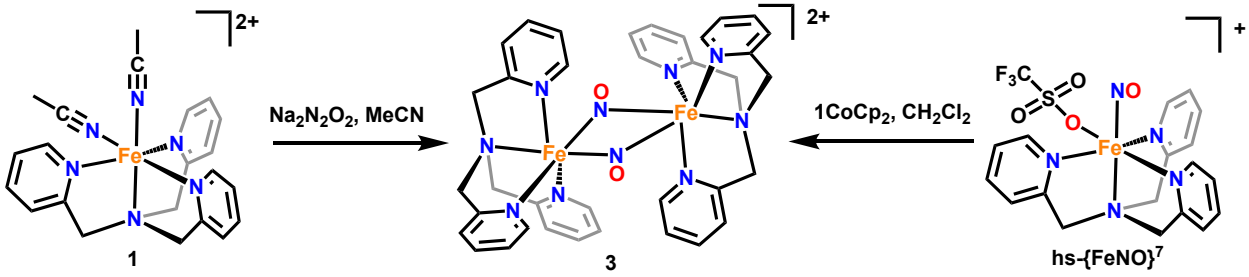

Scheme 5.3 Synthetic routes towards complex **3** using either a hs-{FeNO}^{7} or an Fe(II) precursor.

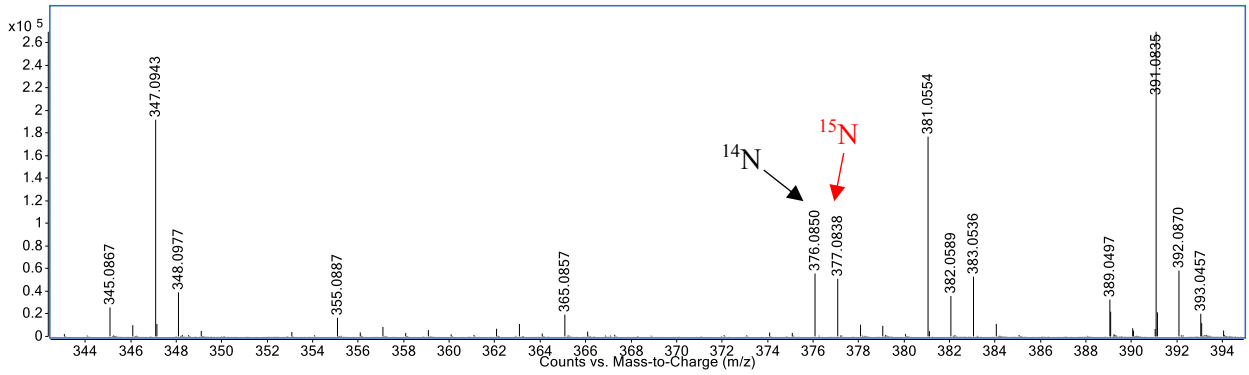

Figure 5.2 Mass spectrometry of the reaction between complex **1** and a mixture of 1:1 $Na_2N_2O_2$:$Na_2{}^{15}N_2O_2$ in MeCN showing formation of a clean 1:1 product ratio of exclusively ^{14}N and ^{15}N products. No isotope exchange was observed in mass spectrometry.

In order to determine the mechanism of this process, I reacted this complex with a 1:1 mixture of $Na_2N_2O_2$ and $Na_2{}^{15}N_2O_2$ in MeCN, with the idea that I could isolate the product and analyze it by IR spectroscopy. However, I discovered that 15-crown-5 has a significantly intense IR signal at ~1353 cm^{-1}, which is the region where the N–O stretch of **3** is located. Based on my previous study on complex **3**, I know that this mode has a relatively weak IR intensity. It is required that the sample has a high degree of purity in order to observe the N–O stretching band. Attempts

to purify 15-crown-5 out of the products obtained in these reactions were unsuccessful. I decided to carry out the reaction in neat condition (without 15-crown-5) at both room temperature and reflux condition. However, due to solubility problems, as well as the decomposition of $Na_2N_2O_2$ at high temperature, I could not obtain enough product for IR spectroscopic characterization. Nevertheless, I was able to obtain mass spectrometry data showing m/z signals at 376.085 for reactions with $Na_2N_2O_2$ and 377.084 when $Na_2{}^{15}N_2O_2$ is used (Figure 5.2). Assuming the molecule is not fragmented during mass spectrometry, I expect an m/z ~ 376.5 if the reaction formed an isotope exchanged product ([$Fe_2(^{14}NO)(^{15}NO)$] diamond core). Here, I propose two different scenarios that can lead to formation of the diamond core product. First, the diamond core of complex **3** can be formed directly through N=N bond scission of the hyponitrite ligand through a one-step mechanism (Scheme 5.4) that involves the formation of a $[Fe_2(N_2O_2)]^{2+}$ dimer. The thermodynamic stability of the diamond core structure (see Chapter 6) then drives the N=N bond cleavage and the formation of **3**. In this case, an isotope exchanged product is not expected. Second, the N=N bond scission could potentially form a transient monomeric hs-$\{FeNO\}^8$ intermediate, which is then rapidly dimerized in solution to form **3** through the mechanism proposed in Chapter 6. However, in this case, an isotope exchange product is expected (Scheme 5.4). Based on our data, I therefore propose that the formation of **3** follows the dimer mechanism that suppressed isotope scrambling.

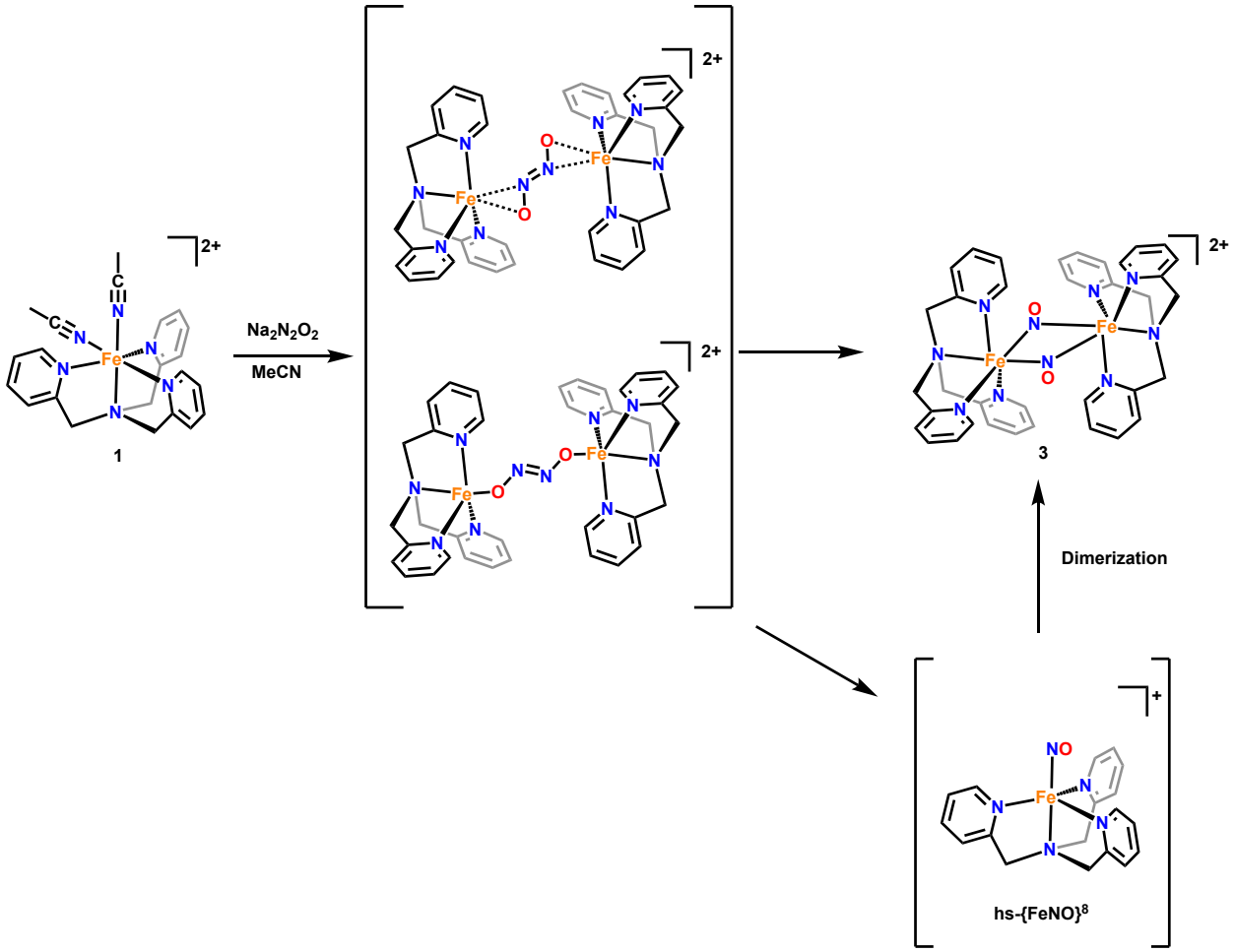

Scheme 5.4 Proposed binding modes of hyponitrite to complex **1** and possible mechanistic scenarios for this reaction to form the isolated complex **3**.

5.2 Synthesis and Characterization of $[Fe_2(BMPA\text{-}PhO)_2](OTf)_2$ (4)

The fact that complex **1** is highly Lewis-acidic is evident from the corresponding NO complex, [Fe(TPA)(OTf)(NO)](OTf), which has an N–O stretching frequency >1800 cm^{-1}. This value is at the upper end of N–O stretches observed for hs-$\{FeNO\}^7$ complexes.[2-4] Note that these complexes generally have Fe(III)-NO^- type electronic structures (see Chapter 1).[5] Here, the highly Lewis-acidic iron center receives strong electron donation from the $^3NO^-$ ligand, causing the high-energy N–O stretching mode. In order to tame the Lewis-acidity of $[Fe(TPA)(MeCN)_2](OTf)_2$, I replaced one of the neutral pyridine donors in TPA with a strongly donating, anionic phenolate

group. The corresponding ligand BMPA-PhOH (= N-(2-hydroxybenzyl)-N,N-bis(2-pyridylmethyl)amine) was synthesized using a reported procedure and characterized by ^{1}H-NMR spectroscopy.[6] Metallation of BMPA-PhOH was carried out using a procedure described in the experimental section of this chapter. The bright yellow complex **4** was characterized by a broad absorption band at 350 nm with a broad shoulder at around 400 nm. Single crystals suitable for X-ray diffraction were grown by slow diffusion of diethyl ether into a saturated solution of **4** in acetonitrile at room temperature, yielding yellow rods. The crystal structure revealed that complex **4** is a dimer with the two iron centers being bridged by the O-atoms of the phenolate arms of the BMPA-PhO^{-} coligands, forming a Fe_2O_2 diamond core (see Figure 5.3). The Fe–O distances in the core are 2.01 and 2.04 Å for the short bonds and 2.15 and 2.16 Å for the longer bonds. Therefore, this core is quite asymmetric. The two iron centers are in pseudo-octahedral coordination environments with the sixth ligand being the triflate counter anion. They are separated by 3.26 Å. This is comparable to FNORs, indicating that complex **4** is a good structural model for the active sites of these enzymes.

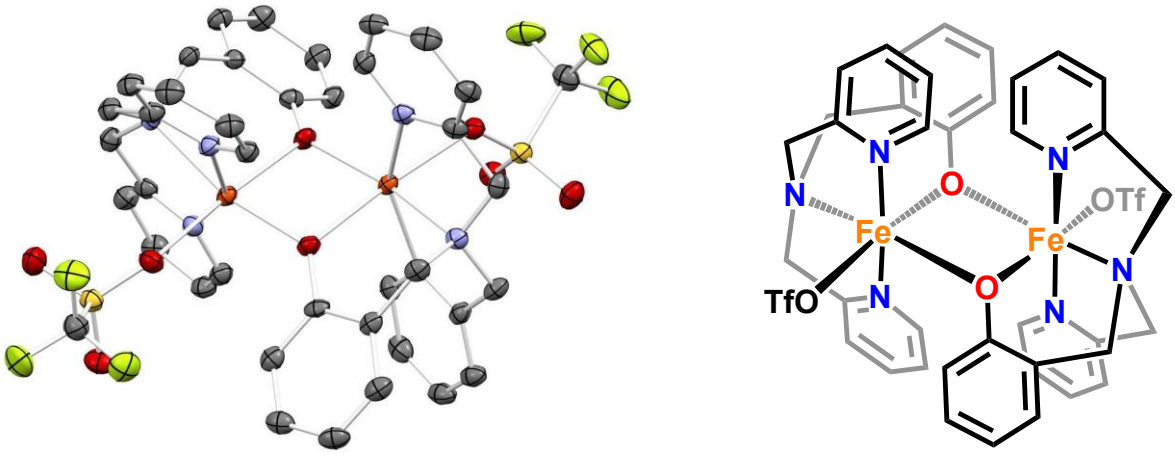

Figure 5.3 Left: Crystal structure of complex **4** with ellipsoids drawn at 50% probability. The triflate counter anion, solvent molecules, and hydrogen atoms are omitted for clarity. Right: ChemDraw structure of complex **4**.

5.3 Characterization of the hyponitrite complex [{Fe_2(BMPA-PhO)$_2$}$_2$(μ-N_2O_2)](OTf)$_2$ (5)

Reaction of complex **4** with $Na_2N_2O_2$/15-crown-5 in MeCN at 25 ^oC overnight led to a color change of the solution from orange to deep red. The solution was then filtered and recrystallization with diethyl ether yielding pure orange plates suitable for X-ray crystallography. The crystal structure revealed a unique dimerization of two molecules of **4** to form a tetra-iron complex, [{Fe_2(BMPA-PhO)$_2$}$_2$(μ-N_2O_2)](OTf)$_2$ (**5**), with the hyponitrite ion bridging the two diiron cores as shown in Figure 5.4. Interestingly, the hyponitrite ion is bound to all four iron centers in the tetramer by both of its N- and O-atoms, which represents a truly unique binding mode that has not been observed before. In this binding mode, each diiron unit is bound to an O- and an N-atom of hyponitrite (Scheme 5.5). The average N–N bond distance (due to disorder in the crystal) of hyponitrite is 1.27 Å, which represents an N–N double bond. This is similar to the N=N bond distance in $Na_2N_2O_2$ (1.26 Å). The average N–O bond distance of the hyponitrite ligand in **5** is 1.35 Å, again comparable to $Na_2N_2O_2$ (1.36 Å). The same is true for the N–N–O bond angle (**5**: 113^o; $Na_2N_2O_2$: 112^o). Hence, despite the coordination of hyponitrite to four iron centers in the tetramer, the ligand does not seem to be activated. This supports the mechanistic conclusions where it was proposed that protonation is necessary in order to activate the bound hyponitrite ligand in FNORs for N_2O generation.[7] Finally, the average Fe–N and Fe–O distances are 2.27 and 2.02 Å, respectively, which indicates that the Fe–O bond is distinctively stronger than the Fe–N bond. Based on this observation, I conclude that hyponitrite prefers O-coordination over N-coordination to non-heme iron centers. This supports the mechanistic proposal for FNORs that N–N bond formation, which leads to the generation of a bridging, N-bound hyponitrite ligand, is immediately followed by hyponitrite rearrangement from N- to O-coordination.[7,8] The Mössbauer

spectrum of complex **5** confirmed the presence of hs-Fe(II) centers. Moreover, the Mössbauer spectrum of a solution of **5** in CH_3CN is unaltered compared to the solid state, which indicates that the tetrameric structure of the complex remains intact in solution. Complex **5** is EPR silent, due to antiferromagnetic coupling of the iron centers within the two phenolate-bridged diiron cores. Previous studies have shown that hyponitrite does not mediate magnetic exchange coupling,[9] and hence, I propose that the two diiron cores in **5** are magnetically isolated.

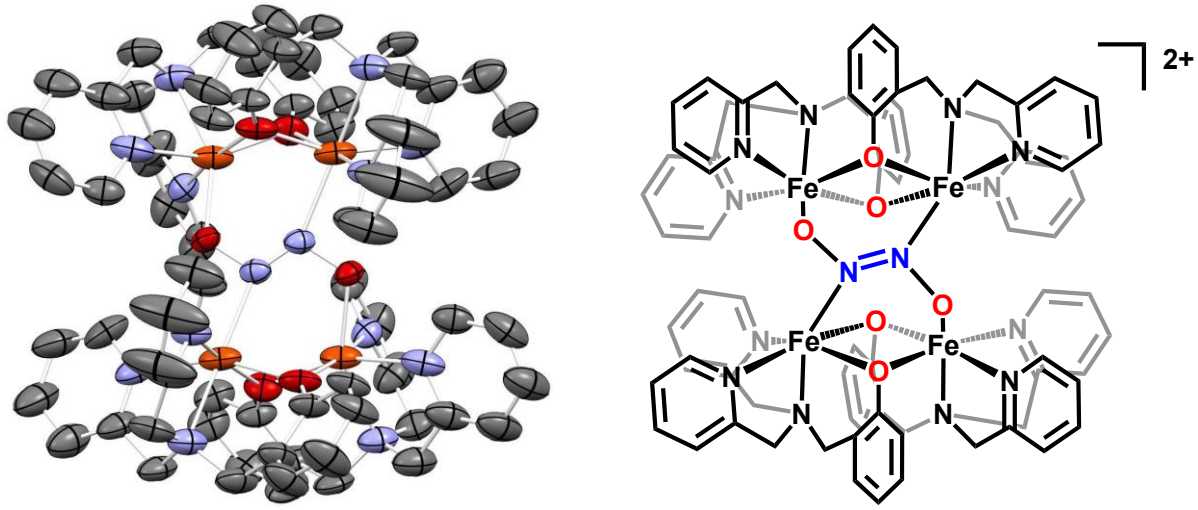

Figure 5.4 Crystal structure of complex **5** with ellipsoids drawn at 50% probability. The triflate counter anion, solvent molecules, and hydrogen atoms are omitted for clarity.

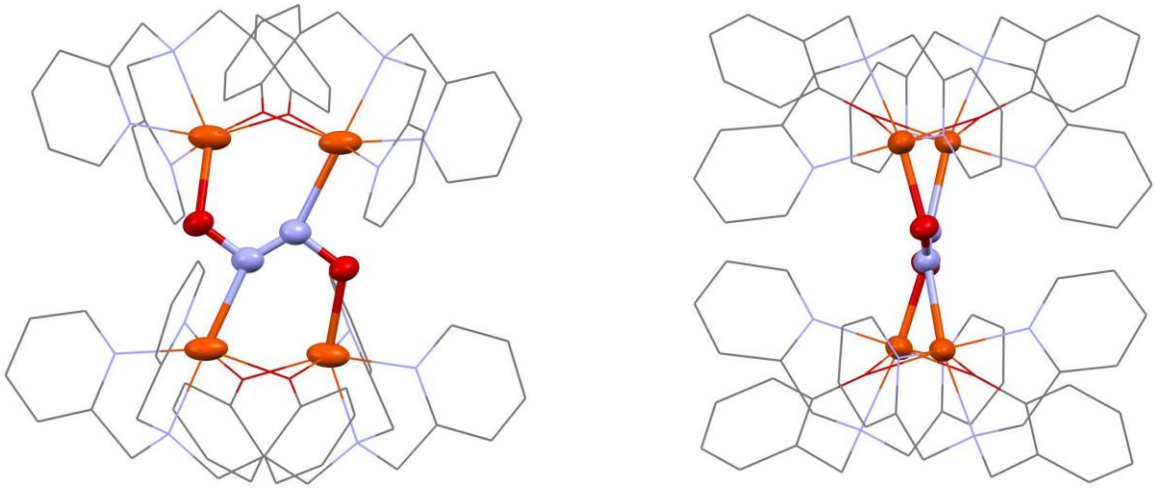

Scheme 5.5 Schematic representation of the crystal structure of **5**, emphasizing the bridging hyponitrite binding mode.

5.4 Reactivity with of $[Fe_2(BMPA\text{-}(^tBu)_2PhO)_2](OTf)_2$ (6)

Due to the lack of steric protection around the iron centers, the cluster $[\{Fe_2(BMPA\text{-}PhO)_2\}_2(\mu\text{-}N_2O_2)](OTf)_2$ is formed. I hypothesized that introduction of sterically protecting groups, such as tert-butyl groups, in the SCS of the complex could prevent the formation of cluster **5** and potentially force the hyponitrite ligand to bind with the end-on binding mode (Figure 5.5, right). This binding mode has previously been observed in the reported heme system by Richter-Addo and co-workers (Figure 5.5, left).[10]

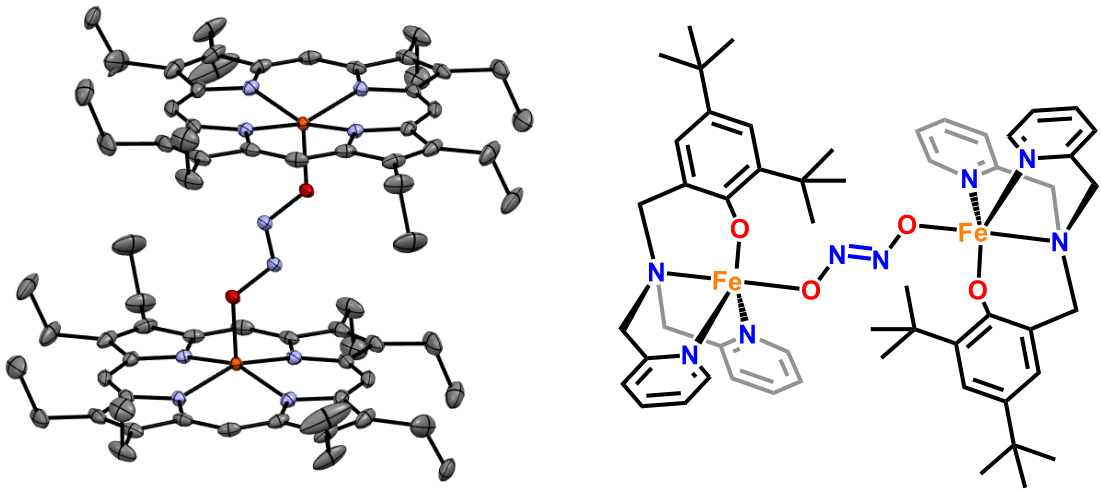

Figure 5.5 Left: crystal structure of the only heme complex reported in the literature so far that binds trans-hyponitrite.[10] Right: Proposed structure of the hyponitrite complex that potentially formed when reacting complex **6** with $Na_2N_2O_2$ salt.

$[Fe_2(BMPA\text{-}(^tBu)_2PhO)_2](OTf)_2$ (**6**) was synthesized according to the procedure mentioned in the experimental section. The newly synthesized complex **6** is pale green, however, it turns green overtime even in the inert environment of the glovebox making it extremely hard to work with. Therefore, I synthesized **6** freshly every time before data collection. Reaction of complex **6** with $Na_2N_2O_2$ in acetonitrile immediately caused a color change of the solution from pale green to dark purple. I then performed gas headspace analysis to see if N_2O was formed after the reaction. The result showed that there was no N_2O (~8%) formation observed via gas headspace detection

at 15 minutes and 24 hours. This implies that potentially the formation of a new hyponitrite complex took place, or that this complex undergoes the same N=N bond scission observed with complex **1**. Further experiments and analysis are required to determine the fate of this complex after reacting with $Na_2N_2O_2$.

5.5 Conclusion

In summary, the work described in this chapter provides key insight into the properties of hyponitrite complexes of non-heme iron centers. First, I show that the Lewis acidity of the Fe(II) center, which is easily gauged by the N–O stretching frequency of the corresponding hs-$\{FeNO\}^7$ complex, is a key feature that determines the stability of a hyponitrite complex. To my surprise, too Lewis-acidic iron centers actually cleave hyponitrite into two NO^- units, followed by further reactions. In the case of the Fe(TPA) unit, formation of a unique $Fe_2(NO)_2$ structure was observed. I propose two possible mechanistic pathways that this reaction can undergo to form the diamond core product, one of which involves the cleaving of the N=N bond to form hs-$\{FeNO\}^8$ transient intermediates. These hs-$\{FeNO\}^8$ complexes then decompose to form complex **3** as observed in a previous study (see Chapter 6). The other pathway is the direct N=N bond cleavage to form the diamond core product from a $[Fe_2(N_2O_2)]^{2+}$ dimeric intermediate, without the formation of the hs-$\{FeNO\}^8$ intermediate. Mass spectrometry data indicates that the latter pathway is operative, as no $^{14}NO/^{15}NO$ isotope scrambling was observed when a mixture of $Na_2(^{14}N_2O_2)/Na_2(^{15}N_2O_2)$ is used in the reaction. Taming the iron center to make it less Lewis-acidic allowed for the isolation of a unique, tetrameric hyponitrite complex, where hyponitrite bridges between two dimeric Fe_2(BMPA-PhO)$_2$ units. This complex was structurally characterized, and the result shows that hyponitrite has a strong preference to bind to the non-heme iron centers via its O atoms, which

supports mechanistic proposals for FNORs that after hyponitrite formation, the ligand would quickly rotate from an N- to an O-coordination mode. Treatment of this complex with acid then leads to the formation of N_2O.

5.6 Experimental Section

Red blocks of complex **2** were grown from an acetonitrile/diethyl ether solution of the compound at 25 ºC. A crystal of dimensions 0.10 x 0.08 x 0.06 mm was mounted on a Rigaku AFC10K Saturn 944+ CCD-based X-ray diffractometer equipped with a low temperature device and a Micromax-007HF Cu-target micro-focus rotating anode (λ = 1.54187 Å), operated at 1.2 kW power (40 kV, 30 mA). The X-ray intensities were measured at 85(1) K with the detector placed at a distance of 42.00 mm from the crystal. A total of 2028 images were collected with an oscillation width of 1.0° in w. The exposure times were 1 sec. for the low angle images, 5 sec. for high angle. Rigaku d*trek images were exported to CrysAlisPro for processing and corrected for absorption. The integration of the data yielded a total of 32,060 reflections to a maximum 2q value of 139.60° of which 4008 were independent and 3579 were greater than 2s(I). The final cell constants were based on the xyz centroids of 10,100 reflections above 10s(I). Analysis of the data showed negligible decay during data collection. The structure was solved and refined with the Bruker SHELXTL (version 2016/6) software package, using the space group P2(1)/n with Z = 2 for the formula $C_{40}H_{42}N_8O_8F_6S_2Fe_2$. All non-hydrogen atoms were refined anisotropically with the hydrogen atoms placed in idealized positions. Full matrix least-squares refinement based on F2 converged at R1 = 0.0598 and wR2 = 0.1635 [based on I > 2sigma(I)], R1 = 0.0662 and wR2 = 0.1760 for all data.

Yellow needles of complex **4** were grown from an acetonitrile/diethyl ether solution of the compound at 25 ºC. A crystal of dimensions 0.16 x 0.11 x 0.09 mm was mounted on a Rigaku AFC10K Saturn 944+ CCD-based X-ray diffractometer equipped with a low temperature device and a Micromax-007HF Cu-target micro-focus rotating anode (λ = 1.54187 Å), operated at 1.2 kW power (40 kV, 30 mA). The X-ray intensities were measured at 85(1) K with the detector placed at a distance of 42.00 mm from the crystal. A total of 2028 images were collected with an oscillation width of 1.0° in w. The exposure times were 1 sec. for the low angle images, 5 sec. for high angle. Rigaku d*trek images were exported to CrysAlisPro for processing and corrected for absorption. The integration of the data yielded a total of 63,339 reflections to a maximum 2q value of 139.11° of which 7873 were independent and 7043 were greater than 2s(I). The final cell constants were based on the xyz centroids of 22,120 reflections above 10s(I). Analysis of the data showed negligible decay during data collection. The structure was solved and refined with the Bruker SHELXTL (version 2016/6) software package, using the space group P2(1)/n with Z = 4 for the formula $C_{40}H_{36}N_6O_8F_6S_2Fe_2$. All non-hydrogen atoms were refined anisotropically with the hydrogen atoms placed in idealized positions. Full matrix least-squares refinement based on F2 converged at R1 = 0.0658 and wR2 = 0.1701 [based on I > 2sigma(I)], R1 = 0.0713 and wR2 = 0.1825 for all data.

Orange plates of complex **5** were grown from a diethyl ether/acetonitrile solution of the compound at -33 ºC. A crystal of dimensions 0.17 x 0.10 x 0.04 mm was mounted on a Rigaku AFC10K Saturn 944+ CCD-based X-ray diffractometer equipped with a low temperature device and a Micromax-007HF Cu-target micro-focus rotating anode (λ = 1.54187 Å), operated at 1.2 kW power (40 kV, 30 mA). The X-ray intensities were measured at 85(1) K with the detector placed at a distance of 42.00 mm from the crystal. A total of 2028 images were collected with an

oscillation width of 1.0° in w. The exposure times were 1 sec. for the low angle images, 10 sec. for high angle. Rigaku d*trek images were exported to CrysAlisPro for processing and corrected for absorption. The integration of the data yielded a total of 83,013 reflections to a maximum 2q value of 138.89° of which 10,090 were independent and 8361 were greater than 2s(I). The final cell constants were based on the xyz centroids of 20,341 reflections above 10s(I). Analysis of the data showed negligible decay during data collection. The structure was solved and refined with the Bruker SHELXTL (version 2018/3) software package, using the space group Fdd2 with Z = 8 for the formula $C_{78}H_{72}N_{14}O_{12}F_6S_2Fe_4$. The structure was refined as a two-component inversion twin. All non-hydrogen atoms were refined anisotropically with the hydrogen atoms placed in idealized positions. Full matrix least-squares refinement based on F2 converged at R1 = 0.0461 and wR2 = 0.1277 [based on I > 2sigma(I)], R1 = 0.0571 and wR2 = 0.1393 for all data. The SQUEEZE subroutine of the PLATON program suite was used to address the disordered solvent in the large cavity present in the structure.

Sodium amalgam preparation

On the benchtop, sodium metal was cut and washed with hexanes before being brought into a glove box. In the glove box, 1.05 grams of sodium metal was added piece by piece to 6 mL of mercury metal which caused an exothermic reaction to happen. After dissolving, the round bottom flask was allowed to sit in a cold well at ice water temperature for 10 minutes. It should be noted that the morphology of the sodium amalgam varied from batch to batch and could be either solid or liquid depending on the batches.

$Na_2{}^{15}N_2O_2$ Trans-hyponitrite Synthesis

Outside the box, 1 gram of $Na^{15}NO_2$ was dissolved 6 mL of deionized water and sparged with a constant stream of N_2 to remove traces of dioxygen before being brought into the glove box.

33 mL of absolute ethanol was sparged with N_2 and brought into the glove box. To the freshly prepared sodium amalgam above, the $Na^{15}NO$ solution was added dropwise. A white cloudy solution formed. Once added, the solution was stirred at room temperature for 30 minutes. The solution was, then, transferred to a 20 mL vial and the aqueous solution was extracted and added to the round bottom flask containing ethanol. A stir bar was added, and the solution was allowed to stir for 2 hours. During this time, a small amount of white powder had formed. The solution was then removed from the glove box and allowed to sit in a -20°C freezer overnight. The product was then filtered and collected on a frit. Yield varied significantly. Average yield below 10%.

Synthesis of Metal Complexes:

$[Fe_2(TPA)_2(OCH_3)_2](OTf)_2$ (2): Under an inert atmosphere, 100 mg of $[Fe(TPA)(CH_3CN)_2](OTf)_2$ was dissolved in a minimal amount of methanol in a 20 ml scintillation vial charged with a stirbar. An excess amount of $Na_2N_2O_2$ was then added to the solution. The reaction was allowed to stir overnight and the solvent was removed under reduced pressure. The crude solid was then redissolved in CH_2Cl_2 and the solution was filtered to remove salt impurity. The filtrate was then concentrated down under vacuum and the solid was redissolved into MeCN. Single crystal suitable for X-ray diffraction is obtained via slow diffusion of ether into acetonitrile at 25^{o}C. A direct synthesis of this complex can be achieved by reacting $[Fe(TPA)(CH_3CN)_2](OTf)_2$ with KOMe directly in methanol. Methanol was then removed under reduced pressure and the resulting crude solid was redissolved into CH_2Cl_2. The mixture was then filtered and the solution was layered with hexane. The solution was allowed to recrystallize at -33 ^{o}C overnight yielding crystalline product that was then collected and dried. Characterization: UV-Vis: 413 nm. Attempts to obtain a good elemental analysis is unsuccessful so far. The complex is paramagnetic based on ^{1}H-NMR due to the weak coupling of the high-spin iron centers.

$[Fe_2(TPA)_2(NO)_2](OTf)_2$ (3): Under an inert atmosphere, 100 mg of complex **1** was dissolved in a minimal amount of MeCN in a 20 ml scintillation vial charged with a stirbar. An excess $Na_2N_2O_2$ was then added to the solution along with 15-crown-5. The reaction was allowed to stir overnight to yield a dark red solution. The resulting solution was then filtered and recrystallize with ether at -33°C multiple times until a minimal amount of 15-crown-5 contamination was left. The resulting solid was collected and characterized. A detailed characterization of this complex is provided in Chapter 6.

$[Fe_2(BMPA\text{-}PhO)_2](OTf)_2$ (4): Under inert atmosphere, 566 mg (1.85 mmol) BMPA-PhOH and 129 mg (1.84 mmol) potassium methoxide were combined in 5 mL MeOH. The resulting suspension was stirred for several minutes, and 599 mg (1.69 mmol) $Fe(OTf)_2$ was then added. The reaction was stirred for 45 min, then filtered. Diethyl ether was added to the filtrate, causing a yellow solid to precipitate. The product was allowed to precipitate at -33°C overnight. The yellow solid was isolated by vacuum filtration and recrystallized from CH_2Cl_2/hexanes. Yield: 593 mg, 63%. Elemental analysis: Expected: C: 47.17, H: 3.56, N: 8.25; Found: C: 47.03, H: 3.75, N: 8.13. UV-Vis: 350 and 400 nm.

$[\{Fe_2(BMPA\text{-}PhO)_2\}_2(\mu\text{-}N_2O_2)](OTf)_2$ (3): Under inert atmosphere, $[Fe_2(BMPA\text{-}PhO)_2](OTf)_2$ was dissolved in a minimal amount of MeCN in a 20 ml scintillation vial charged with a stirbar. An excess amount of $Na_2N_2O_2$ was then added with 15-crown-5 and the reaction was allowed to stir overnight. The solution was filtered and the resulting solution was recrystallized by slow diffusion with ether at -33°C to obtain single crystals that are suitable for X-ray diffraction. UV-Vis: 446 nm. We were unable to obtain a sufficient amount of complex for elemental analysis.

$[Fe_2(BMPA\text{-}tBu_2PhO)_2](OTf)_2$: In the glovebox, 629 mg (1.50 mmol) BMPA-tBu_2PhOH was dissolved in methanol with 104 mg (1.48 mmol) of KOMe and stirred for 5 minutes. 487 mg (1.38 mmol) of $Fe(OTf)_2$ was then added resulting in an immediate color change to a deep yellow/green color. The reaction was allowed to stir for 5 hours. The solvent was then removed under reduced pressure. Minimal amount of tetrahydrofuran (THF) was added to dissolve and the solution was passed through a syringe filter. The filtrate was then precipitated with hexanes in the glovebox freezer at -33°C overnight. A pale green solid product was collected after filtration through a frit. Yield 550 mg, 59%. We were unable to obtain elemental analysis of this complex due to its high instability even in the inert environment of the glove box.

IR Gas Headspace Analysis for N_2O Detection With New Calibration Curve:

N_2O quantification was carried out by gas headspace analysis using infrared spectroscopy. The general protocol for gas headspace analysis is described in the following: to a sealed 25 ml round-bottom flask containing 7 μmol of complex $[Fe(TPA)(MeCN)_2](OTf)_2$ and 7 μmol of $Na_2N_2O_2$, 2.5 ml of MeCN with excess 15-crown-5 (2 time excess with respect to $Na_2N_2O_2$) was syringed into the sealed round-bottom flask. The reaction was allowed to stir for 15 minutes before the gas headspace was transferred by vacuum into a sealed gas IR cell with CaF_2 windows. Quantification of N_2O was performed via integration of the prominent IR features at 2235 and 2212 cm^{-1} of this molecule (N-N stretching vibration) against separately determined N_2O standards, which were generated from the breakdown of Piloty's acid in basic solution under exactly the same conditions. The advantage of using Piloty's acid to construct the calibration curve is that this compound is a solid that can be weighted out at high accuracy. Hence, exact amounts of N_2O can be generated in this way. The disadvantage is that Piloty's acid has to be used in an aqueous environment, which is different from the organic solvents used for the reaction of

[Fe(TPA)(MeCN)$_2$](OTf)$_2$ with NO gas. However, the error generated due to the somewhat different solubility of N_2O in water and organic media (at the concentrations used for the experiments) is well within the ± 10% error note above.

N_2O Calibration Curve General Procedure. The calibration curve was generated using two different stock solutions. All solutions prepared outside the glovebox were sparged with N_2 and brought into the glovebox.

Data points for < 5 µmol N_2O. A stock solution of about 0.1 M NaOH was prepared by dissolving 0.4042 g of NaOH pellets in 100 mL of DI water. In a glovebox, a 0.0234 M stock solution of Piloty's acid (PA) was prepared by dissolving 0.0810 g of PA in 20.0 mL of DI water.

Data points for > 5 µmol N_2O. A stock solution of about 0.1 M NaOH was prepared by dissolving 0.2495 g of NaOH pellets in 62.5 mL of DI water. In a glovebox, a 0.0464 M stock solution of PA was prepared by dissolving 0.084 g of PA in 10.0 mL of DI water.

General procedure. To a 25 mL round bottom flask, 0.1 mL of PA stock solution and 0.4 mL of DI water were added. The flask was capped with a septum and copper wire. To this flask, 2 mL of NaOH stock solution was injected. After about 3 hours, the gas headspace was collected for 20 seconds using a gas IR cell. The N_2O yield was obtained by integrating the absorbance spectrum from 2150-2275 cm^{-1}. Each data point was obtained in triplicate.*

Table 5.1 Data point for the calibration curve (0.6-5 µmol)

µmol N_2O Expected	0.0234 M PA solution	Degassed H_2O	NaOH solution	Area Obtained
0.5846	0.05 mL	0.45 mL	2.0 mL	0.2763
0.5846	0.05 mL	0.45 mL	2.0 mL	0.2980

0.5846	0.05 mL	0.45 mL	2.0 mL	0.2738
1.169	0.10 mL	0.40 mL	2.0 mL	0.6230
1.169	0.10 mL	0.40 mL	2.0 mL	0.7601
1.169	0.10 mL	0.40 mL	2.0 mL	0.8337
2.3385	0.20 mL	0.30 mL	2.0 mL	1.460
2.3385	0.20 mL	0.30 mL	2.0 mL	1.330
2.3385	0.20 mL	0.30 mL	2.0 mL	1.512
3.5077	0.30 mL	0.20 mL	2.0 mL	1.998
3.5077	0.30 mL	0.20 mL	2.0 mL	2.087
3.5077	0.30 mL	0.20 mL	2.0 mL	1.776
4.6769	0.40 mL	0.10 mL	2.0 mL	2.995
4.6769	0.40 mL	0.10 mL	2.0 mL	2.804
4.6769	0.40 mL	0.10 mL	2.0 mL	2.887

Table 5.2 Data point for the calibration curve (7-9.2 μmol)

μmol N_2O Expected	0.0464 M PA solution	Degassed H_2O	NaOH solution	Area Obtained
6.9635	0.30 mL	0.20 mL	2.0 mL	4.38357
6.9635	0.30 mL	0.20 mL	2.0 mL	4.18873
9.2846	0.40 mL	0.10 mL	2.0 mL	5.61328
9.2846	0.40 mL	0.10 mL	2.0 mL	6.29651
9.2846	0.40 mL	0.10 mL	2.0 mL	5.84426

* Only two points were used for the 6.9635 μmol point due to an outlier

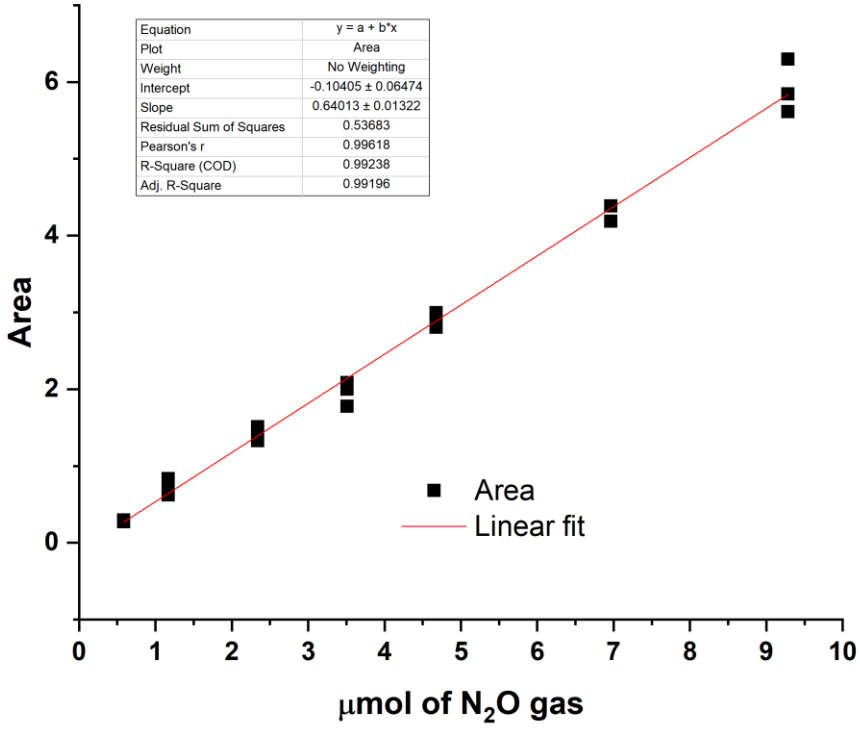

Figure 5.6 New calibration curve generated using method mentioned above

[Fe(TPA)(CH$_3$CN)$_2$](OTf)$_2$ + hyponitrite: N$_2$O yields in methanol

General Procedure (7 μmol N$_2$O Expected)

In a glovebox, 0.0090 g of [Fe(TPA)(CH$_3$CN)$_2$](OTf)$_2$ and 0.0016 g of Na$_2$N$_2$O$_2$ were added to a 25 mL round bottom flask charged with a stirbar. The flask was then sealed with a septum and copper wire. A solution containing 11.2 μL of 15-crown-5 in 2.50 mL of methanol was injected into the flask. The reaction was allowed to stir for 3 hours and the gas headspace was evacuated for 20 seconds into a gas cell. The details for the analysis have been previously described. The results were obtained in duplicate for this reaction yield more than 100% N$_2$O indicating side reaction of excess Na$_2$N$_2$O$_2$ decomposition in methanol.

5.7 References

1. McArthur, S.; Baird, M. C. Oxyfunctionalization of polystyrene by hydrogen peroxide using non-heme iron catalysts. *Eur. Polym. J.* **2014**, *55*, 170-178.
2. Dong, H. T.; Speelman, A. L.; Kozemchak, C. E.; Sil, D.; Krebs, C.; Lehnert, N. The $Fe_2(NO)_2$ Diamond Core: A Unique Structural Motif in Non-Heme Iron-NO Chemistry. *Angew. Chem. Int. Ed.* **2019**, *131*, 17859-17863.
3. Berto, T. C.; Hoffman, M. B.; Murata, Y.; Landenberger, K. B.; Alp, E. E.; Zhao, J.; Lehnert, N. Structural and Electronic Characterization of Non-Heme Fe(II)-Nitrosyls as Biomimetic Models of the Fe_B Center of Bacterial Nitric Oxide Reductase (NorBC). *J. Am. Chem. Soc.* **2011**, *133*, 16714–16717.
4. Berto, T. C.; Speelman, A.; Zheng, S.; Lehnert, N. Mono- and Dinuclear Non-Heme Iron-Nitrosyl Complexes: Models for Key Intermediates in Bacterial Nitric Oxide Reductases. *Coord. Chem. Rev.* **2013**, *257*, 244-259.
5. Brown, C. A.; Pavlosky, M. A.; Westre, T. E.; Zhang, Y.; Hedman, B.; Hodgson, K. O.; Solomon, E. I. Spectroscopic and Theoretical Description of the Electronic Structure of S = 3/2 Iron-Nitrosyl Complexes and Their Relation to O_2 Activation by Non-Heme Iron Enzyme Active Sites *J. Am. Chem. Soc.* **1995**, *117*, 715-732.
6. Mayilmurugan, R.; Visvaganesan, K.; Suresh, E.; Palaniandavar, M. Iron(III) Complexes of Tripodal Monophenolate Ligands as Models for Non-Heme Catechol Dioxygenase Enzymes: Correlation of Dioxygenase Activity with Ligand Stereoelectronic Properties. *Inorg. Chem.* **2009**, *48*, 8771-8783.
7. Biswas, S.; Kurtz, D. M.; Montoya, S. R.; Hendrich, M. P.; Bominaar, E. L. The Catalytic Role of a Conserved Tyrosine in Nitric Oxide-Reducing Non-heme Diiron Enzymes. *ACS Catal.* **2020**, *10*, 8177-8186.
8. Van Stappen, C.; Lehnert, N. Mechanism of N-N Bond Formation by Transition Metal-Nitrosyl Complexes: Modeling Flavodiiron Nitric Oxide Reductases. *Inorg. Chem.* **2018**, *57*, 4252-4269.
9. Berto, T. C.; Xu, N.; Lee, S. R.; McNeil, A. J.; Alp, E. E.; Zhao, J.; Richter-Addo, G. B.; Lehnert, N. Characterization of the Bridged Hyponitrite Complex $\{[Fe(OEP)]_2(m\text{-}N_2O_2)\}$: Reactivity of Hyponitrite Complexes and Biological Relevance. *Inorg. Chem.* **2014**, *53*, 6398-6414.
10. Xu, N.; Abucayon, E. G.; Powell, D. R.; Richter-Addo, G. B. A bridged di-iron porphyrin hyponitrite complex as a model for biological N_2O production from hyponitrite. *Nitric Oxide* **2016**, *52*, 16-20.

Chapter 6

The $Fe_2(NO)_2$ Diamond Core: A Unique Structural Motif in Non-Heme Iron-NO Chemistry

Adapted from published article: Dong, H. T.; Speelman, A. L.; Kozemchak, C.; Sil, D.; Krebs, C.*; Lehnert, N.* "The $Fe_2(NO)_2$ Diamond Core: A Unique Structural Motif In Non-Heme Iron-NO Chemistry", *Angew. Chem. Int. Ed.* **2019**, 58, 17695-17699.

Acknowledgement: I would like to acknowledge Dr. Amy L. Speelman and Claire E. Kozemchak for their initial characterizations on the project. I would like to thank Dr. Debangsu Sil and Prof. Carsten Krebs at the Pennsylvania State University who performed all the Mössbauer experiments and the corresponding data analysis. I would like to thank Dr. Jiyong Zhao, Dr. Esen E. Alp, and Dr. Michael Y. Hu who have assisted me during the process of collecting NRVS data at the Argonne National Laboratory.

The coordination chemistry of non-heme iron centers with nitroxyl is not well developed. Recent studies on model complexes for flavodiiron NO reductases (FNORs) have demonstrated that stable high-spin (hs) diferrous dinitrosyl complexes, [hs-$\{FeNO\}^7$]$_2$, can be activated by reduction to the hs-$\{FeNO\}^8$, or Fe(II)-nitroxyl, state for N_2O formation.[1,2] FNORs are important enzymes in bacterial pathogenesis, as they protect infectious microbes from the mammalian immune defense agent NO.[3] Whereas few mononuclear non-heme iron-NO model complexes have been shown to generate N_2O upon reduction to the hs-$\{FeNO\}^8$ state,[4] the main reactivity of these complexes seems to be disproportionation, leading to the formation of dinitrosyl iron complexes (DNICs):[5,6]

$$2\ \text{hs-}\{FeNO\}^7 + 2e^- \rightarrow 2\ \text{hs-}\{FeNO\}^8 \rightarrow \{Fe(NO)_2\}^{10} + Fe(II) \quad (1)$$

However, the mechanism of this disproportionation, which constitutes an elegant pathway for the generation of DNICs from simple non-heme iron centers, is unknown. Clearly, more work is necessary to elucidate the biologically-relevant reactivity of non-heme hs-$\{FeNO\}^8$ complexes. DNICs of $\{Fe(NO)_2\}^{9/10}$ type are important in mammalian physiology, as they serve as a major pool of NO.[7,8] In addition, DNICs with histidine ligation have been proposed to form at the non-heme diiron core of the ferric uptake regulation protein (Fur),[9] in serum albumin,[10] and in ferritin.[11] In this regard, understanding the reactivity of hs-$\{FeNO\}^8$ complexes provides important insight into how diiron sites can be predispositioned for the diverging functions of N_2O or DNIC formation. However, the unstable nature of non-heme hs-$\{FeNO\}^8$ complexes has so far prevented the isolation of any intermediates prior to DNIC formation.[12]

I further investigated the reactivity of hs-$\{FeNO\}^8$ complexes with TPA (tris(pyridylmethyl)amine) and related coligands. In particular, I serendipitously discovered a $Fe_2(NO)_2$ diamond core structure, which is unprecedented in non-heme iron-NO chemistry.[13] This core structure is stabilized by a change in spin state of the iron centers to low-spin (ls) Fe(II). In contrast, a TPA derivative with a weaker ligand field that cannot support the spin-state change to ls proceeds to DNIC formation. These complexes were further characterized by X-ray crystallography, and Mössbauer and vibrational spectroscopy.

6.1 Synthesis and Characterization of [Fe(TPA)(NO)(OTf)](OTf) (1)

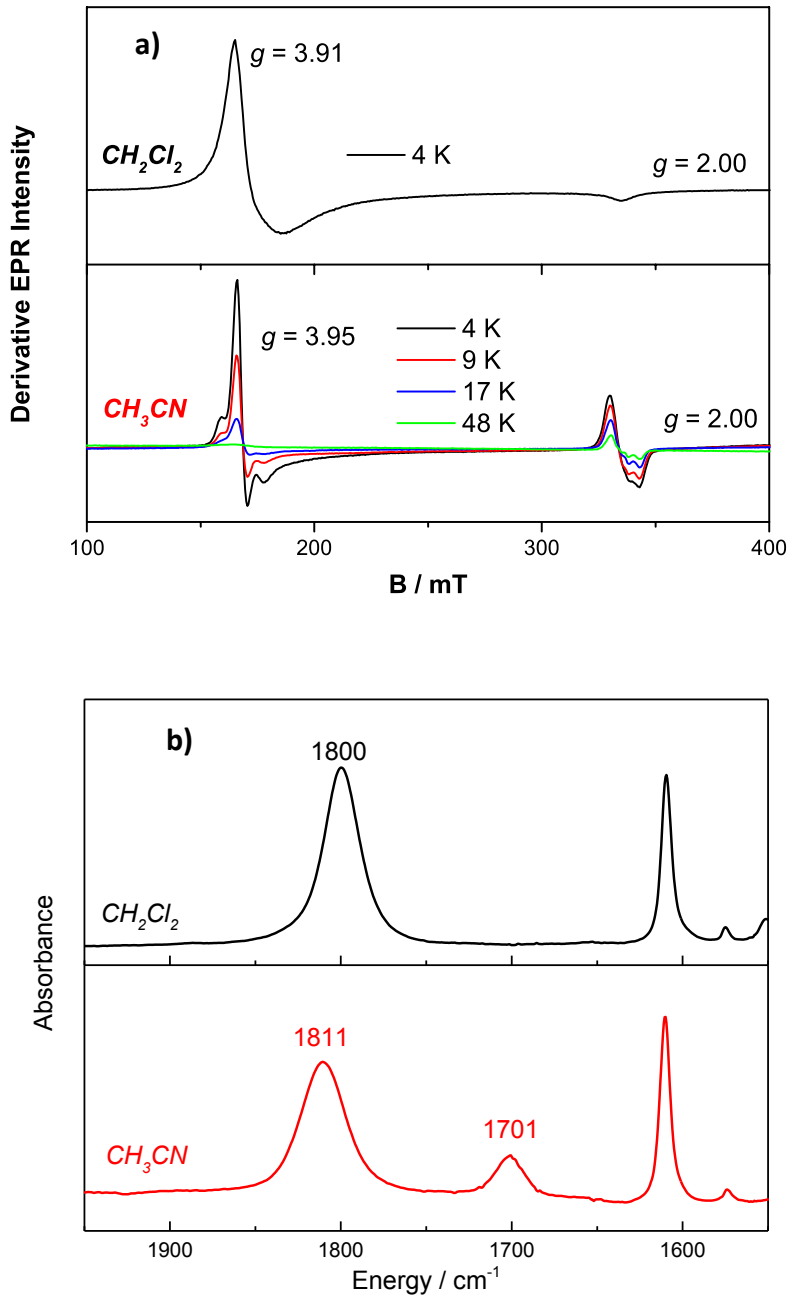

Figure 6.1. Panel a) EPR spectrum of **1** in CH_2Cl_2 at 4 K showing 100% of the hs-{FeNO}^{7} complex with S_t = 3/2 (top) vs. the EPR spectrum of **1** in CH_3CN at various temperatures, where a noticable portion of the compound is converted to a ls-{FeNO}^{7} complex with S_t = 1/2. **Panel b)** Solution IR spectrum of **1** in CH_2Cl_2 at room temperature, showing the N-O stretch at 1800 cm^{-1}, which belongs to the hs-{FeNO}^{7} complex (top) vs. the solution IR spectrum of **1** in CH_3CN at room temperature, showing conversion of a fraction of **1** to a ls complex with the N-O stretch at 1701 cm^{-1}.

The ligand TPA was synthesized according to reported procedures, and characterized by ^{1}H-NMR spectroscopy.[14] Metallation of TPA was carried out using $Fe(OTf)_2$•$2CH_3CN$ in CH_3CN to obtain a pure red solid of $[Fe(TPA)(CH_3CN)_2](OTf)_2$. Synthesis of [Fe(TPA)(NO)(OTf)](OTf) (**1**) was accomplished by reacting the red solution of $[Fe(TPA)(CH_3CN)_2](OTf)_2$ in CH_3CN with excess NO gas, which led to an immediate color change to black. Complex **1** was isolated as a pure black solid upon crystallization. The formation of **1** is evident from UV-Vis spectroscopy, which shows the disappearance of the intense bands at 320 and 380 nm of the ferrous precursor, and the appearance of new bands at 326, 403, 490 and 655 nm upon reaction with NO. The solid state IR spectrum of complex **1** shows the characteristic N-O stretching band of a hs-$\{FeNO\}^7$ complex at 1806 cm^{-1}, which shifts to 1766 cm^{-1} with ^{15}NO and 1732 cm^{-1} with $^{15}N^{18}O$ (Figure 6.2, right). The cyclic voltammogram of **1** is unusual, and shows two irreversible redox events at -690 mV and -1240 mV versus Fc^+/Fc, respectively. The first event corresponds to the one-electron reduction of complex **1**, forming an unstable hs-$\{FeNO\}^8$ complex, **1red**. This wave remains irreversible, even when the scan is stopped prior to the second redox event. The second redox event likely originates from a new species formed from **1red**. EPR spectra of **1** in CH_2Cl_2 show an axial signal at g_{eff} = 3.91 and 2.00, characteristic of a non-heme hs-$\{FeNO\}^7$ complex with S_t = 3/2 (Figure 6.1a, top). Surprisingly, the EPR spectrum of **1** in CH_3CN shows a new EPR signal at g = 2, indicating the partial formation of a ls-$\{FeNO\}^7$ complex with S_t = 1/2 in this solvent (Figure 6.1a, bottom). This observation is supported by the appearance of a new signal at 1701 cm^{-1} in the solution IR spectrum of **1** in CH_3CN (Figure 6.1b, bottom). In this regard it should be noted that ferrous TPA complexes are close to the spin crossover point as previously reported.[15] In our case, the coordination of the solvent CH_3CN is likely responsible for the spin change behavior, according to the equilibrium:

$$[Fe(TPA)(NO)(OTf)]^{+} + CH_3CN <==> [Fe(TPA)(NO)(CH_3CN)]^{2+} + OTf^{-} \quad (2)$$

where the CH_3CN-coordinated compound is then ls. To test this hypothesis further, I prepared the analogous hs-{FeNO}^{7} complex with the weakly-coordinating tetrafluoroborate (BF_4^-) counter ion, **1-BF$_4$**. In the solid state, this complex shows the N-O stretch at 1795 cm^{-1}. In CH_3CN solution, the EPR spectrum of **1-BF$_4$** now shows the major signal at g = 2.00, indicating dominant formation of the ls (S_t = 1/2) complex [Fe(TPA)(NO)(CH_3CN)])(BF_4)$_2$. In the solution IR spectrum of **1-BF$_4$** in CH_3CN, the N-O stretch is observed at 1701 cm^{-1}, identical to complex **1** in CH_3CN, indicating that the same ls species forms. These observations strongly support our hypothesis that CH_3CN-coordination is the cause for the spin state change in complex **1**. This conclusion is further support by density functional theory (DFT) calculations (B3LYP*/TZVP), which show that the hs state of complex **1** is 3 kcal/mol lower in energy in comparison to the ls state. Upon replacing the bound triflate in **1** with a CH_3CN solvent molecule, the hs and ls states become isoenergetic, with the ls state at slightly lower energy (0.34 kcal/mol). Spin density analysis shows that the ls complex (with CH_3CN bound) has a Fe(II)-NO• type electronic structure, typically observed for six-coordinate ferrous heme-nitrosyls.[16]

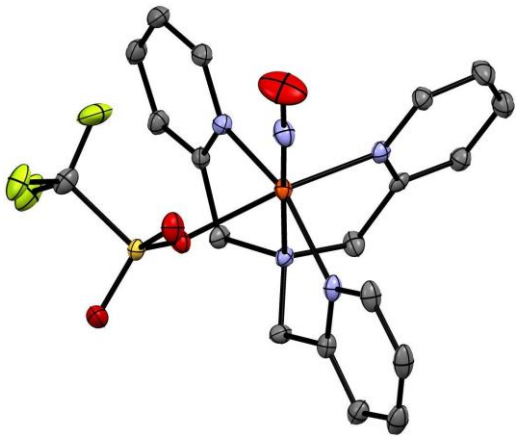

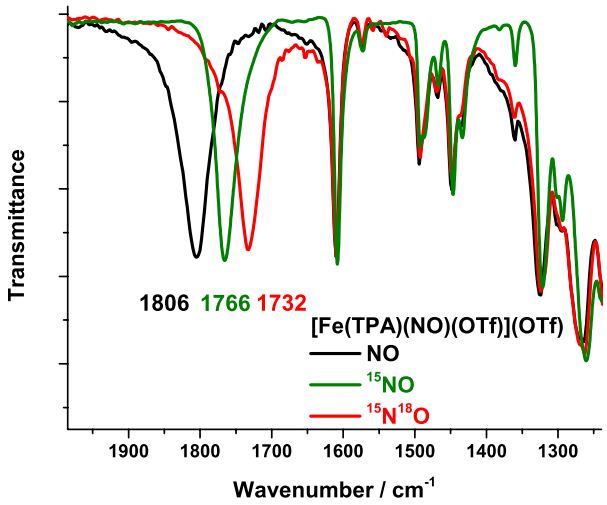

Figure 6.2 Left: Crystal structure of complex **1** with ellipsoids drawn at 50% probability. The triflate counter anion, solvent molecules, and hydrogen atoms are omitted for clarity. Right: IR spectra of complex **1** with isotopic labeled NO gas.

Crystals suitable for X-ray diffraction were obtained via diffusion of diethyl ether into a saturated solution of **1** in acetonitrile (Figure 6.2, left). As has been observed previously for other non-heme hs-$\{FeNO\}^7$ complexes, **1** exhibits a pseudo-octahedral geometry with a triflate counter ion bound in the sixth coordination site. Complex **1** shows Fe-NO and N-O bond lengths of 1.76 and 1.14 Å, respectively. Interestingly, the Fe-N-O angle is 170°, which is surprising, considering that there is not much steric hindrance present in the TPA ligand scaffold. Similar linear Fe-N-O angles have been observed in other hs-$\{FeNO\}^7$ complexes with ν(N-O) > 1800 cm^{-1}.[17] This indicates that the linear Fe-N-O angle in **1** originates from electronic factors, i.e. a very covalent Fe-NO bond due to an electron-poor Fe center.[17,18]

6.2 Serendipitous Discovery of the Two Conformers of Complex 1 Using Nuclear Resonance Vibrational Spectroscopy (NRVS)

To further investigate the exact electronic structure of **1** I performed NRVS at the Advanced Photon Source at Argonne National Lab. This technique is very useful for investigating the vibrational properties of iron complexes, due to its sensitivity to all vibrations involving the ^{57}Fe center. I decided to characterize complex **1** further using this technique to hopefully investigate its unique electronic structure. In a previous study by Berto et al using the analogous complex with the perchlorate counterion, [Fe(TPA)(NO)$(ClO_4)_2$, a mixture of NO complexes was observed with the major peak located around 495 cm^{-1}.[19] Therefore, I expected to see a peak around this frequency for **1**, with only a change in counter anion to triflate. Interestingly, upon collecting NRVS spectra of the first sample I brought to the beamline, I observed the Fe-NO stretch at 533 cm^{-1} (Figure 6.3). This is surprisingly higher than that of [Fe(TPA)(NO)$(ClO_4)_2$, which led us to

believe that this sample might have decomposed. A duplicate was also brought to the beamline as a backup sample, and surprisingly, in this case the Fe-NO stretch is observed at the usual position, 495 cm^{-1} (Figure 6.3). It is important to note that both samples were checked with IR spectroscopy, before packing the NRVS sample holders, and both show the same N-O stretch of 1806 cm^{-1}. Intrigued by this observation, I hypothesize that maybe I had accidentally prepared two different isomers of the same hs-$\{FeNO\}^7$ complex (Figure 6.4). These two isomers are indistinguishable by any other techniques except for NRVS. To further investigate this possibility, I performed DFT calculation to see if I can predict this difference in the Fe-NO stretch by just changing the trans ligand to the NO molecule in the complex. The DFT calculations were able to replicate the experimental data with a excellent agreement. Specifically, while these two isomers essentially have the same N-O stretching frequency in the calculations (1882(h) vs 1890(v) cm^{-1} for B3LYP/TZVP or 1779(h) vs 1789(v) cm^{-1} for BP86/TZVP), but the Fe-NO stretching frequencies are drastically different. As shown in Figure 6.3, the vertical isomer with the NO ligand being trans to the tertiary amine has a higher Fe-NO stretch than the horizontal isomer with the NO ligand being trans to a pyridyl nitrogen. There is a 27 cm^{-1} difference in the stretching frequency in the DFT calculations, which is an underestimate compared to the experimental difference of 41 cm^{-1}. Interestingly, there is no other product observed after reduction of multiple batches of [Fe(TPA)-(NO)(OTf)](OTf), which consistently produce the same product (see below). Therefore, there is no observable difference in reactivity between these two isomers. Overall, this result demonstrates the power of NRVS, which is very sensitive towards the coordination environment around the ^{57}Fe center.

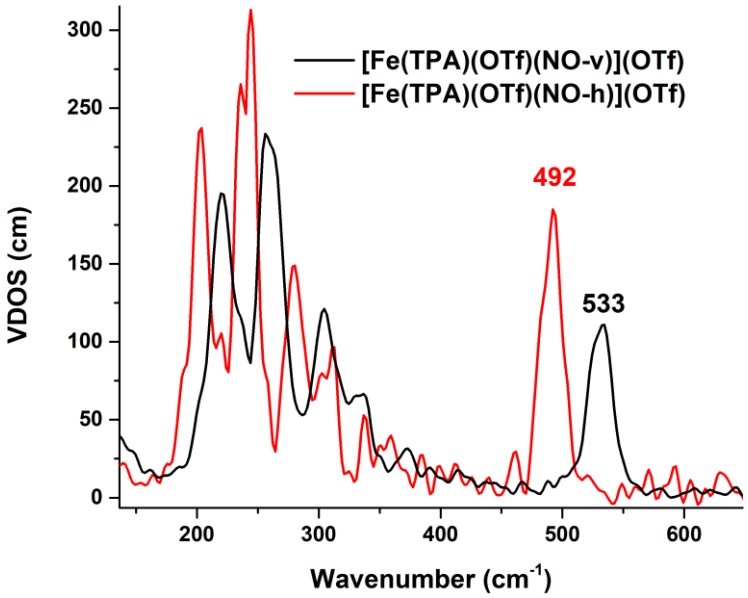

Figure 6.3 NRVS data of the two forms of complex **1** in the solid state.

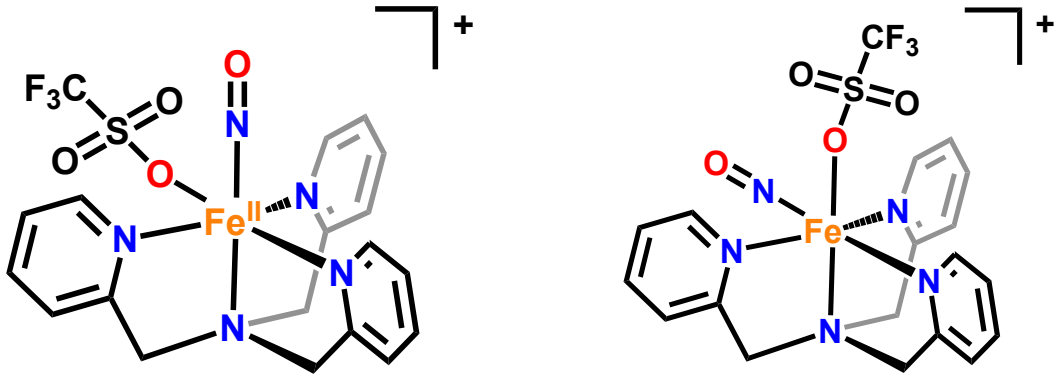

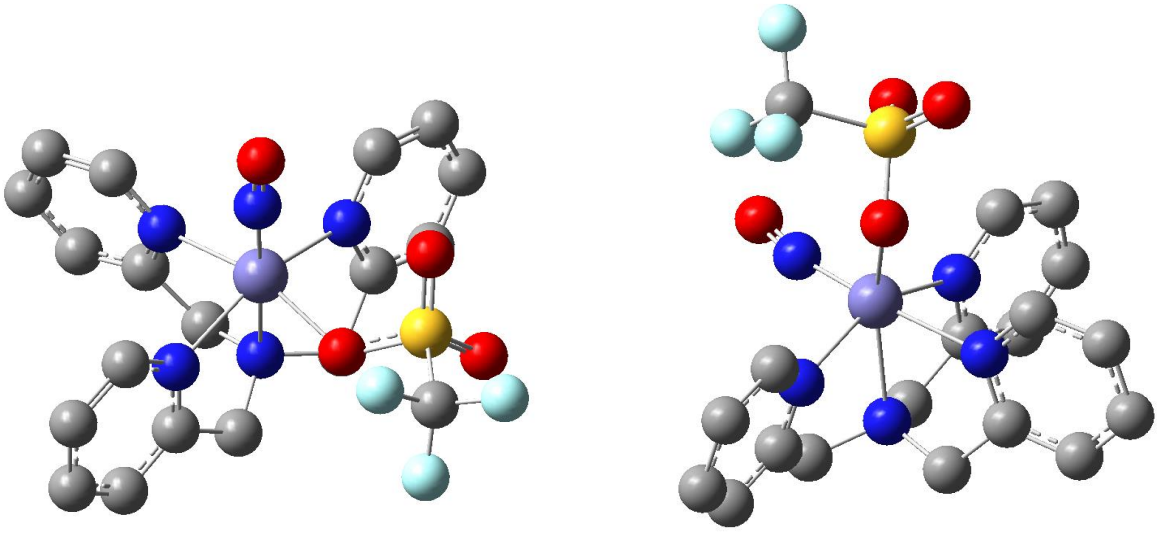

Figure 6.4 ChemDraw of the two forms of complex **1** and their DFT optimized structures.

6.3 DNIC Formation after Reduction of [Fe(BMPA-tBu$_2$PhO)(NO)(OTf)]

As a control, I prepared an analogous complex with a ligand that provides a weaker ligand field (according to the spectrochemical series), to test whether formation of complex **2** is dependent on the ligand field strength. Previous studies have shown fast DNIC formation from our hs-{FeNO}^{8} model complex, [Fe(TMG$_2$dien)(NO)]$^+$.[12] Similar reactivity is observed for our new hs-{FeNO}^{7} complex [Fe(BMPA-tBu$_2$PhO)(NO)(OTf)] (**3**), which contains the weak field ligand [N-(3,5-di-tert-butyl-2-hydroxybenzyl)-N,N-di-(2-pyridylmethyl)]amine (BMPA-tBu$_2$PhOH). Here, metallation of BMPA-tBu$_2$PhOH was carried out using KOMe and Fe(OTf)$_2$•2CH$_3$CN in MeOH to obtain a pure yellow solid of [Fe(BMPA-tBu$_2$PhO)(OTf)] after purification. Nitrosylation of this yellow solid in THF using dried NO gas resulted in the formation of pure complex **3**. Complex **3** shows an EPR spectrum with an axial signal at g_{eff} = 3.91 and 2.00, characteristic of a non-heme hs-{FeNO}^{7} complex with S_t = 3/2 regardless of the solvents (Figure 6.5).

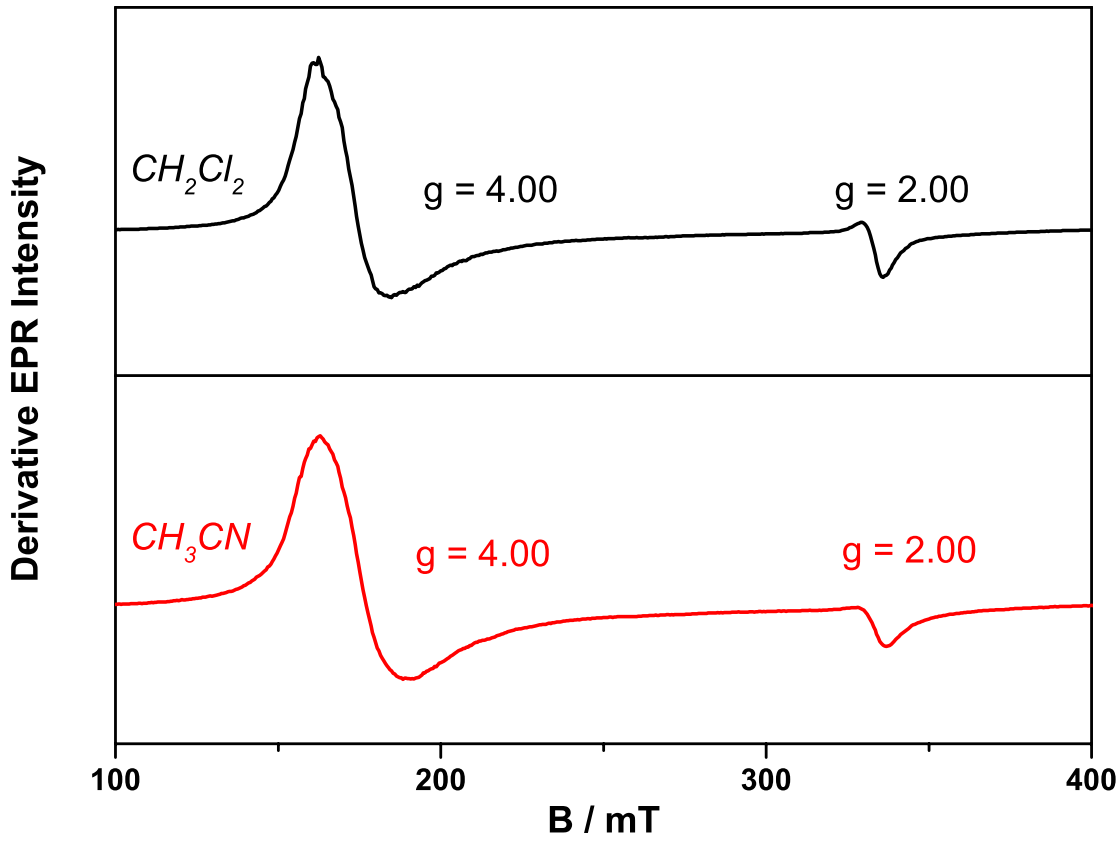

Figure 6.5 EPR spectrum of **3** at 4 K in CH_2Cl_2 (top) and CH_3CN (bottom), showing 100% of the hs-{FeNO}^{7} complex with $S_t = 3/2$.

The solid state IR spectrum of **3** shows a typical υ(N-O) = 1752 cm^{-1}. Crystals suitable for X-ray diffraction were obtained via diffusion of pentane into a tetrahydrofuran solution of **3**. The structure (shown in Figure 6.6, left) exhibits Fe-NO and N-O bond lengths of 1.78 and 1.10 Å, respectively, and an Fe-N-O angle of 163°. The cyclic voltammogram of **3** shows an irreversible signal at -1.07 V vs. Fc^+/Fc (Figure S12), thus allowing us to use $CoCp_2$ to reduce **3** to the hs-{FeNO}^{8} product, **3red**. Upon reduction with 1 eq. of $CoCp_2$, the N-O stretch at 1752 cm^{-1} of **3** immediately disappears, and two new features appear at 1632 and 1692 cm^{-1}, which are typical for

{Fe(NO)$_2$}^{10} DNICs (Figure 6.6, right).[12] However, just as in the previous studies, no intermediate of the process (following eqn. 1) can be observed.

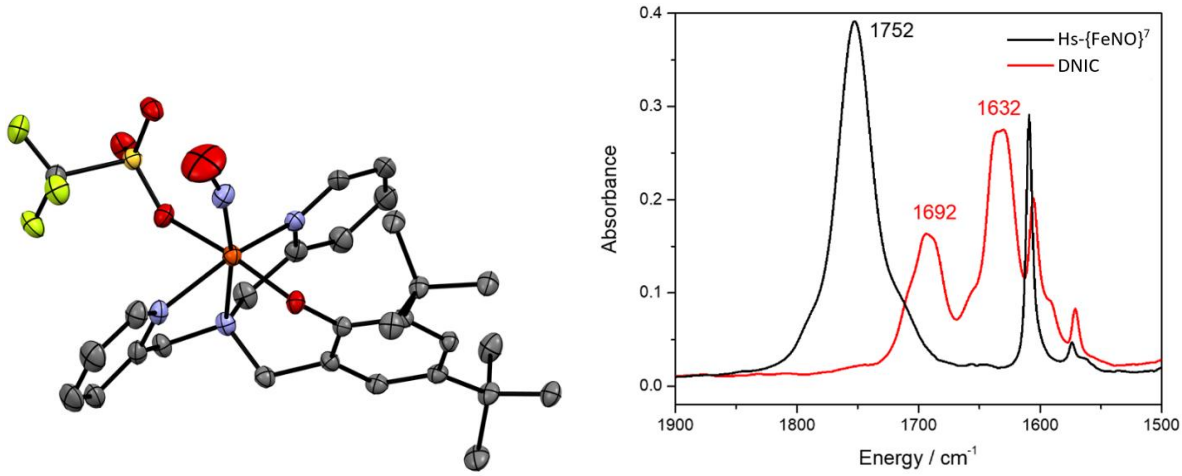

Figure 6.6 Left: Crystal structure of the hs-{FeNO}^{7} precursor complex [Fe(BMPA-tBu$_2$PhO)(OTf)(NO)]. All H atoms are omitted for clarity. Right: Solution IR spectra showing the characteristic N-O stretching bands of the starting material and the DNIC product after one-electron reduction.[13]

6.4 Characterization of the Product after Reduction of 1

Upon reduction of **1** with 1 eq. of $CoCp_2$ in CH_2Cl_2 (in which **1** is 100% hs) the solution immediately changes color from black to bright orange, indicating the formation of a new species (**2**). UV-Vis spectroscopic titration of **1** with $CoCp_2$ shows a complete transformation of **1** with one equivalent of reductant via appearance of a new, highly intense band at 445 nm. Both solid state and solution IR spectra show the disappearance of the intense N-O stretching band of **1** upon reduction to **2**, but surprisingly, no new band is observed at ~2220 cm^{-1} (N_2O) and within the 1600-1800 cm^{-1} region (expected for DNIC and hs-{FeNO}^{8} complexes). This indicates the possibility of NO dissociation from our metal complex upon reduction. However, mass spectrometry shows an m/z of 376.09 that shifts to 377.09 with ^{15}NO and 379.09 with $^{15}N^{18}O$. This proves that NO is still bound to the reduction product; however, the N-O stretch must have somehow shifted to significantly lower energy (<1500 cm^{-1}). At the same time, the ^{1}H-NMR spectrum of the isolated

product **2** shows a normal diamagnetic NMR spectrum, and all the protons of the ligand scaffold can be identified and integrated accordingly. The Evans method further confirms that the compound is strictly diamagnetic at room temperature. The Mössbauer isomer shift of **2** (δ = 0.31 mm/s) supports the formation of diamagnetic low-spin Fe(II) centers (Figure 6.7). This suggests the clean formation of an S_t = 0 species upon reduction of **1**, instead of the expected DNIC formation according to eqn. 1.

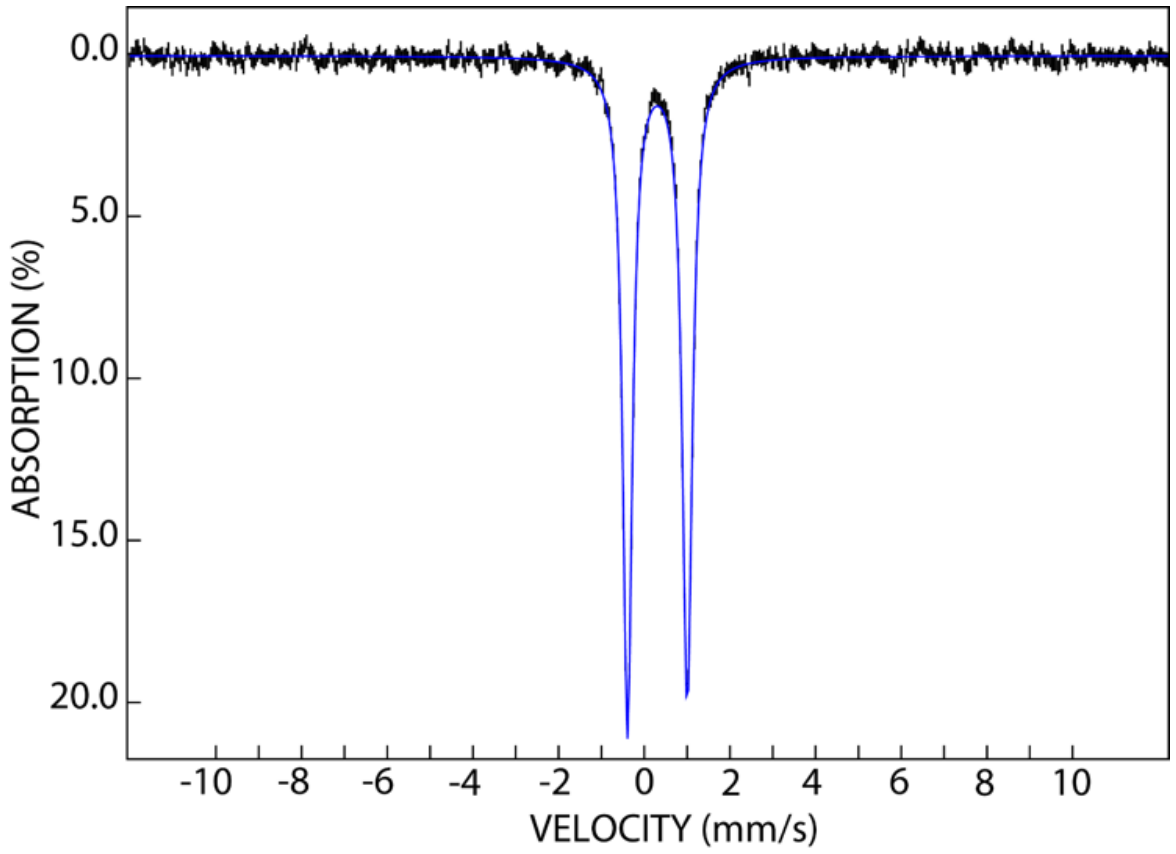

Figure 6.7 Mössbauer spectrum of complex **2** recorded at 4.2 K in an external 53-mT magnetic field applied parallel to the propagation direction of the γ beam. The experimental data are shown as black vertical bars. The blue line is a simulation using the following parameters: δ = 0.31 mm/s, $|\Delta E_Q|$ = 1.40 mm/s.

To determine the exact nature of the reduced product, crystals suitable for X-ray diffraction were grown from diffusion of diethyl ether into a saturated solution of **2** in acetonitrile. To our surprise, complex **2** is formed by the dimerization of two hs-$\{FeNO\}^8$ units, bridged by the two

NO molecules (Figure 6.8, left), with a molecular formula of $[Fe_2(TPA)_2(NO)_2](OTf)_2$. *To our knowledge, this is the first observation of an $Fe_2(NO)_2$ core in non-heme iron-NO chemistry*. Further characterization by IR spectroscopy reveals the antisymmetric (as) N-O stretching frequency of **2** at 1350 cm^{-1} that shifts to 1330 cm^{-1} with ^{15}NO and 1306 cm^{-1} with $^{15}N^{18}O$ (Figures 6.8, right). In comparison, the hs-$\{FeNO\}^8$ complex $[Fe(TMG_3tren)(NO)]^+$ shows ν(N-O) at 1618 cm^{-1}.[12] The low N-O stretching frequencies observed for **2** indicate coordination of singlet NO^-, i.e. complex **2** contains two ls-Fe(II) centers (S = 0) bound to two $^1NO^-$ units (S = 0) and is therefore strictly diamagnetic.

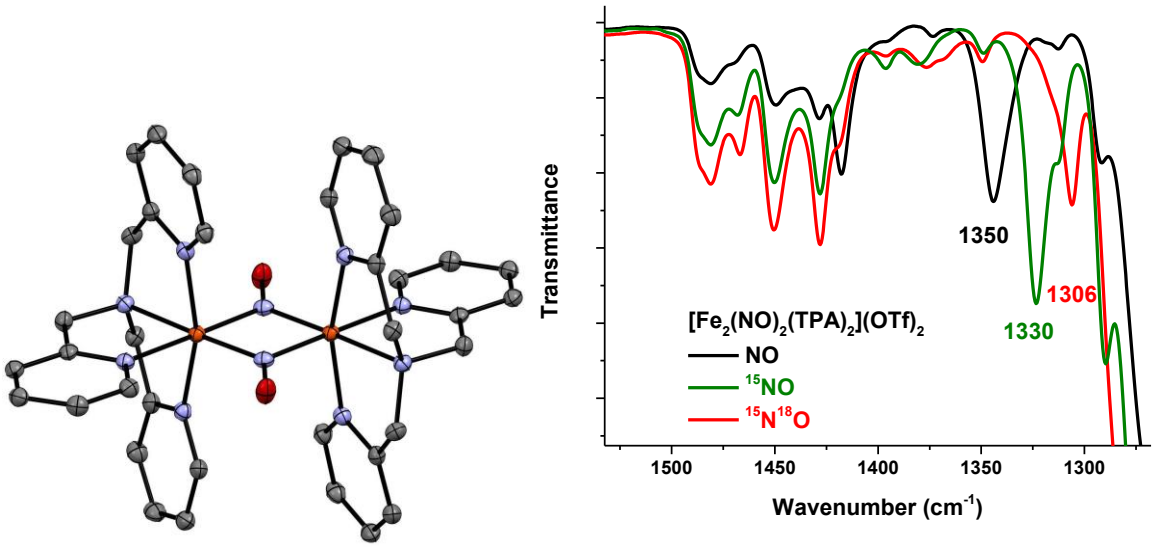

Figure 6.8 Crystal structure of complex **2** with ellipsoids drawn at 50% probability. The triflate counter anion, solvent molecules, and hydrogen atoms are omitted for clarity.

To further explore the electronic properties of this new complex, DFT calculations were performed. Geometry optimization of **2** with diamagnetic, bridged ls-$\{FeNO\}^8$ centers (using BP86/TZVP, which has been shown to give good structures for nitrosyl complexes)[20,21] shows good agreement with the structural parameters of **2**. Subsequent frequency calculations predict υ_{as}(N-O) = 1364 cm^{-1} and υ_{sym}(N-O) = 1399 cm^{-1} with BP86/TZVP, where υ_{sym}(N-O) is not IR

active (due to the centrosymmetric $Fe_2(NO)_2$ core). The calculated υ_{as}(N-O) is in very good agreement with experiment. Calculated Mössbauer parameters are also in excellent agreement with experimentally determined parameters (δ = 0.31(exp)/0.28(calc) mm/s and $|\Delta E_Q|$ = 1.40(exp)/1.66(calc) mm/s) and indicate that the Fe centers are in the ls +II state (Figure 6.8, right). As predicted by DFT, I do not observe the symmetric N-O stretch of complex **2**. Interestingly, DFT calculations with hybrid functionals like B3LYP overestimate the stretching frequencies of the bridging NO ligands in the diamond core. In contrast, calculations where both of the iron centers are in the hs state immediately quench to the $S_t = 0$ spin state with various functional and basis set combinations, suggesting that the ls state of this complex is favorable, thus preventing us from directly calculating the energy of the analog of **2** where the Fe(II) centers are hs.

Further characterization of complex **2** using NRVS revealed a vibrational feature at 765 cm^{-1} that shifts to 748 cm^{-1} with ^{15}NO labeling, and which originates from the Fe-NO symmetric stretching mode that is mixed with Fe-N-O bending mode. (Figure 6.9). A second signal observed at 596 cm^{-1} in the NRVS data shifts to 587 cm^{-1} with ^{15}NO labeling, which likely originates from the Fe-N-O the out of plan bending mode of the Fe-N-O core. These assignments are supported by DFT results with high degree of agreement. This significant increase in the strength of the Fe-NO bond to 765 cm^{-1} correspond to the change in the electronic structure when the $^3NO^-$ ligand spin change to a bridging $^1NO^-$ ligand upon dimerization.

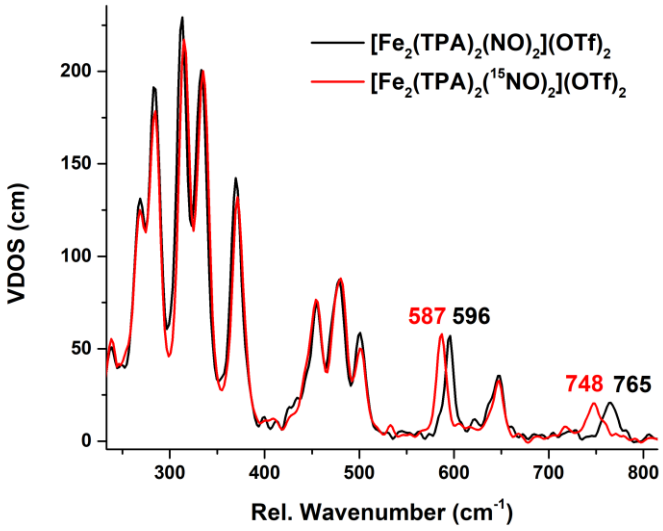

Figure 6.9 NRVS spectra of complex 2 in solid state.

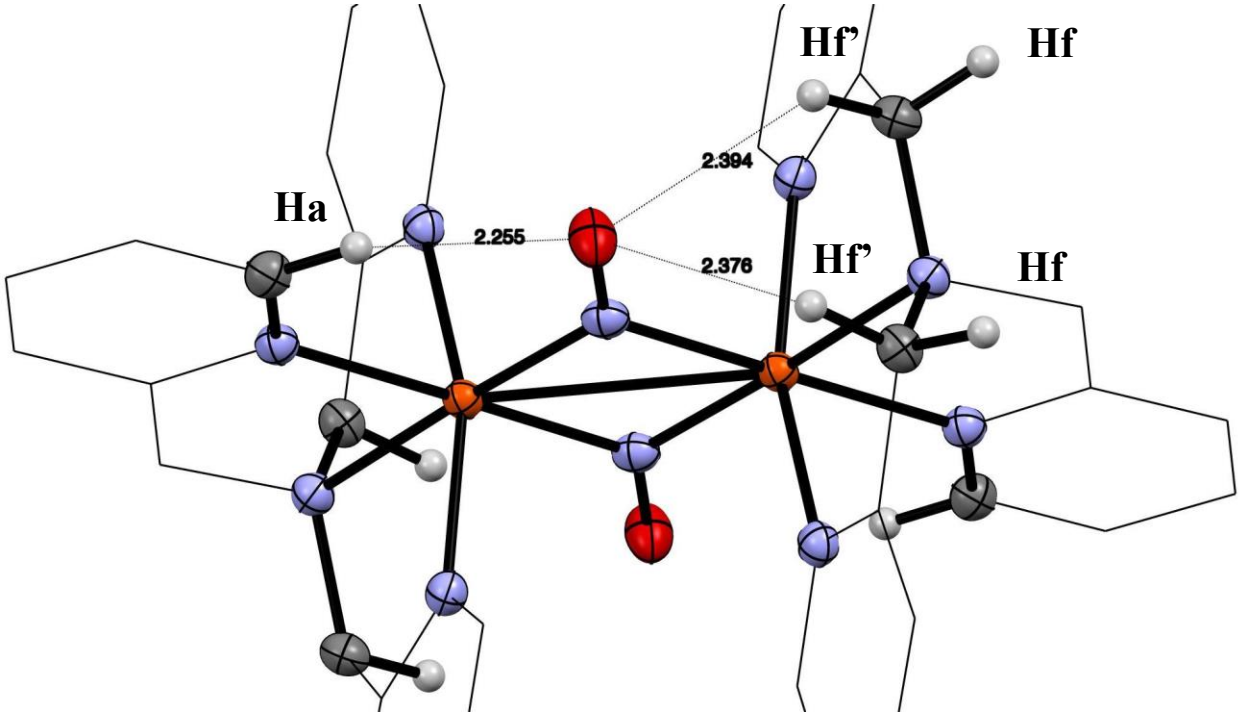

Figure 6.10 Crystal structure of complex 2 showing the distance of the agostic-type interactions between the hydrogen of the C-H bond of the coligand and the $^{1}NO^{-}$ ligand.

Complex **2** is completely diamagnetic, therefore, NMR techniques are powerful tools to understand and confirm the structure of this complex in the solution state. The assignment of the proton signals in the ^{1}H-NMR spectra of $[Fe(TPA)_2(NO)_2](OTf)_2$ was performed using a

combination of ^{13}C-NMR, HSQC, HMBC, and COSY. To our surprise, the assignment of these signals was complicated and challenging due to the unusual shift of some of the signals. The assignment of the protons and carbons are made based on the result from 2D-NMR experiment as shown in figure 6.11-13.

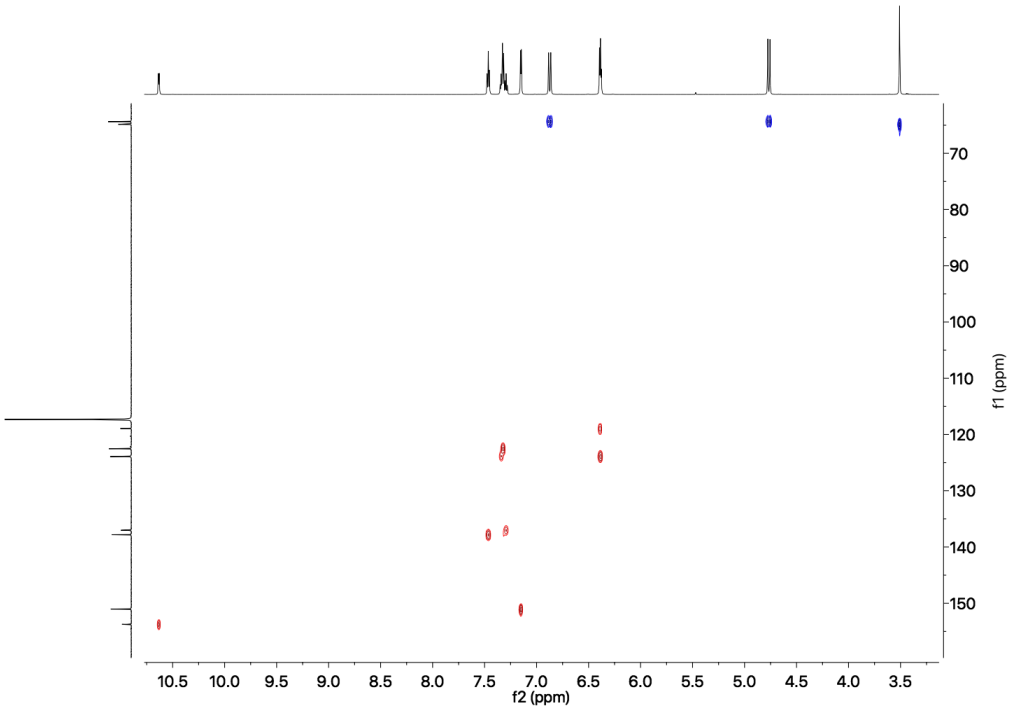

Figure 6.11 2D-NMR HSQC of complex **2** in CD_3CN.

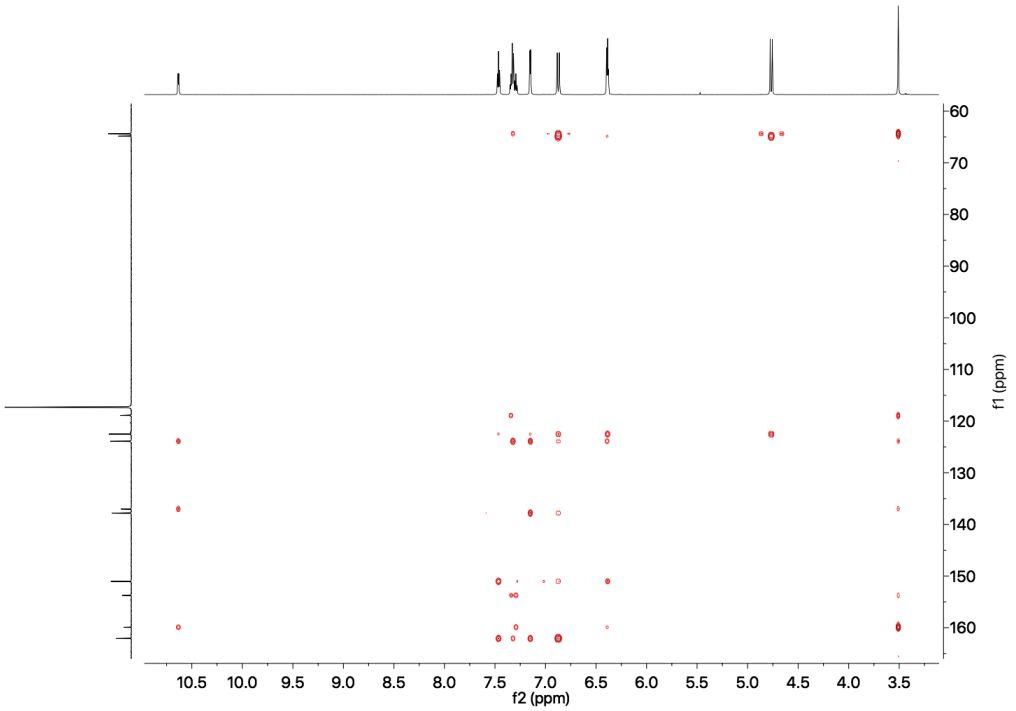

Figure 6.12 2D-NMR HMBC of complex **2** in CD_3CN.

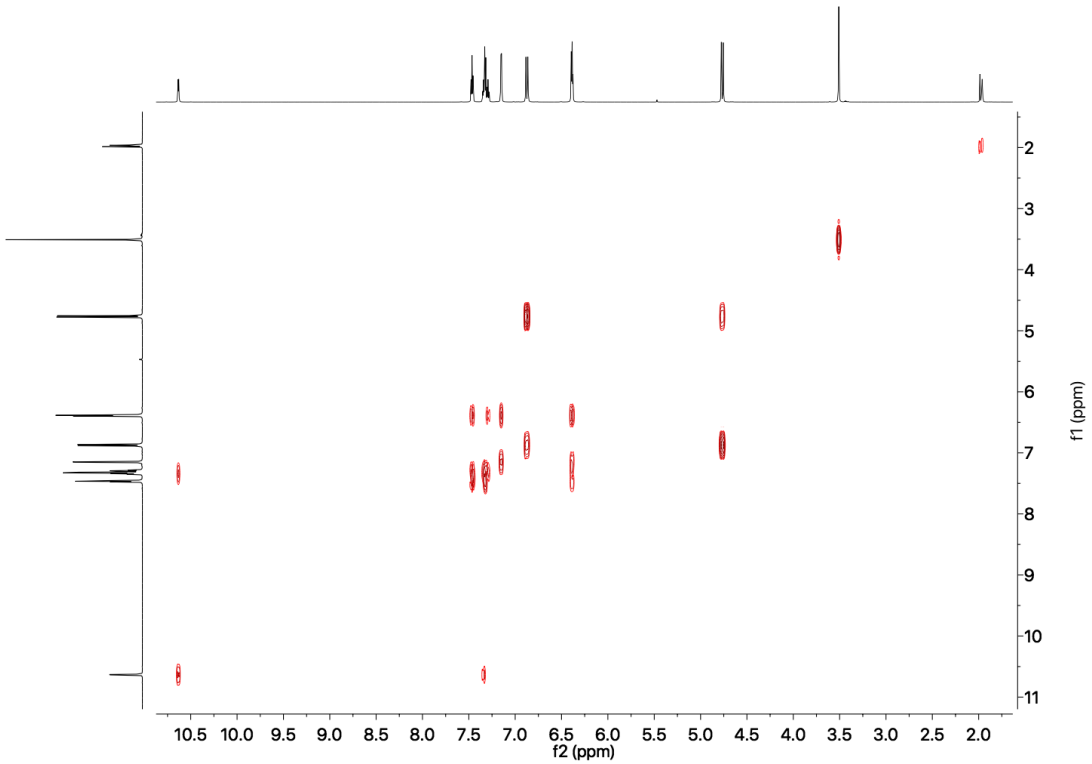

Figure 6.13 COSY of complex **2** in CD_3CN.

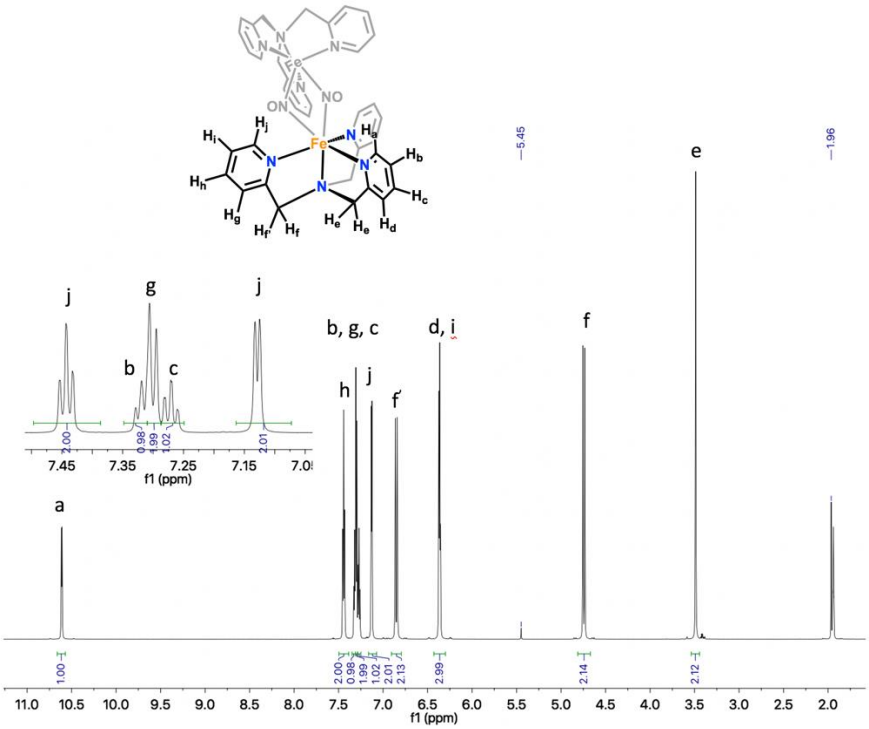

Figure 6.14 ^{1}H-NMR of complex 2 in CD_3CN, showing a completely diamagnetic NMR spectra, supporting the St = 0 assignment of 2, which is further confirmed by Evans method. The spectrum is referenced against solvent residual signal. Assignment of proton peaks are confirmed by 2D-NMR techniques. The fragment of 2 with proton labeled is shown.

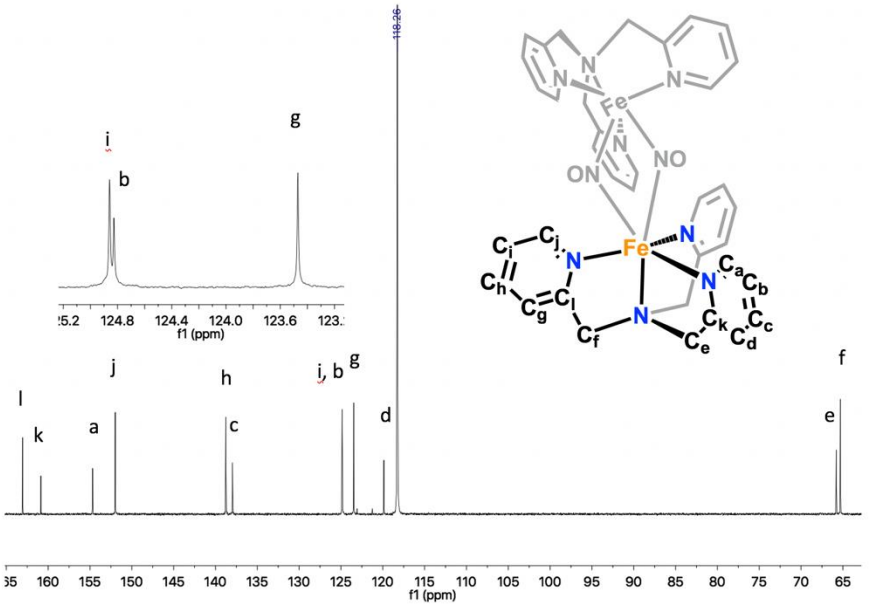

Figure 6.15 ^{13}C-NMR of complex **2** in CD_3CN. The spectrum is referenced against solvent residual signal. The assignment of carbon signals is confirmed by 2D-NMR experiments.

Based on the assignment, Hf' and Ha are significantly shifted downfield in the NMR spectrum compared to their counterparts Hf and Hj, by about 2.11 ppm (Figure 6.14-15). Close examination of the crystal structure reveals a surprising agostic interaction of the Hf' with the oxygen atom of one of the $^1NO^-$ ligands. The Hf'-O distances are 2.39 and 2.38 Å and the H_a-O distance is 2.26 Å, which are reasonable for this type of interaction (Figure 6.10). The Hf' and Hf signals are split into two separate doublets that are shifted to 6.86 and 4.75 ppm (2.11 ppm difference), respectively. Hf' is shifted downfield due to the H-bond with the oxygen of the $^1NO^-$ ligand, which deshields the proton nuclei. Therefore, this agostic-type interaction puts Hf' and Hf into a different chemical environment. The chemical shift of the these H_a protons is around 8.50 ppm for the pure TPA ligand; however, in complex **2**, the signal of Ha is shifted to 10.61 ppm (2.11 ppm difference) which is also due to the agnostic-type interaction with the $^1NO^-$ ligand. This result shows that the $^1NO^-$ ligand is very negatively charged, thus making it capable of forming H-bonds with C-H groups that are in close proximity. To further analyze the strength of this hydrogen-bonding interaction, the quantum atom in molecule (QT-AIM) analysis was used. In addition, the hydrogen bond strength was calculated based on the ^{1}H-NMR shifts using equation previously reported ($E_{HB}(\Delta\delta_{Hf'}) = \Delta\delta_{Hf'} + (0.4 \pm 0.2)$) .[22] The experimental results show that the interaction energy between Ha and O is 16.2 kJ/mol, while the bond between Hf' and O is worth about 10.5 kJ/mol. This is in great agreement with QT-AIM analysis using the optimized structure of complex **2**. In this case, the bond strength is predicted to be 15.9 kJ/mol and 11.2 kJ/mol for Hf'-O and Ha-O, respectively. This is a rare observation of a hydrogen bond between a C-H group and a coordinated NO, making this unique complex even more interesting.

6.5 Oxidation of Complex 2 to Form The Mixed Valent Diamond Core Complex

Cyclic voltammetry performed on the dimer **2** reveals a quasi-reversible redox event at $E_{1/2}$ = -296 mV vs Fc+/Fc (Figure 6.16). A UV-Vis titration of **2** with $FcPF_6$ shows that there is a significant change from the signal at 444 nm to a signal at 415 nm upon oxidation. EPR spectroscopy reveals a signal at g = 2.00, typical for S = 1/2 complexes, in agreement with a oxidation of the diamagnetic diamond core to form a mixed-valent product (Figure 6.17). Based on DFT calculations, this mixed-valent diamond core complex, $[Fe_2(TPA)_2(NO)_2](OTf)_3$, is a type III mixed valent complex with delocalized spin. NRVS spectroscopy reveals that the signal at 765 cm^{-1} of complex **2** is shifted to 747 cm^{-1} in the oxidized product, indicating only a small change in bonding upon oxidation, and most importantly, that the diamond core remains intact in the oxidized product (Figure 6.18).

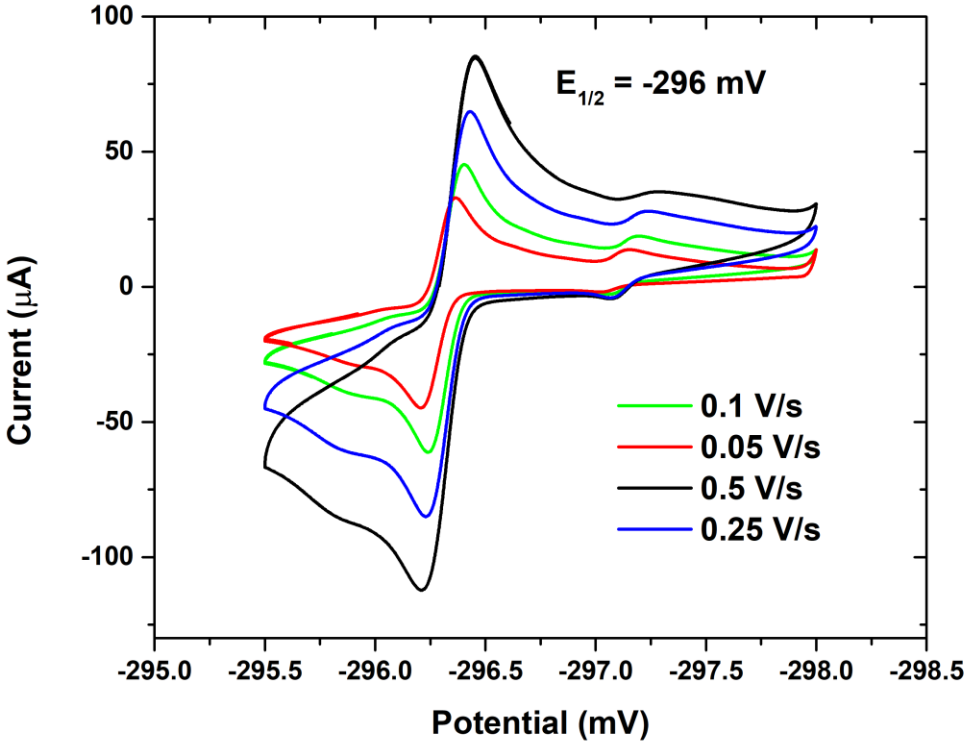

Figure 6.16 Cyclic voltammogram of complex **2** in CH_3CN at 5 mM concentration in TBA.OTf solution at 0.1 M concentration.

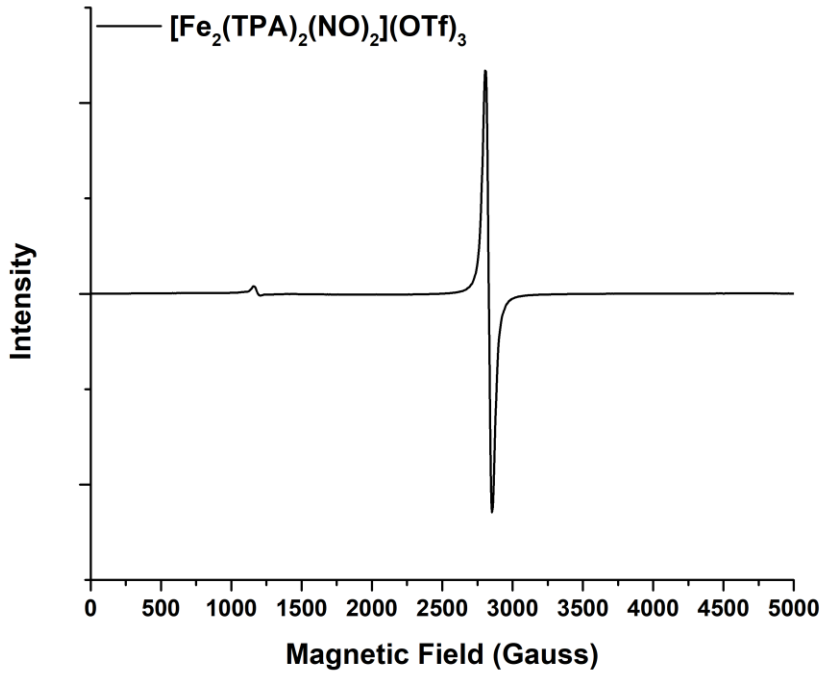

Figure 6.17 X-band EPR spectrum of the mixed valent complex in CH_3CN in CH_2Cl_2 at 2 mM concentration at 4 K.

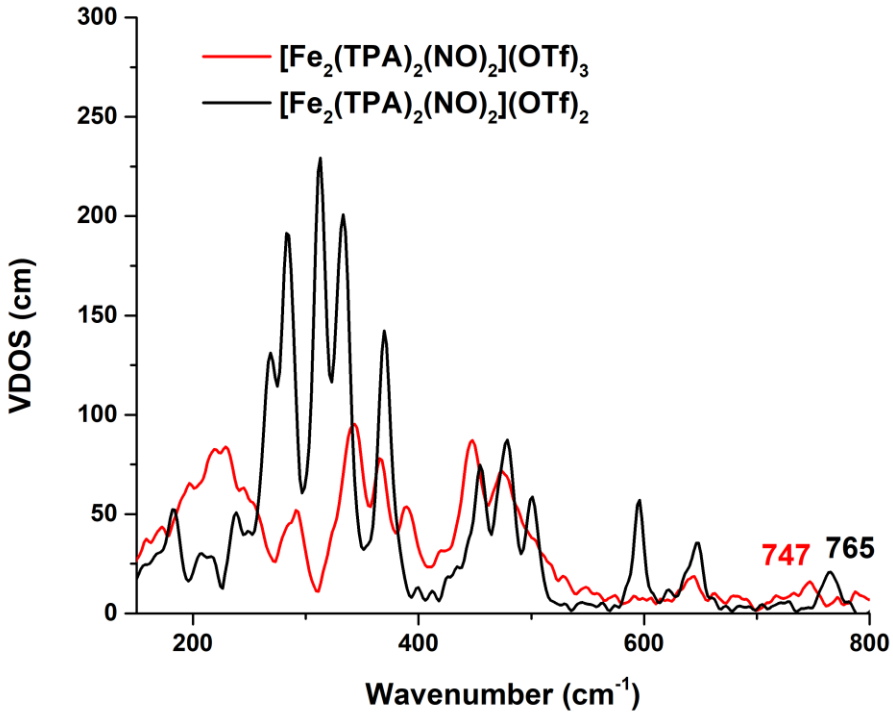

Figure 6.18 Solution state NRVS spectrum of the mixed valent complex overlay with the solid state NRVS spectrum of complex **2** showing the change after oxidation.

6.6 Conclusion

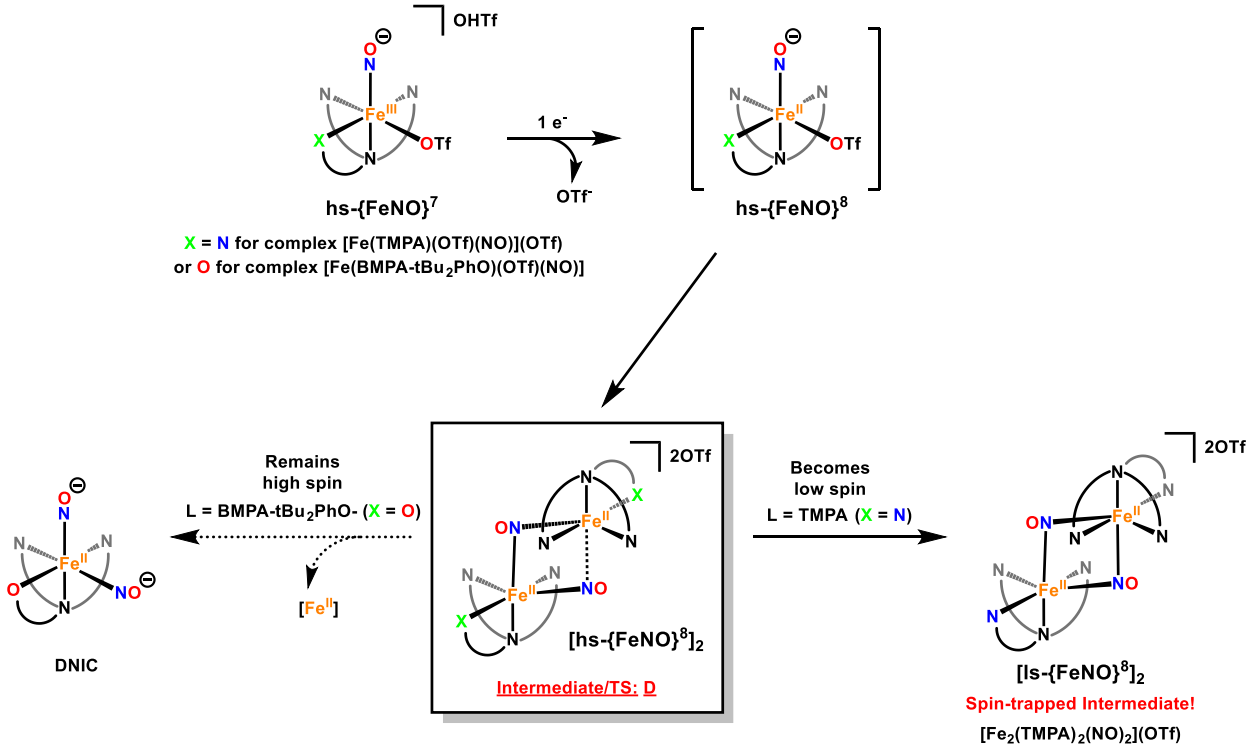

Scheme 6.1 Proposed mechanism for DNIC formation from hs-{FeNO}^{8} complexes based on the recent discovery of $[Fe_2(TMPA)_2(NO)_2](OTf)_2$.[13]

In conclusion, I have discovered a new structural motif in non-heme iron-nitrosyl chemistry, an $Fe_2(NO)_2$ diamond core with two bridging NO ligands (complex **2**), generated from the reduction of the non-heme hs-{FeNO}^{7} complex **1**. I propose that the initially formed {FeNO}^{8} complex (after reduction) is hs, but that upon dimerization the Fe centers undergo a spin crossover to ls, which leads to the stabilization of the $Fe_2(NO)_2$ core. The studies on the analogous complex **3** show that this reactivity is unique for the TPA ligand scaffold, which has a ligand field that is on the borderline of spin-crossover. Spectroscopic data show that dimeric complex **2** contains ls-Fe(II) with bound $^1NO^-$ ligands, and hence, is diamagnetic. It is interesting to note that dimerization of mononuclear hs-{FeNO}^{8} complexes has been proposed to be the key process in

the formation of N_2O and DNICs, as also suggested by stoichiometry. To further support the idea that the one-electron reduced form of complex **1** (**1red**) is a hs-$\{FeNO\}^8$ species, DFT calculations were performed on **1red** (with triflate as the 6th ligand) in both the ls and hs state (using B3LYP*/TZVP). The results show that the hs state is clearly the ground state of **1red**, being 15 kcal/mol lower in energy compared to the ls state. Although previous studies have shown that DNICs are a common reaction product of hs-$\{FeNO\}^8$ complexes, their mechanism of formation has remained elusive. I speculate that the dimeric structure of **2** could be a model for the corresponding intermediate that is responsible for DNIC formation (Scheme 6.1). Here, the $\{FeNO\}^8$ units would remain hs in the dimer, which, after loss of Fe(II), generates a DNIC. In this sense, the $Fe_2(NO)_2$ structural motif observed in **2** is a perfect template for the formation of DNICs Because the N-O stretch of **2** is in an unexpected region, it is possible that these types of intermediates have been overlooked in previous protein and model complex studies. Given the close proximity of the iron centers in iron-sulfur proteins, this type of intermediate could potentially be formed. Nevertheless, whether a bridging structure like **2** exists in Nature remains to be seen.

6.7 Experimental Section

Reactions were generally performed using inert gas (Schlenk) techniques. All solvents were dried and freeze pump thawed to remove dioxygen and water. Preparation and handling of air sensitive materials was performed under a dinitrogen atmosphere in an MBraun glovebox, equipped with a circulating purifier (O_2, H_2O <0.1 ppm). Nitric oxide (99.95%) was first passed through an Ascarite II column and then a -80 ^oC cold trap to remove higher nitrogen oxide impurities prior to use.

Mass spectrometry experiments were conducted on an Agilent 6230 TOF HPLC-MS with manual injection. Compounds were dissolved in CH_2Cl_2 and then injected directly into the instrument.

Structure Determination: Brown plates of complex **1** were grown from an acetonitrile/diethyl ether solution of the compound at 22 deg. C. A crystal of dimensions 0.20 x 0.14 x 0.08 mm was mounted on a Rigaku AFC10K Saturn 944+ CCD-based X-ray diffractometer equipped with a low temperature device and a Micromax-007HF Cu-target micro-focus rotating anode (λ = 1.54187 Å) operated at 1.2 kW power (40 kV, 30 mA). The X-ray intensities were measured at 85(1) K with the detector placed at a distance of 42.00 mm from the crystal. A total of 3808 images were collected with an oscillation width of 1.0° in ω. The exposure times were 2 sec. for the low angle images, 12 sec. for high angle. The integration of the data yielded a total of 35,038 reflections to a maximum 2θ value of 136.48° of which 4698 were independent and 4600 were greater than $2\sigma(I)$. The final cell constants were based on the xyz centroids of 18,779 reflections above $10\sigma(I)$. Analysis of the data showed negligible decay during data collection; the data were processed with CrystalClear 2.0 and corrected for absorption.[1] The structure was solved and refined with the Bruker SHELXTL (version 2018/3) software package, using the space group P1bar with Z = 2 for the formula $C_{20}H_{18}N_5O_7F_6S_2Fe$.[2] All non-hydrogen atoms were refined anisotropically with the hydrogen atoms placed in idealized positions. Full matrix least-squares refinement based on F2 converged at R1 = 0.0311 and wR2 = 0.0843 [based on I > 2□(I)], R1 = 0.0315 and wR2 = 0.0846 for all data.

Purple blocks of complex **2** were grown from an acetonitrile/diethyl ether solution of the compound at -33 deg. C. A crystal of dimensions 0.12 x 0.10 x 0.10 mm was mounted on a Rigaku AFC10K Saturn 944+ CCD-based X-ray diffractometer equipped with a low temperature device

and a Micromax-007HF Cu-target micro-focus rotating anode (λ = 1.54187 Å) operated at 1.2 kW power (40 kV, 30 mA). The X-ray intensities were measured at 85(1) K with the detector placed at a distance of 42.00 mm from the crystal. A total of 2028 images were collected with an oscillation width of 1.0° in ω. The exposure times were 1 sec. for the low angle images, 3 sec. for high angle. Rigaku d*trek images were exported to CrysAlisPro for processing and corrected for absorption.[3] The integration of the data yielded a total of 31,405 reflections to a maximum 2θ value of 138.32° of which 3875 were independent and 3769 were greater than 2σ(I). The final cell constants were based on the xyz centroids of 18,500 reflections above 10σ(I). Analysis of the data showed negligible decay during data collection. The structure was solved and refined with the Bruker SHELXTL (version 2016/6) software package, using the space group P2(1)/c with Z = 2 for the formula $C_{38}H_{36}F_6Fe_2N_{10}O_8S_2$. All non-hydrogen atoms were refined anisotropically with the hydrogen atoms placed in idealized positions. Full matrix least-squares refinement based on F2 converged at R1 = 0.0314 and wR2 = 0.0847 [based on I > 2□(I)], R1 = 0.0323 and wR2 = 0.0856 for all data.

Purple plates of complex **3** were grown from a tetrahydrofuran/pentane solution at 22 deg. C. A crystal of dimensions 0.31 x 0.14 x 0.02 mm was mounted on a Bruker SMART APEX-I CCD-based X-ray diffractometer equipped with a low temperature device and fine focus Mo-target X-ray tube (λ = 0.71073 A) operated at 1500 W power (50 kV, 30 mA). The X-ray intensities were measured at 85(1) K; the detector was placed at a distance of 5.070 cm from the crystal. A total of 2410 frames were collected with a scan width of 0.5°in ω and 0.45°in phi with an exposure time of 30 s/frame. The integration of the data yielded a total of 58,299 reflections to a maximum 2θ value of 56.62°of which 7563 were independent and 5739 were greater than 2σ(I). The final cell

constants (Table S16) are based on the xyz centroids of 9982 reflections above 10σ(I). Analysis of the data showed negligible decay during data collection; the data were processed with SADABS and corrected for absorption. The structure was solved and refined with the Bruker SHELXTL (version 2018/3) software package, using the space group C2/c with Z = 4 for the formula $C_{28}H_{34}N_4O_5F_3SFe$. All non-hydrogen atoms were refined anisotropically with the hydrogen atoms placed in idealized positions. Full matrix least-squares refinement based on F2 converged at R1 = 0.0402 and wR2 = 0.0928 [based on I > 2□(I)], R1 = 0.0623 and wR2 = 0.1052 for all data. The bound CF_3SO_3□ ligand is disordered and was refined with partial occupancy orientations constrained to sum to one.

Synthesis:

The ligand **TPA** was synthesized according to reported procedures and purity was confirmed by NMR spectroscopy.[7] ^{1}H-NMR (400 MHz, $CDCl_3$): δ 8.52 (ddd, 3H), 7.64 (td, 3H), 7.58 (s, 2H), 7.56 (s, 1H), 7.13 (ddd, 3H), 3.87 (s, 6H)

The ligand **BMPA-tBu$_2$PhOH** was synthesized according to reported procedures and purity was confirmed by NMR spectroscopy.[8] Yield: 365 mg, 88%. ^{1}H NMR (400 MHz, $CDCl_3$): 10.62 (s, 1H); 8.55 (d, 2H); 7.63 (t, 2H); 7.37 (d, 2H); 7.20 (s, 1H); 7.15 (t, 2H); 6.87 (s, 1H); 3.88 (s, 4H); 3.80 (s, 2H); 1.45 (s, 9H); 1.26 (s, 9H).

[Fe(TPA)(CH$_3$CN)$_2$](OTf)$_2$: Under an inert atmosphere, 498 mg (1.15 mmol) $Fe(OTf)_2$•$2CH_3CN$ and 351 mg (1.21 mmol) TPA were combined in 8 mL of CH_3CN. The reaction was stirred for 2 hours, at which point 80 mL of diethyl ether was added, causing a red solid to precipitate. Filtration gave the title compound as a red solid. Yield: 789 mg, 95%. The ^{1}H-NMR and UV-Visible spectra of this complex are in accordance with previous literature reports.[9]

[Fe(TPA)(NO)(OTf)](OTf) (1): Under an inert atmosphere, 200 mg (0.28 mmol) of $[Fe(TPA)(CH_3CN)_2](OTf)_2$ was dissolved in a minimal volume of CH_3CN and exposed to excess NO gas, causing the solution to change color from red to dark brown. The product was precipitated by addition of 24 mL of diethyl ether. Filtration afforded the title compound as a dark brown powder. Yield: 130 mg, 68%. Single crystals suitable for X-ray diffraction were grown by vapor diffusion of diethyl ether into a concentrated CH_3CN solution of **1** in a Schlenk tube, charged with NO gas. ^{1}H-NMR for the perchlorate analog has been reported by our laboratory previously[10] (400 MHz, CD_2Cl_2, all peaks appear as broad singlets): δ 102.1, 72.2, 64.0, 63.0, -5.0 ppm. Characterization: Elemental anal. calcd. for $C_{20}H_{18}F_6FeN_5O_7S_2$: C, 35.62; H, 2.69; N, 10.39; found (%): C, 35.73; H, 2.73; N, 10.13.

$[Fe_2(TPA)_2(NO)_2](OTf)_2$ (2): Under an inert atmosphere, 200 mg (0.30 mmol) of complex **1** was dissolved in a minimal volume of CH_2Cl_2 and 1 equivalent of $CoCp_2$ was added into the solution, causing the immediate color change from dark brown to orange. A minimum amount of hexane was then added to crystallize the product out overnight, which gave a crude solid mixture of **2** and a cobaltocenium impurity. The crude product was then filtered and the resulting solid was washed with a minimum amount of cold tetrahydrofuran to wash out more cobaltocenium salt. The remaining solid was dissolved in acetonitrile and a minimum amount of diethyl ether was added to recrystallize overnight. The solution was then filtered again to obtain the pure complex **2** as a black crystalline solid. ^{1}H-NMR (700 MHz, CD_3CN): δ 10.61 (dd, 2H), 7.44 (td, 4H), 7.29 (m, 8H), 7.12 (m, 4H), 6.85 (d, 4H), 6.36 (m, 6H), 4.73 (d, 4H), 3.48 (s, 4H). Characterization: Elemental anal. calcd. for $C_{38}H_{36}F_6Fe_2N_{10}O_8S_2$: C, 43.44; H, 3.45; N, 13.33; found (%):C, 43.55; H, 3.53; N, 13.39. Mass spectrometry m/z: calcd. for the cationic half fragment $C_{18}H_{18}FeN_5O$:

376.22; Found: 376.09. Mass spectrometry m/z: calcd. for the ^{15}NO labelled cationic fragment $C_{18}H_{18}FeN_5O$: 377.09; Found: 377.09.

The preparation of complexes **1** and **[Fe(TPA)(NO)](BF$_4$)$_2$ (1-BF$_4$)** is similar, except that $Fe(BF_4)_2$•$2CH_3CN$ is used in the latter case as the iron source.

[Fe(BMPA-tBu$_2$PhO)(OTf)]: Under an inert atmosphere, 629 mg (1.50 mmol) of BMPA-tBu$_2$PhOH and 104 mg of (1.48 mmol) potassium methoxide were combined in 5 mL of methanol. The suspension was stirred briefly, and 487 mg (1.38 mmol) $Fe(OTf)_2$ was then added. The reaction turned green. After approximately 5 hours, the reaction was filtered and solvent is removed under reduced pressure. The solid was taken up in THF and excess ethanethiol was added. After the reaction had stirred for 45 minutes, all volatiles were removed under reduced pressure. The resulting material was recrystallized from THF/hexanes, giving a pale green solid. Yield: 550 mg, 59%.

[Fe(BMPA-tBu$_2$PhO)(NO)(OTf)] (3): Under an inert atmosphere, 200 mg [Fe(BMPA-tBu$_2$PhO)]OTf was dissolved in 5 mL THF and exposed to excess NO gas. The solution immediately turned purple. The reaction was stirred under NO headspace for 30 minutes. Hexanes was then added, and the product was allowed to precipitate at -33 °C overnight. The solution was filtered under inert atmosphere to give the title compound as a purple solid. Yield: 181 mg, 86%. Single crystals suitable for x-ray diffraction were grown by slow diffusion of pentane into a concentrated THF solution.

Spin state changes in 1 and 1-BF$_4$. It is interesting to note that both complexes **1** and **3** have triflate bound as the sixth ligand, and even though these complexes are prepared and/or recrystallized in CH_3CN solution, the triflate remains bound in the solid state. This indicates that triflate is actually a quite strong ligand for these high-spin (hs) $\{FeNO\}^7$ complexes. Moreover,

the change in the N-O stretch between the solid and the CH_2Cl_2 solution state for these complexes is very small (1806 vs. 1800 cm^{-1} for **1**, and 1752 vs. 1752 cm^{-1} for **3**), again indicating that these complexes remain six-coordinate in solution with the triflate bound as the sixth ligand. In CH_3CN solution, however, complex **1** shows formation of a distinct amount of low-spin (ls) complex (by solution IR and EPR), which we attribute to the equilibrium:

$$[Fe(TPA)(NO)(OTf)]^{+}\ (hs) + CH_3CN \leftrightarrows [Fe(TPA)(NO)(CH_3CN)]^{2+}\ (ls) + OTf^{-}$$

where the CH_3CN-bound form is actually ls. In order to interrogate this point further, we then prepared the complex **1-BF_4** where the triflate is replaced by the much more weakly coordinating counter ion BF_4^-. This complex is again hs in the solid state and when dissolved in CH_3CN, shows formation of a large fraction of the ls complex. In solution at room temperature, the hs state is still dominant, although it is not a priori clear whether this fraction of the complex is either five-coordinate or six-coordinate with BF_4^- bound. The hs N-O band in the solution IR spectrum is broad and shows at least two components, and the exact nature of these species it not clear. Upon cooling and freezing the solution, more of the CH_3CN-bound complex forms, driven by entropy, resulting in an EPR spectrum that now almost exclusively shows the ls state. In comparison to **1**, the EPR data in CH_3CN solution therefore show quite clearly that it is indeed CH_3CN coordination that is responsible for the formation of the ls state of **1**.

6.8 References

1. Dong, H. T.; White, C. J.; Zhang, B.; Krebs, C.; Lehnert, N. Non-Heme Diiron Model Complexes Can Mediate Direct NO Reduction: Mechanistic Insight into Flavodiiron NO Reductases. *J. Am. Chem. Soc.* **2018**, *140*, 13429-13440.
2. White, C. J.; Speelman, A. L.; Kupper, C.; Demeshko, S.; Meyer, F.; Shanahan, J. P.; Alp, E. E.; Hu, M.; Zhao, J.; Lehnert, N. The Semireduced Mechanism for Nitric Oxide Reduction by Non-Heme Diiron Complexes: Modeling Flavodiiron Nitric Oxide Reductases. *J. Am. Chem. Soc.* **2018**, *140*, 2562-2574.

3. Khatua, S.; Majumdar, A. Flavodiiron nitric oxide reductases: Recent developments in the mechanistic study and model chemistry for the catalytic reduction of NO. *J. Inorg. Biochem.* **2015**, *142*, 145-153.
4. Confer, A. M.; McQuilken, A. C.; Matsumura, H.; Moënne-Loccoz, P.; Goldberg, D. P. A Nonheme, High-Spin {FeNO}8 Complex that Spontaneously Generates N2O. *J. Am. Chem. Soc.* **2017**, *139*, 10621-10624.
5. Kindermann, N.; Schober, A.; Demeshko, S.; Lehnert, N.; Meyer, F. Reductive Transformations of a Pyrazolate-Based Bioinspired Diiron–Dinitrosyl Complex. *Inorg. Chem.* **2016**, *55*, 11538-11550.
6. Tonzetich, Z. J.; Héroguel, F.; Do, L. H.; Lippard, S. J. Chemistry of Nitrosyliron Complexes Supported by a β-Diketiminate Ligand. *Inorg. Chem.* **2011**, *50*, 1570-1579.
7. Hickok, J. R.; Sahni, S.; Shen, H.; Arvind, A.; Antoniou, C.; Fung, L. W. M.; Thomas, D. D. Dinitrosyliron complexes are the most abundant nitric oxide-derived cellular adduct: biological parameters of assembly and disappearance. *Free Radical Biol. Med.* **2011**, *51*, 1558-1566.
8. Lewandowska, H.; Kalinowska, M.; Brzóska, K.; Wójciuk, K.; Wójciuk, G.; Kruszewski, M. Nitrosyl iron complexes—synthesis, structure and biology. *Dalton Trans.* **2011**, *40*, 8273-8289.
9. D'Autréaux, B.; Horner, O.; Oddou, J.-L.; Jeandey, C.; Gambarelli, S.; Berthomieu, C.; Latour, J.-M.; Michaud-Soret, I. Spectroscopic Description of the Two Nitrosyl−Iron Complexes Responsible for Fur Inhibition by Nitric Oxide. *J. Am. Chem. Soc.* **2004**, *126*, 6005-6016.
10. Boese, M.; Mordvintcev, P. I.; Vanin, A. F.; Busse, R.; Mülsch, A. S-Nitrosation of Serum Albumin by Dinitrosyl-Iron Complex. *J. Biol. Chem.* **1995**, *270*, 29244-29249.
11. Lee, M.; Arosio, P.; Cozzi, A.; Chasteen, N. D. Identification of the EPR-Active Iron-Nitrosyl Complexes in Mammalian Ferritins. *Biochemistry* **1994**, *33*, 3679-3687.
12. Speelman, A. L.; White, C. J.; Zhang, B.; Alp, E. E.; Zhao, J.; Hu, M.; Krebs, C.; Penner-Hahn, J.; Lehnert, N. Non-heme High-Spin {FeNO}6–8 Complexes: One Ligand Platform Can Do It All. *J. Am. Chem. Soc.* **2018**, *140*, 11341-11359.
13. Dong, H. T.; Speelman, A. L.; Kozemchak, C. E.; Sil, D.; Krebs, C.; Lehnert, N. The $Fe_2(NO)_2$ Diamond Core: A Unique Structural Motif in Non-Heme Iron-NO Chemistry. *Angew. Chem. Int. Ed.* **2019**, *131*, 17859-17863.
14. Wang, J.; Li, C.; Zhou, Q.; Wang, W.; Hou, Y.; Zhang, B.; Wang, X. Photocatalytic hydrogen evolution by Cu(ii) complexes. *Dalton Trans.* **2016**, *45*, 5439-5443.
15. Zang, Y.; Kim, J.; Dong, Y.; Wilkinson, E. C.; Appelman, E. H.; Que, L. Models for Nonheme Iron Intermediates: Structural Basis for Tuning the Spin States of Fe(TPA) Complexes. *J. Am. Chem. Soc.* **1997**, *119*, 4197-4205.
16. Praneeth, V. K. K.; Näther, C.; Peters, G.; Lehnert, N. Spectroscopic Properties and Electronic Structure of Five- and Six-Coordinate Iron(II) Porphyrin NO Complexes: Effect of the Axial N-Donor Ligand. *Inorg. Chem.* **2006**, *45*, 2795-2811.
17. Li, J.; Banerjee, A.; Pawlak, P. L.; Brennessel, W. W.; Chavez, F. A. Highest Recorded N–O Stretching Frequency for 6-Coordinate {Fe-NO}7 Complexes: An Iron Nitrosyl Model for His3 Active Sites. *Inorg. Chem.* **2014**, *53*, 5414-5416.
18. Berto, T. C.; Hoffman, M. B.; Murata, Y.; Landenberger, K. B.; Alp, E. E.; Zhao, J.; Lehnert, N. Structural and Electronic Characterization of Non-Heme Fe(II)–Nitrosyls as Biomimetic Models of the FeB Center of Bacterial Nitric Oxide Reductase. *J. Am. Chem. Soc.* **2011**, *133*, 16714-16717.
19. Berto, T. C.; Hoffman, M. B.; Murata, Y.; Landenberger, K. B.; Alp, E. E.; Zhao, J.; Lehnert, N. Structural and Electronic Characterization of Non-Heme Fe(II)-Nitrosyls as

Biomimetic Models of the Fe_B Center of Bacterial Nitric Oxide Reductase (NorBC). *J. Am. Chem. Soc.* **2011**, *133*, 16714–16717.
20. Fujisawa, K.; Soma, S.; Kurihara, H.; Dong, H. T.; Bilodeau, M.; Lehnert, N. A cobalt–nitrosyl complex with a hindered hydrotris(pyrazolyl)borate coligand: detailed electronic structure, and reactivity towards dioxygen. *Dalton Trans.* **2017**, *46*, 13273-13289.
21. Van Stappen, C.; Lehnert, N. Mechanism of N–N Bond Formation by Transition Metal–Nitrosyl Complexes: Modeling Flavodiiron Nitric Oxide Reductases. *Inorg. Chem.* **2018**, *57*, 4252-4269.
22. Afonin, A. V.; Vashchenko, A. V.; Sigalov, M. V. Estimating the energy of intramolecular hydrogen bonds from 1H NMR and QTAIM calculations. *Org. Biomol. Chem.* **2016**, *14*, 11199-11211.

Chapter 7

Exploring the Limits of Dative Boratrane Bonding: Iron as a Strong Lewis Base in Low-Valent Non-Heme Iron-Nitrosyl Complexes

Adapted from published article: Dong, H. T.; Chalkley, M. J.; Paul H. Oyala; Zhao, J.; Alp, E. E.; Hu, M. Y.; Peters, J. C.; Lehnert, N. Exploring the Limits of Dative Boratrane Bonding: Iron as a Strong Lewis Base in Low-Valent Non-Heme Iron-Nitrosyl Complexes. *Inorg. Chem.* **2020**, *59*, 14967-14982.

Acknowledgement: I would like to thank Dr. Matthew J. Chalkley, Dr. Paul H. Oyala, and Prof. Jonas C. Peters for their ^{57}Fe samples preparation and pulsed EPR data collection and the corresponding data analysis. I would like to thank Dr. Jiyong Zhao, Dr. Esen E. Alp, and Dr. Michael Y. Hu who have assited me during the process of collecting NRVS data at the Argonne National Laboratory.

In **Chapter 7**, I present a full spectroscopic and electronic structure analysis of the unique $[Fe(TPB)(NO)]^{+/0/-}$ series.[1] The Peters lab has previously reported the synthesis and characterization of these complexes; however, a concrete conclusion about their electronic structure is still up for debate.[2] I collaborated with the Peters group to perform a detail electronic structure investigation using NRVS and DFT. In these complexes, a second redox-active unit, namely a borane, is positioned in close proximity to the metal by the ligand architecture. Ambiphilic ligands that utilize Lewis base donors both to coordinate a metal center and position a Lewis acid (LA) in its proximity have become increasingly popular in the past two decades.[3-5] However, given the constraints imposed by the ligand scaffolds used, evaluating the degree of M-LA bonding is often challenging.

Herein, I demonstrate the utility of force constants derived from quantum-chemistry centered normal coordinate analysis (QCC-NCA) of nuclear resonance vibrational spectroscopy (NRVS) data in deconvoluting the electronic structure and bonding at Fe in a highly covalent ligand sphere comprised of nitrosyl, boratrane, and phosphine ligands (Scheme 7.1). I find that, despite their low formal Fe redox states, an NO^+ redox state with strong Fe-NO π-bonds is maintained throughout the redox series. This is made possible because of the high degree of structural and electronic flexibility in the TPB ligand, demonstrated via the breaking of an η^4-BCCP donor interaction present in the most oxidized complex, and formation of a reverse dative Fe→B bond in the most reduced complex. Similarly, a reverse dative Fe→B bond has also been identified in the structurally related $[Fe(TPB)(N_2)]^-$ complex by NRVS, underscoring the relevance of this interaction in promoting small molecule functionalization (*i.e.*, N_2 fixation).[6] These conclusions are corroborated by continuous wave and pulse electron paramagnetic resonance spectroscopy (EPR) and density functional theory (DFT) calculations.

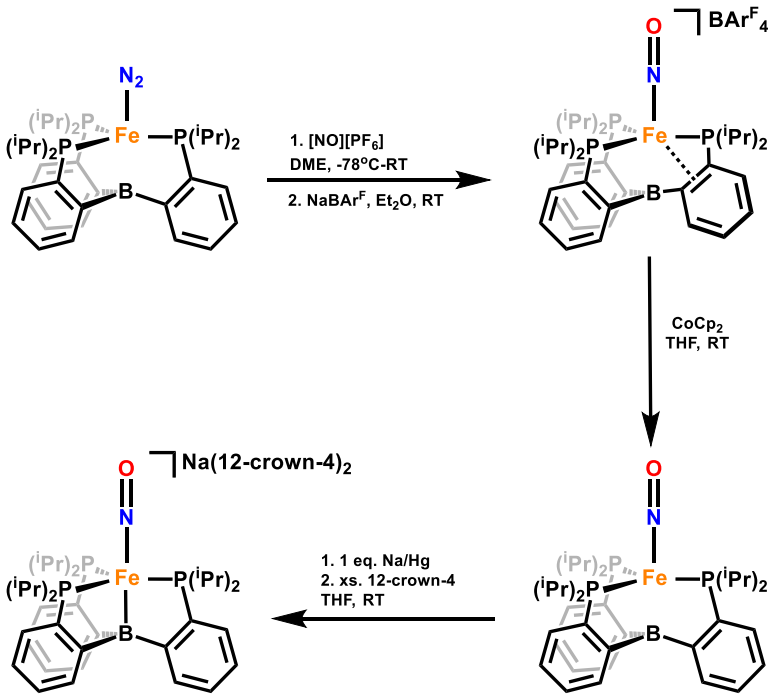

Scheme 7.1 Reaction scheme for the [Fe(TPB)(XY)] complexes.

7.1 Nuclear Resonance Vibrational Spectroscopy (NRVS) for the ls-{FeNO}$^{8-10}$ Series

The Fe-NO bonding in the ls-{FeNO}$^{8-10}$ series is evaluated and analyzed herein based on NRVS measurements (see Figure 1). NRVS is a vibrational technique that selectively detects vibrations that involve the ^{57}Fe center, making it well-suited for the identification of Fe-ligand stretching and bending modes. The experimental NRVS data of the ls-{FeNO}^{8} complex reveal an intense band at 610 cm^{-1} and weaker signals at 537 and 540 cm^{-1}. The feature at 610 cm^{-1} is assigned to the Fe-NO stretch (see below), whereas those at 537 and 540 cm^{-1} are in the correct range for Fe-N-O bending modes. With an Fe-NO stretch of 610 cm^{-1}, this complex has one of the strongest transition metal-NO bonds observed to this date and the strongest for an iron compound,[7] surpassing even ls-{FeNO}^{6} complexes in hemes (with typical Fe-NO stretching frequencies around 590 cm^{-1}).[8,9] In IR spectroscopy, the N-O stretch of this complex is observed at 1745 cm^{-1}. The NRVS data of the ls-{FeNO}^{10} complex are remarkably similar to those of the ls-{FeNO}^{8} species described above. In particular, its Fe-NO stretch is observed as the most intense signal at 602 cm^{-1}, with the weaker features at 525 and 543 cm^{-1} again associated with Fe-N-O bending modes (see Figure 1). The N-O bond of this complex is the weakest (and most activated) in the series, with an N-O stretching frequency of 1568 cm^{-1} as determined by IR spectroscopy.

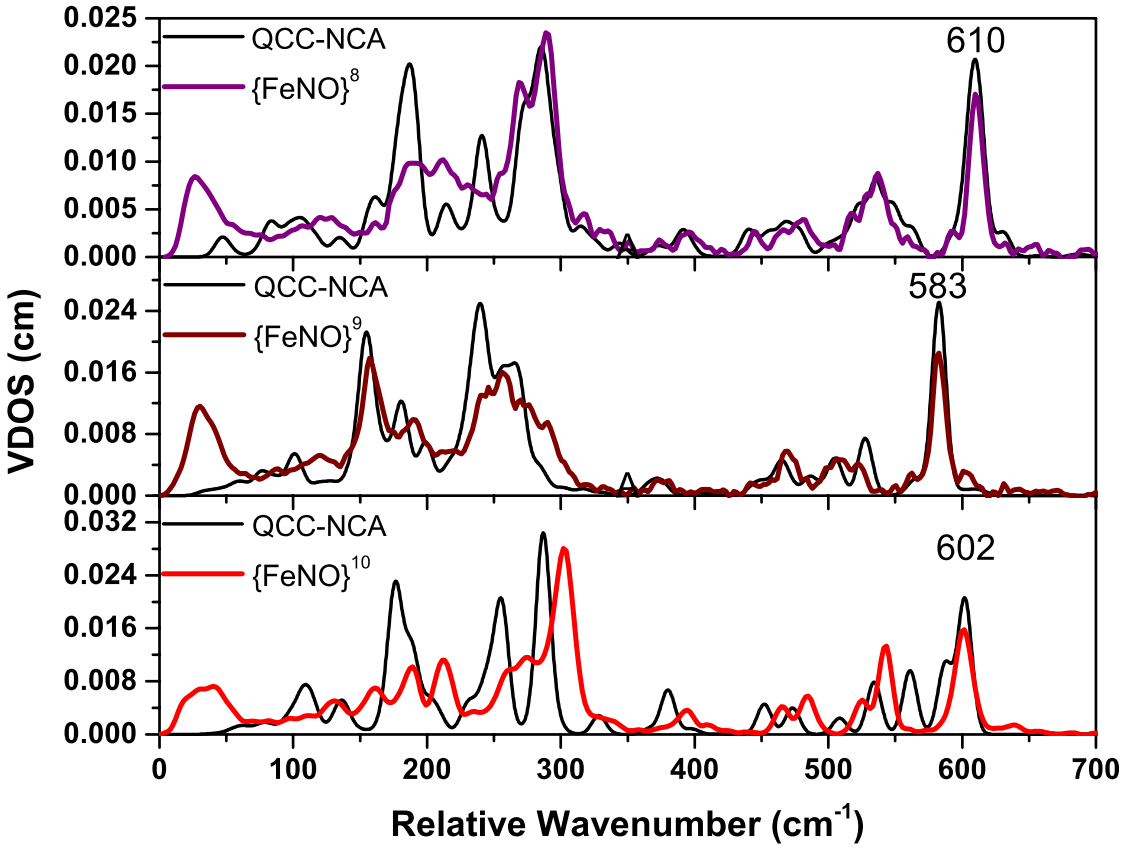

Figure 7.1 Experimental NRVS VDOS data of the ls-{FeNO}^{8} complex [Fe(TPB)(NO)](BAr$^{F}_{4}$) (purple), the ls-{FeNO}^{9} complex [Fe(TPB)(NO)] (brown) and the ls-{FeNO}^{10} complex [Na(12-crown-4)$_2$][Fe(TPB)(NO)] (red) vs QCC-NCA fits (black).

The intense, high-energy NRVS feature of the ls-{FeNO}^{9} species, observed at 583 cm^{-1}, is again assigned to the Fe-NO stretch. This mode is significantly shifted compared to 610 cm^{-1} ($\Delta\nu$ = -27 cm^{-1}) and 602 cm^{-1} ($\Delta\nu$ = -19 cm^{-1}) in the other two complexes, respectively, which, as I will show below, is due to spin polarization. The Fe-N-O bending modes are similarly shifted as well (506 and 522 cm^{-1}, see Figure 1). The N-O stretch of this complex is located at 1667 cm^{-1}.

In summary, comparison of the Fe-NO and N-O stretching frequencies along the ls-{FeNO}$^{8-10}$ series does not reveal a consistent trend. In a simple π-backbonding model (between the Fe-d and NO(π*) orbitals), I would anticipate that concomitant with the observed stepwise

weakening of the N-O bond along the ls-{FeNO}$^{8\text{-}10}$ series there would be a stepwise strengthening of the Fe-NO bond. Instead, for the ls-{FeNO}$^{8/9}$ pair, both the Fe-NO and N-O stretching frequencies (and bond strengths) decrease in the ls-{FeNO}^{9} compound. This trend is then reversed in the ls-{FeNO}$^{9/10}$ pair (now showing a pattern that would be in line with an increase in π-backbonding upon reduction), creating a discontinuity in the observed behavior. Thus, it is clear that a more detailed analysis, one that considers all available experimental data supported by electronic structure calculations, is necessary.

7.2 DFT Calibration for the ls-{FeNO}$^{8\text{-}10}$ Series

In our previous report, the ls-{FeNO}^{8} and ls-{FeNO}^{10} complexes were described as closed shell systems, on the basis of their diamagnetic ground states (from multinuclear nuclear magnetic resonance (NMR) spectroscopy). Alternatively, diamagnetic ground states could also arise from strong antiferromagnetic coupling between a hs iron center and a triplet NO^- ligand, which is often observed for non-heme Fe-NO complexes.[10] Furthermore, a recent interrogation of a related redox series, $[Fe(TPB)(NNMe_2)]^{+/0/-}$, by experiment and theory revealed antiferromagnetic coupling between the Fe center and a hydrazyl radical anion, $[NNMe_2]^{\bullet-}$ in some redox states.[11] Therefore, I decided to re-evaluate whether the ground states of the $[Fe(TPB)(NO)]^{+/0/-}$ complexes are best described by closed shell (CS) or broken-symmetry (BS) wave functions. As in previous work, I applied both the gradient-corrected functional BP86 and the hybrid functional B3LYP, now in combination with the TZVP basis set, for these calculations.[12-16] While BP86 has previously been shown to be a reliable functional in predicting geometric structures and spectroscopic properties of iron-nitrosyl complexes, B3LYP tends to underestimate the covalency of the Fe-N-O moiety.[17,18] However, hybrid functionals like B3LYP

with a higher percentage of Hartree-Fock exchange often allow for the geometry optimization of BS states in strongly spin-coupled systems, which is difficult with gradient-corrected functionals like BP86.

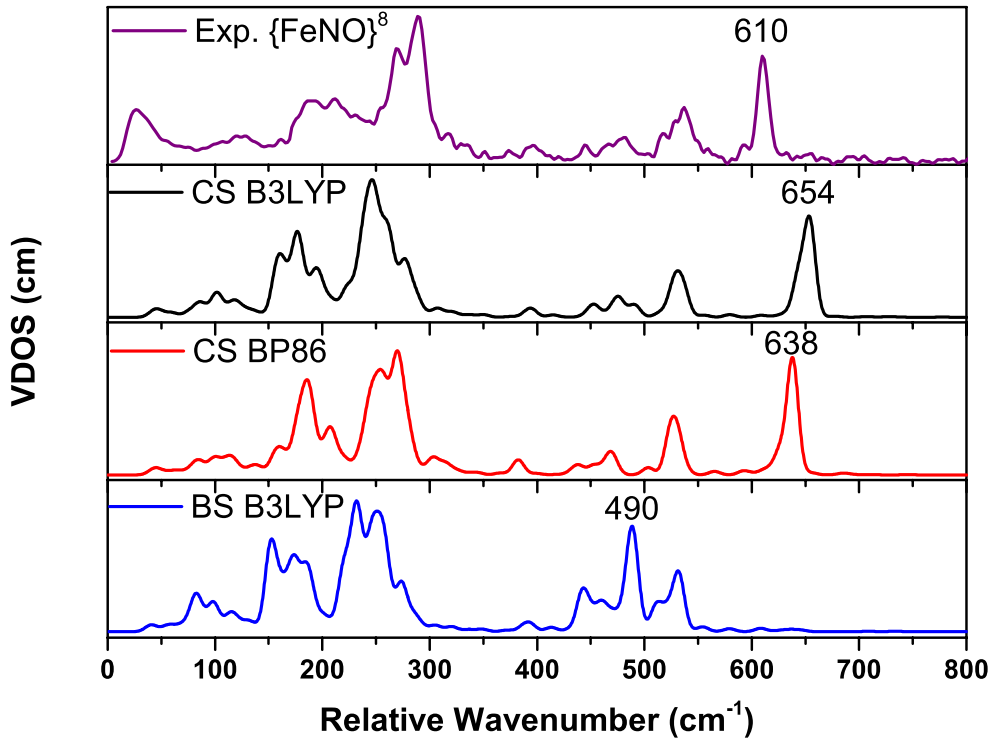

Figure 7.2 Experimental NRVS VDOS data of the ls-{FeNO}^{8} complex (top) in comparison with the spectra generated by closed-shell (middle) and broken-symmetry (bottom) calculations, using the indicated functionals together with the TZVP basis set.

To our surprise, the structural features derived from X-ray crystallography were well-reproduced by both the CS and BS state in B3LYP calculations on the ls-{FeNO}^{8} complex. For example, the N-O bond length only deviates by 0.01 Å for both states (1.16/1.17/1.17 Å for exp/CS/BS). Similarly, the Fe-NO bond distance shows very good agreement with the experimental data, with just 0.01-0.02 Å deviation for both states (1.66/1.65/1.68 Å for exp/CS/BS). Both calculations show moderate agreement with the experimental Fe-B bond distance (2.31/2.37/2.37 Å for exp/CS/BS). Finally, the BS state shows better agreement with the

experimental data for the Fe-N-O angle (176/172/175° for exp/CS/BS). Thus, although purely structural comparisons do not distinguish between a CS or BS electronic structure for the ls-{FeNO}^{8} complex, the accuracy of the predicted NRVS spectra is dramatically different, as shown in Figure 2. Whereas the predicted spectrum for CS shows very good agreement with experiment, the BS calculation shows large deviations from the experimental data (Fe-NO stretch: 610/654/490 cm^{-1} for exp/CS/BS). Interestingly, the BS-predicted Fe-NO stretch at 490 cm^{-1} is in line with experimentally determined Fe-NO stretching frequencies in complexes featuring $^3NO^-$ ligands,[10,19,20] suggesting that the disagreement is not an artifact of the calculation. In summary, this result shows that the CS wavefunction provides a better representation of the ground state electronic structure of the ls-{FeNO}^{8} complex, which differs from most other (trigonal-bipyramidal) non-heme iron-NO complexes.[10,21-23]

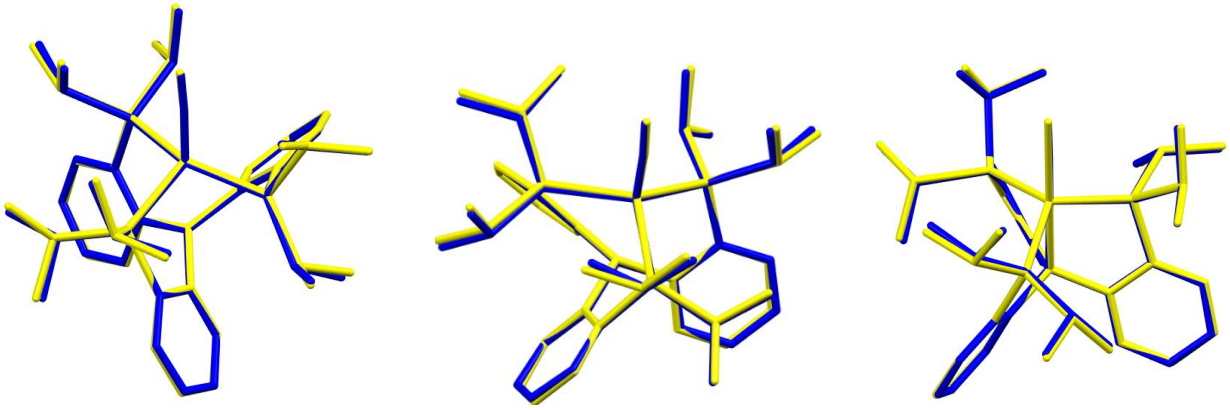

Figure 7.3 Overlay of crystal structures (blue) and the BP86/TZVP-optimized structures (yellow) of the ls-{FeNO}$^{8-10}$ series, $[Fe(TPB)(NO)]^{+/0/-}$, showing excellent agreement between the DFT-predictions and the experimental structures.

Comparing CS solutions calculated with both B3LYP and BP86, I find that the BP86 functional not only better reproduces the vibrational and structural data for the ls-{FeNO}$^{8-10}$ series, but is also able to accurately predict the isomer shift (δ) and quadrupole splitting ($|\Delta_{eq}|$) derived from Mössbauer spectroscopy and the hyperfine parameters derived from pulse EPR

spectroscopy (Table 1). Thus, I confirm that a CS, highly covalent description of the ground state in the $[Fe(TPB)(NO)]^{+/0/-}$ complexes is most appropriate.

Table 7.1 Experimental structural and spectroscopic data versus computational results for the series of ls-$\{FeNO\}^{8-10}$ complexes.

	ls-$\{FeNO\}^8$		**ls-$\{FeNO\}^9$**		**ls-$\{FeNO\}^{10}$**	
	Exp.	**BP86**	**Exp.**	**BP86**	**Exp.**	**BP86**
Geometric Parameters (Å and degrees)						
d(N–O)	1.16	1.18	1.19	1.19	1.22	1.21
d(Fe–NO)	1.66	1.66	1.67	1.66	1.65	1.65
d(Fe–B)	2.31	2.32	2.45	2.42	2.45	2.46
<Fe–N–O	176	174	176	176	179	180
d(Fe–P)	2.28	2.33	2.28	2.30	2.21	2.24
d(Fe–P)	2.28	2.33	2.30	2.32	2.21	2.24
d(Fe–P)	2.29	2.31	2.35	2.37	2.23	2.24
P-Fe-P	100	99	106	107	115	116
P-Fe-P	101	101	111	110	116	116
P-Fe-P	154	154	126	126	116	116
Spectroscopic Parameters: Vibrational (cm^{-1}, mdyn/Å and mdyn•Å)						
ν(Fe–NO)	610	638	583	621	602	633
ν(N-O)	1745	1751	1667	1692	1568	1607
δ_{lb}**(Fe-N-O)**	540/537	531/525	522/506	516/508	543/525	561/535
f(Fe-NO)	4.53	4.95	4.15	4.80	4.45	5.07
f(N-O)	12.5	12.4	11.3	11.5	9.79	10.1
f(Fe-B)	0.51	0.51	0.42	0.42	1.56	1.56
Spectroscopic Parameters: Mössbauer (mm/s)						
δ	0.24	0.30	0.26	0.25	0.17	0.20
ΔE_Q	1.50	1.43	0.91	0.81	1.62	1.53
Spectroscopic Parameters: Pulse EPR (MHz)						
A(^{14}N)	-	-	-6.0, -8.3, 3.8	-0.8, -5.1, 8.8	-	-
A(^{11}B)	-	-	14.7, 14.7, 18.0	-15.2, -15.6, -20.3	-	-

The BP86-optimized structures show very good agreement with the crystal structures of all three compounds, as further demonstrated by the structural overlays in Figure 3. The ls-$\{FeNO\}^8$ complex has a distinct distorted trigonal-bipyramidal geometry, where one of the P-Fe-P angles in the trigonal plane is expanded to 154° allowing for an unusual intramolecular η^4-BCCP interaction.

Both of these features are well reproduced in the DFT optimized structure. As the compound is reduced to the ls-{FeNO}^{9} state, the complex becomes more symmetric (closer to an actual trigonal-bipyramidal geometry), and the unusually large P-Fe-P angle decreases from 154^{o} to 126^{o}. The ls-{FeNO}^{10} complex is the most symmetric with only about 1^{o} difference between the three P-Fe-P angles.

The BP86 calculations reproduce the vibrational properties of the ls-{FeNO}$^{8-10}$ complexes, especially the Fe-NO and N-O stretching frequencies, quite well with respect to experimental data (Figures S1). Importantly, the calculations capture the lack of a correlation between the change in Fe-NO and N-O stretching frequencies along the ls-{FeNO}$^{8-10}$ series (see Table 1). Thus, I use these calculations as the basis to further analyze the NRVS data and refine the force constants of the Fe-N-O units in the three complexes. In this way, I further address the question of whether the reduction along the ls-{FeNO}$^{8-10}$ series is metal- or NO-based.

7.3 QCC-NCA for the ls-{FeNO}$^{8-10}$ Series

To obtain simulations of the NRVS data of the ls-{FeNO}$^{8-10}$ complexes and determine high-quality (experimental) force constants for their Fe-N-O units, a quantum-chemistry centered normal coordinate analysis (QCC-NCA) was performed.[11,24] This process allows us to correct the DFT-calculated force constants, vibrational frequencies and NRVS intensities by fitting the experimental NRVS data, starting from the DFT-predicted force field. In this way, I obtain high-quality force constants for the modes of interest that afford detailed insight into the changes in Fe-NO and N-O bonding along the ls-{FeNO}$^{8-10}$ series, independent of potential vibrational (mode) mixing. In the spirit of the QCC-NCA approach,[24] only the small number of force constants relevant to the Fe-N-O unit are varied, while the DFT-predicted force constants of the [Fe(TPB)] frame are kept unchanged.

For the ls-{FeNO}^{8} complex, the Fe-NO force constant was corrected from the calculated value of 4.95 to 4.53 mdyn/Å to fit the Fe-NO stretch at 610 cm^{-1} (DFT-calculated value: 638 cm^{-1}). Since the Fe-N-O unit is close to linear, the Fe-N-O unit has two linear bending vibrations, which are assigned to the modes at 537 and 540 cm^{-1} in the NRVS data, with force constants of 0.41 and 0.57 mdyn•Å. The relatively high anisotropy of the two linear bends is consistent with the strong deviation from trigonal symmetry in the FeP_3 plane. The experimental N-O force constant of 12.5 mdyn/Å is close to the initial, DFT-calculated value. Vibrational assignments are listed in Table 2, and the experimental and QCC-NCA simulated NRVS data are compared in Figure 1. All force constants that were fit are listed in Table 3.

Table 7.2 Experimental NRVS data vs. QCC-NCA simulation results (in cm^{-1}) and vibrational assignments for the ls-{FeNO}$^{8-10}$ series.

	ls-{FeNO}^{8}		**ls-{FeNO}^{9}**		**ls-{FeNO}^{10}**	
	Exp.	**QCC-NCA**	**Exp.**	**QCC-NCA**	**Exp.**	**QCC-NCA**
ν(Fe–N)	610	610	583	583	602	602
ν(N-O)	1745	1745	1667	1667	1568	1568
δ(Fe-N-O)	537	535	506 (500)	506 (504)	525	536
δ(Fe-N-O)	540	544	522	527	543	570

The same process was applied to the ls-{FeNO}^{9} and ls-{FeNO}^{10} compounds, and the resulting QCC-NCA simulated NRVS data are compared to experiment in Figure 1. Vibrational assignments are provided in Table 2, and key force constants of the ls-{FeNO}$^{8-10}$ series are listed in Tables 2 and 4. Reduction of the ls-{FeNO}^{8} to the ls-{FeNO}^{9} complex causes both the Fe-NO and N-O bonds to become weaker (with force constants decreasing from 4.53/12.5 to 4.15/11.3 mdyn/Å, respectively), confirming that this unusual drop in both the Fe-NO and N-O stretching frequencies is not caused by unforeseen mode mixing.

Whereas this trend is not in agreement with a simple change in π-backbonding, as discussed above, this type of behavior actually resembles that observed for the hs-{FeNO}$^{7/8}$ complexes,

[Fe(TMG$_3$tren)(NO)]$^{2+/+}$, where reduction leads to a decrease in π-donation from the $^3NO^-$ ligand to the hs-Fe center.[10] Reduction from the ls-{FeNO}^{9} to the ls-{FeNO}^{10} state causes a further weakening of the N-O bond (N-O force constant: 11.3 vs 9.79 mdyn/Å), but at the same time, the Fe-NO bond now becomes stronger (Fe-NO force constant: 4.15 to 4.45 mdyn/Å). This is opposite to the trend observed for the ls-{FeNO}$^{8/9}$ pair, but in agreement with the trends derived from the vibrational frequencies (see above).

A distinct Fe-B stretching mode is not observed in the experimental NRVS data. Because of this, I was unable to optimize the corresponding Fe-B force constants via the QCC-NCA process, and Table 3 lists the DFT-calculated Fe-B force constants. Nonetheless, the close agreement between the DFT-predicted and the experimental force constants gives us confidence that the Fe-B force constants are accurate (±10%).

Table 7.3 Summary of key force constants.

Force Constant	**ls-{FeNO}^{8}**	**ls-{FeNO}^{9}**	**ls-{FeNO}^{10}**	**{FeN$_2$}^{9}**	**Force Constant**
Fe–NO	4.53	4.15	4.45	2.62	**Fe–N$_2$**
Fe–B	0.51	0.42	1.56	1.21	**Fe–B**
N–O	12.5	11.3	9.79	14.9	**N–N**
Fe–P$_4$/P$_5$/P$_6$	1.40/1.56/1.91	1.03/1.17/0.98	1.96/1.99/1.93	3.06/1.36/1.32	**Fe–P$_4$/P$_5$/P$_6$**
Fe–N–O$_{lb}$	0.41	0.46	0.54	0.51	**Fe–N–N$_{lb}$**
Fe–N–O$_{lb}$	0.57	0.43	0.54	0.62	**Fe–N–N$_{lb}$**

In the ls-{FeNO}^{8} and ls-{FeNO}^{9} complexes, the Fe-B interaction is relatively weak, with a calculated force constant of ~0.5 mdyn/Å. Reduction to the ls-{FeNO}^{10} state then causes a remarkable increase in the Fe-B bond strength, with the Fe-B force constant increasing to 1.56 mdyn/Å. The data thus suggest that an Fe-B single bond forms in the ls-{FeNO}^{10} state via a reverse dative bond with the Fe center serving as a Lewis base, donating a pair of electrons to the borane Lewis acid. This clearly shows that d_{z^2} is doubly occupied in the ls-{FeNO}^{10} state. Relatedly, a dative $B^- \rightarrow Cu$ bond has previously been identified computationally and spectroscopically in $[Cu(TPB)]^-$, [25] and Fe-B flexibility has been implicated as a key feature in stabilizing Fe across formal redox states.[26,27]

7.4 Pulse EPR Measurements of the ls-{FeNO}^{9} Complex – Done by the Peters Lab

The ls-{FeNO}^{9} complex [Fe(TPB)(NO)] has an $S_t = 1/2$ ground state and is therefore EPR active. As previously reported, this complex displays an axial EPR signal (g = 1.99, 1.99, 2.45) with a large g_z value (2.45). This is consistent with the approximate trigonal-bipyramidal geometry of the complex and an electronic structure in which the electron hole is mostly located in the *xy*-plane (with the Fe-NO vector corresponding to the *z*-axis) and on the metal center (directly indicated by the large *g* shift). This leads to strong 2nd order spin-orbit coupling in the *z* direction. Indeed, similar axial EPR spectra with large g_z shifts have been measured for a number of TPB and P_3^{Si} (features Si in place of B) complexes with similar electronic structures (*i.e.*, e_g^3 ground states).[28] As these complexes vary primarily in the identity of their axial ligand, information about that Fe-L interaction can be extracted from the *g*-anisotropy. This is further analyzed in the Discussion section, in direct comparison to the isoelectronic N_2-adduct $[Fe(TPB)(N_2)]^-$.

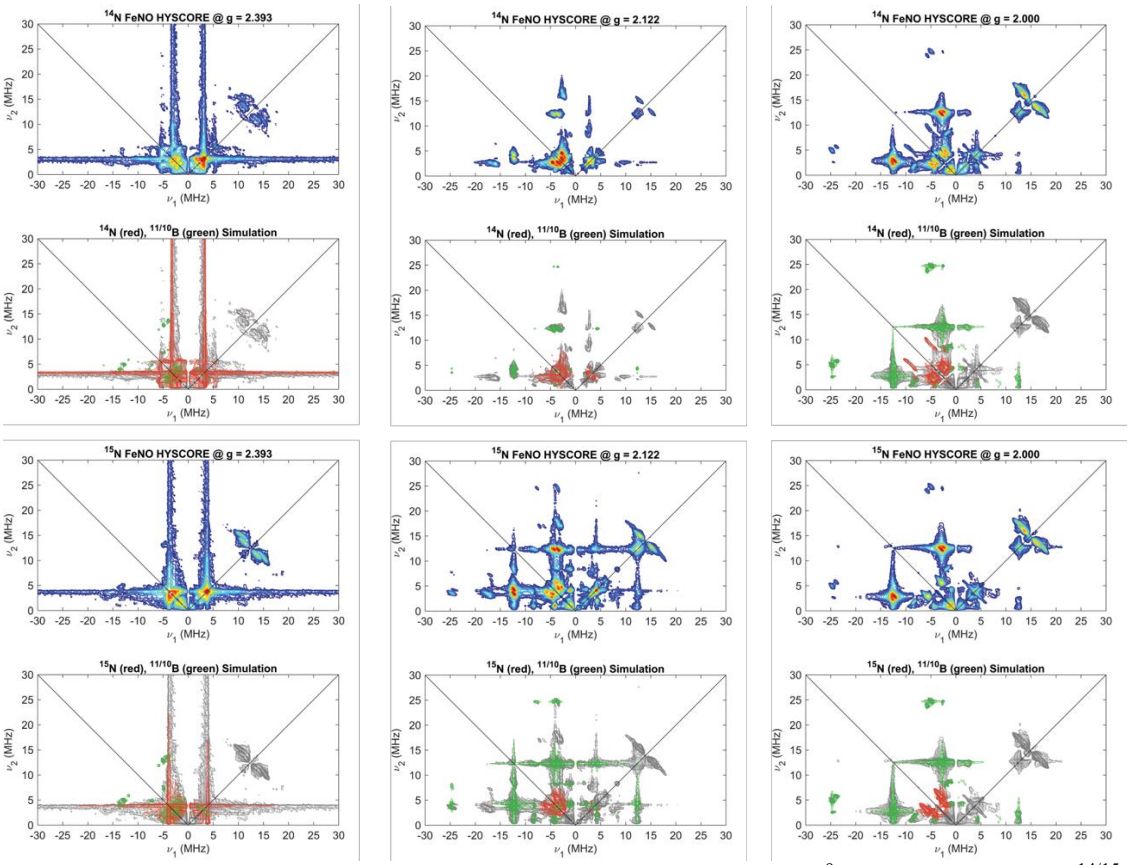

Figure 7.4 Field-dependent X-band HYSCORE spectra of the ls-{FeNO}^{9} complex [Fe(TPB)($^{14/15}$NO)]. The experimental data are plotted in color in the top panels, ranging from dark blue to red in increasing intensity. These same data are plotted in grey in the bottom panels, with $^{14/15}$N and ^{11}B simulations overlaid in red and green, respectively. Unsimulated features centered around 15 MHz in the (+,+) quadrant arise from weakly coupled ^{1}H nuclei of the ligand or from solvent. Acquisition parameters: Temperature = 7 K; microwave frequency = 9.711 GHz; B_0 = 290 mT (g = 2.393), 327 mT (g = 2.122), 347 mT (g = 2.000); MW pulse length ($\pi/2$, π) = 8 ns, 16 ns; τ = 142 ns (g = 2.393), 144 ns (g = 2.122), 136 ns (g = 2.000); t_1 = t_2 = 100 ns; Δt_1 = Δt_2 = 16 ns; shot repetition time (srt) = 1 ms.

Interestingly, if we include all (P_3^E)Fe-L complexes (E = B in TPB, Si) with an e_g^3 ground state for which an X-ray structure and EPR spectrum has been measured, we find a strong linear correlation between Δg_z and the Fe–P distance (R^2 = 0.92). This suggests that the covalency of the Fe-P bond and/or the out-of-plane displacement of the Fe center might play a key role in determining Δg_z. Furthermore, we find that the Fe center in [Fe(TPB)(NO)] has a Δg_z that lies between those found for formally Fe^I and Fe^{III} ions in (P_3^E)Fe-L complexes. Given the vibrational and computational data are consistent with an NO^+ ligand state and thus the Fe is formally Fe^{-I},

this demonstrates the tremendous ability of a covalently bonded NO^+ ligand to accept electron density.

Analysis of X-band hyperfine sublevel correlation (HYSCORE) spectroscopy acquired on samples prepared with natural abundance (^{14}N) and ^{15}N labeled NO bound (see Figure 4) allowed us to accurately determine relatively weak hyperfine coupling constants to the coordinated $^{14/15}N(O)$ and ^{11}B centers, providing further insight into the electron spin distribution in the complex. The observed coupling to the ^{14}N nucleus is largely axial consistent with the axial g-tensor observed in the CW EPR measurements. Simulation of the ^{15}N HYSCORE data allowed for determination of the nitrogen hyperfine coupling tensor as $A(^{15}N)$ = [8.4, 11.6, -5.4] MHz, independent of any influence from the nuclear quadrupole interaction present in the natural abundance data due to the presence of the $I = 1$ ^{14}N nucleus. Accounting for the relative gyromagnetic ratios of $^{14/15}N$ ($\gamma^{14}N/\gamma^{15}N = -0.7129$) the ^{14}N hyperfine coupling tensor is $A(^{14}N)$ = [-6.0, -8.3, 3.8] MHz, which can be decomposed into an isotropic component $a_{iso}(^{14}N) = -3.5$ MHz and an anisotropic component of $T(^{14}N)$ = [−2.5, −4.8, 7.3] MHz. The small a_{iso} value indicates that minimal spin (estimated: 0.002 e^-) is an a_1-type orbital (s or p_z) with most spin (estimated: 0.065 e^-) in the e-symmetric p_x and p_y set. These results would be consistent with a spin polarization mechanism that transfers electron density from the $d_{xy}/d_{x^2-y^2}$ orbitals into the p_x/p_y orbitals of the NO ligand. The total spin density of −0.07 e^- on the N atom is consistent with the DFT predictions for a CS state. Comparison of these hyperfine parameters with those similarly extracted for $[Fe(TPB)(NNMe_2)]^{+/-}$ further supports the CS rather than a BS electronic ground state for the ls-$\{FeNO\}^9$ complex.

Comparison of the HYSCORE data of the ^{14}N and ^{15}N isotopologues allows for accurate determination of not only the hyperfine coupling constants, but also the *electric* interaction of the

$I = 1$ ^{14}N nuclear quadrupole with the inhomogeneous electric field induced by electron density in p-orbitals at the nucleus. This interaction is parameterized by the nuclear quadrupole coupling constant (e^2qQ/h = 0.8) and the electric field gradient (EFG) asymmetry (η = 0). The low magnitude of e^2qQ/h and negligible EFG rhombicity indicates nearly spherical charge density about the nitrogen nucleus in this complex, in agreement with the linear Fe-N-O unit and equal spin distribution in the p_x and p_y orbitals.

The hyperfine coupling to boron with A(^{11}B) = [14.7, 14.7, 18.0] MHz can be decomposed into a_{iso}(^{11}B) = 15. 8 MHz and a small anisotropic contribution of T(^{11}B) = [−1.1, −1.1, 2.2] MHz. These data indicate that significantly less electron density is on that ligand (0.006 e^- in a_1 type orbitals and 0.017 e^- in e-type orbitals) and are consistent with the DFT results. We interpret these results as being consistent with the lack of available orbitals of appropriate symmetry to accept electron density from the xy-plane via spin polarization. X-band ENDOR experiments to determine the hyperfine coupling to ^{31}P of the phosphine ligands are best modeled with a single class of fairly isotropic coupling constants, A(^{31}P) = [82, 70, 70] MHz, which corresponds to a_{iso}(^{31}P) = 74 MHz and an anisotropic component of T(^{31}P) = [8, −4, −4] MHz. The large hyperfine coupling to the ^{31}P centers again supports the idea that the electron hole is mostly located in the *xy*-plane.

7.5 Electronic Structure Analysis

The ls-{FeNO}^{8} Complex has eight valence electrons, as indicated by the Enemark-Feltham index, and, as discussed above, the complex has a closed-shell singlet ground state, which means that of the total seven valence MOs (5 Fe(d) + 2 NO(π*) orbitals), four valence MOs are doubly occupied, and three are empty. The MOs themselves are strongly mixed, and Scheme 7.2 represents a simplified version of the bonding scheme. Here, the Fe-N-O unit corresponds to the

molecular *z*-axis. The strong distortion away from C_3 symmetry towards a T-shaped geometry in the FeP_3 plane, characterized by a large P-Fe-P angle (154°), causes a large energy splitting between the d_{xy} and $d_{x^2-y^2}$ orbitals of 1.97 eV, as indicated in Scheme 7.3. In this geometry, the lower energy orbital, d_{xy} (HOMO-1), is essentially σ-nonbonding with respect to the phosphine ligands (80% Fe character). Whereas, the lowest unoccupied molecular orbital (LUMO), the empty $d_{x^2-y^2}$ orbital, shows strong antibonding (σ*) interactions with the in-plane phosphine donors (see Scheme 7.3). Unexpectedly, the $d_{x^2-y^2}$ orbital also has a strong admixture of one of the NO(π*) orbitals (38% Fe, 14% NO), but because the MO is unoccupied, it does not play a role for bonding in the ls-$\{FeNO\}^8$ complex. This type of admixture, however, becomes relevant in the more reduced species.

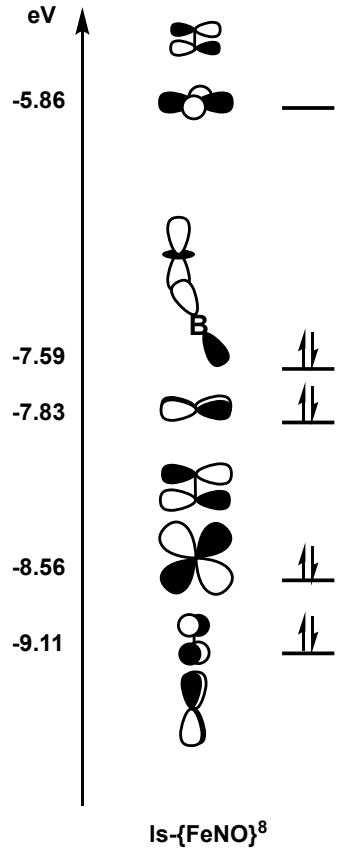

Scheme 7.2 Schematic MO diagram of the ls-$\{FeNO\}^8$ complex, calculated with BP86/TZVP.

The highest occupied molecular orbital (HOMO) of the ls-{FeNO}^{8} complex is the doubly-occupied d_{z^2} orbital, which has a notable contribution from the unoccupied boron(p)-orbital (43% Fe, 12% B). This leads to a stabilization of the d_{z^2} orbital, which normally is the highest energy orbital in a trigonal-bipyramidal coordination geometry. This weak Lewis base (Fe) – Lewis acid (B) interaction (Fe-B force constant: 0.51 mdyn/Å) is indicative of a fractional Fe-B bond order. Hence, despite the relatively short Fe-B distance (2.31 Å), the bonding between the doubly-occupied d_{z^2} orbital and the unoccupied boron(p)-orbital is reduced by poor orbital overlap resulting from the tilt of the $BC(Ph)_3$ plane away from the Fe-B axis.

The lowest-lying valence orbitals are the doubly-occupied, Fe-NO π-bonding combinations of the d_{xz}_π^*_x and d_{yz}_π^*_y orbitals (HOMO-2 and HOMO-3). These bonds are very covalent, with about 60% Fe(d) and 30% NO(π*) contribution.

Based on this analysis, and assigning MOs to the atom or group with the dominant charge contribution, the ls-{FeNO}^{8} complex can formally be assigned an Fe(0)-NO^+ type electronic structure with all 8 valence electrons originating primarily from the Fe center, and two very strong π-backbonds with the NO^+ ligand (consistent with the large Fe-NO force constant of 4.53 mdyn/Å). The presence of an NO^+ ligand explains the absence of spin polarization in this system. This is similar to six-coordinate ls-{FeNO}^{6} complexes in hemes, which have been shown to have a closed-shell Fe(II)-NO^+ type ground state with no spin polarization.[14,29] In this sense, the FeNO unit in the ls-{FeNO}^{8} complex could be considered an electronic analog to that of heme ls-{FeNO}^{6} complexes, where two additional electrons of the Fe center are stabilized by the d_{z^2}–B(p) interaction. This becomes more evident in the ls-{FeNO}^{10} system (see below).

Finally, the crystal structure of the ls-{FeNO}^{8} complex reveals a unique π-bond between the iron center and the C=C bond of one of the aromatic benzene rings. This interaction is unique

in the ls-{FeNO}^{8} complex and explains the observed, significant contributions of phenyl orbitals to the valence MOs in this complex, which complicates the analysis. However, this interaction does not affect the FeNO moiety significantly.

The ls-{FeNO}^{9} Complex has an EPR-active S_t = 1/2 ground state, which provides additional spectroscopic handles to further interrogate its ground state electronic structure. Due to spin-polarization effects, the α- and β-spin covalencies differ in the ls-{FeNO}^{9} complex, which complicates the analysis of its electronic structure. As we might expect based on its more C_3-symmetric structure, reduction of the ls-{FeNO}^{8} complex results in an orbital ordering more similar to that of a canonical trigonal bipyramid (see Scheme 7.3). The SOMO of the ls-{FeNO}^{9} complex is the $d_{x^2-y^2}$ orbital, as indicated in Scheme 7.4, pointing towards an iron-based reduction (in agreement with the EPR results). Because of this, the Fe-P covalency in the xy-plane is reduced, and the energy splitting between the $d_{x^2-y^2}$ and d_{xy} orbitals decreases to 1.02 eV. Accordingly, the d_{xy} orbital is now higher in energy than the d_{z^2} orbital, and becomes the SOMO-1. The two lowest energy valence orbitals remain the Fe-NO π-bonding interactions, which again correspond to the bonding combinations of the d_{xz} and d_{yz} orbitals and the NO($\pi^*_{x/y}$) orbitals. Finally, the d_{z2} orbital is again lowered in energy by the Fe-B interaction. Scheme 7.4 shows the resulting bonding scheme of the ls-{FeNO}^{9} complex, which points towards an unusual Fe(−I)-NO^+ type ground state.

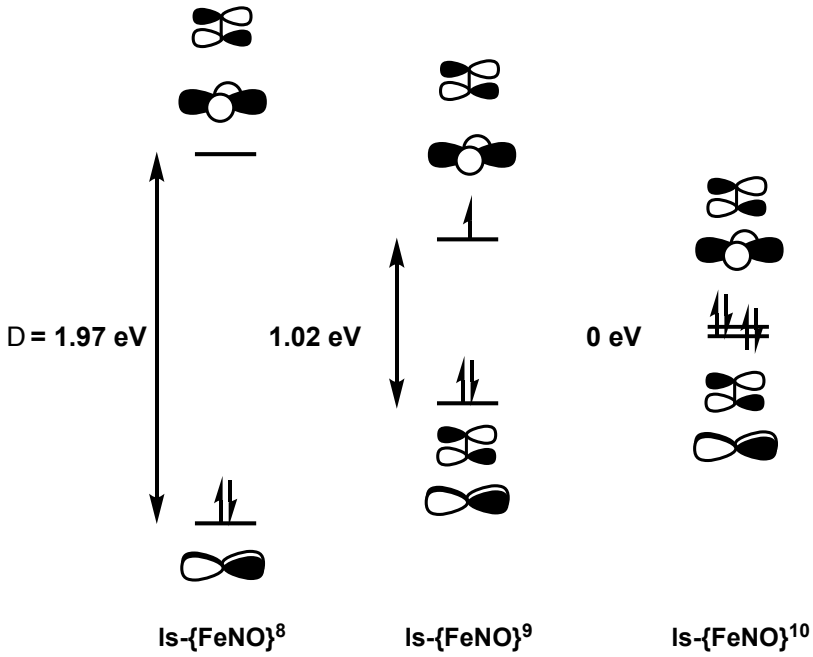

Scheme 7.3 Ligand field splitting between the $d_x2_{-y}2$ and the d_{xy} orbitals, as a function of the FeP_3 geometry in the *xy*-plane.

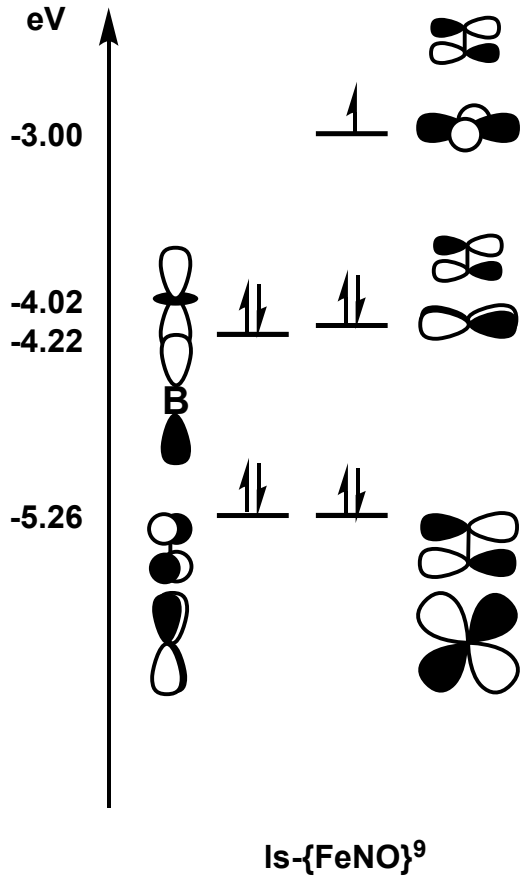

Scheme 7.4 Schematic MO diagram of the ls-{FeNO}^{9} complex, calculated with BP86/TZVP.

The experimental data show that the Fe-NO bond becomes weaker upon reduction of the ls-{FeNO}^{8} to the ls-{FeNO}^{9} state, as reflected by a drop of the corresponding Fe-NO force constant from 4.53 to 4.15 mdyn/Å and of the Fe-NO stretch from 610 to 583 cm^{-1}. This indicates a reduction in the covalency of the two Fe-NO π-bonds in the ls-{FeNO}^{9} state. The DFT calculations underestimate the weakening of the Fe-NO stretch ($\Delta = -27$ cm^{-1} experimentally versus −17 cm^{-1} by DFT) and the weakening of the N-O stretch ($\Delta = -78$ cm^{-1} experimentally versus −59 cm^{-1} by DFT). Nonetheless, DFT captures the seemingly counterintuitive trend that the Fe-NO and N-O bond both weaken upon reduction.

Due to spin polarization, both Fe-NO π-bonds are stronger and more covalent in β-spin compared to α-spin, which manifests itself in the appearance of about −0.1 negative spin density on the NO ligand, in the $\pi^*_{x/y}$ orbitals. This finding is supported by the pulse EPR measurements, showing weak, mostly anisotropic hyperfine coupling with the ^{14}N atom of the coordinated NO ligand. Based on this finding alone, one would predict that the N-O stretch should increase in energy in the reduced complex, but this is not the case experimentally. The reason for the sharp drop in the N-O stretch from 1745 to 1667 cm^{-1} upon reduction requires an increase in the occupation of the NO($\pi^*_{x/y}$) orbitals in the reduced complex, without increasing the Fe-NO bond strength. This in fact is the case. As shown in Scheme 7.4, both the $d_{x^2-y^2}$ SOMO (41% Fe(d) and 4% NO character) and the doubly-occupied d_{xy} orbital (63% Fe(d) and 5% NO character) of the ls-{FeNO}^{9} complex show a distinct admixture of the NO($\pi^*_{x/y}$) orbitals. Occupation of these MOs effectively transfers electron density into the NO($\pi^*_{x/y}$) orbitals, weakening the N-O bond, but <u>without</u> significantly affecting the Fe-NO bond strength. Although one might initially dismiss this orbital interaction as an artefact of DFT, the available data show that this is a real effect.

Indeed, it is significant and likely underestimated in the DFT calculations, considering the larger experimental shift in the N-O stretch ($\Delta = -78$ cm^{-1}) compared to $\Delta = -59$ cm^{-1} predicted by DFT. Using a linear scaling approach, I can roughly estimate from the N-O stretches of free NO^+ (2387 cm^{-1}) and NO (1876 cm^{-1}; $\Delta \approx 500$ cm^{-1}) that a shift in the N-O stretch of ~80 cm^{-1} requires an increase in the occupation of the NO($\pi^*_{x/y}$) orbitals by 0.16 electrons (assuming similar electronic structures), which is slightly underestimated in the calculations (Loewdin charges for NO: ls-{FeNO}^{8}: +0.02; ls-{FeNO}^{9}: -0.11, $\Delta(e^-) = 0.13$).

Further support for the importance of spin polarization effects to the bonding in the ls-{FeNO}^{9} complex is that the Fe-B interaction is predicted to be similarly polarized. Except in this case the relevant ligand orbital is B(p_z) with asymmetry in the d_{z^2}–B(p_z) interaction. This bond is distinctively more covalent in β-spin (22% B(p_z) admixture into d_{z^2}) compared to α-spin (10% B(p_z) contribution), again resulting in about −0.1 negative spin density on the boron atom. This is supported by the pulse EPR measurements, showing weak hyperfine coupling to the ^{11}B nucleus with a relatively larger component of its unpaired spin in an a_1-type (s or p_z) orbital. The DFT calculations predict that the Fe-B bond interaction becomes slightly weaker in the ls-{FeNO}^{9} compared to the ls-{FeNO}^{8} complex (due to the spin polarization), although in the absence of any vibrational information, it is difficult to confirm this. Therefore, I consider the Fe-B bond to be largely unchanged in the ls-{FeNO}^{9} complex.

Based on these observations, it is puzzling that despite the iron-based reduction in the ls-{FeNO}^{9} relative to the ls-{FeNO}^{8} complex, both the experimental and DFT-calculated Mössbauer isomer shifts only show a very small change (see Table 1). The main reason for this finding is the fact that the occupation of the $d_{x^2-y^2}$ orbital in the ls-{FeNO}^{9} complex leads to the weakening of the Fe-P interactions, since the $d_{x^2-y^2}$ orbital is Fe-P antibonding. This is reflected in

the corresponding Fe-P force constants, which drop from an average value of ~1.6 mdyn/Å to ~1.1 mdyn/Å upon reduction. This decrease in the Fe-P bonding partially compensates for the electron that is added to the $d_{x^2-y^2}$ orbital, as does the transfer of electron density from the *xy*-plane to the NO(π^*) orbitals (see above). This "redox buffering" causes a negligible change in the effective nuclear charge of the iron center upon reduction, and minimizes the change in the Mössbauer isomer shift.

The ls-{FeNO}^{10} Complex is completely diamagnetic with a CS ground state, as shown in Scheme 7.5. Compared to the ls-{FeNO}^{9} complex, the extra electron is located in the $d_{x^2-y^2}$ orbital, completing the d^{10} shell of the iron center. Therefore, once again, the reduction is iron-centered. As a consequence of the now $[d_{xy},d_{x^2-y^2}]^4$ electron configuration, the ls-{FeNO}^{10} complex adapts an almost perfect trigonal symmetry of the FeP_3 unit, causing the d_{xy} and $d_{x^2-y^2}$ orbitals to form a degenerate set (Scheme 7.3).

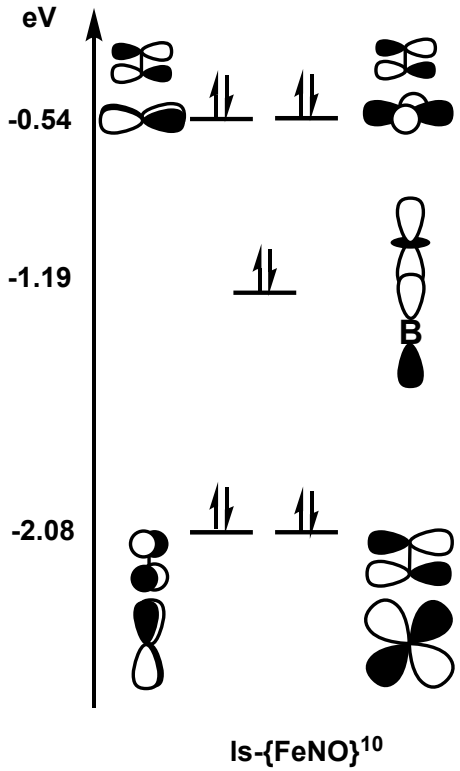

Scheme 7.5 Schematic MO diagram of the ls-{FeNO}^{10} complex, calculated with BP86/TZVP.

In agreement with this analysis, both orbitals show identical charge contributions, with 62% Fe(d) character and a 5% contribution from the NO(π*) orbitals. Likewise, the lowest lying valence orbitals are also a now degenerate d_{xz}/d_{yz} pair. This pair shows 53% Fe(d) and 38% NO(π*) contributions, indicating the presence of a very covalent Fe-NO bond, similar to that in the ls-{FeNO}^{8} complex (60% Fe and 30% NO). Indeed, the similar orbital contributions of the corresponding d_{xz}_π^*_x and d_{yz}_π^*_y bonding pairs and the similar Fe-NO force constants of 4.53 and 4.45 mdyn/Å are strongly suggestive of similar Fe-NO bonding interactions in the ls-{FeNO}^{8} and ls-{FeNO}^{10} complexes. Nonetheless, the N-O stretching frequency in the ls-{FeNO}^{10} complex is 177 cm^{-1} lower than in the ls-{FeNO}^{8} complex, and the N-O force constant is reduced by about 2.7 mdyn/Å. As discussed for the ls-{FeNO}^{9} compound, this is best explained not by increased Fe-NO π-backbonding but rather by the transfer of electron density from the xy-plane into the NO(π*) orbitals. Indeed, in the ls-{FeNO}^{10} complex, the $d_{xy}/d_{x^2-y^2}$ pair contains 5% NO(π*) character each, as indicated in Scheme 7.5. Once again, this likely represents a lower bound on the magnitude of this effect, given the reduction in the N-O stretching frequency (Δ_{exp} = −99 cm^{-1} vs Δ_{DFT} = −85 cm^{-1} compared to ls-{FeNO}^{9}) is underestimated in the calculations.

Due to the formal d^{10} configuration, the Fe center becomes unusually low-valent (Fe(−II)) in the ls-{FeNO}^{10} complex. However, this charge accumulation on the Fe center is largely compensated by a dramatic strengthening of the Fe-B interaction, indicated by the increase in the Fe-B force constant to 1.56 mdyn/Å, which corresponds to the formation of an Fe-B σ single bond. Here, the iron center becomes a Lewis base and donates one electron pair, located in the doubly-occupied d_{z^2} orbital, to the boron center, which therefore functions as a Lewis acid in the ls-{FeNO}^{10} complex. This mechanism is key to the stabilization of the ls-{FeNO}^{10} system. Because of the formation of a full Fe-B single bond, the d_{z^2} orbital drops in energy after reduction

and is now located significantly below the $d_{xy}/d_{x^2-y^2}$ degenerate pair. Orbital analysis further reveals that the corresponding (bonding) MO has 35% Fe(d) and 23% B(p_z) charge contributions (the rest is ligand contribution), in agreement with a very covalent Fe-B interaction. Thus, the ls-$\{FeNO\}^{10}$ complex has an Fe(-II)-NO^+ type electronic structure, but with the electron pair in the d_{z^2} orbital being strongly stabilized by donation to the boron Lewis acid. In this sense, the ls-$\{FeNO\}^{10}$ complex contains two non-innocent ligands and could be designated as ls-$\{BFeNO\}^{10}$.

Curiously, the ls-$\{FeNO\}^{10}$ complex has the Fe center with the most positive effective nuclear charge, based on the Mössbauer isomer shift. I attribute the positive isomer shift of the complex relative to the ls-$\{FeNO\}^9$ system to (a) the newly formed Fe-B single bond, which reduces the electron density on the Fe center, and (b) the onset of Fe-P backbonding. Our observations emphasize the uniqueness of the TPB coligand scaffold and its ability to stabilize extremely low-valent metal centers through an adjustable interaction between the metal center and the empty p_z orbital of boron. Surprisingly, the effect on the N-O bond strength observed for the ls-$\{FeNO\}^8$ and ls-$\{FeNO\}^{10}$ pair is not so much due to changes in the Fe-NO π-bond itself, but due to a secondary effect, i.e. the admixture of NO(π*) character into the $d_{x^2-y^2}/d_{xy}$ orbital pair as discussed above.

7.6 Discussion

In previously characterized redox series of Fe-NO complexes, Mössbauer spectroscopy has been a key tool for understanding the redox state of the Fe center. In the cyclam-ac supported Fe-NO series from Wieghardt and coworkers, the change in isomer shift (δ) across redox states is linear ($\Delta\delta \sim 0.2$ mm/s per redox state), which has been interpreted in terms of NO-centered redox changes, dramatically affecting the Fe-NO bond and, in turn, the isomer shift.[30,31] In the TMG_3tren supported Fe-NO series from Lehnert and coworkers even larger changes in the isomer shift are

observed (Δδ ~ 0.4 mm/s per redox state), which, in combination with other findings, was taken as evidence of Fe-centered redox changes.[10,32] More recently, Meyer's hs-{FeNO}$^{7-9}$ series with the TIMEN^{Mes} coligand has also been shown to follow metal-centered reductions, with changes in isomer shift of Δδ ~ 0.2 mm/s.[23]

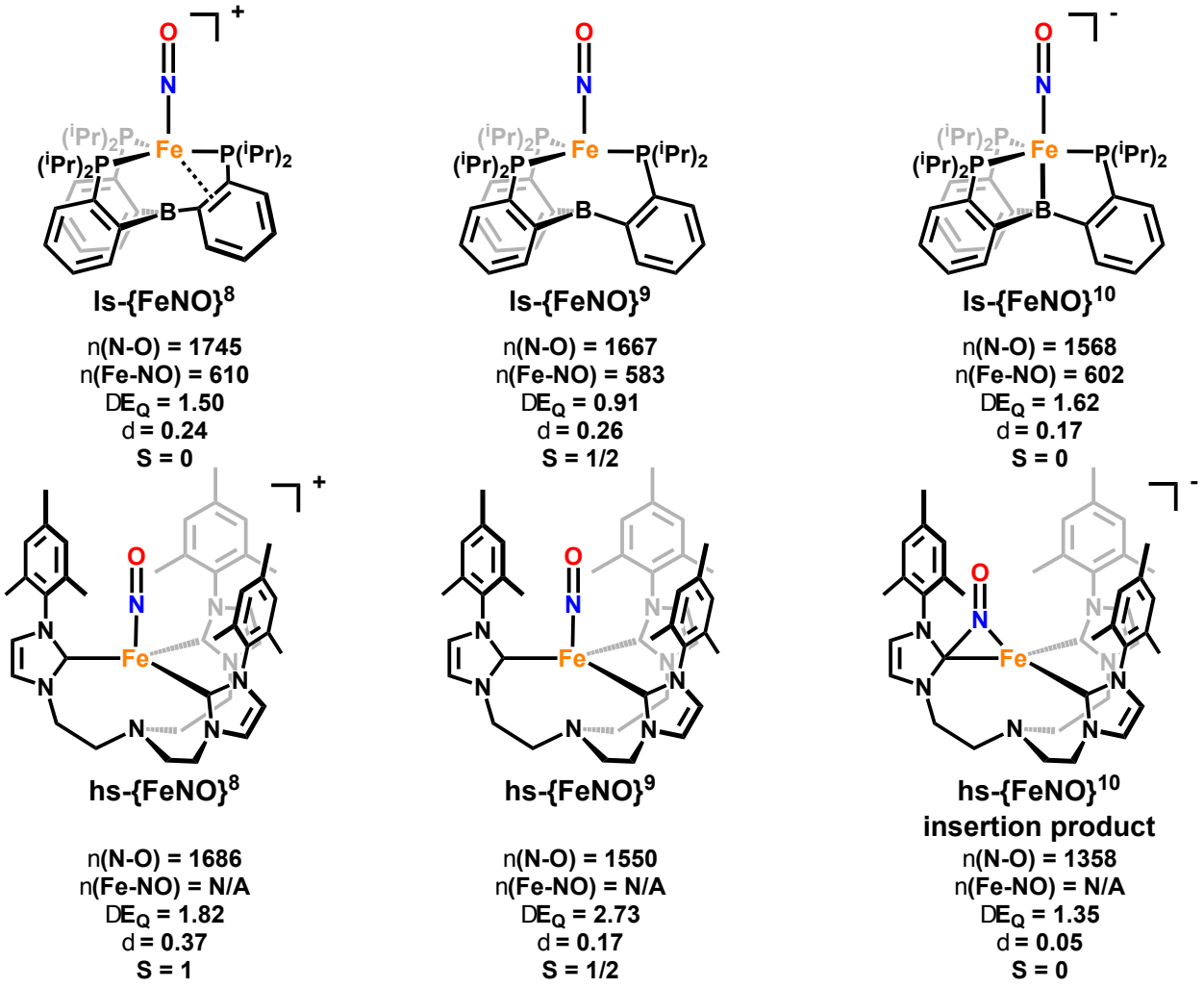

Figure 7.5 Comparison between the [Fe(TPB)(NO)]$^{+/0/-}$ and the [Fe(TIMEN^{Mes})(NO)]$^{+/0/-}$ series. Stretching frequencies ν are in cm^{-1}, ΔE_Q and δ are in mm/s. S is the total spin of the complex.

A direct comparison between the [Fe(TPB)(NO)]$^{+/0/-}$ and the [Fe(TIMEN^{Mes})(NO)]$^{+/0/-}$ complexes in Figure 6 highlights the stark contrast in stability and reactivity of these low-valent FeNO systems.[33] In addition, the FeNO redox series studied here presents a notable difference to

the previously reported examples in that the Mössbauer isomer shift does not trend linearly with the redox state of the complex, and the complete range spans less than 0.1 mm/s (0.17-0.26).[2] This small overall range speaks to a consistent effective nuclear charge at Fe across our redox series. Similar observations have been reported in a recent study by Moore et al. on a bimetallic Fe-Ti system. In this case, redox-induced changes of the effective nuclear charge at Fe are buffered by the Lewis-acidic Ti center. Thus, changes in the covalency of the Fe-Ti interaction minimize changes in the isomer shift across the redox series.[34] The main objective of this study was therefore to interrogate the electronic structural changes of the FeNO unit in our $[Fe(TPB)(NO)]^{+/0/-}$ series, and to identify the origins of the "redox-buffering". For this purpose, I used different spectroscopic methods, especially NRVS and pulse EPR, coupled to DFT calculations.

The ls-$\{FeNO\}^8$ complex has a low-spin, diamagnetic ground state with Fe-NO and N-O stretching frequencies of 610 and 1745 cm^{-1}. Whereas optimized structures cannot distinguish between possible closed-shell (CS) and broken-symmetry (BS) electronic ground states, the predicted NRVS data (especially the Fe-NO stretch) clearly show that the CS state is the better description of the ground state of the complex (see Figure 2). These findings highlight the unreliability of deriving electronic structural information purely from geometric structures. This reminds us that a bond distance only probes the minimum of a potential energy surface (pes), whereas a vibrational frequency probes the curvature of the pes around the energy minimum, which is a much more sensitive gauge for electronic structure and the strength of a bond. Hence, vibrational data (especially stretching frequencies, in the absence of significant mode-mixing) provide a superior measure of bond strength. The electronic structure of the ls-$\{FeNO\}^8$ complex is best described as Fe(0)-NO^+, with two strong, highly covalent Fe-NO π-backbonds (see below).

The d_{z^2} orbital is doubly occupied and undergoes a weak but distinct interaction with the boron center, and the LUMO of the complex is the $d_{x^2-y^2}$ orbital.

Upon one-electron reduction, the $d_{x^2-y^2}$ orbital becomes singly occupied, leading to an S_t = 1/2 ground state in the ls-$\{FeNO\}^9$ complex. The resulting spin-polarization (directly visible as hyperfine coupling interactions as measured by pulse EPR methods) perturbs both the Fe-NO and Fe-B interactions, which become weaker. This is reflected by a drop in the Fe-NO stretching frequency to 583 cm^{-1}. In the Fe-NO π-backbonding picture, this should lead to an increase in the N-O stretch, but this is counteracted by further occupation of the NO(π*) orbitals via unusual mixing with the $d_{x^2-y^2}$ and d_{xy} orbitals, which causes the N-O stretch to drop to 1667 cm^{-1}.

Lastly, reduction to the diamagnetic ls-$\{FeNO\}^{10}$ state leads to the double occupation of the $d_{x^2-y^2}$ orbital. The strength of Fe-NO bond is restored, evident from an increase in the Fe-NO stretch to 602 cm^{-1}. This increase in Fe-NO π-backbonding (compared to the ls-$\{FeNO\}^9$ complex) as well as the further occupation of the NO(π*) orbitals (via mixing with the $d_{xy}/d_{x^2-y^2}$ pair) causes a significant drop in the N-O stretch to 1568 cm^{-1}. Based on all of these observations, I conclude that the Fe-NO π-bonds are essentially unchanged along the ls-$\{FeNO\}^{8-10}$ series. Counterintuitively, the "weak link" in this series is actually the ls-$\{FeNO\}^9$ complex, due to spin polarization. Importantly, this significant effect of spin polarization on a metal-ligand bond is often proposed but can rarely be directly observed, as in the NO complexes described in this paper.

The Fe^n-NO^+ (n = 0, -1, -2) electronic structure descriptions for our ls-$\{FeNO\}^{8-10}$ complexes include a very strong π-backbond, so from a charge perspective the complexes are on average best described as Fe^{n+1}-NO(neutral). Considering that the occupied d_{xz} and d_{yz} orbitals involved in π-backbonding have roughly 30 - 35% NO(π*) character, in line with the low N-O stretching frequencies of the series, the Fe^n-NO^+ description is certainly pushed to an extreme here,

especially in the ls-{FeNO}^{10} complex, where the charges are estimated around $Fe^{-0.6}$-$NO^{-0.4}$. Nevertheless, besides applying the IUPAC rule ("the winner takes it all"), I also believe that the Fe^{n}-NO^{+}/strong π-backbond description has merit and is the most accurate representation of the electronic structure of the complexes. The two strong π-backbonds lead to the transfer of roughly the same amount of α- and β-spin electron density back from Fe^{n} to the NO^{+} ligand (in all complexes), leading to charge accumulation on the NO ligand, *without generating any spin* (hence, atypically, the ligand is NO(neutral), but not NO•). Thus, this does not correspond to an actual electron transfer, as *an electron has a charge and a spin* but rather is an effect of metal-ligand covalency. If an actual electron transfer were to happen, the electronic structure would change to an open shell (BS) ground state like Fe^{n+1}-NO• or Fe^{n+2}-NO^{-}, where the spin(s) of the NO• (S = 1/2) or $^{3}NO^{-}$ (S =1) ligand would likely couple antiferromagnetically to the unpaired electrons of the iron center to which the ligand is directly bound. However, as I demonstrate in this paper, such broken symmetry descriptions are not in agreement with the experimental vibrational (NRVS) data, and can therefore be ruled out. This finding is further supported by the pulse EPR data, showing only small ^{14}N hyperfine coupling constants in the ls-{FeNO}^{9} complex. This difference is not semantic, as our previous work on ferric heme-nitrosyls has shown that the closed-shell Fe^{n}-NO^{+}/strong π-backbond versus open shell Fe^{n+1}-NO• ground states lead to different electronic properties and Fe-NO/N-O bond strengths of the complexes.[14]

It is notable and worth emphasizing that although the d_{z^2} orbital of Fe is doubly occupied throughout the redox series, only the ls-{FeNO}^{10} complex has a strong Fe-B single bond. Thus, iron only adopts a high degree of Lewis base character upon reduction to formal Fe(−II), not at Fe(0). Through this reverse dative Fe→B bond, the redox non-innocent tri(aryl)borane subunit of the TPB ligand system can de facto serve as a redox buffer or electron reservoir by storing two

electrons on site (with minimal effect on the Fe-XY bond of an axially coordinated diatomic). In this way, the Fe(TPB) platform shifts the accessible redox states of the complex down by 2, and the anionic complex can be best described as ls-$\{BFeNO\}^{10}$. Thus, although the electron density at Fe is similar in the cationic and anionic complexes, the NO ligand is far more activated due to the NO(π^*) admixture into the $d_{xy}/d_{x^2-y^2}$ pair. In comparison, the only other known, stable ls-$\{FeNO\}^{10}$ complex is Hieber's anion, $[Fe(CO)_3(NO)]^-$.[35-37] In this case, the three strongly π-backbonding CO ligands take on the role of the boron Lewis acid, and allow for the stabilization of the highly reduced iron center in this unusual compound.

I suggest that Fe→B bond formation should be an important mechanism for storing electrons that can facilitate small molecule functionalization steps, such as axial ligand protonations that oxidize the metal. Such a role has previously been articulated in the context of N_2 fixation catalysis mediated by Fe(TPB).[26,38] However, the key intermediate prior to N_2 functionalization, $[Fe(TPB)(N_2)]^-$ (or $\{FeN_2\}^9$ in analogy to the Enemark-Feltham notation), is isoelectronic to the ls-$\{FeNO\}^9$ complex, and hence might not be expected to have a signficant Fe→B bond. Both complexes can be described as Fe(-I) systems with bound N_2 and NO^+ ligands, respectively.

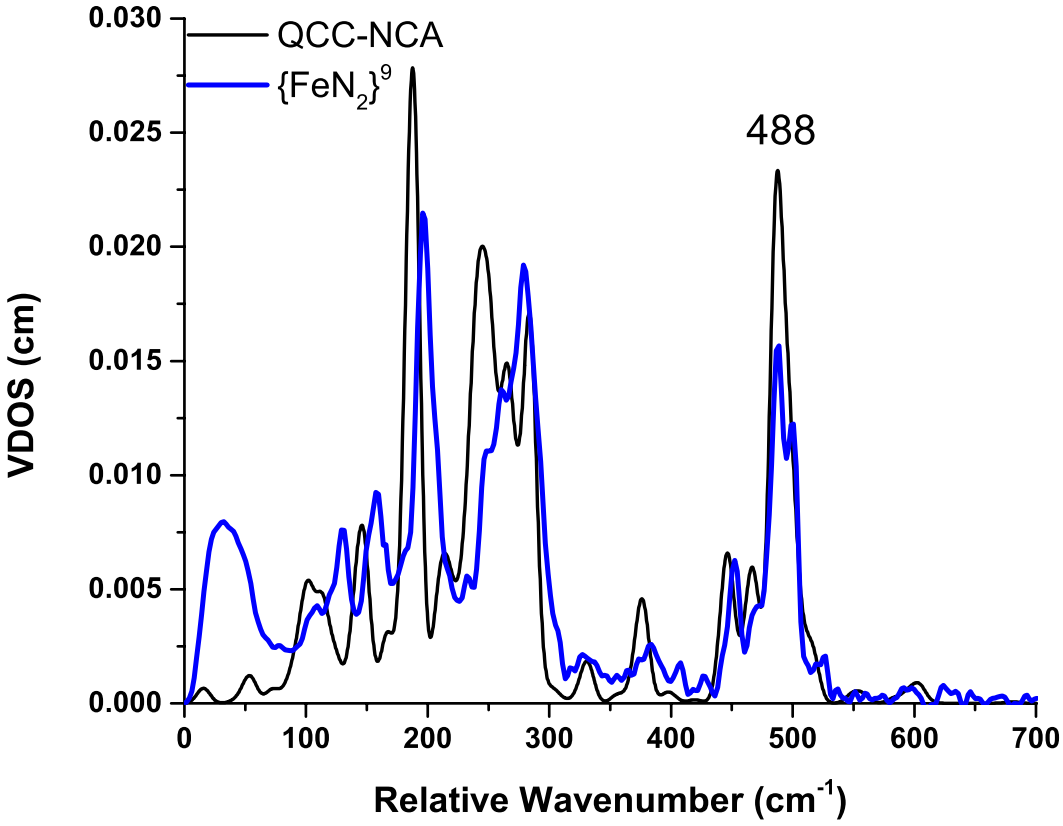

Figure 7.6 Experimental NRVS VDOS data of the $\{FeN_2\}^9$ complex $[Na(12\text{-crown-}4)_2][Fe(TPB)(N_2)]$ (blue) vs a QCC-NCA fit (black).

I therefore evaluated the $\{FeN_2\}^9$ complex by NRVS coupled to QCC-NCA analysis to determine the extent of an Fe→B interaction (Figure 5). The $\{FeN_2\}^9$ species shows a much weaker Fe-N bond compared to the ls-$\{FeNO\}^9$ complex, with the Fe-NN stretch observed at 488 cm^{-1} (corresponding to an Fe-N force constant of 2.62 mdyn/Å, compared to 4.15 mdyn/Å for ls-$\{FeNO\}^9$; see Table 3). In turn, a significantly stronger Fe-B interaction is observed in the $\{FeN_2\}^9$ complex (Fe-B force constant 1.21 vs. 0.42 mdyn/Å). Thus, the formally Fe(-I) center is much less stabilized by N_2 than by NO^+, consistent with their relative π-accepting abilities. Accordingly, in the N_2 complex, formation of an Fe-B σ-bond already occurs at the d^9 state. These data provide

further support for the hypothesis that Fe-B bonding is critical for achieving productive small molecule functionalization, including N_2 fixation, in this system.[26,38]

These observations serve to underscore that the formation of a reverse dative interaction between a transition metal Lewis base and a main group Lewis acid cannot be reliably predicted by formal oxidation states. Thus, even at highly reduced metal centers such as these, there remains significant ambiguity as to whether, and the extent to which, reverse dative interactions form. This ambiguity is often true in ambiphilic ligands, such as TPB, where the relatively soft reverse dative M→Lewis acid (LA) interaction can be dominated by the stronger dative Lewis base (LB)→M interactions.[3-5,39,40,41]

Although the presence of Fe-B interactions in the ls-$\{FeNO\}^{8\text{-}10}$/$\{FeN_2\}^9$ complexes cannot be directly observed in the NRVS data, internal calibration of the DFT predicted Fe-B force constants using the experimentally validated Fe-N and Fe-P interactions provides significant confidence in the theoretical predictions. Furthermore, the formation of an Fe-B bond in the ls-$\{FeNO\}^{10}$ complex is supported by the significant upfield shift of the ^{11}B NMR chemical shift relative to the ls-$\{FeNO\}^8$ species (19.9 ppm vs 36.6 ppm).[2] These predictions run counter to the expectations based on a simple geometric analysis and led us to evaluate how predicted Fe-B force constants correlate with more typically used geometric measures of M→LA bonding, the M-LA distance and the degree of pyramidalization at the LA.[5]

In the ls-$\{FeNO\}^{8\text{-}10}$ series, the Fe-B distance is by far the shortest in ls-$\{FeNO\}^8$ and is identical, within error, in the ls-$\{FeNO\}^{9/10}$ congeners. Nonetheless, the ls-$\{FeNO\}^{10}$ complex has a significantly larger Fe-B force constant (1.56/0.41/0.52 for ls-$\{FeNO\}^{10/9/8}$; see Table 3). The short Fe-B distance in ls-$\{FeNO\}^8$ is a result of the aforementioned η^4-BCCP→Fe interaction, a

reminder that even in highly related complexes the M-LA distance can be a poor measure of the M→LA bonding.

Similarly, although both $[Fe(TPB)(N_2)]^-$ ($f_{Fe\text{-}B}$ = 1.21 mdyn/Å) and $[Fe(TPB)(NO)]^-$ ($f_{Fe\text{-}B}$ = 1.56 mdyn/Å) feature significant pyramidalization at boron ($\Sigma(<_{CBC})$ = 332.0°, and 331.0°), an identical degree of pyramidalization is also observed in $[Fe(TPB)(NNMe_2)]^-$ $\Sigma(<_{CBC})$ = 332.1°); nonetheless, the latter features a much weaker Fe-B bond ($f_{Fe\text{-}B}$ = 0.44 mdyn/Å).[11] Just as structural comparisons were insufficient to differentiate between CS and BS wavefunctions, they are insufficient for evaluating the Fe→B interaction. While other spectroscopic techniques, such as NMR and pulse EPR, can provide insight into M→LA bonding, vibrational spectroscopy provides a powerful tool to directly interrogate such interactions without the limitations of spin selection rules. In combination with theoretical methods, this enables a thorough mapping of the degree of M→LA bonding.

Since both the ls-$\{FeNO\}^9$ and $\{FeN_2\}^9$ complexes have paramagnetic S_t =1/2 ground states, further comparisons on their electronic structures can be made using EPR spectroscopy. Based on this work and previous DFT studies, the SOMO of both complexes is the $d_{x^2-y^2}$ orbital, with a d^9 valence electron configuration.[6] This situation is analogous to tetragonal Cu(II) complexes, and one might therefore expect a large g_z value to originate from spin-orbit coupling (SOC) in the z-direction between the ground state and the d_{xy} excited state. This is in fact the case, but interestingly, the *g*-tensor of the NO^+ complex (g = 1.99, 1.99, 2.45) is significantly more axial (larger Δg_z) than that of the N_2 complex (g = 2.04, 2.04, 2.31). Based on the usual 2nd order SOC formalism,[42,43] the larger Δg_z shift of the ls-$\{FeNO\}^9$ complex can result from three possibilities: (a) a distinctly larger spin-orbit coupling constant (which is unlikely), (b) a smaller covalency

factor for the $d_{x^2-y^2}$ and d_{xy} orbitals, or (c) a reduction in the energy splitting between the $d_{x^2-y^2}$ and d_{xy} orbitals.

From the crystal structures, we observe a greater out-of-plane shift for the Fe center in the NO^+ complex, which could reduce the $d_{x^2-y^2}/d_{xy}$ energy splitting and, in this way, increase the g shift. However, this possibility is not supported by the DFT calculations, which show a very similar energy gap between the $d_{x^2-y^2}$ and the d_{xy} orbital (1.02 vs. 0.96 eV).[44] On the other hand, the DFT calculations point to substantially different orbital covalencies for $d_{x^2-y^2}$ in these complexes (50% $d_{x^2-y^2}$ character in the N_2 compared to 63% in the NO^+ complex). Using these numbers and starting from g_z = 2.45 in the ls-$\{FeNO\}^9$ complex, the g_z value for the $\{FeN_2\}^9$ complex would be predicted to be 2.35, in very good agreement with experiment. Based on this result, I conclude that the differential covalency of the $d_{x^2-y^2}$ orbital is to a large degree responsible for the difference in g_z values between these complexes.

In summary, the EPR data further support the notion of an approximate d^9 ground state in the ls-$\{FeNO\}^9$ and $\{FeN_2\}^9$ complexes, where the larger g_z shift in the former complex is due to the much stronger Fe-NO compared to the Fe-NN bond (evident from the corresponding stretching frequencies), affecting the metal-ligand covalencies in the *xy*-plane.

7.7 Conclusions

The electronic descriptions developed here for the ls-$\{FeNO\}^{8-10}$ series are in agreement with all available spectroscopic data, and emphasize the special role of the TPB ligand in allowing for the storage of two electrons in the Fe-B bond, enabling the Fe(TPB) complex to reach a very low oxidation state while allowing for the utilization of these two extra electrons for reductive catalysis. This complements the more conventional approach in small molecule model chemistry of storing electrons in the π* orbitals of supporting ligands with extended π-systems. A prominent

example for this approach is the bis(imino)pyridine ligand platform, shown in Figure 7, left.[45,46] These approaches are reminiscent of that used by Nature, in which larger metalloclusters, such as Fe-S cluster, are electron-loaded before activating small molecules. Prominent examples of this strategy include the nitrogenase and CO dehydrogenase enzymes (see Figure 7, right).[47-50] While in the case of Fe(TPB) a very low formal oxidation state at Fe must be reached in order for the borane to adopt this special role, tuning of M→LA interactions potentially provides a route to small molecule activation under milder conditions.

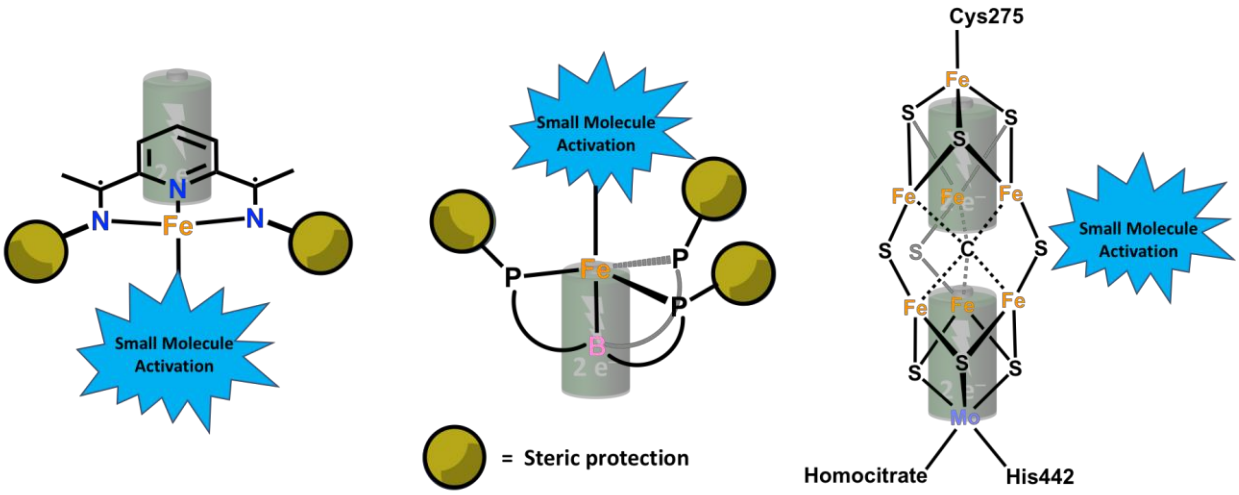

Figure 7.7 Left: In typical non-innocent ligands, like the bis(imino)pyridine system, electrons can be stored in a ligand π system. **Middle:** The TPB ligand used here is unusual, as it stores two electrons in a Fe→B dative bond. **Right:** In the active site of the enzyme nitrogenase, iron-sulfur cluster are used for electron storage. In all cases, the electrons stored in this way can then be utilized for small-molecule activation.

7.8 Experimental Section

All complexes including ^{57}Fe complexes were prepared as previously reported and obtained as pure compounds, as determined by Mössbauer and IR spectroscopy.[2] Efforts to label the complexes with ^{15}NO were largely unsuccessful. However, trace amounts of the ls-{FeNO}^{9} complex [Fe(TPB)(^{15}NO)], sufficient for pulse EPR measurements, could be obtained via reaction of [Fe(TPB)(N_2)] with [TBA][$^{15}NO_2$] followed by extraction by pentane and filtration through celite.

NRVS measurements. Nuclear resonance vibrational spectroscopy (NRVS) data were obtained as described previously[3] at beamline 3-ID at the Advanced Photon Source (APS) at Argonne National Laboratory. Samples were loaded in copper sample holders with lucite lids. During data collection, samples were maintained at cryogenic temperatures using a liquid helium-cooled cryostat. Spectra of solid samples were recorded from 0 to +90 meV in 0.25 meV steps. Multiple scans were taken, normalized to the intensity of the incident beam, and added together to achieve adequate signal to noise ratios; the final spectra represent averages between 6 and 10 scans. The program Phoenix[4] was used to convert the raw NRVS data to the vibrational density of states (VDOS).

Pulse EPR measurements for the ls-{FeNO}^{9} complex. All pulse X-band ($\nu \approx 9.7$ GHz) EPR and electron nuclear double resonance (ENDOR) experiments were performed using a Bruker (Billerica, MA) ELEXSYS E580 pulse EPR spectrometer equipped with a Bruker MD-4 resonator. Temperature control for experiments at 7 K was achieved using an ER 4118HV-CF5-L Flexline Cryogen-Free VT cryostat manufactured by ColdEdge (Allentown, PA), while ENDOR experiments at 5 K were performed using an Oxford Instruments CF935 helium flow cryostat. An Oxford Instruments Mercury ITC was used for temperature regulation with both cryostats.

X-band Electron spin-echo detected field swept spectra (ESE-EPR) were acquired using the 2-pulse Hahn echo sequence ($\frac{\pi}{2} - \tau - \pi - \tau - echo$), while the magnetic field was varied. The "CW-EPR like" 1st derivative spectrum was generated by use of the pseudomodulation function in EasySpin, an EPR simulation toolbox for use with Matlab.[51,52]

Pulse X-band ENDOR was acquired using the Davies pulse sequence ($\pi - T_{RF} - \pi_{RF} - T_{RF} - \pi/2 - \tau - \pi -$ echo), where T_{RF} is the delay between mw pulses and RF pulses, π_{RF} is the length of the RF pulse and the RF frequency is randomly sampled during each pulse sequence.

X-band Hyperfine sublevel correlation (HYSCORE) spectra were acquired using the 4-pulse sequence ($\pi/2 - \tau - \pi/2 - t_1 - \pi - t_2 - \pi/2$ – echo), where τ is a fixed delay, while t_1 and t_2 are independently incremented by Δt_1 and Δt_2, respectively. The time domain data was baseline-corrected (third-order polynomial) to eliminate the exponential decay in the echo intensity, apodized with a Hamming window function, zero-filled to eight-fold points, and fast Fourier-transformed to yield the 2-dimensional frequency domain. The intensity of this FT data was plotted as a series of contours on a logarithmic scale, in colors ranging from blue to red in increasing intensity.

EPR Simulations. Simulations of all EPR data were achieved using the EasySpin simulation toolbox (release 5.2.28) with Matlab 2019a.[51] For more details of these simulations, I refer readers to the SI.

DFT Calculations using Gaussian 09 and Normal Coordinate Analysis. Geometry optimization of the ls-{FeNO}$^{8-10}$ complexes was carried out using the BP86 and B3LYP functionals with the TZVP basis set, using both closed shell and broken symmetry wavefunctions (see text). All calculations were performed using the program Gaussian 09.[53] Subsequent frequency calculations on the optimized structures show no imaginary frequencies, indicating that true energy minima were obtained. The DFT-calculated force constants in Cartesian coordinates were extracted from the Gaussian output files and transformed into internal coordinates using a modified version of the program Redong. Modified normal coordinate analysis (NCA) programs based on QCPE 576 were used for the subsequent fitting of the experimental NRVS data. The fitting was performed by adjusting a minimal set of force constants (in the spirit of the QCC-NCA approach)[54] to reproduce the vibrations of the Fe-N-O units in the ls-{FeNO}$^{8-10}$ series of complexes (see text).

DFT Calculations using ORCA 4.0. The Gaussian-optimized structures of the ls-$\{FeNO\}^{8-10}$ complexes were used for following single-point calculations (BP86/TZVP) with ORCA 4.0 to predict Mössbauer and EPR parameters, and to further analyze the electronic structures of the complexes. This includes the use of unrestricted corresponding orbitals (UCOs) for the ls-$\{FeNO\}^{9}$ complex.[55]

7.9 References

1. Dong, H. T.; Chalkley, M. J.; Oyala, P. H.; Zhao, J.; Alp, E. E.; Hu, M. Y.; Peters, J. C.; Lehnert, N. Exploring the Limits of Dative Boratrane Bonding: Iron as a Strong Lewis Base in Low-Valent Non-Heme Iron-Nitrosyl Complexes. *Inorg. Chem.* **2020**, *59*, 14967-14982.
2. Chalkley, M. J.; Peters, J. C. A Triad of Highly Reduced, Linear Iron Nitrosyl Complexes: $\{FeNO\}^{8-10}$. *Angew. Chem. Int. Ed.* **2016**, *55*, 11995-11998.
3. Jones, J. S.; Gabbaï, F. P. Coordination- and Redox-Noninnocent Behavior of Ambiphilic Ligands Containing Antimony. *Acc. Chem. Res.* **2016**, *49*, 857-867.
4. Braunschweig, H.; Dewhurst, R. D. Transition metals as Lewis bases: "Z-type" boron ligands and metal-to-boron dative bonding. *Dalton Trans.* **2011**, *40*, 549-558.
5. Bouhadir, G.; Bourissou, D. In *The Chemical Bond III: 100 years old and getting stronger*; Mingos, D. M. P., Ed.; Springer International Publishing: Cham, 2017, p 141-201.
6. Vyas, N.; Kumar, A.; Ojha, A. K.; Grover, A. Electronic structure of iron dinitrogen complex [(TPB)FeN2]2−/1−/0: correlation to Mössbauer parameters. *RSC Adv.* **2020**, *10*, 7948-7955.
7. Mingos, D. M. P. *Nitrosyl Complexes in Inorganic Chemistry, Biochemistry and Medicine II*; Springer-Verlag Berlin Heidelberg, 2014; Vol. 154.
8. McQuarters, A. B.; Kampf, J. W.; Alp, E. E.; Hu, M.; Zhao, J.; Lehnert, N. Ferric Heme-Nitrosyl Complexes: Kinetically Robust or Unstable Intermediates? *Inorg. Chem.* **2017**, *56*, 10513-10528.
9. Soldatova, A. V.; Ibrahim, M.; Olson, J. S.; Czernuszewicz, R. S.; Spiro, T. G. New Light on NO Bonding in Fe(III) Heme Proteins from Resonance Raman Spectroscopy and DFT Modeling. *J. Am. Chem. Soc.* **2010**, *132*, 4614-4625.
10. Speelman, A. L.; White, C. J.; Zhang, B.; Alp, E. E.; Zhao, J.; Hu, M.; Krebs, C.; Penner-Hahn, J.; Lehnert, N. Non-heme High-Spin $\{FeNO\}^{6-8}$ Complexes: One Ligand Platform Can Do It All. *J. Am. Chem. Soc.* **2018**, *140*, 11341-11359.
11. Thompson, N. B.; Oyala, P. H.; Dong, H. T.; Chalkley, M. J.; Zhao, J.; Alp, E. E.; Hu, M.; Lehnert, N.; Peters, J. C. Electronic Structures of an [Fe(NNR2)]+/0/– Redox Series: Ligand Noninnocence and Implications for Catalytic Nitrogen Fixation. *Inorg. Chem.* **2019**, *58*, 3535-3549.
12. Lehnert, N.; Galinato, M. G. I.; Paulat, F.; Richter-Addo, G. B.; Sturhahn, W.; Xu, N.; Zhao, J. Nuclear Resonance Vibrational Spectroscopy applied to [Fe(OEP)(NO)]: the Vibrational

Assignments of Five-Coordinate Ferrous Heme Nitrosyls and Implications for Electronic Structure. *Inorg. Chem.* **2010**, *49*, 4133-4148.
13. Goodrich, L. E.; Paulat, F.; Praneeth, V. K. K.; Lehnert, N. Electronic Structure and Reactivity of Heme-Nitrosyls and Its Significance for Nitric Oxide Sensing, Transport, and Catalysis in Biological Systems. *Inorg. Chem.* **2010**, *49*, 6293–6316.
14. Praneeth, V. K. K.; Paulat, F.; Berto, T. C.; DeBeer George, S.; Näther, C.; Sulok, C. D.; Lehnert, N. Electronic Structure of Six-Coordinate Iron(III)-Porphyrin NO Adducts: the Elusive Iron(III)-NO(radical) State and Its Influence on the Properties of these Complexes. *J. Am. Chem. Soc.* **2008**, *130*, 15288-15303.
15. Soma, S.; Van Stappen, C.; Kiss, M.; Szilagyi, R. K.; Lehnert, N.; Fujisawa, K. Distorted Tetrahedral Nickel-Nitrosyl Complexes: Spectroscopic Characterization and Electronic Structure. *J. Biol. Inorg. Chem.* **2016**, *21*, 757-775.
16. Hunt, A. P.; Lehnert, N. The Thiolate Trans Effect in Heme $\{FeNO\}^6$ Complexes and Beyond: Insight into the Nature of the Push Effect. *Inorg. Chem.* **2019**, *58*, 11317-11332.
17. Fujisawa, K.; Soma, S.; Kurihara, H.; Dong, H. T.; Bilodeau, M.; Lehnert, N. A cobalt-nitrosyl complex with a hindered hydrotris(pyrazolyl)borate coligand: detailed electronic structure, and reactivity towards dioxygen. *Dalton Trans.* **2017**, *46*, 13273-13289.
18. Van Stappen, C.; Lehnert, N. Mechanism of N–N Bond Formation by Transition Metal–Nitrosyl Complexes: Modeling Flavodiiron Nitric Oxide Reductases. *Inorg. Chem.* **2018**, *57*, 4252-4269.
19. Berto, T. C.; Hoffman, M. B.; Murata, Y.; Landenberger, K. B.; Alp, E. E.; Zhao, J.; Lehnert, N. Structural and Electronic Characterization of Non-Heme Fe(II)-Nitrosyls as Biomimetic Models of the Fe_B Center of Bacterial Nitric Oxide Reductase (NorBC). *J. Am. Chem. Soc.* **2011**, *133*, 16714–16717.
20. Berto, T. C.; Speelman, A.; Zheng, S.; Lehnert, N. Mono- and Dinuclear Non-Heme Iron-Nitrosyl Complexes: Models for Key Intermediates in Bacterial Nitric Oxide Reductases. *Coord. Chem. Rev.* **2013**, *257*, 244-259.
21. Confer, A. M.; McQuilken, A. C.; Matsumura, H.; Moënne-Loccoz, P.; Goldberg, D. P. A Nonheme, High-Spin $\{FeNO\}^8$ Complex that Spontaneously Generates N_2O. *J. Am. Chem. Soc.* **2017**, *139*, 10621-10624.
22. Fujisawa, K.; Soma, S.; Kurihara, H.; Ohta, A.; Dong, H. T.; Minakawa, Y.; Zhao, J.; Alp, E. E.; Hu, M. Y.; Lehnert, N. Stable Ferrous Mononitroxyl $\{FeNO\}^8$ Complex with a Hindered Hydrotris(pyrazolyl)borate Coligand: Structure, Spectroscopic Characterization, and Reactivity Toward NO and O_2. *Inorg. Chem.* **2019**, *58*, 4059-4062.
23. Keilwerth, M.; Hohenberger, J.; Heinemann, F. W.; Sutter, J. r.; Scheurer, A.; Fang, H.; Bill, E.; Neese, F.; Ye, S.; Meyer, K. A Series of Iron Nitrosyl Complexes $\{Fe–NO\}^{6–9}$ and a Fleeting $\{Fe–NO\}^{10}$ Intermediate en Route to a Metalacyclic Iron Nitrosoalkane. *J. Am. Chem. Soc.* **2019**, *141*, 17217-17235.
24. Lehnert, N. In *Computational Inorganic and Bioinorganic Chemistry*; John Wiley & Sons, Chichester, UK: Encyclopedia of Inorganic Chemistry, 2009; Vol. 2009, p 123-140.
25. Moret, M.-E.; Zhang, L.; Peters, J. C. A Polar Copper–Boron One-Electron σ-Bond. *J. Am. Chem. Soc.* **2013**, *135*, 3792-3795.
26. Thompson, N. B.; Green, M. T.; Peters, J. C. Nitrogen Fixation via a Terminal Fe(IV) Nitride. *J. Am. Chem. Soc.* **2017**, *139*, 15312-15315.
27. Moret, M.-E.; Peters, J. C. N2 Functionalization at Iron Metallaboratranes. *J. Am. Chem. Soc.* **2011**, *133*, 18118-18121.

28. Gunderson, W. A.; Suess, D. L. M.; Fong, H.; Wang, X.; Hoffmann, C. M.; Cutsail Iii, G. E.; Peters, J. C.; Hoffman, B. M. Free H2 Rotation vs Jahn–Teller Constraints in the Nonclassical Trigonal (TPB)Co–H2 Complex. *J. Am. Chem. Soc.* **2014**, *136*, 14998-15009.
29. McQuarters, A. B.; Kampf, J.; Alp, E. E.; Hu, M. Y.; Zhao, J.; Lehnert, N. Ferric Heme-Nitrosyl Complexes: Kinetically Robust or Unstable Intermediates? *Inorg. Chem.* **2017**, *56*, 10513-10528.
30. Serres, R. G.; Grapperhaus, C. A.; Bothe, E.; Bill, E.; Weyhermüller, T.; Neese, F.; Wieghardt, K. Structural, Spectroscopic, and Computational Study of an Octahedral, Non-Heme $\{Fe\text{-}NO\}^{6\text{-}8}$ Series: $[Fe(NO)(cyclam\text{-}ac)]^{2+/+/0}$. *J. Am. Chem. Soc.* **2004**, *126*, 5138-5153.
31. Speelman, A.; Lehnert, N. Heme versus Non-Heme Iron-Nitroxyl $\{FeN(H)O\}^{8}$ Complexes: Electronic Structure and Biologically Relevant Reactivity. *Acc. Chem. Res.* **2014**, *47*, 1106-1116.
32. Speelman, A.; Zhang, B.; Krebs, C.; Lehnert, N. Structural and Spectroscopic Characterization of a High-Spin $\{FeNO\}^{6}$ Complex with an Iron(IV)-NO^{-} Electronic Structure. *Angew. Chem. Int. Ed.* **2016**, *55*, 6685-6688.
33. Yoshikawa, S.; Shinzawa-Itoh, K.; Yamashita, E.; Tsukihara, T. In *Handbook of Metalloproteins*; Messerschmidt, A., Huber, R., Poulos, T., Wieghardt, K., Eds.; Wiley: Chichester, England, 2001; Vol. 1.
34. Moore, J. T.; Chatterjee, S.; Tarrago, M.; Clouston, L. J.; Sproules, S.; Bill, E.; Bernales, V.; Gagliardi, L.; Ye, S.; Lancaster, K. M.; Lu, C. C. Enhanced Fe-Centered Redox Flexibility in Fe–Ti Heterobimetallic Complexes. *Inorg. Chem.* **2019**, *58*, 6199-6214.
35. Burkhardt, L.; Vukadinovic, Y.; Nowakowski, M.; Kalinko, A.; Rudolph, J.; Carlsson, P.-A.; Jacob, C. R.; Bauer, M. Electronic Structure of the Hieber Anion $[Fe(CO)3(NO)]^{-}$ Revisited by X-ray Emission and Absorption Spectroscopy. *Inorg. Chem.* **2020**, *59*, 3551-3561.
36. Hieber, W.; Beutner, K. Notizen: Über Nitrosyltricarbonylferrat(— I), $[Fe(CO)3NO]^{\ominus}$. *Zeitschrift für Naturforschung B* **1960**, *15*, 323-324.
37. Klein, J. E. M. N.; Miehlich, B.; Holzwarth, M. S.; Bauer, M.; Milek, M.; Khusniyarov, M. M.; Knizia, G.; Werner, H.-J.; Plietker, B. The Electronic Ground State of $[Fe(CO)3(NO)]^{-}$: A Spectroscopic and Theoretical Study. *Angew. Chem. Int. Ed.* **2014**, *53*, 1790-1794.
38. Anderson, J. S.; Rittle, J.; Peters, J. C. Catalytic conversion of nitrogen to ammonia by an iron model complex. *Nature* **2013**, *501*, 84-87.
39. Hill, A. F. An Unambiguous Electron-Counting Notation for Metallaboratranes. *Organometallics* **2006**, *25*, 4741-4743.
40. Parkin, G. A Simple Description of the Bonding in Transition-Metal Borane Complexes. *Organometallics* **2006**, *25*, 4744-4747.
41. Bouhadir, G. B., D. In *Ligand Design in Metal Chemistry*; Vol. 2016, p 237-269.
42. Arai, H.; Igarashi, Y.; Kodama, T. The structural genes for nitric oxide reductase from *Pseudomonas aeruginosa*. *Biochim. Biophys. Acta* **1995**, *1261*, 279-284.
43. Sharma, A.; Roemelt, M.; Reithofer, M.; Schrock, R. R.; Hoffman, B. M.; Neese, F. EPR/ENDOR and Theoretical Study of the Jahn–Teller-Active [HIPTN3N]MoVL Complexes (L = N–, NH). *Inorg. Chem.* **2017**, *56*, 6906-6919.
44. Butland, G.; Spiro, S.; Watmough, N. J.; Richardson, D. J. Two Conserved Glutamates in the Bacterial Nitric Oxide Reductase Are Essential for Activity but Not Assembly of the Enzyme. *J. Bacteriol.* **2001**, *183*, 189-199.
45. Delle Chiaie, K. R.; Biernesser, A. B.; Ortuño, M. A.; Dereli, B.; Iovan, D. A.; Wilding, M. J. T.; Li, B.; Cramer, C. J.; Byers, J. A. The role of ligand redox non-innocence in ring-opening

polymerization reactions catalysed by bis(imino)pyridine iron alkoxide complexes. *Dalton Trans.* **2017**, *46*, 12971-12980.
46. Stieber, S. C. E.; Milsmann, C.; Hoyt, J. M.; Turner, Z. R.; Finkelstein, K. D.; Wieghardt, K.; DeBeer, S.; Chirik, P. J. Bis(imino)pyridine Iron Dinitrogen Compounds Revisited: Differences in Electronic Structure Between Four- and Five-Coordinate Derivatives. *Inorg. Chem.* **2012**, *51*, 3770-3785.
47. Hoffman, B. M.; Lukoyanov, D.; Yang, Z.-Y.; Dean, D. R.; Seefeldt, L. C. Mechanism of Nitrogen Fixation by Nitrogenase: The Next Stage. *Chem. Rev.* **2014**, *114*, 4041-4062.
48. Van Stappen, C.; Decamps, L.; Cutsail, G. E.; Bjornsson, R.; Henthorn, J. T.; Birrell, J. A.; DeBeer, S. The Spectroscopy of Nitrogenases. *Chem. Rev.* **2020**.
49. Can, M.; Armstrong, F. A.; Ragsdale, S. W. Structure, Function, and Mechanism of the Nickel Metalloenzymes, CO Dehydrogenase, and Acetyl-CoA Synthase. *Chem. Rev.* **2014**, *114*, 4149-4174.
50. Holm, R. H.; Lo, W. Structural Conversions of Synthetic and Protein-Bound Iron–Sulfur Clusters. *Chem. Rev.* **2016**, *116*, 13685-13713.
51. Stoll, S.; Schweiger, A. EasySpin, a comprehensive software package for spectral simulation and analysis in EPR. *J. Magn. Reson.* **2006**, *178*, 42-55.
52. Hyde, J. S.; Pasenkiewicz-Gierula, M.; Jesmanowicz, A.; Antholine, W. E. Pseudo field modulation in EPR spectroscopy. *Appl. Magn. Reson.* **1990**, *1*, 483.
53. Frisch, M. J.; Trucks, G. W.; Schlegel, H. B.; Scuseria, G. E.; Robb, M. A.; Cheeseman, J. R.; Scalmani, G.; Barone, V.; Mennucci, B.; Petersson, G. A.; Nakatsuji, H.; Caricato, M.; Li, X.; Hratchian, H. P.; Izmaylov, A. F.; Bloino, J.; Zheng, G.; Sonnenberg, J. L.; Hada, M.; Ehara, M.; Toyota, K.; Fukuda, R.; Hasegawa, J.; Ishida, M.; Nakajima, T.; Honda, Y.; Kitao, O.; Nakai, H.; Vreven, T.; Montgomery, J. A.; Peralta, J. E.; Ogliaro, F.; Bearpark, M.; Heyd, J. J.; Brothers, E.; Kudin, K. N.; Staroverov, V. N.; Kobayashi, R.; Normand, J.; Raghavachari, K.; Rendell, A.; Burant, J. C.; Iyengar, S. S.; Tomasi, J.; Cossi, M.; Rega, N.; Millam, J. M.; Klene, M.; Knox, J. E.; Cross, J. B.; Bakken, V.; Adamo, C.; Jaramillo, J.; Gomperts, R.; Stratmann, R. E.; Yazyev, O.; Austin, A. J.; Cammi, R.; Pomelli, C.; Ochterski, J. W.; Martin, R. L.; Morokuma, K.; Zakrzewski, V. G.; Voth, G. A.; Salvador, P.; Dannenberg, J. J.; Dapprich, S.; Daniels, A. D.; Farkas; Foresman, J. B.; Ortiz, J. V.; Cioslowski, J.; Fox, D. J. Gaussian 09, Revision B.01. *Wallingford CT* **2009**.
54. Praneeth, V. K. K.; Näther, C.; Peters, G.; Lehnert, N. Spectroscopic Properties and Electronic Structure of Five- and Six-Coordinate Iron(II) Porphyrin NO Complexes: Effect of the Axial N-Donor Ligand. *Inorg. Chem.* **2006**, *45*, 2795-2811.
55. Neese, F. The ORCA program system. *Wiley Interdisciplinary Reviews: Computational Molecular Science* **2011**, *2*, 73-78.

Chapter 8

Conclusion

Reduction of NO to N_2O is an important reaction employed by pathogens to overcome the toxicity of NO gas in human immune defense.[1] As a result, they can proliferate and cause chronic infections in humans. It has been shown in enzymology that non-heme diiron active sites, such as those found in FNORs, are capable of mediating the NO reduction reaction.[2-5] Understanding of the mechanism of how NO reduction is carried out by FNORs is beneficial for the development of new treatments and therapies for chronic bacterial infections. While studies on the *Tm* FDP have shown that the hs-$[\{FeNO\}^7]_2$ adduct is the crucial intermediate formed right before the detection of N_2O,[2,3] the exact mechanism of how these two, seemingly stable, hs-$\{FeNO\}^7$ units can undergo efficient N-N coupling (via the so-called direct reduction mechanism) to form N_2O is still unclear. Kurtz and coworkers proved that the diferrous reactive state of *Tm* FDP can reduce NO directly to N_2O via the removal of the FMN cofactor from the enzyme.[3] The single turnover in this experiment is slow, taking ~120 seconds, but nevertheless, this result demonstrates that FDPs can generate N_2O in the absence of the FMN cofactor. At the same time, multiple model complex studies have shown that N_2O formation in these hs-$[\{FeNO\}^7]_2$ model systems is only possible via at least one-electron reduction to the hs-$\{Fe(NO)\}^7$/hs-$\{Fe(NO)\}^8$ state. These observations raise questions regarding the role of the FMN cofactor in the enzymes and whether it is needed/utilized for NO reduction under turnover conditions. If direct reduction of NO is possible in the enzymes, as the

biochemical studies suggest, then what are the key properties that allow FNORs to mediate this reaction in a way that model complexes (so far) have not been able to? Vice versa, what design elements are needed that would allow a model complex to directly reduce NO? These are key questions regarding the mechanism of FNORs that are addressed in this thesis.

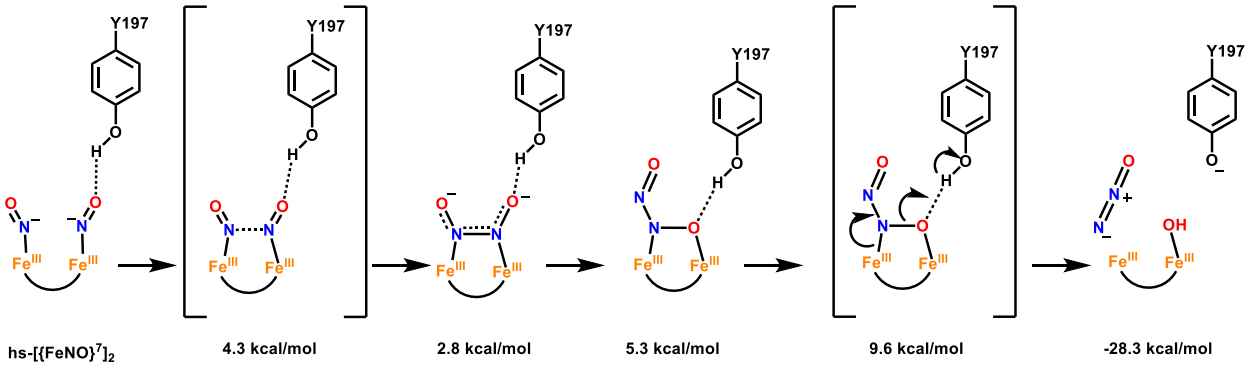

Scheme 8.1 Direct coupling mechanism involving Y197, as proposed by Chen and coworkers.[6] Energies indicated in the figure are relative to the starting [hs-{FeNO}^{7}]$_2$ complex. Boxed letters correspond to reaction steps. Transition states are indicated in brackets.

One hint in this regard comes from recent biochemical (mutagenesis) experiments on *Tm* FDP and computational (QM/MM) studies. Here, it is shown that hydrogen bonding residues in the SCS, specifically the conserved Y197, play a critical role in the N–N bond formation reaction that leads to the generation of a hyponitrite intermediate (Scheme 8.1).[6,7] The mutagenesis experiments on *Tm* FDP revealed that removal of the SCS hydrogen bond in the Y197F variant completely shut down the NO reduction reaction.[7] Other factors (Scheme 8.2) that could affect the ability of a diiron core to mediate NO reduction are geometric considerations (Fe···Fe distance,

(O)N–Fe–Fe–N(O) dihedral angle, etc.) and electronic properties of the core. I, therefore, started a comprehensive investigation to identify the key features that enable the direct NO reduction in diiron centers in order to adopt these strategies into the next generation of FNOR model complexes. In particular, the synthesis, characterization, and reactivity of the first model complex of FNORs that directly reduces NO to N_2O is reported in this thesis. Along with this, the degree of activation of the hs-$\{FeNO\}^7$ unit in this complex is addressed, and it is shown that N–O stretching frequencies ≤ 1700 cm^{-1} are indicative of reactive hs-$\{FeNO\}^7$ units that are activated for direct NO reduction. In addition, a diiron core with coplanar NO binding sites is a key requirement for this reaction. I further started the synthesis and characterization of model complexes of FNORs with NHC(O)R-type hydrogen bond donors in the SCS, and initial results on the NO reactivity of corresponding diiron complexes are reported as well. Finally, the coordination chemistry of non-heme iron complexes with hyponitrite is discussed, to investigate how hyponitrite interacts with non-heme iron centers, and how this may relate to its ability to produce N_2O.

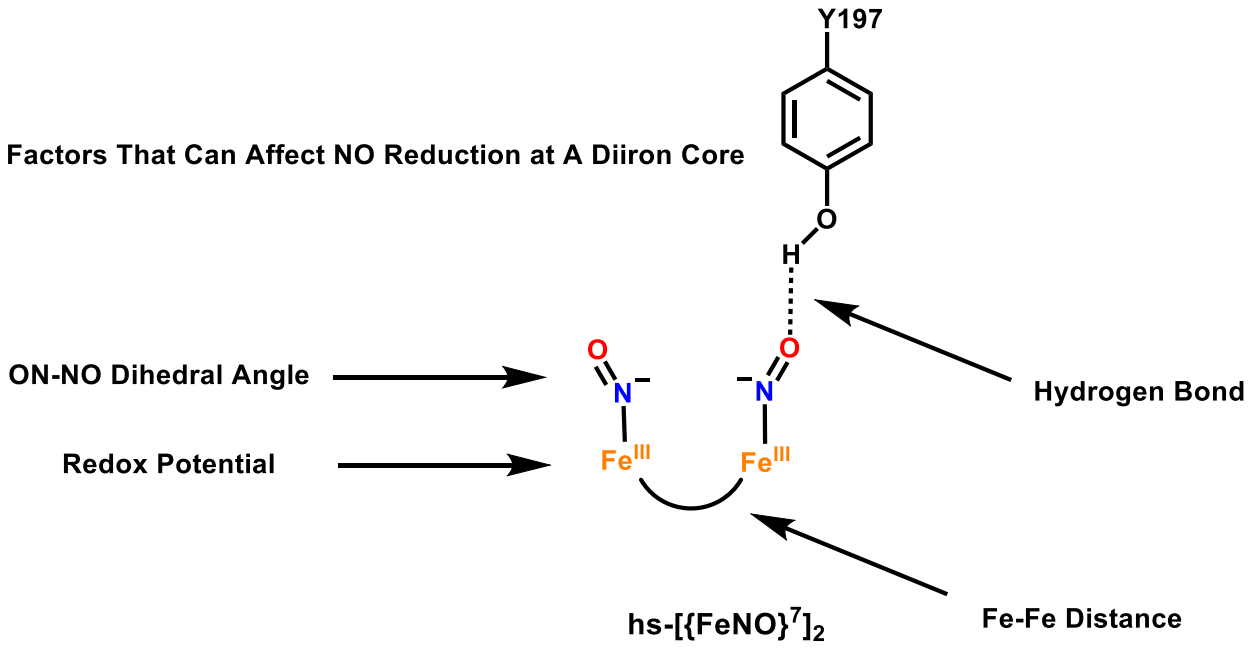

Scheme 8.2 Factors to consider in FNORs that can affect the ability of the diiron core to mediate NO reduction.

As mentioned above, hs-[{FeNO}^{7}]$_2$ model complexes require reduction to the reactive hs-{FeNO}^{8} state to induce N_2O formation. This process, as well as the geometric and electronic properties of the resulting hs-{FeNO}^{8} centers, have been studied in detail by former graduate students Corey White and Amy Speelman.[8-10] Since hs-{FeNO}^{8} complexes are reactive, one interesting question is what other reactions these species can undergo, besides N_2O formation in diiron cores. A reaction of mononuclear hs-{FeNO}^{8} complexes that has been reported is the formation of dinitrosyl iron complexes (DNICs).[9,11-13] However, these studies did not address the intermediates formed in the process of DNIC formation. In this thesis, the synthesis and characterization of different mononuclear hs-{FeNO}^{7} complexes are reported, as well as the reactivity of the corresponding, one-electron reduced hs-{FeNO}^{8} species. This effort led to the isolation and characterization of a novel complex with a unique $Fe_2(NO)_2$ diamond core, in line with a previously proposed dimerization mechanism for DNIC formation from mononuclear hs-{FeNO}^{8} complexes. In addition, the investigation of the electronic structures of iron-nitrosyl complexes beyond the {FeNO}^{8} state, using spectroscopic and theoretical methods, is reported. This project was carried out in collaboration with Peters and coworkers (CalTech).

8.1 Summary of Thesis

In **Chapter 2**, the synthesis of the new model complex [Fe^{II}_2((Py$_2$PhO$_2$)MP)(OPr)$_2$]$^-$, featuring the tri-anionic ligand [(Py$_2$PhO$_2$)MP]$^{3-}$, is reported and its reactivity with NO is investigated.[14] The key difference between this new model complex and its BPMP$^-$ analog, [Fe_2(BPMP)(OPr)]$^{2+}$, is the more negative reduction potential (different by ~1V) of the former. This drastic shift in reduction potential is the key to unlock the direct reduction of NO to N_2O in this complex. Indeed, [Fe^{II}_2((Py$_2$PhO$_2$)MP)(OPr)$_2$]$^-$ spontaneously reduces NO to N_2O

quantitatively at room temperature, while $[Fe_2(BPMP)(OPr)]^{2+}$ stabilizes the hs-$[\{FeNO\}^7]_2$ intermediate (complex $[Fe_2(BPMP)(OPr)(NO)_2]^{2+}$), making the former the first model complex of FNORs capable of direct reduction of NO to N_2O. This reaction is catalytic and quantitative amounts of N_2O were accomplished through several cycles in the presence of excess acetic acid and $CoCp_2$. Due to the extremely reducing irons, this reaction proceeded even at -80 ^oC, albeit slower and with lower N_2O yields (10-30%) due to unproductive side reactions at low temperature. Interestingly, in the low-temperature studies, a small amount of a hs-$[\{FeNO\}^7]_2$ species was also observed, but could not be characterized further. When warmed up to room temperature, in the presence of excess NO gas, the reaction returned to the original productive pathway and quantitative amounts of N_2O were again observed.

Chapter 3 expands on the work discussed in Chapter 2, in particular to determine the degree of activation of the hs-$\{FeNO\}^7$ units required to enable direct NO reduction to N_2O. I hypothesized that by separating the two irons and breaking the coplanar geometry, I could stop the direct NO reduction and trap the activated hs-$\{FeNO\}^7$ complex. By using a truncated derivative of the ligand $[(Py_2PhO_2)MP]^{3-}$, I hoped to obtain a monomeric hs-$\{FeNO\}^7$ complex with a primary coordination environment that is similar to the iron centers in $[Fe^{II}_2((Py_2PhO_2)MP)(OPr)_2]^+$, and then study its chemical properties. For this purpose, the model complex $[\{Fe(MPA\text{-}(^tBuMePhO)_2)\}_2]$, in which the coligand is further decorated with sterically protective groups, was synthesized and characterized. Despite the steric protection from the tert-butyl substituents on the phenolate rings, this complex forms a dimeric precursor with the two iron centers bridged by the oxygen atoms of the phenolates to form an Fe_2O_2 diamond core structure. Importantly, reaction of $[\{Fe(MPA\text{-}(^tBuMePhO)_2)\}_2]$ with excess NO gas produced the monomeric, stable hs-$\{FeNO\}^7$ complex $[Fe(MPA\text{-}(^tBuMePhO)_2)(NO)]$. This compound has the lowest N–O stretching frequency

observed in a monomeric hs-{FeNO}^{7} complex to this date, at 1689 cm^{-1}. Consequently, a low Fe–NO stretch of 467 cm^{-1} was observed using NRVS, in agreement with the direct correlation of the Fe–NO and N–O stretching frequencies in hs-{FeNO}^{7} complexes, a consequence of their electronic structure (first shown by former graduate student Tim Berto).[15] This result suggests that the proposed hs-[{FeNO}^{7}]$_2$ intermediate formed by reaction of [Fe$^{II}_2$((Py$_2$PhO$_2$)MP)(OPr)$_2$]$^-$ with NO is extremely activated due to the strongly reducing iron centers. As a result, this provides the extra driving force needed to reduce NO directly. Accordingly, removal of the steric protection provided by the bulky tert-butyl substituents in [MPA-(PhO)$_2$]$^{2-}$ leads to a new model complex, [{Fe(MPA-(PhO)$_2$)}$_2$], which is now capable of directly reducing NO to N$_2$O. However, due to the lack of proper preorganization of the iron centers with open cis coordination sites, as in [Fe$^{II}_2$((Py$_2$PhO$_2$)MP)(OPr)$_2$]$^-$, NO reduction by [{Fe(MPA-(PhO)$_2$)}$_2$] is much slower, and proceeds over 8 hours. Nevertheless, this makes [{Fe(MPA-(PhO)$_2$)}$_2$] only the second model complex capable of directly reducing NO to N$_2$O. The yield of N$_2$O formation topped off at 81% due to formation of unreactive iron-nitrosyl byproducts. This study demonstrates that hs-{FeNO}^{7} species with N–O stretching frequencies ≤ 1700 cm^{-1} are activated for direct NO reduction. However, a coplanar diiron core is critically important to make this an efficient process.

Though I have shown above that model complexes can indeed reduce NO directly to N$_2$O, by tuning the reduction potential of the diiron core, it is important to note that native FNORs do not operate at such negative redox potentials. Instead, FNORs contain a beautifully crafted network of hydrogen bonding residues around the active site to assist with NO reduction.[7] It is likely that FNORs can directly reduce NO to N$_2$O without reaching such negative redox potentials by using SCS hydrogen bonds to assist in NO activation. These hydrogen bonds, therefore, "compensate" for the less reducing iron centers in the enzymes compared to [Fe$^{II}_2$((Py$_2$PhO$_2$)MP)(OPr)$_2$]$^-$.

In **Chapter 4**, new model complexes based on our original $BPMP^-$ ligand scaffold are presented, which carry NHC(O)R-type hydrogen bond donors in the SCS. Several starting materials were prepared and characterized first, specifically, $[Fe_2(BPMP\text{-}NHCOC(CH_3)_3)(OAc)](OTf)_2$ **(1)** and $[Fe_2(BPMP\text{-}NHCOC(CH_3)_3)(MeOH)_2](OTf)_3$ **(2)**, with one and no bridging carboxylate ligands. Further studies showed that the oxygen atoms of the amide substituents used in these ligands have a strong tendency to bind to the iron centers, competing with NO. This competitive binding lowers the apparent binding constants of NO to the diiron core of **1**, leading to low nitrosylation yields and NO lability in solution. Upon reacting **1** with NO gas, IR spectroscopy indicated the formation of NO complexes in solution, although the corresponding IR band for the N-O stretch was unusually weak. I crystallized and characterized one of the species from such reactions, and obtained the diiron mononitrosyl complex $[Fe_2(BPMP\text{-}NHCOC(CH_3)_3)(OAc)(NO)](OTf)$ **(3)**. This was surprising, as these types of complexes are exceedingly rare with only one report in the literature. However, EPR and solution IR studies further showed that this complex is only a minor species in the reaction mixture. Injection of NO gas into a solution of **3** resulted in the increase of the intensity of the N-O stretching band in IR spectroscopy, indicative of the formation of some amount of the dinitrosyl complex. On the other hand, nitrosylation of **2** yielded a complex with a more intense N-O stretching band observed via IR spectroscopy. This observation implies that this complex binds NO better, due to the extra coordination sites that are not blocked by a bridging carboxylate. I propose that complex $[Fe_2(BPMP\text{-}NHCOC(CH_3)_3)(NO)_2](OTf)_3$ **(4)** formed after nitrosylation, but further structural characterization is needed to prove this point. Due to the proposed binding of both amide O atoms to the iron centers in **4**, the NO ligands do not actually experience any hydrogen bonding. In summary, the application of amide groups as hydrogen-bond donors in the SCS of our $BPMP^-$

complexes is problematic, and the goal of achieving hydrogen bonding to the coordinated NO ligands could likely not be accomplished, although some interesting compounds were nevertheless obtained. In future studies, we will use amine groups instead where such problems can be avoided (see below).

Following N–N bond formation in the hs-[{FeNO}^{7}]$_2$ complex, the next key intermediate that is proposed to form in FNORs is a hyponitrite complex.[6,7,16] However, the chemistry of hyponitrite with non-heme iron centers has not been investigated much in the literature. In **Chapter 5**, I describe my work on the coordination chemistry of hyponitrite with non-heme iron complexes. Here, I reacted two ferrous non-heme iron complexes, [Fe(TPA)(MeCN)$_2$](OTf)$_2$ and [Fe$_2$(BMPA-PhO)$_2$](OTf)$_2$, with pre-formed hyponitrite ($Na_2N_2O_2$). I discovered that protic solvents, such as methanol, decompose $Na_2N_2O_2$ to form N_2O, and hence, are unsuitable reaction media. The reaction of [Fe(TPA)(MeCN)$_2$](OTf)$_2$ with $Na_2N_2O_2$ in acetonitrile yielded [Fe$_2$(TPA)$_2$(NO)$_2$](OTf)$_2$, which is a new compound that is discussed in detail in Chapter 6. Here, I propose that the high Lewis acidity of the Fe(TPA) unit causes the N–N bond of hyponitrite to break. The less Lewis acidic complex [Fe$_2$(BMPA-PhO)$_2$](OTf)$_2$, on the other hand, does not break the N–N bond, but instead, allowed for the stabilization of a novel hyponitrite cluster, [{Fe$_2$(BMPA-PhO)$_2$}$_2$(μ-N_2O_2)](OTf)$_2$. Here, the hyponitrite ligand is sandwiched between two diiron units. The average N–N bond distance (due to disorder in the crystal) of hyponitrite is 1.27 Å, which represents an N–N double bond. This is similar to the N–N bond distance in $Na_2N_2O_2$ (1.26 Å). The average N–O bond distance of the hyponitrite ligand in [{Fe$_2$(BMPA-PhO)$_2$}$_2$(μ-N_2O_2)](OTf)$_2$ is 1.35 Å, again comparable to $Na_2N_2O_2$ (1.36 Å). Therefore, despite coordination to four iron centers, the hyponitrite ligand is not activated, thus allowing me to crystallize and characterize the cluster. This study therefore provides the foundation for future studies on

hyponitrite complexes with our dimeric complexes, like $[Fe_2(BPMP)(OPr)]^{2+}$, to explore which coordination modes of hyponitrite to diiron cores lead to an activation of this ligand. These studies will be continued by new graduate student Michael Lengel.

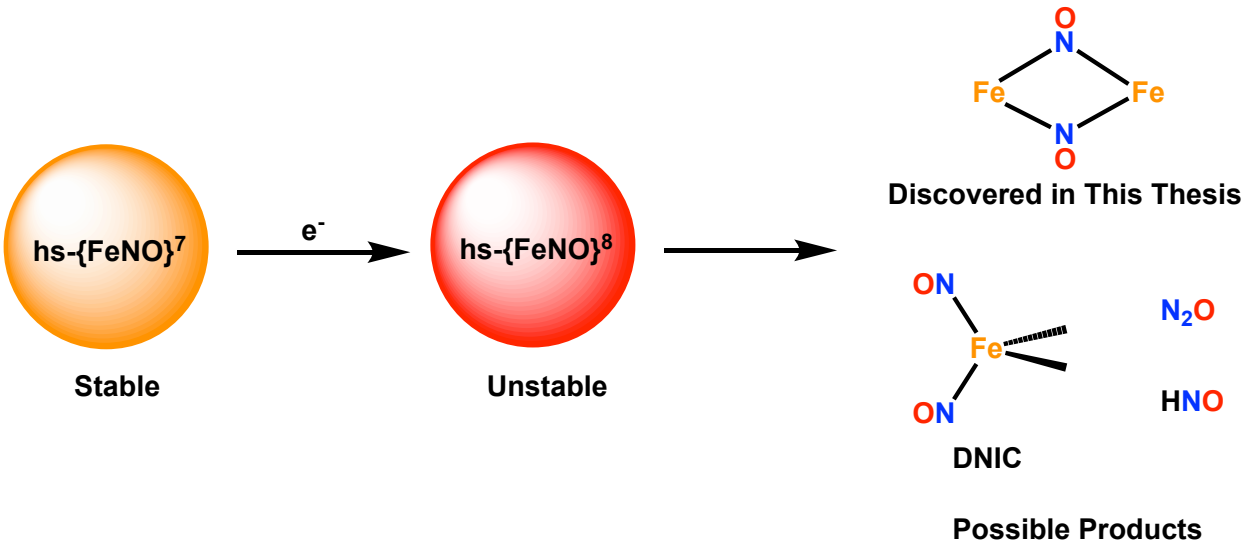

Scheme 8.3 Known possible products from the decomposition of unstable hs-$\{FeNO\}^8$ complexes. This includes the novel diamond core structural motif that is discovered and studied in detail for the first time in this thesis.

Studies presented in **Chapter 6** investigated the reactivity of mononuclear hs-$\{FeNO\}^8$ complexes. For this purpose, I reacted hs-$\{FeNO\}^7$ complexes with primary coordination spheres similar to that of $[Fe_2(BPMP)(OPr)(NO)_2]^{2+}$ (using TPA and BMPA-tBu_2PhO^- ligands) with one equivalent of $CoCp_2$ and characterized the reaction products. The weak field ligand BMPA-PhO^- stabilizes the hs S = 3/2 complex [Fe(BMPA-tBu_2PhO)(NO)(OTf)], which does not change spin state regardless of solvent coordination (instead of triflate). Reduction of [Fe(BMPA-tBu_2PhO)(NO)(OTf)] with $CoCp_2$ yielded a typical dinitrosyl iron complex (DNIC), which is a commonly observed decomposition product of hs-$\{FeNO\}^8$ complexes (Scheme 8.3).[9,17-19] In contrast, characterization of [Fe(TPA)(OTf)(NO)](OTf) revealed an unusual electronic structure where coordination of the solvent acetonitrile induces a spin state change to ls (S = 1/2). Reduction

of [Fe(TPA)(OTf)(NO)](OTf) with $CoCp_2$ yielded a diamagnetic product. X-ray crystallography revealed the formation of the novel dimeric complex $[Fe_2(TPA)_2(NO)_2](OTf)_2$ with a diamond core motif bridged by NO ligands. I propose that this complex is formed through dimerization of two hs-$\{FeNO\}^8$ moieties that undergo an immediate spin change upon dimerization. Through these observations, I propose that dimeric diamond core structures, like in $[Fe_2(TPA)_2(NO)_2](OTf)_2$, are potentially the intermediates on the pathway towards DNIC formation. Due to the spin change upon dimerization, this type of intermediate is "trapped" in $[Fe_2(TPA)_2(NO)_2](OTf)_2$. This is the first report of such diamond core species in non-heme iron chemistry.

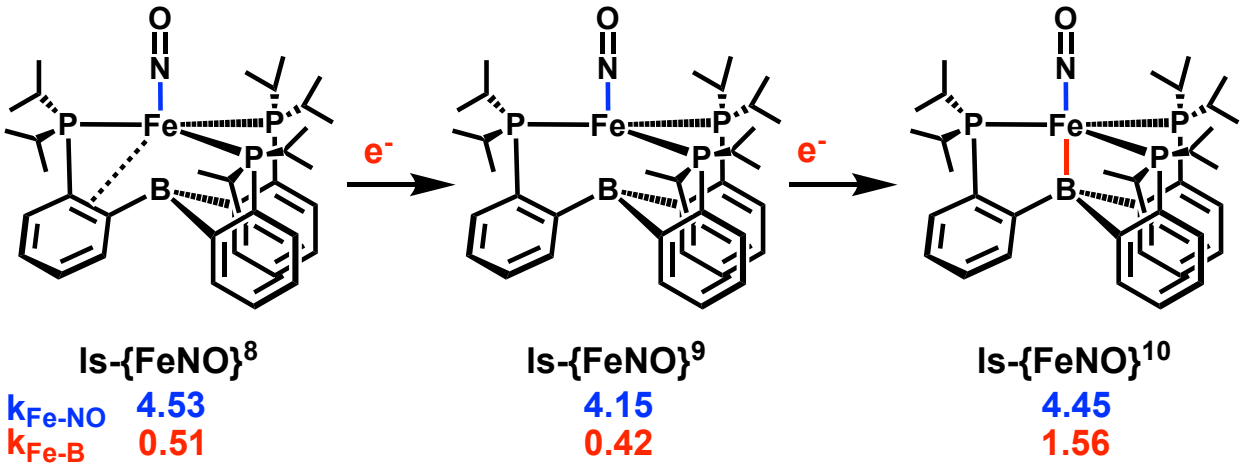

Figure 8.1 Force constants showing weak Fe-B interactions in the ls-$\{FeNO\}^{8,9}$ complexes, but a covalent bond is formed in the ls-$\{FeNO\}^{10}$ complex.

In **Chapter 7**, I explored the electronic structure of a series of iron nitrosyl complexes, $[Fe(TPB)(NO)]^{+/0/-}$, beyond the $\{FeNO\}^8$ state. Using spectroscopy and theoretical methods, I determined the exact electronic structure of this series in collaboration with Jonas Peters' group at CalTech. I pinpointed the factors that help stabilize these complexes in such unusual oxidation states. All three complexes are low-spin iron-nitrosyls with a bound NO^+ ligand. Specifically, the electronic structure of the ls-$\{FeNO\}^8$ complex is best described as Fe(0)-NO^+, with two strong,

highly covalent Fe-NO π-backbonds. The d_{z^2} orbital is doubly occupied and undergoes a weak but distinct interaction with the boron center in the ligand backbone (as shown in the force constants of the Fe-B interaction, Figure 8.1). The LUMO of the complex is the $d_{x^2-y^2}$ orbital. Upon one-electron reduction, the $d_{x^2-y^2}$ orbital becomes singly occupied, leading to an $S_t = 1/2$ ground state in the ls-{FeNO}^{9} complex. The resulting spin-polarization perturbs both the Fe-NO and Fe-B interactions, which become weaker. This is reflected by a drop in the Fe-NO stretching frequency to 583 cm^{-1}. In the Fe-NO π-backbonding picture, this should lead to an increase in the N-O stretch, but this is counteracted by further occupation of the NO(π*) orbitals via unusual mixing with the $d_{x^2-y^2}$ and d_{xy} orbitals, which causes the N-O stretch to drop to 1667 cm^{-1}. Finally, reduction to the diamagnetic ls-{FeNO}^{10} state leads to the double occupation of the $d_{x^2-y^2}$ orbital. The strength of Fe-NO bond is restored, evident from an increase in the Fe-NO stretch to 602 cm^{-1}. This increase in Fe-NO π-backbonding (compared to the ls-{FeNO}^{9} complex) as well as the further occupation of the NO(π*) orbitals (via mixing with the $d_{xy}/d_{x^2-y^2}$ pair) causes a significant drop in the N-O stretch to 1568 cm^{-1}. It is worth emphasizing that although the d_{z^2} orbital of Fe is doubly occupied throughout the redox series, only the ls-{FeNO}^{10} complex has a strong Fe-B single bond. Thus, iron only adopts a high degree of Lewis base character upon reduction to formal Fe(−II), not at Fe(0). Through this reverse dative Fe→B bond, the redox non-innocent tri(aryl)borane subunit of the TPB ligand system can de facto serve as a redox buffer or electron reservoir by storing two electrons on site (with minimal effect on the Fe-XY bond of an axially coordinated diatomic). In this way, the Fe(TPB) platform shifts the accessible redox states of the complex down by 2, and the anionic complex can be best described as ls-{BFeNO}^{10}. This unique ability of this ligand scaffold to buffer extra electron density in an extremely low valent state is the key to unlock the unique chemistry of the Fe(TPB) platform in small molecule activation, most famously for N_2.[20]

8.2 Future Directions

My work in Chapter 2 shows that reduction potential is a key property that allows for the direct NO reduction pathway to be activated. However, due to the quite negative reduction potentials of this complex, I could not observe any intermediate, not even the $[\{FeNO\}^7]_2$ adduct, prior to N–N bond formation. A future goal is to have a model complex with a reduction potential that is closer to FNORs. I speculate that such a complex can still carry out direct NO reduction, but at a much slower rate, which might allow for the observation of intermediates of the reaction using spectroscopy, especially at low temperature. Therefore, a future direction of this project is to dampen the strong donicity of the ligand $[(Py_2PhO_2)MP]^{3-}$ to a lower level by replacing one of the phenolate groups in the ligand scaffold by a pyridine, resulting in the ligand $[(Py_3PhO)MP]^{2-}$ (Figure 8.2, Right). This modification was shown in a previous study to shift the reduction potential of a corresponding diiron complex more positively compared to $[Fe^{II}_2((Py_2PhO_2)MP)(OPr)_2]^-$,[21] putting this new ligand system closer to the reduction potential of native FNORs. Preliminary experiments conducted on the complex $[Fe^{II}_2((Py_3PhO)MP)(OAc)_2]$ showed that this compound is indeed able to mediate the direct reduction of NO to N_2O. Importantly, nitrosylation of $[Fe^{II}_2((Py_3PhO)MP)(OAc)_2]$ at -80 ^oC showed a significant amount of a $[hs\text{-}\{FeNO\}^7]_2$ complex formed, which will allow for the study of this intermediate going forward.[22] By varying the reaction temperature, other intermediates might be accessible as well with this complex.

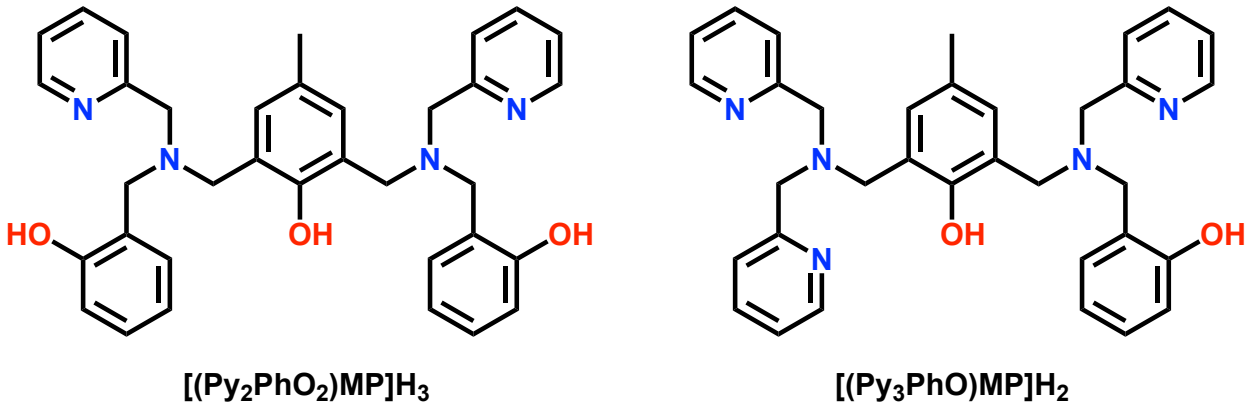

Figure 8.2 Left: ChemDraw of the ligand $H_3[(Py_2PhO_2)MP]$ used in Chapter 2. Right: The proposed $[(Py_3PhO)MP]H_2$ ligand proposed for reduction potential tuning.

FNORs are extremely efficient at NO reduction even though they operate at a relatively mild reduction potential. Nature typically engineers the active sites of enzymes, using both primary and secondary coordination groups, to carry out reactions as efficiently as possible. As discussed above, several DFT and experimental studies have emphasized the importance of a SCS tyrosine residue for NO reduction, by hydrogen bonding to one of the bound NO ligands, and mediating N-N bond formation. In Chapter 4, I carried out initial investigations on the effects of SCS hydrogen bond donors on the structure and reactivity of hs-$[\{FeNO\}^7]_2$ complexes, using amide groups installed on the $BPMP^-$ ligand scaffold. However, these amide groups bind strongly to iron via their O atoms, which greatly complicates matters. To overcome this problem, I propose to use amine groups instead of amides, because in this case, the SCS groups cannot directly bind to the iron centers and interfere with the coordination of NO.

In preliminary studies, I prepared the ligand $H[BPMP\text{-}NH_2]$ which contains primary amines instead of amides in the SCS, incapable of coordinating to the iron centers and competing with NO ligation, using a reported procedure.[23] Metallation of this ligand was carried out similarly to the complexes described in Chapter 4. The reaction yielded a bright yellow complex with the proposed chemical structure $[Fe_2(BPMP\text{-}NH_2)(OAc)](OTf)_2$ **(5)**. Mössbauer spectroscopy

revealed a clean quadrupole doublet with an isomer shift δ = 1.19 mm/s and a quadrupole doublet ΔE_Q = 2.58 mm/s. Nitrosylation of the yellow solution of **5** in CH_2Cl_2 yielded a dark brown solution. After recrystallization with hexane, a dark brown solid was collected. UV-Vis spectroscopy of the brown solid revealed a new band at 383 nm. Importantly, IR spectroscopy of a KBr pellet of the complex showed two new bands at 1762 and 1718 cm^{-1}, indicative of the formation of an asymmetric [hs-$\{FeNO\}^7$]$_2$ complex with two chemically inequivalent NO ligands. In the structure of this complex, $[Fe_2(BPMP\text{-}NH_2)(OAc)(NO)_2](OTf)_2$ **(6)**, I propose that one of the NO ligands is involved in hydrogen bonding with an SCS amine group, whereas the other one is not. The proposed structure is shown in the Appendix (Figure A1, left). The other primary amine likely forms a hydrogen bond with the bridging acetate, which would mimic the exact asymmetry of the FNOR active site. This is an exciting result that demonstrates that the use of amine SCS groups might be a fruitful route to explore the effect of hydrogen bonds on the geometric and electronic structure of hs-$\{FeNO\}^7$ units, and how this might affect reactivity.

In addition, the cyclic voltammogram of **6** shows an irreversible reduction event at -460 vs Fc^+/Fc (Appendix, Figure A1, left). It is worth noting that the reported reduction potential of $[Fe_2(BPMP)(OPr)(NO)_2](OTf)_2$ is -1.1 V vs Fc^+/Fc. This implies that the presence of a hydrogen bond has a dramatic effect on the reduction potential of the hs-$\{FeNO\}^7$ unit. These results are very promising, but further work needs to be conducted to solidify these conclusions, and further explore the potential role of the SCS in FNORs. Additional data obtained on complex **6** and discussion are provided in the Appendix.

we can further fine tune the hydrogen bonds of the ligand H[BPMP-NH_2] by modifying the primary amines into secondary amines with either an aryl ring (Ph-R type groups with R = electron withdrawing groups (EWGs): -NO_2, -COOR', -F or electron donating groups (EDGs):

^{t}Bu, -NH_2, -OR) or more bulky alkyl groups for steric protection (Scheme 8.4 and Figure 8.3). By introducing EDGs and EWGs, we can tune the acidity of the amines and in this way, the strength of the resulting hydrogen bonds, to find the right hydrogen bond strength that is required for either direct NO reduction, or the potential stabilization of the key hyponitrite intermediate. The initial studies should focus on modifying the SCS of $BPMP^{-}$ type ligands that can stabilize the [hs-$\{FeNO\}^7]_2$ intermediate. However, other ligands such as $[(Py_3PhO)MP]^{3-}$ could also be considered for the purpose of tuning the reduction potential at the same time (Figure 8.3). Ultimately, this approach would allow us to design a "perfect" model complex of FNORs, which can directly reduce NO to N_2O, and which can be tuned to potentially observe further intermediates of the reaction.

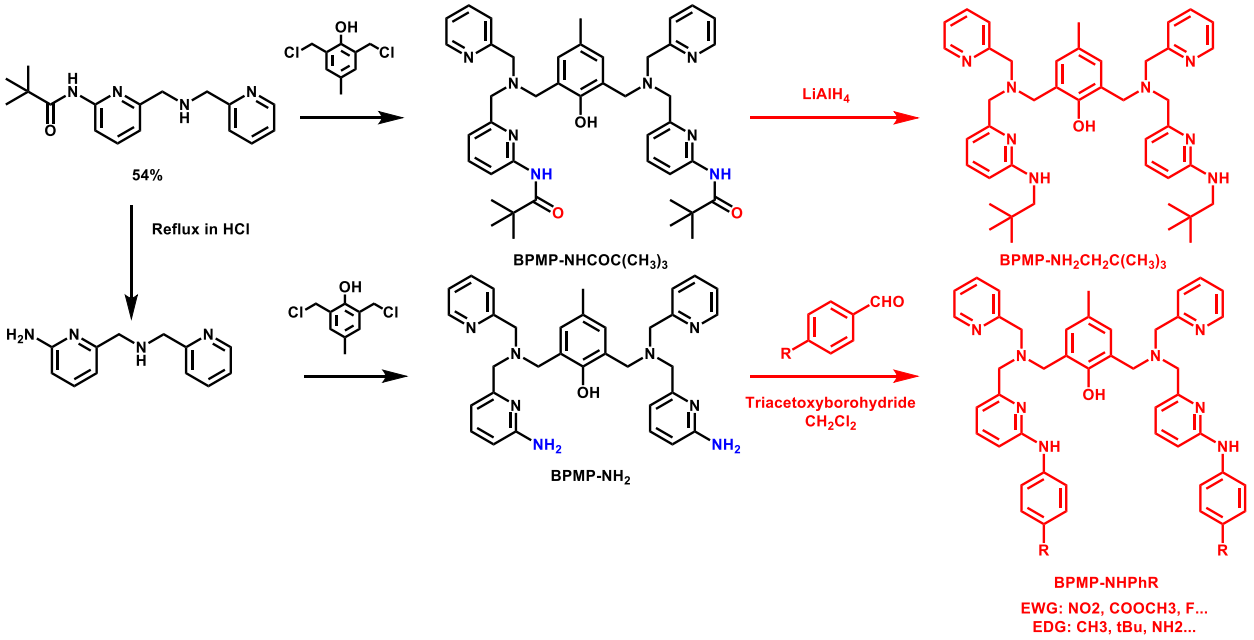

Scheme 8.4 Reported ligand synthesis for BPMP-NH_2 and proposed synthesis for new derivatives of this ligand that incorporate different EDG and EWG to tune the acidity of the proton of the amine substituent.[23] Additionally, a synthetic route for the transformation of the amide groups of the BPMP-$NHCOC(CH_3)_3$ ligand into secondary amines is proposed.

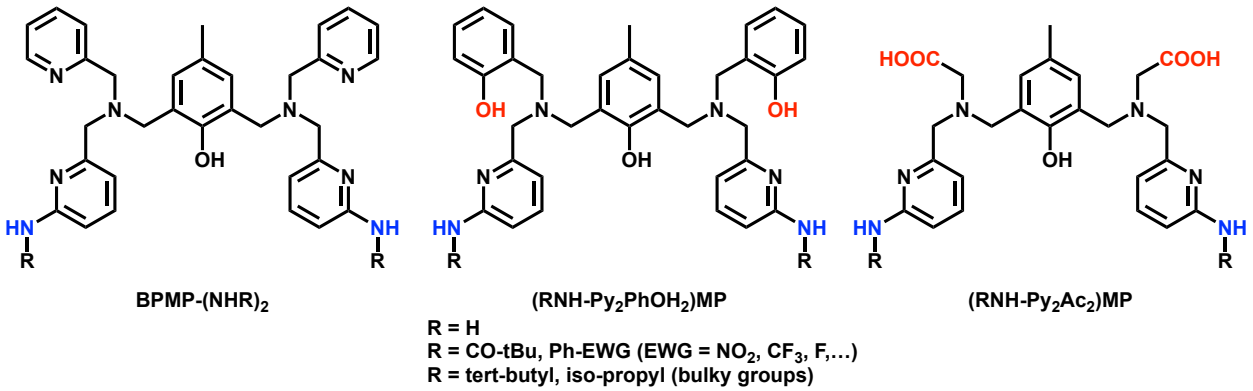

Figure 8.3 Proposed ligand modifications for different scaffolds that feature hydrogen bond donors in the SCS, suitable for modeling FNORs.

In Chapter 5, the coordination chemistry of hyponitrite with non-heme iron complexes is explored. However, these complexes are not the best models for the active site of FNORs. The future direction of this project should be to study the chemistry of hyponitrite with complexes such as $[Fe_2(BPMP)(OPr)]^{2+}$, $[Fe_2((Py_2PhO_2)MP)(OPr)_2]^{-}$, $[Fe_2(BPMP\text{-}NH_2)(OAc)]^{2+}$, etc., as described in this thesis. Using these model complexes, with structural and chemical properties that better reflect those of the active sites of FNORs, we can potentially isolate and characterize a hyponitrite complex on the pathway towards N_2O formation. Additionally, we could introduce Lewis acids into the putative hyponitrite complexes, such as $[Fe_2(BPMP)(OPr)(N_2O_2)]$. These Lewis acids can potentially help isolate or activate stable hyponitrite complexes, or change the coordination mode of the hyponitrite ligand (Figure 8.4). The investigation of the relationship between the coordination mode of hyponitrite to non-heme diiron cores and the activation of the ligand towards N_2O formation would provide key insights into the reaction mechanism of not only FNORs, but other NO reductases as well.

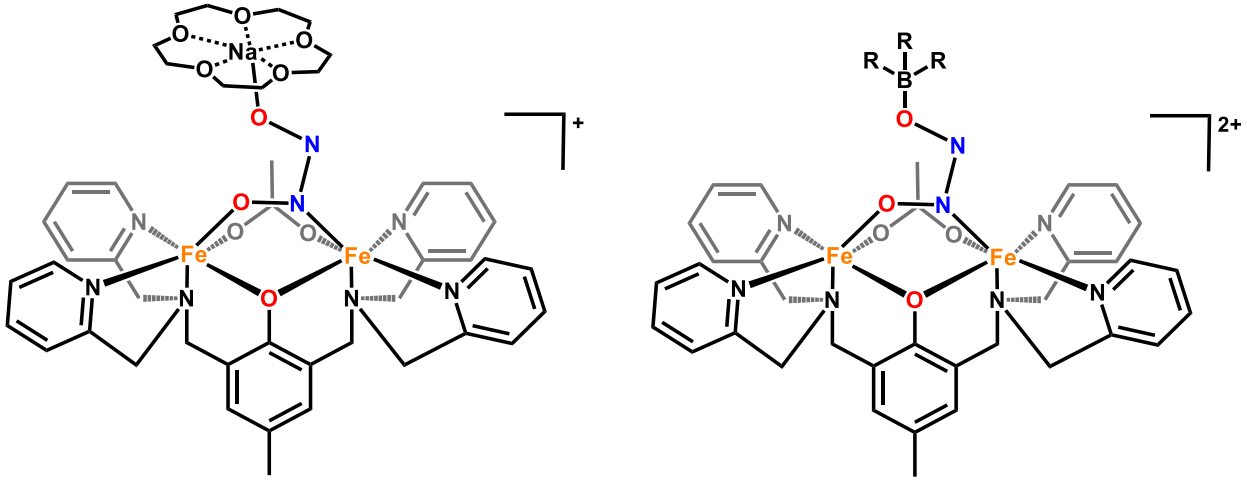

Figure 8.4 Proposed alternative coordination mode of hyponitrite in non-heme iron complex [{Fe_2(BMPA-PhO)$_2$}$_2$(μ-N_2O_2)](OTf)$_2$ under the influences of different Lewis acids.

8.3 References

1. Khatua, S.; Majumdar, A. Flavodiiron Nitric Oxide Reductases: Recent Developments in the Mechanistic Study and Model Chemistry for the Catalytic Reduction of NO. *J. Inorg. Biochem.* **2015**, *142*, 145-153.
2. Caranto, J. D.; Weitz, A.; Giri, N.; Hendrich, M. P.; Kurtz, D. M., Jr. . A Diferrous-Dinitrosyl Intermediate in the N_2O-Generating Pathway of a Deflavinated Flavo-Diiron Protein. *Biochemistry* **2014**, *53*, 5631–5637.
3. Caranto, J. D.; Weitz, A.; Hendrich, M. P.; Kurtz, D. M., Jr. The Nitric Oxide Reductase Mechanism of a Flavo-Diiron Protein: Identification of Active-Site Intermediates and Products. *J. Am. Chem. Soc.* **2014**, *136*, 7981–7992.
4. Kurtz, D. M., Jr. Flavo-Diiron Enzymes: Nitric Oxide or Dioxygen Reductases? *Dalton Trans.* **2007**, 4115-4121.
5. Hayashi, T.; Caranto, J. D.; Wampler, D. A.; Kurtz, D. M., Jr.; Moënne-Loccoz, P. Insights into the Nitric Oxide Reductase Mechanism of Flavodiiron Proteins from a Flavin-Free Enzyme. *Biochemistry* **2010**, *49*, 7040−7049.
6. Lu, J.; Bi, B.; Lai, W.; Chen, H. Origin of Nitric Oxide Reduction Activity in Flavo-Diiron NO Reductase: Key Roles of the Second Coordination Sphere. *Angew. Chem. Int. Ed.* **2019**, *58*, 3795-3799.
7. Biswas, S.; Kurtz, D. M.; Montoya, S. R.; Hendrich, M. P.; Bominaar, E. L. The Catalytic Role of a Conserved Tyrosine in Nitric Oxide-Reducing Non-heme Diiron Enzymes. *ACS Catal.* **2020**, *10*, 8177-8186.
8. White, C. J.; Speelman, A. L.; Kupper, C.; Demeshko, S.; Meyer, F.; Shanahan, J. P.; Alp, E. E.; Hu, M.; Zhao, J.; Lehnert, N. The Semireduced Mechanism for Nitric Oxide Reduction by Non-Heme Diiron Complexes: Modeling Flavodiiron Nitric Oxide Reductases. *J. Am. Chem. Soc.* **2018**, *140*, 2562-2574.

9. Speelman, A. L.; White, C. J.; Zhang, B.; Alp, E. E.; Zhao, J.; Hu, M.; Krebs, C.; Penner-Hahn, J.; Lehnert, N. Non-heme High-Spin {FeNO}$^{6-8}$ Complexes: One Ligand Platform Can Do It All. *J. Am. Chem. Soc.* **2018**, *140*, 11341-11359.
10. Speelman, A.; Zhang, B.; Krebs, C.; Lehnert, N. Structural and Spectroscopic Characterization of a High-Spin {FeNO}^{6} Complex with an Iron(IV)-NO$^-$ Electronic Structure. *Angew. Chem. Int. Ed.* **2016**, *55*, 6685-6688.
11. Fujisawa, K.; Soma, S.; Kurihara, H.; Ohta, A.; Dong, H. T.; Minakawa, Y.; Zhao, J.; Alp, E. E.; Hu, M. Y.; Lehnert, N. Stable Ferrous Mononitroxyl {FeNO}^{8} Complex with a Hindered Hydrotris(pyrazolyl)borate Coligand: Structure, Spectroscopic Characterization, and Reactivity Toward NO and O_2. *Inorg. Chem.* **2019**, *58*, 4059-4062.
12. Speelman, A. L.; Lehnert, N. Characterization of a High-Spin Non-Heme {FeNO}^{8} Complex: Implications for the Reactivity of Iron Nitroxyl Species in Biology. *Angew. Chem. Int. Ed.* **2013**, *52*, 12283-12287.
13. Confer, A. M.; McQuilken, A. C.; Matsumura, H.; Moënne-Loccoz, P.; Goldberg, D. P. A Nonheme, High-Spin {FeNO}^{8} Complex that Spontaneously Generates N_2O. *J. Am. Chem. Soc.* **2017**, *139*, 10621-10624.
14. Dong, H. T.; White, C. J.; Zhang, B.; Krebs, C.; Lehnert, N. Non-Heme Diiron Model Complexes Can Mediate Direct NO Reduction: Mechanistic Insight into Flavodiiron NO Reductases. *J. Am. Chem. Soc.* **2018**, *140*, 13429-13440.
15. Berto, T. C.; Hoffman, M. B.; Murata, Y.; Landenberger, K. B.; Alp, E. E.; Zhao, J.; Lehnert, N. Structural and Electronic Characterization of Non-Heme Fe(II)-Nitrosyls as Biomimetic Models of the Fe_B Center of Bacterial Nitric Oxide Reductase (NorBC). *J. Am. Chem. Soc.* **2011**, *133*, 16714–16717.
16. Van Stappen, C.; Lehnert, N. Mechanism of N-N Bond Formation by Transition Metal-Nitrosyl Complexes: Modeling Flavodiiron Nitric Oxide Reductases. *Inorg. Chem.* **2018**, *57*, 4252-4269.
17. Kindermann, N.; Schober, A.; Demeshko, S.; Lehnert, N.; Meyer, F. Reductive Transformations of a Pyrazolate-Based Bioinspired Diiron−Dinitrosyl Complex. *Inorg. Chem.* **2016**, *55*, 11538-11550.
18. Tonzetich, Z. J.; Héroguel, F.; Do, L. H.; Lippard, S. J. Chemistry of Nitrosyliron Complexes Supported by a β-Diketiminate Ligand. *Inorg. Chem.* **2011**, *50*, 1570-1579.
19. Tonzetich, Z. J.; Do, L. H.; Lippard, S. J. Dinitrosyl Iron Complexes Relevant to Rieske Cluster Nitrosylation. *J. Am. Chem. Soc.* **2009**, *131*, 7964-7965.
20. Anderson, J. S.; Rittle, J.; Peters, J. C. Catalytic conversion of nitrogen to ammonia by an iron model complex. *Nature* **2013**, *501*, 84-87.
21. Neves, A.; Aires de Brito, M.; Drago, V.; Griesar, K.; Haase, W. A new asymmetric N5O2-donor binucleating ligand and its first FeIIFeIII complex as a model for the redox properties of uteroferrin. *Inorg. Chim. Acta* **1995**, *237*, 131-135.
22. Neves, A.; Aires de Brito, M.; Drago, V.; Griesar, K.; Haase, W. A new asymmetric N5O2-donor binucleating ligand and its first FeIIFeIII complex as a model for the redox properties of uteroferrin. *Inorganica Chimica Acta* **1995**, *237*, 131-135.
23. Comba, P.; Gahan, L. R.; Mereacre, V.; Hanson, G. R.; Powell, A. K.; Schenk, G.; Zajaczkowski-Fischer, M. Spectroscopic Characterization of the Active $Fe^{III}Fe^{III}$ and $Fe^{III}Fe^{II}$ Forms of a Purple Acid Phosphatase Model System. *Inorg. Chem.* **2012**, *51*, 12195-12209.

Appendix

A.1 Chapter 8

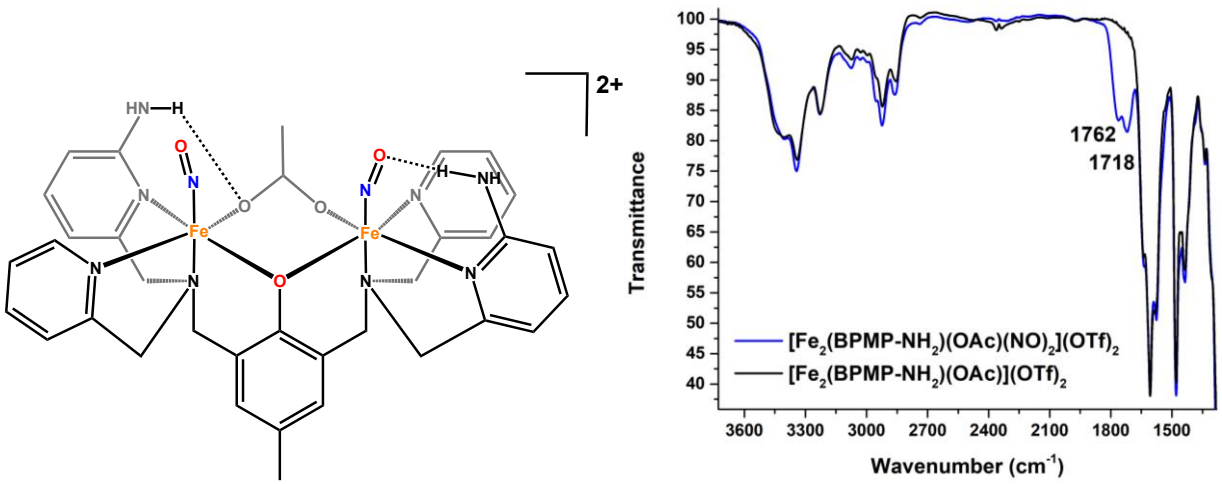

Figure A1 Left: ChemDraw of the proposed structure of the dinitrosyl complex **6**. Right: ATR IR spectra of **5** and **6** in the solid state taken in a KBr pellet.

Since primary amines are EDGs, the ligand supposed to be more donating, thus shifts the redox potential more negatively if primary coordination plays an important role. However, the redox potential shifted positively in this case, implied that the primary effect is the hydrogen bonds in the SCS which activated one of the hs-$\{FeNO\}^7$ moiety and decreased the barrier for semireduction. Reduction of **6** with one equivalent of $CoCp_2$ resulted in the complete disappearance of the NO stretching bands and a new band at 1692 cm^{-1} was revealed. Spectro-electro chemistry with IR spectroscopy showed a significant amount of N_2O formation immediately upon reduction, concomitant with the disappearance of the NO stretching bands

(Figure A1, right). Therefore, **6** can undergo semireduction, similar to $[Fe_2(BPMP)(OPr)(NO)_2](OTf)_2$, to form N_2O. Fascinatingly, IR spectroscopy under spectro-electro chemistry condition at -800 mV further revealed that the two NO signals did not disappear simultaneously. The stronger N–O band at 1762 cm^{-1} disappeared before the second one at 1718 cm^{-1} diminished along with another signal at 1762 cm^{-1} (Figure A2 and A3). This observation supports the asymmetry induced by the hydrogen bonds between the two NO ligands, mimicking the active site of FNORs. Future studies will focus on characterizing the product formed after reduction and the identity of the species formed at both room temperature and -80°C.

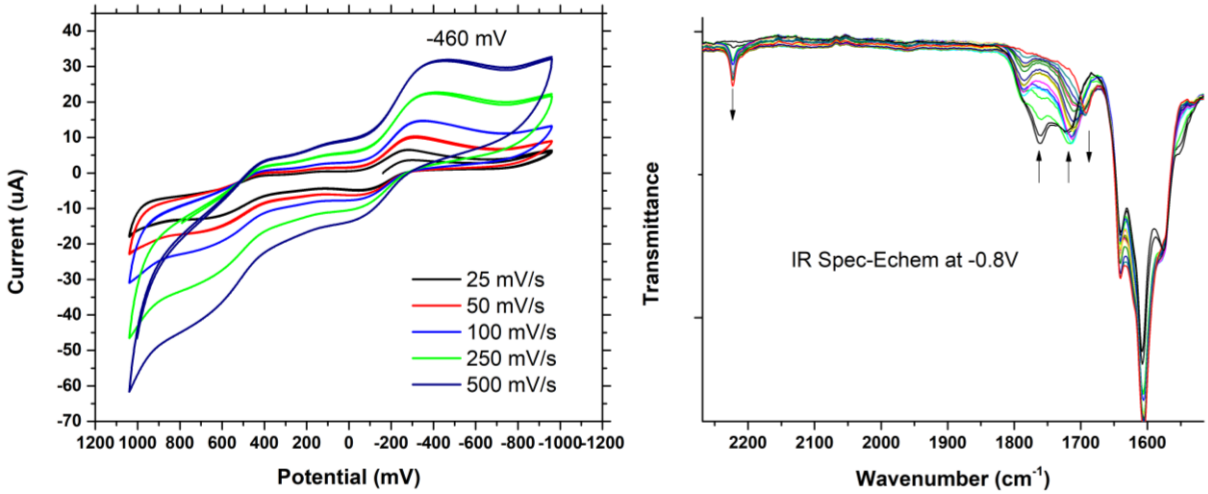

Figure A2 Left. Cyclic Voltammogram of complex **6** vs Fc^+/Fc. Right. IR Spec-Echem with potential holding at -0.8 V showing slow asymmetric decade of the two NO signals to form N_2O and a new signal at 1691 cm^{-1}.

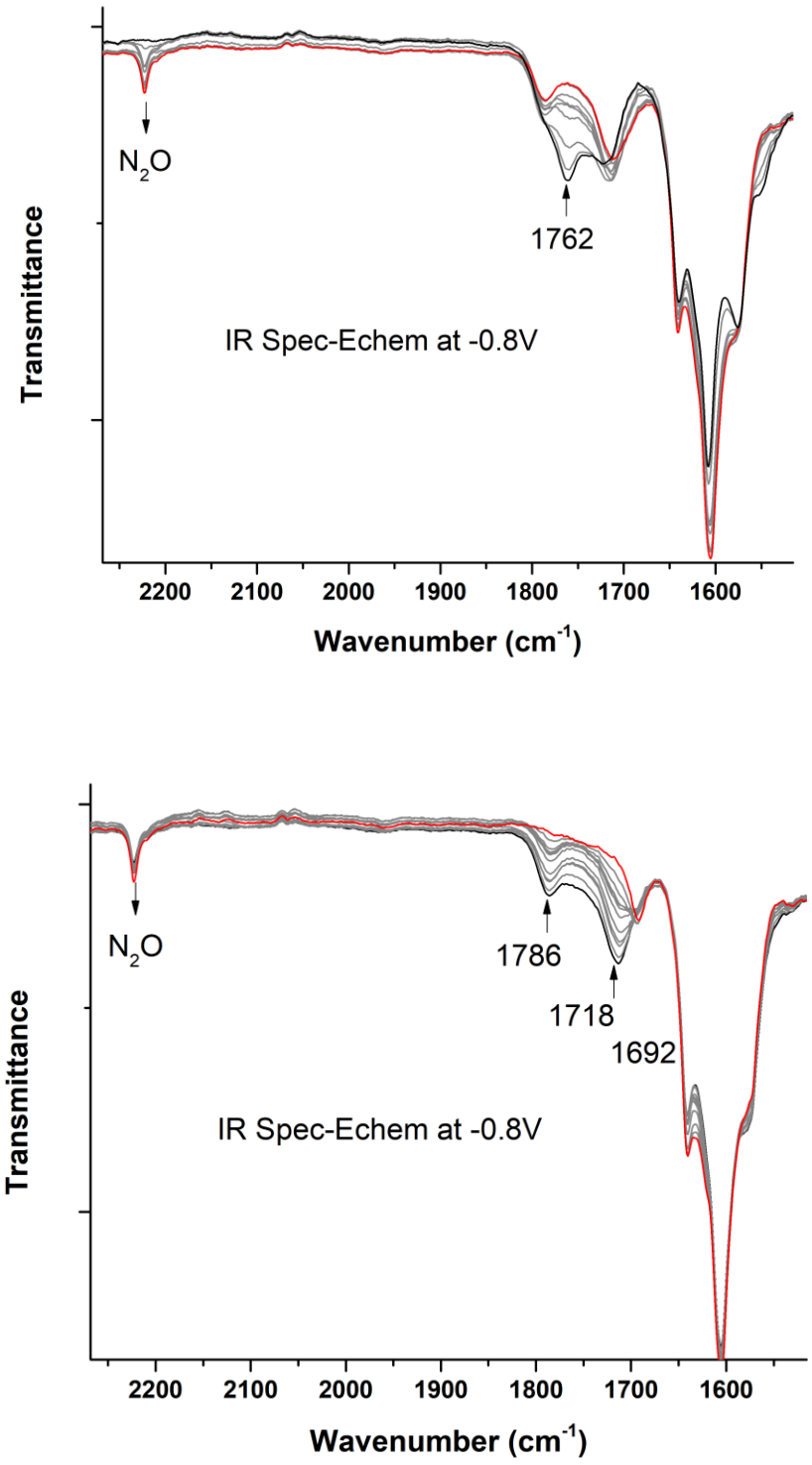

Figure A3 Break down of the changes in solution IR when **6** is reduced under spectro-electro chemistry conditions.